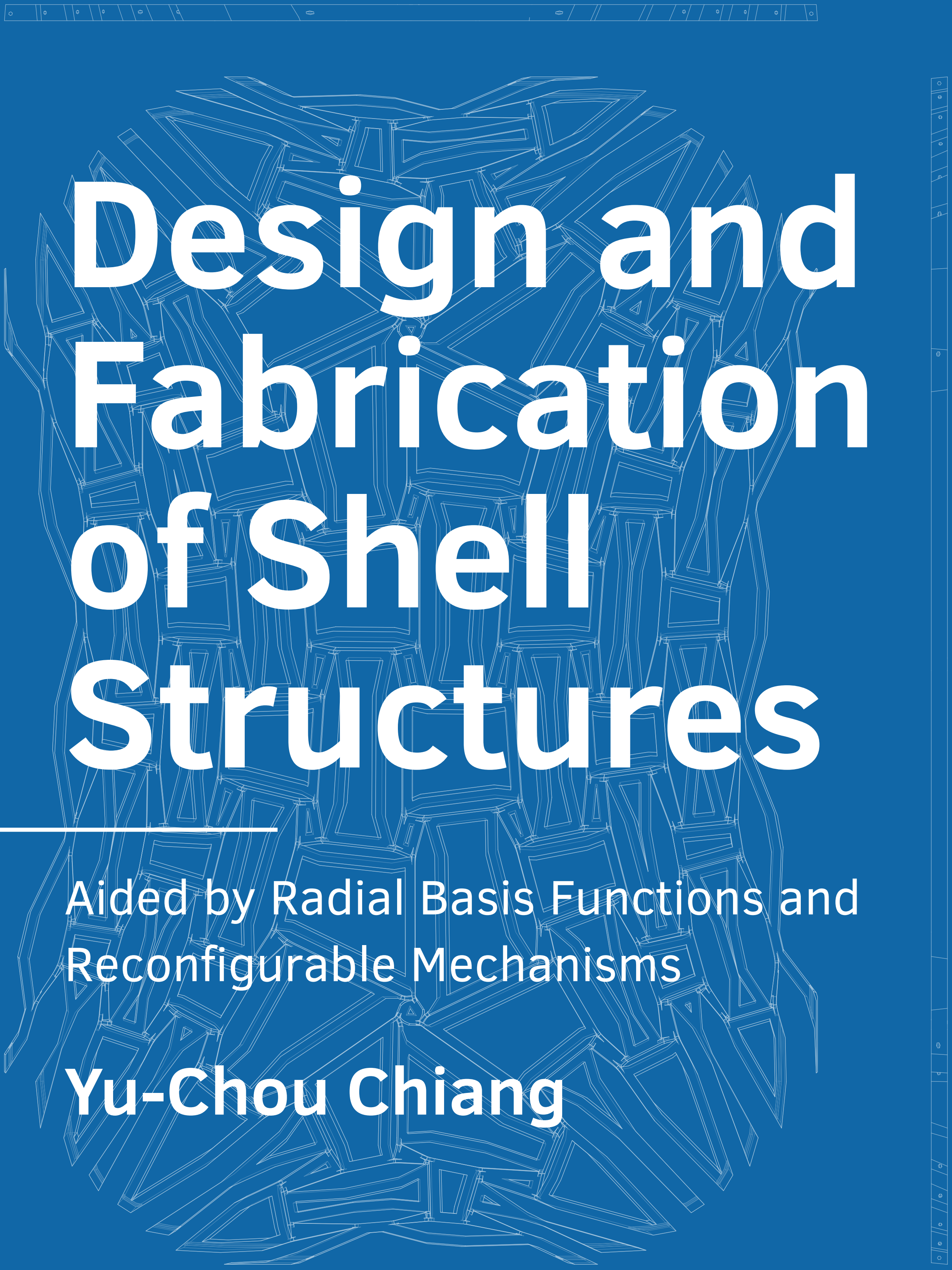

Design and Fabrication of Shell Structures

Aided by Radial Basis Functions and Reconfigurable Mechanisms

Yu-Chou Chiang

Design and Fabrication of Shell Structures

Aided by Radial Basis Functions and Reconfigurable Mechanisms

Yu-Chou Chiang

A+BE | Architecture and the Built Environment | TU Delft BK

22#03

Design | Sirene Ontwerpers, Véro Crickx

Cover image | Plan and elevation drawings of the hoop-actuated mechanism as shown in section 6.3. Its flat configuration is on the front cover, whilst the doublecurved configuration is on the back cover.

Keywords | Shell structure; Funicular form-finding; Radial basis functions; Fabrication-aware design; Architectural geometry; Reconfigurable mechanism

ISBN 978-94-6366-508-7
ISSN 2212-3202

This dissertation is open access at https://doi.org/10.7480/abe.2022.03

Unless otherwise specified, all the photographs in this thesis were taken by the author. For the use of illustrations effort has been made to ask permission for the legal owners as far as possible. We apologize for those cases in which we did not succeed. These legal owners are kindly requested to contact the author.

Design and Fabrication of Shell Structures

AIDED BY RADIAL BASIS FUNCTIONS AND RECONFIGURABLE MECHANISMS

Dissertation

for the purpose of obtaining the degree of doctor
at Delft University of Technology,
by the authority of the Rector Magnificus Prof.dr.ir. T.H.J.J. van der Hagen,
chair of the Board for Doctorates,
to be defended publicly on
Tuesday the 1st of February 2022 at 15:00 o'clock

by

Yu-Chou Chiang

Master of Science in Civil Engineering,
National Taiwan University, Taiwan,
born in Taoyuan, Taiwan.

This dissertation has been approved by the promotors.

Composition of the doctoral committee:

Rector Magnificus	chairperson
Prof.dr. M. Overend	Delft University of Technology, promotor
Dr.ir. F.A. Veer	Delft University of Technology, promotor
Independent members:	
Prof.dr. A.A. Zadpoor	Delft University of Technology
Prof.dr. H. Pottmann	King Abdullah University of Science and Technology, Saudi Arabia
Prof. A. McRobie	University of Cambridge, United Kingdom
Prof.dr. S. Adriaenssens	Princeton University, United States
Prof.dr.ir. L.J. Sluys	Delft University of Technology, reserve member
Other member:	
Ir. A. Borgart	Delft University of Technology, supervisor

Taiwan
Ministry of
Education

In dedication to my mother 黄秀珍,
as well as my wife 林郁文.

Acknowledgements

This dissertation could not have reached its current state without the invaluable input from my supervisors, peers, friends, and family.

First, I have to express my gratitude to my current supervision team. Prof. Mauro Overend helped me to sharpen my arguments as well as to perfect this dissertation. Dr. Fred Veer pointed out my writing blind spots and taught me how to overcome them. Andrew Borgart guided me with enlightening references whenever I lost orientation and whose kind, patient encouragement picked me up every time I fell.

I am also indebted to Pim Buskermolen for proofreading the early drafts of this dissertation, Peter Eigenraam for sharing his wonderful teaching techniques with me, Ate Snijder for his sense of humor, Dr. Li Qengpeng for his valuable advice and Dr. Charalampos Andriotis for his encouraging words.

Equal thanks also go to my first supervision team. Prof. Peter Luscuere provided me with the life-changing opportunity to start this journey. I would also like to thank Dr. Henriette Bier for sharing her radical ideas regarding digital design and fabrication. Dr. Sina Mostafavi, who led me into parametric design and robotic operation, also shared his insights on the architectural industry as well as memorable afternoon strolls.

I am also beholden to Veronika Laszlo for her kind help on various personal and nonpersonal occasions. I am also grateful to Tessa Vermeulen and Song Bo for their administrative support, Jan van Beek for his stress-easing consultations, and Adam Radford for his excellent English coaching.

Prototypes of this dissertation could not have been completed without support from Teun Verkerk at Science Centre Delft and Paul de Ruiter at the Chair of Design Informatics who granted me access to 3D printers, Hsieh Chi-Hua at OH Precision who granted me access to water-jets, Dr. Chen Cheng-Chen at Tamkang University gave me access to CNC machines, and Dr. Chung Min-Jay at National Taiwan University for kindly allowing me to use the facilities at their workshop. I would like to thank the group of helping hands who assembled the 4m-span pavilion at Tamkang University and National Taiwan University. The group consists of Chen Chia-Chun, Chen Chia-Hung, Jeremy Chen, Chen Chung-Ta, Chen Weilin, Chen Yu, Chien Chen-Hsuan, Chiu Chi-Kuei, Lin Chin-Ying, Lu Zong-Lin, Tsai Po-Wei, Wu Yu-Xian.

The continuous support of Dr. Hervé Capart, my master's thesis supervisor, was pivotal when I switch my academic path from hydraulic engineering to structural design. Without his encouragement, I would not have dared to choose this research topic, which was seldom mentioned in my bachelor's curriculum.

I will also treasure the company of fellow Taiwanese PhD researchers, including Cinco Hsinko Yu, Chiu Po-Sheng, Chen Po-Ju, Lin Min, as well as PhD researchers in room 01.West.250, including Miktha Alkadri, Nick ten Caat, Du Tiantian, Berk Ekici, Guo Xiao, Pan Wang, Prateek Wahi, Yang Ding, to name just a few.

I would also like to express my gratitude to my parents Chaing Jen-Hsiang and Huang Hsiu-Chen as well as my sister Chaing Yu-Yun for their unconditional love and support, despite my long absence from home. My final thank you is to my soulmate, Lin Yu-Wen, for her unwavering support, for showing me the importance of being kinder to myself, and for reminding me that there is a world outside of academia.

NOTATION

$x,\ y,\ z$	Cartesian coordinates [length]
$\mathbf{x}$	Position vector
$\xi,\ \eta,\ \zeta$	Cartesian coordinates of reciprocal diagram corresponding to $x,\ y$, and z, respectively [length]
$\boldsymbol{\xi}$	Position vector of reciprocal diagram corresponding to $\mathbf{x}$

$d_x,\ d_{xx}$	Operator for derivatives, especially for in text expressions, such that $d_x f(x) = \frac{d}{dx} f(x)$ and $d_{xx} f(x) = \frac{d^2}{dx^2} f(x)$
$F(x, y)$	Airy stress function
$F^*(\xi, \eta)$	Reciprocal diagram corresponding to $F(x, y)$
$\mathbf{H}$	Hessian matrix or Hessian operator
$\mathbf{J}$	Jacobian matrix
$N_{xx},\ N_{yy}$	Normal stress resultants per unit horizontal length [force / length]
N_{xy}	Shear stress resultants per unit horizontal length [force / length]
$\widetilde{N}_{xx},\ \widetilde{N}_{yy}$	Normal stress resultants per unit curved length [force / length]
$\widetilde{N}_{xy}$	Shear stress resultants per unit curved length [force / length]
$p_x,\ p_y,\ p_z$	Loads per unit horizontal area [force / length^2]
$P_x,\ P_y$	Integrals such that $P_x = \int p_x\, dx$ and $P_y = \int p_y\, dy$
$\mathbb{R}$	The set of real numbers
$S(x, y)$	Self-accompanying surface
$\mathbf{A}^{\mathrm{T}}$	Transpose of an arbitrary matrix $\mathbf{A}$
$Z(x, y)$	Shape function (middle surface) of a membrane shell

λ_i	Magnitude coefficient of the radial basis function ϕ_i
∇	Gradient operator
$\partial_x,\ \partial_{xy}$	Operator for partial derivatives, especially for in-text expressions, such that $\partial_x f(x, y) = \frac{\partial}{\partial x} f(x, y)$ and $\partial_{xy} f(x, y) = \frac{\partial^2}{\partial x \partial y} f(x, y)$
$\phi_i(\lVert \mathbf{x} - \boldsymbol{\mu}_i \rVert; \rho_i)$	Radial basis function of $\mathbf{x}$ with center $\boldsymbol{\mu}_i$ and shape coefficient ρ_i

$:$	Operator for double-inner product of two same size matrices, such that $\mathbf{A}{:}\mathbf{B} = \sum_i \sum_j A_{ij} B_{ij}$

CONTENTS

SUMMARY

SHELL STRUCTURES carry loads with their thin yet curved shapes. Being thin means shells require little material, which is desirable for minimizing embodied carbon footprints. However, the feature of being curved implies shells require immense effort to design and fabricate. This is due to curved surfaces are geometrically more complex to be defined and built than planar or linear structural members. To address the challenges, this dissertation consists of three parts: developing a design algorithm based on radial basis functions (RBFs), inventing a fabrication technique based on reconfigurable mechanisms, and producing prototypes based on the new algorithm and mechanism.

The first part of this dissertation introduces a new algorithm based on RBFs for designing smooth membrane shells. The algorithm has a breakthrough in that it unifies three features that were incompatible with one another in the existing methods. First, the algorithm can take a stress distribution as input and then generate the shape of the membrane that is beyond the capability of conventional finite element analysis. Second, the algorithm can take a shape as an input and output the stress distribution. This is not attainable for mainstream form-finding algorithms, such as the Force Density Method. Third, the algorithm can take not only a vertical load into account but also horizontal loads. These are critical for shells in seismic-prone areas, although often they are omitted in existing form-finding methods, such as Thrust Network Analysis.

The second part of the dissertation presents a new system of flat-to-curved mechanisms. Thus, a shell can be fabricated in flat configurations and deployed into double-curved states. Such a mechanism consists of panels connected by nearly vertical but slightly tilted hinges. The tilted hinges and panels are distributed in a pattern that allows the mechanism to contract non-homogeneously and thus induce the change of the mechanism's Gaussian curvature. Prototypes made from 3D printing and water-jet cutting can be transformed from flat configurations into double-curved states, validating this mechanical system.

The last part of this dissertation demonstrates the integral application of the RBFs form-finding algorithm and the flat-to-curved mechanisms. The prototypes designed and produced deliver form-found shapes that have spans ranging from 0.2 to 4 meters.

This dissertation contributes to the development and distribution of shell structures by developing computer algorithms and digital fabrication techniques to minimize the hurdles of designing and fabricating shell structures.

SAMENVATTING

SCHAAL CONSTRUCTIES zijn in staat om door hun gekromde vorm belastingen te dragen, ondanks hun geringe dikte. Doordat schalen dun kunnen zijn door hun gekromde vorm hebben ze relatief weinig materiaal nodig, wat noodzakelijk is om de CO2-voetafdruk te kunnen verminderen. Het feit dat een schaal gekromd is, en vaak zelfs dubbel, heeft tot gevolg dat hun maakbaarheid complex is. De reden hiervoor is dat gekromde vlakken geometrisch die niet ontwikkelbaar zijn niet opgebouwd kunnen worden door enkel vlakke onderdelen. Deze dissertatie wil deze problematiek adresseren, en bestaat derhalve uit drie onderdelen: de ontwikkeling van een computer algoritme gebaseerd op “radial basis functions (RBFs)”, de ontwikkeling van een fabricage methode gebaseerd op herconfiguurbare mechanismen, en het produceren van prototypes gebaseerd op de nieuwe algoritme en fabricage methode.

Het eerste gedeelte van deze dissertatie introduceert een nieuw computer algoritme gebaseerd op RBFs voor het ontwerpen van membraan schalen met een vloeiende vorm, welke hun belasting kunnen afdragen zonder de noodzaak om gebruik te maken van momenten en dwarskrachten. Het algoritme is een doorbraak omdat het de volgende drie eigenschappen verenigd die in andere bestaand methoden in deze combinatie niet voorkomen. Ten eerste kan het algoritme een spanningsverdeling als uitgangspunt nemen om de vorm van een membraan schaal te genereren die verder gaat dan de mogelijkheden van een conventionele eindige elementen methode. Als tweede, kan het algoritme ook werken als een wederkerige methode en een vorm nemen als uitgangspunt en een daarbij behorende spanningsverdeling produceren. Dit is niet mogelijk met gevestigde methoden zoals “force density”. Als derde, kan het algoritme naast verticale ook horizontale belastingen verwerken in relatie tot vormen van membraan schalen. Horizontale krachten zijn van belang in gebieden met seismische activiteit en worden vaak veronachtzaamt in bestaande vorm ontwikkelingsmethode, zoals “thrust network analysis”.

In het tweede gedeelte van de dissertatie wordt een nieuwe soort mechanisme gepresenteerd om van een plat vlak een gekromd vlak te maken. Op deze manier kan een schaal gefabriceerd worden uit ongelijke vlakke panelen die hergeconfigureerd kunnen worden om een dubbel gekromd vlak te vormen. De panelen zijn onderling verbonden door bijna verticale scharnieren die licht gekanteld zijn. De panelen zijn in het platte vlak dusdanig gerangschikt in een patroon die toelaat dat door een verandering van de kromming van Gauss in de scharnieren een gekromd vlak volgt. De vlakke panelen zijn gemaakt met behulp van 3D printen en water straal snijden.

In het derde en laatste gedeelte van de dissertatie wordt het RBFs algoritme gebruik voor het vinden van verschillende vormen voor membraan schalen die vervolgens worden uitgevoerd met vlakke panelen die via het ontwikkelde mechanisme principe een gekromd vlak vormen. Deze prototypes hebben overspanningen van 0,2 tot 4 meter.

Deze dissertatie draagt bij tot de ontwikkeling en disseminatie van schaal constructies, door middel van de ontwikkelde computer algoritme en de digitale fabricage techniek die helpen om de complexiteiten van het construeren van schaal constructies te overkomen.

1

INTRODUCTION

The [membrane] shell is the most honest of structures...,
which lends itself less than any other structure
to attempts to hide inadequate design
under camouflage or cladding.

Jörg Schlaich[1]

---

[1] as cited in Holgate, 1997, p.13

Membrane shells carry loads with their curved shapes and in-plane tension and compression, collectively called membrane stresses. Well-designed membrane shells are typically much thinner than their bending-dominated equivalents, such as slabs. Thus, shells are considered efficient structures in terms of material usage. These thin shells also arguably deliver a side benefit: elegance (von Meiss, 2000; Schlaich, 2004). Aesthetics, however, is not the main focus of this dissertation. Instead, this dissertation investigates how to obtain ideal shapes for shells and how to fabricate them physically.

Most structural systems, such as floors or girder bridges mobilize internal bending moments and shear forces to carry loads to the supports. These structures must have certain thicknesses to exert bending moments. Shell-like structures (e.g., masonry vaults and arches) on the contrary carry the self-weight and external loads with little bending moments. However, shaping these shell-like structures so that bending moments are minimized, is not a trivial exercise. Medieval stonemasons relied on empirical knowledge to design and explore new forms that have minimized bending moments (Addis, 2007). Since the 17th century, scientists and engineers have developed more rigorous methods to find and explore forms free of bending moments (Heyman, 1977, 1995). These explorative processes are now called *form-finding*. In recent decades, researchers have developed computational algorithms for widening the range of these structural solutions.

The established algorithms require input (e.g., anticipated force flow) to find the corresponding form but provide no recommendation on how to modify inputs in order to approximate a certain desired shape. The first significant contribution of this dissertation is the development of an algorithm based on a numerical method—radial basis functions. The algorithm takes either an initial stress flow or shape as input. The algorithm then generates the corresponding shape or stress flow as output.

Although the form-found shapes are material-efficient structures, they might not always be the most economical solution, given that substantial labor is needed to fabricate the double-curved shapes of shells. The scarcity of concrete and steel made concrete shells popular in the 1950s. Soon afterwards, in the 1970s, the heydays finished (Meyer & Sheer, 2005), when the labor cost for the curved form-work increased, outweighing the savings in materials. From a sustainable development point of view, whilst materials are inexpensive to buy, they are costly in terms of embodied greenhouse gas emissions and the corresponding impact on the climate. The pressing need to reduce embodied emissions and the availability of new computational design and emerging fabrication methods may lead to a resurgence of shells. To be more specific, the curved shell surface can now be discretized into a series of flat elements using theories developed in discrete differential geometry (Pottmann, Liu, Wallner, Bobenko, & Wang, 2007). Meanwhile, computer-controlled machines can cut industrially mass-produced flat materials into the desired shapes with minimal labor hours (Mitchell, 2001; Zipkin, 2001). Thus the components of shells can be fabricated economically.

Even if the components can be fabricated economically, some considerable work is still required to assemble them. The second notable contribution of this dissertation is reducing the work needed for assembly, by extending the theory of discrete differential geometry to discretize double-curved surfaces into a flat mechanism that consists of interconnected flat panels. The mechanism can be later reconfigured into a pre-defined double-curved shape. In combination with the above-mentioned form-finding algorithm, the mechanism can deliver some form-found shell structures.

OUTLINE OF THE INTRODUCTION CHAPTER

Section 1.1 reviews the historical development of form-finding methods for designing shell structures. Section 1.2 identifies the research objectives for developing a form-finding algorithm. Section 1.3 discusses existing strategies for constructing double-curved shells. Section 1.4 proposes the research objectives for fabrication and construction. Section 1.5 provides the outline of the rest of the dissertation.

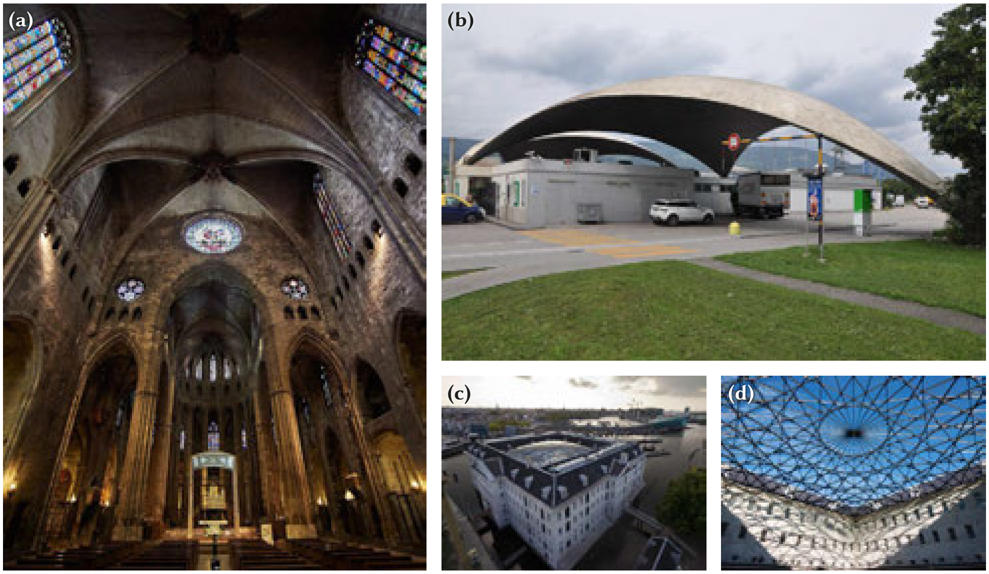

Figure 1.1: Examples of built shell structures. (a) The widest vaulted nave in the world (22.98m), Girona Cathedral, Spain. (b) *Raststätte Deitingen* [Deitingen Service Station], Deitingen, Switzerland. (c) Courtyard of the Dutch Maritime Museum, Amsterdam, the Netherlands. [Source: (a) llondru@flickr; (b) Peter Eigenraam; (c) BRS Building Systems. (d) Ney & Partners - www.photo-daylight.com]

1.1. REVIEW OF MEMBRANE SHELLS AND FORM-FINDING

A shell is a thin and curved structure (Williams, 2014). The small thickness implies that the bending rigidity is much lower than its stretch rigidity. When a shell carries loads with in-plane tension and compression (membrane actions), and does not rely on bending moments, the shell is referred to as a *membrane shell* (Calladine, 1989; Csonka, 1987).

Built membrane shells. Several types of structures belong to the general collection of membrane shells. Examples include: medieval masonry vaults, concrete shells, membrane structures that were erected in the late 20th century, and contemporary glazed roofs.

Masonry has almost no tension capacity in the mortar joint, and thus has limited bending moment capacity (Heyman, 1995). This property does not cause stonemasons many problems when building walls or columns, which are largely in compression, but it is more challenging when a structure has to span over an opening. To span between columns, ancient Greeks used monolithic stone lintels to avoid a joint, but the bending moment still

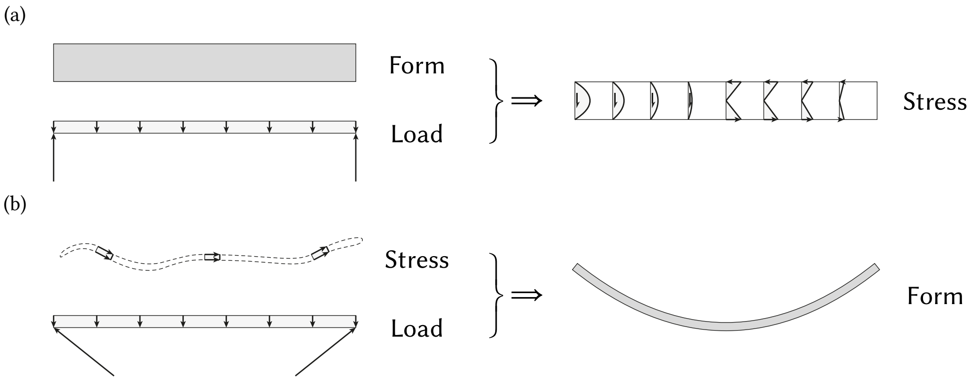

Figure 1.2: The differences between conventional structural design and form-finding. (a) In conventional structural design, the form is predefined. Then structural engineers calculate the stress distribution under a certain load case. (b) In form-finding, stress, load, and boundary conditions are given beforehand. Then the designers seek forms that meet the prescribed conditions.

requires the lintels to be expensive and bulky even for a moderate span. The Romans, on the other hand, developed arches to avoid tensile forces. In arches, only compressive forces occur. Thus arches can span much greater lengths even with a more economical, although sometimes weaker, material: bricks. This efficient structural system evolved into domes and vaults. A notable example is the Girona Cathedral, built in the 15th century, which has a vaulted nave with a width of around 23 meters (figure 1.1a).

In the 20th century, steel-reinforced concrete was a novel material in buildings. Architects and engineers explored its expressiveness and mouldability (before hardening). Concrete can be cast in any shape, and the steel bars reinforce the concrete into a composite material capable of withstanding tensile forces. Reinforced concrete can span or even cantilever a moderate distance, allowing architects to explore new design shapes. For example, reinforced concrete enabled modernist architect Le Corbusier (1887-1965) to explore his revolutionary "ribbon window". However, the shapes of the vaults are still relevant for reinforced concrete. While Le Corbusier's Villa Savoye in Poissy suffers from rainwater leaks, the compression-only concrete shells designed by Heinz Isler (1926-2009) show only tiny cracks. These concrete shells are leakage-proof and almost maintenance-free (Chilton, 2000). Furthermore, if designed correctly, they can be very thin. Heinz Isler covered the 30-by-30m SicliSA factory floor with a 90mm-thick shell (figure 1.1b). The structures scholar David Billington (1927-2018) termed the concrete shells as *new vaults* (1983). The term adequately suggests the similarity between masonry vaults and concrete shells.

Architects, engineers, and builders keep exploiting these efficient structural forms further. Examples include the Great Court of British Museum in London (designed by Foster + Partners, engineered by Buro Happold, built by Waagner-Biro), Dutch Maritime Museum in Amsterdam (designed and engineered by Ney & Partners, built by BRS Building Systems, see figure 1.1c-d), and the Terminal of Daxing Airport in Beijing (designed by Zaha Hadid Architects, engineered by Buro Happold, built by Beijing Urban Construction Group).

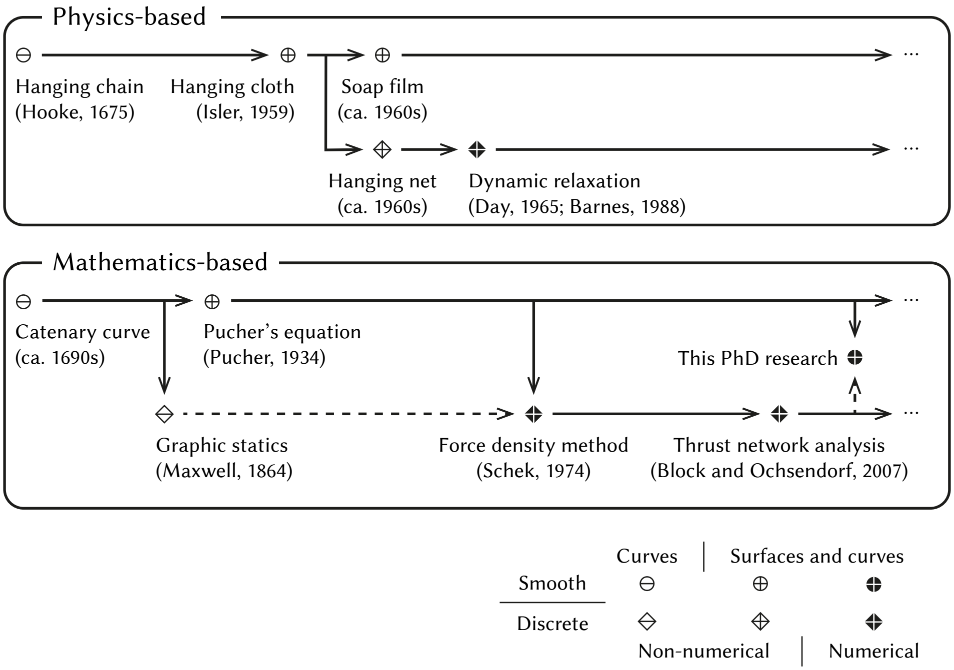

Figure 1.3: Development and classification of form-finding methods

Concepts of form-finding. Form-finding allows engineers to find the material-efficient forms of structures. In the mainstream construction industry, structural sectional design is about analyzing stresses or displacements of a structure for certain load case(s). If the stresses or displacements exceed the limits, the designer merely adjusts the dimension or thickness of the structural members. Almost inevitably, arbitrarily designed structures (e.g., linear beams) act in bending, which requires deep sections or substantial reinforcement to resist the stresses or limit the displacements. *Form-finding* works the other way around. Conditions of stresses, load, and boundary supports are provided beforehand, then seeks any proper form that meets those prescribed conditions (e.g., a rope carries axial force only, under vertical load, and is anchored at the ends). By doing this, the structure designer can actively seek a geometrical shape that permits a much more slender and efficient profile for the structure (figure 1.2).

The Romans showed that the curved arches outperform Greek flat lintels in terms of structural efficiency. The Romans as well as medieval stonemasons achieved these designs with heuristic knowledge rather than rigorous scientific theory (Addis, 2007). It was only in the 17th century that developments in science, especially statics, when systematic inquiries into the shapes and stresses of shells began to arise. The development of finding simple 2D curves was in the late 17th to the 19th century. Research progressed to 3D surfaces in the 20th century. In recent decades, computational algorithms have been developed to carry out the task of form-finding. Methods for finding 2D curves and 3D surfaces can now be classified as either physics-based and mathematics-based. The first group only returns shapes in stable equilibrium states, while the second group provides both stable and unstable shapes. Figure 1.3 provides a brief overview and the chronological sequence of the development in these two groups. More details are discussed in the upcoming paragraphs.

1.1.1. FORM-FINDING METHODS FOR 2D FUNICULAR CURVES.

Curves that carry loads with tension forces are often described as *funicular*. The adjective *funicular* comes from Latin and means “of a rope or cord”. Since a rope or cord practically takes up no bending moment, it can only take up tensile force. In a structural context, *funicular* means tension-only. The most famous *funicular* or tension-only curve is the *catenary curve*. The curve is defined by the shape of a chain under a gravitational load that is uniformly distributed along its length. When the curve is inverted and constructed as a compression-only structure, some scholars call the structure “anti-funicular” (Pinto & Fonseca, 2020). However, other scholars also refer to compression-only structures as a subset of the generalized funicular structures (Ochsendorf & Block, 2014; “Funicular structure”, 2021).

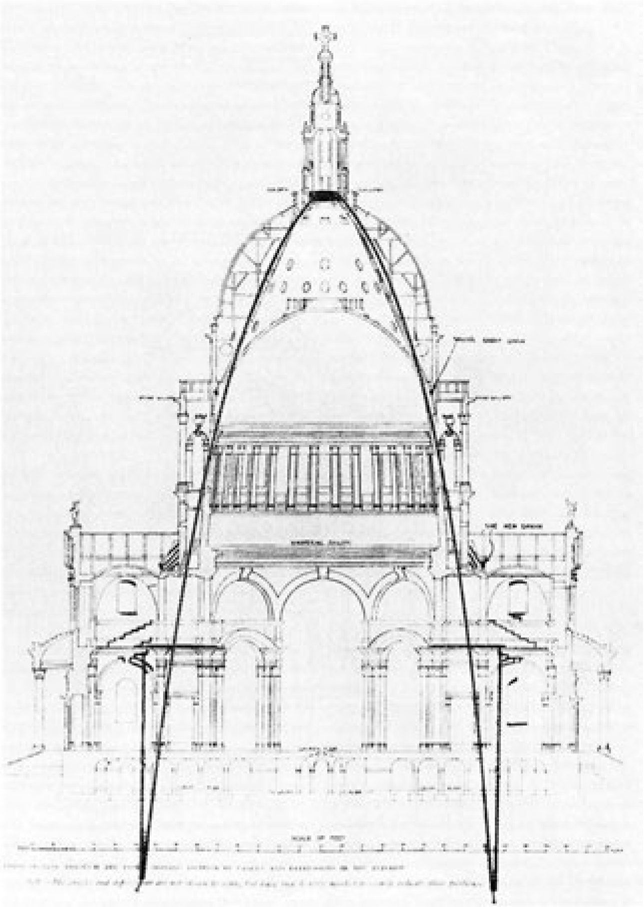

Figure 1.4: Physical form-finding can be used to design a masonry dome supporting a heavy lantern. A reversed hanging chain has been superimposed on the section of Saint Paul’s Cathedral, London. [Source: Addis, 2007]

Physical. There are multiple ways to derive the shape of funicular curves. Making use of physical experiments is probably the most intuitive method. In the 17th century, the scientist Robert Hooke (1635-1703) gave insight into determining the shape of an arch. He suggested "as hangs the flexible line, so but inverted will stand the rigid arch" (as translated from the original Latin expression in Heyman, 1995). This depiction can be credited as the first *physical form-finding method*. Indeed, a bending-pliable chain can rest only when it reaches the shape with which it carries the gravitational load in pure tension. When the shape is inverted, the shape can work in pure compression, forming an ideal arch.

One of Hooke's friends, Christopher Wren (1632-1723), applied the notion of the inverted catenary to the design of the Saint Paul's Cathedral, London. One can trace the shape of the structural dome of Saint Paul's Cathedral with a chain. In figure 1.4, the heavier center segment represents the heavier lantern crowning the dome.

Mathematical. The equilibrium of a hanging chain can also be described mathematically (see equations (3.5a-b)). Different load distributions and anchoring positions will result in different shapes of chains. For a vertical load uniformly distributed along the *horizontal distance*, the shape is as simple as a parabolic curve ($z = x^2$). For a vertical load uniformly distributed along the *tilting length*, the shape can be a hyperbolic cosine ($z = \cosh x$) or the *catenary curve*. The analytical expressions are contributions of notable mathematicians around the 1690s, including Jakob Bernoulli (1655-1705) and Gottfried Leibniz (1646-1716) (Carlson, 2021).

When loads on a chain are concentrated at discrete points, the shape of the chain can also be determined with a drawing. In this case, the smooth curve is discretized into bars and nodes. James Clerk Maxwell (1831-1879) presented his *reciprocal diagrams* (Maxwell, 1864, 1868, 1870), which use a closed polygon to confirm equilibrium of a node. In the reciprocal diagrams, two nodes connected by a common bar are represented by two polygons sharing an edge. This graphical method is sometimes called the *Cremona diagram* or *graphic statics* (Cremona, 1875). The method was adopted by Antoni Guadí (1852-1926), who designed the compound of vaulted walkways and retaining walls of Park Güell (figure 1.5).

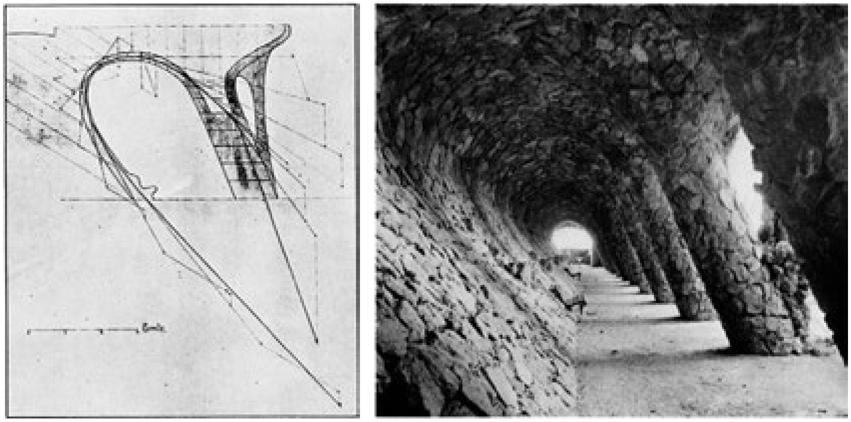

Figure 1.5: Graphical form-finding used by Antoni Guadí to design his retaining walls in Park Güell, Barcelona. [Source: Collins, 1963]

1.1.2. FORM-FINDING METHODS FOR 3D MEMBRANE SURFACES.

Mathematical. With the advances in mathematics, especially calculus, in the 19th and 20th centuries, scientists and engineers started to use partial differential equations to describe more sophisticated problems. The equation governing the equilibrium of membrane shells is *Pucher's equation* (see equation (2.20)), which was provided by A. Pucher in 1934 (Timoshenko & Woinowsky-Krieger, 1959). Some analytical solutions to this equation were built into physical structures by Félix Candela (1910-1997) in his hyperbolic shells (figure 1.6). Various solutions based on various boundary conditions have also been selectively documented by Heyman (1977) and Csonka (1987).

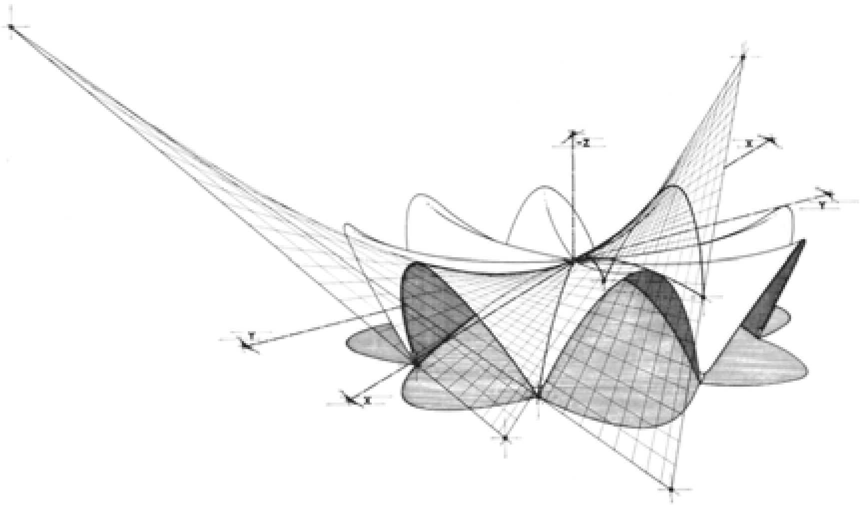

Figure 1.6: A Candela's hypar shell—Restaurant, Xochimilco—completed in 1958. (Illustrated by Francisco Fuentes for Faber, 1963, p. 194)

Physical. Analytical solutions can provide interesting shapes on certain boundary arrangements. However, due to the limitation of mathematical "closed-form expressions", analytical solutions are only available for a small number of boundary conditions. Physical form-finding methods have no such limitations.

As a rope can naturally rest in a pure-tension state, a fabric can similarly find a pure-tension state. This technique was promoted by Heinz Isler (1926-2009) at the first congress of the International Association for Shell Structure in 1959 (Chilton, 2000). He used hanging cloths and latex membranes to find shapes of free-form shells (figure 1.1b). These physical models allow designers to intuitively manipulate the shapes by shortening threads or rearranging the supports.

Frei Otto (1925-2015) also used physical models to design the Institute for Lightweight Structures in Stuttgart, a tent-like membrane structure. For this, he used the soap film method. Threads that bounded the soap film were converted into tension cables, while the soap film was translated into a wire mesh (figure 1.7).

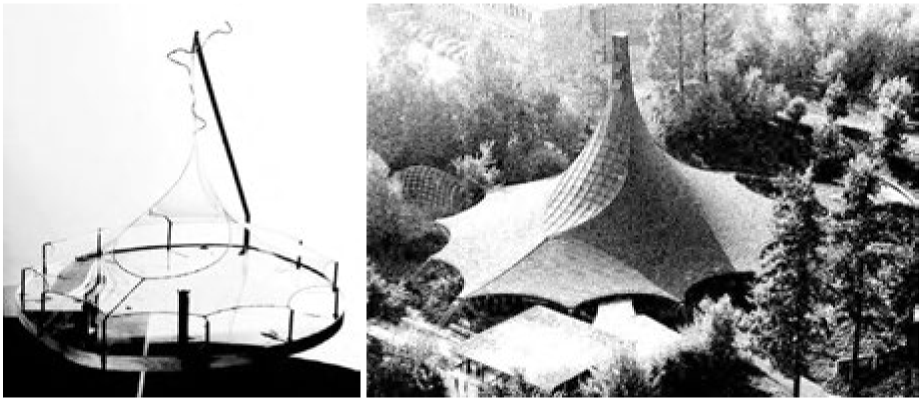

Figure 1.7: Soap film model (left) and the built structure (right) as designed by Frei Otto. [Source: von Buelow, 2007]

1.1.3. Numerical methods for form-finding 3D membrane surfaces.

Computational methods approach form-finding in two ways: simulating physical hanging nets or numerically solving mathematical formulae.

Physics-based. The methods based on simulating physical experiments include *dynamic relaxation*, introduced by A. S. Day in 1965 (as cited in Barnes, 1988). This method simulates how a flexible net starts to move when external loads are applied, how the net then deforms and dissipates excessive kinetic energy, and how it ultimately rests in a state of equilibrium.

Mathematics-based. Methods in the second category provide numerical solutions to equilibrium configurations by adjusting all numerical variables, including the positions of nodes and the forces in bars (Veenendaal & Block, 2012). The most prominent methods include the *force density method* (Schek, 1974), the methods of *thrust network analysis* (Block & Ochsendorf, 2007) and *self-supporting surface* (Vouga, Höbinger, Wallner, & Pottmann, 2012).

A distinctive difference between these two categories is that the physics-based methods can only deliver *stable* equilibrium states (e.g., a hanging rod), while the mathematics-based methods can deliver both physically *stable* and *unstable* equilibrium (e.g., both hanging and standing rods). For instance, the funnel-shaped shell in figure 1.8, which has a stress mixture of both tension and compression, can only be found by a mathematics-based method (Rippmann & Block, 2013).

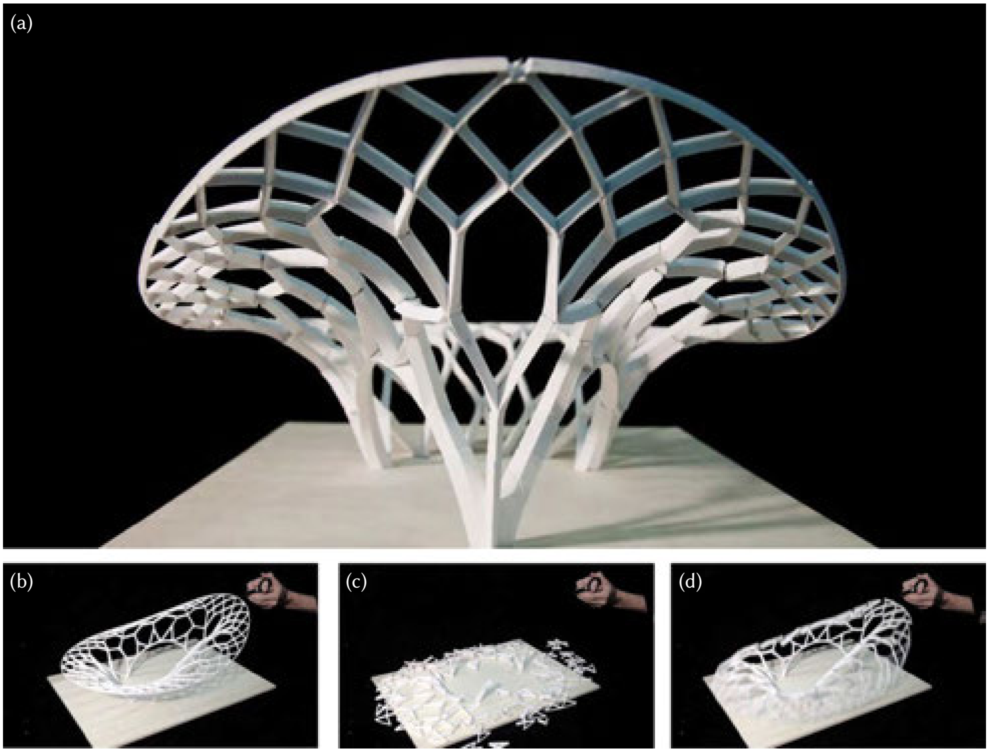

Figure 1.8: A funnel shell derived from the Thrust Network Analysis. (a) The 3D printed prototype. (b-d) The collapse of the shell when the outer tie is cut. [Source: Rippmann & Block, 2013]

1.2. Research objectives and approach for form-finding

1.2.1. Objectives

Although the established methods have enabled designers to deliver spectacular shells, there are still some limitations. With a more general design and form-finding tool, it is hoped that more shells can be designed and built.

Statics. The statics of membrane shells is governed by Pucher's equation, which might be overlooked in many architecture and engineering curricula. The first objective of this research is to explain and discuss this governing equation and related statics theories, namely the Airy stress function and Maxwell's reciprocal diagrams.

Two-way algorithm. The established numerical form-finding methods in both physics-based and mathematics-based groups rely on discretized meshes. The arrangements of edges, along with the assigned parameters (e.g., stiffness constants for dynamic relaxation and force densities for the force density method), affect the flow of stresses (or load path) and the form-found results. It is, however, generally unclear how to find a suitable set of parameters that would result in the desired shape. Therefore, the second objective of this research is to establish a form-finding algorithm that works in both directions: to find the shape based on the stress and find the stress based on the shape.

Horizontal loads. Classical form-finding problems generally focus on gravitational loads whereas built structures are subject to multiple types of loads, including horizontal, such as seismic loads or wind loads (Michiels, Adriaenssens, & Dejong, 2019). Theoretically, form-finding methods are compatible with multiple load cases (Heyman, 1977, 1995), but horizontal loads are often omitted in the form-finding process and only considered in finite element modeling. The third objective is to incorporate horizontal loads in the form-finding algorithm.

Stress visualization. Established algorithms mostly focus on the resulting form, which is generally straightforward to render as a 3D surface. Stress flow, on the other hand, can be rather complex to represent visually. The lack of visualization tools hinders communication among architects, engineers, and constructors or between teachers and students. The fourth objective is to develop a stress visualization component for the proposed form-finding method, which can translate a nebulous stress tensor field into a legible visual representation.

1.2.2. PROPOSED APPROACH

This dissertation discusses the relevant theories of statics and identifies the relationships among load, stress, and shape. These are stated in the partial differential equation—Pucher's equation, and thus fulfill the first objective listed in section 1.2.1. Then, the research uses *radial basis functions* to establish an algorithm for finding solutions to Pucher's equation. When the load and one of the stress and shape functions are given, the other can be derived from Pucher's equation. This feature allows the resulting algorithm to work in the two directions as explained above and satisfy the second objective. The load in Pucher's equation contains vertical and horizontal components, which allows the resulting algorithm to fulfill the third objective. Instead of using meshes to represent the stress and shape discretely, the *radial basis functions* represent the stress and shape smoothly. The smooth stress field allows the algorithm to trace the stress flow easily, and thus benefits the realization of the fourth objective.

Notably, the approach of using *radial basis functions* is novel. To the best of the author's knowledge, it has not been applied to solve form-finding problems. The method of radial basis functions (RBF) is a numerical method that emerged in the late 1980s (Buhmann, 2003). Compared with the popular finite element method, which can be traced back to the 1940s, the RBFs method is still in development. Its structure and features are further introduced in chapter 3.

1.3. INTERRELATED DESIGN AND CONSTRUCTION

Although a form-found shape is a material-efficient design, the finished design still needs to consider other aspects, such as the division between components, design drawing, fabrication of each component, and assembling.

Division and connections. Buildings are often larger than fabrication or transportation machinery; thus buildings consist of numerous smaller components. In the design phase, designers have to divide a structure into individual parts, so that components can be fabricated separately before assembling them into the designed configuration. This division and assembly affect how forces are transmitted across components. Therefore a holistic structural design must also take into account fabrication and assembly to design the division appropriately.

For medieval masonry vaults, the term for this geometric technique to divide the massive structure into individual blocks is *stereotomy* (Rippmann & Block, 2011; Calvo-Lópe, 2020). The division is often carefully designed and crafted since it is part of the finished structure, as shown in figure 1.9. Furthermore, in contemporary architectural discourse, the term *tectonics* is used to refer to the artistically designed and crafted connections between components or materials, especially when material, artisanship, and structural expression are thoughtfully integrated (Frampton, 1983, 1995; Leach, Turnbull, & Williams, 2004; Schumacher, 2014).

Figure 1.9: Vault above *Capilla de los Reyes* [Kings' Chapel] in the Convent of Saint Dominic, Valencia. [Source: Calvo-Lópe, 2020]

Figure 1.10: A 6-axis articulated robot tracing a free-form curve with a milling cutter

Free-form design and fabrication. Mitchell (2001) suggested master builders "tend to draw what they can build, and build what they can draw" which effectively depicts the convention of the architecture-engineering-construction (AEC) industry. Especially in the late 20th century, buildings tended to stay in orthogonal grids, which were (and still are) easy to denote, efficient to produce, and practical to use. The stereotomy-like artisanship, a labor-intensive process, had lost its market share. Concrete shells, which require curved formworks, also declined from their heyday in the 1950s (Meyer & Sheer, 2005).

The introduction of computers revolutionzed the way designers draw. The emergence of computer-aided design (CAD) software has allowed designers to denote construction drawings with mouse and keyboard rather than with ruler and compass. Digital line segments and arcs express primary geometric forms (e.g., corner-rounded rectangular). Furthermore, the computational splines (e.g., Bézier curves, non-uniform rational B-splines, or NURBS) permit designers to freely denote irregular curves and surfaces. Additionally, digital models can generate renderings and animations in the virtual environment.

Regarding free-form construction, free forms might be only buildable either with tedious manual labor or with computer numerically controlled (CNC) machinery. The CNC machines (e.g., gantry, articulated robots) redraw the curves with *end effectors* (e.g., milling cutters, water-jet nozzles, extruders of 3D printers) in the physical world (figure 1.10). Then, the physical materials can take shape according to the designer's intention. For instance, 3D printing slicers (e.g., Cura) can translate a polyhedron into a tool path. A 3D printer can then redraw the path with its extruder to complete the print. For more sophisticated production processes, designers may use *parametric design* software (e.g., *Grasshopper 3D* (2020)) to break a design down into connected curves. Computer-aided manufacturing (CAM) software (e.g., *KUKA|prc* (2019)) can translate the connected curves into a machine-readable tool path for a CNC machine (e.g., KUKA robot). Once the design is a batch of components with a similar topology, the tool path can be generated efficiently in a batch process.

Free-from assemblies from planar elements. Although it is possible to build a free-form structure with free-form components (or free-form formworks for casting), this approach is generally not economically feasible. Given most industrially produced construction materials have prismatic shapes (e.g., steel I-beams, extruded aluminum) or planar geometries (e.g., float glass, plywood broads), it is more practical to assemble a free-form structure from linear or planar materials. Pottmann (2013) summarized this practical approach as *fabrication-aware design*, also known as *design for manufacture & assembly (DFMA)*.

Theories from discrete differential geometry are used to discretize a curved surface into a series of flat quadrilaterals or a *planar quadrilateral mesh* (figure 1.11). This allows the builder to make the most efficient use of mass-produced planar materials. The planar panels may be supported by a grid-like structure. Preferably, the linear members of the mesh shall also be non-twisting and co-axial at the nodes (torsion-free nodes). However, this is only possible when certain geometric conditions are fulfilled. *Principal meshes* fulfill such conditions and thus can be built of planar panels and torsion-less nodes (figure 1.12; Pottmann, Liu, et al., 2007). Generally, the divisions between panels have to follow *principal curvatures* of the surfaces, hence the name.

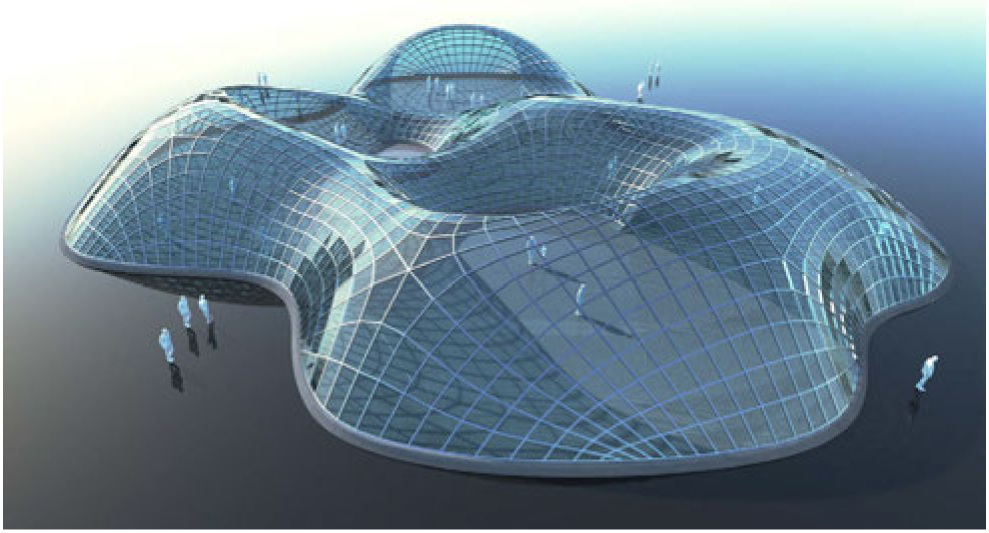

Figure 1.11: A planar quadrilateral mesh. [Source: Kilian et al., 2017]

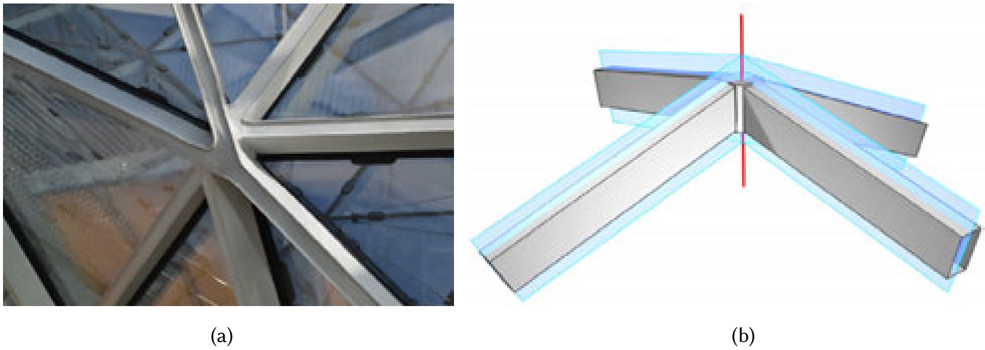
(a)

(b)

Figure 1.12: Nodes with torsion (a) and without torsion (b). [Source: Tellier et al., 2020]

1.4. Research objectives and approach for fabrication and construction

1.4.1. Objectives

Although quite a few studies on shell design and free-from construction have been conducted, there are still some issues that deserve more investigation.

Logistics. After discretizing free-form shells into components, the components can be fabricated by CNC machines using mass customization. The remaining critical step is to assemble all the components. As each component often has a unique shape, the logistics are challenging and involve indexing components, sequences of fabrication, stacking, transportation, hoisting, and assembling. One of the objectives of this dissertation is to explore a potential strategy that can reduce these logistic challenges.

Prototyping. Dividing double-curved surfaces into flat panels is an economical way of fabricating components for free-form surfaces. Although some established theories and methods for executing such a task exist, the theories and methods are not well-known and under-utilized in architectural designs. Showcasing such methods in prototyping would increase awareness. The final objective is to implement relevant methods in prototyping to raise awareness of the methods as well as validate them.

1.4.2. Proposed approach

This dissertation utilizes theories from discrete differential geometry to discretize smooth shells obtained from the RBF algorithm into planar panels. Furthermore, this research develops a reconfigurable mechanism with which the components are pre-assembled in a flat configuration. The mechanism can then be deployed into the prescribed curved state. By reducing the on-site component count, logistical challenges can be reduced. To carry out the final objective, proposed methods are implemented to design prototypes. Relevant CAD-CAM software and CNC machines will also be employed.

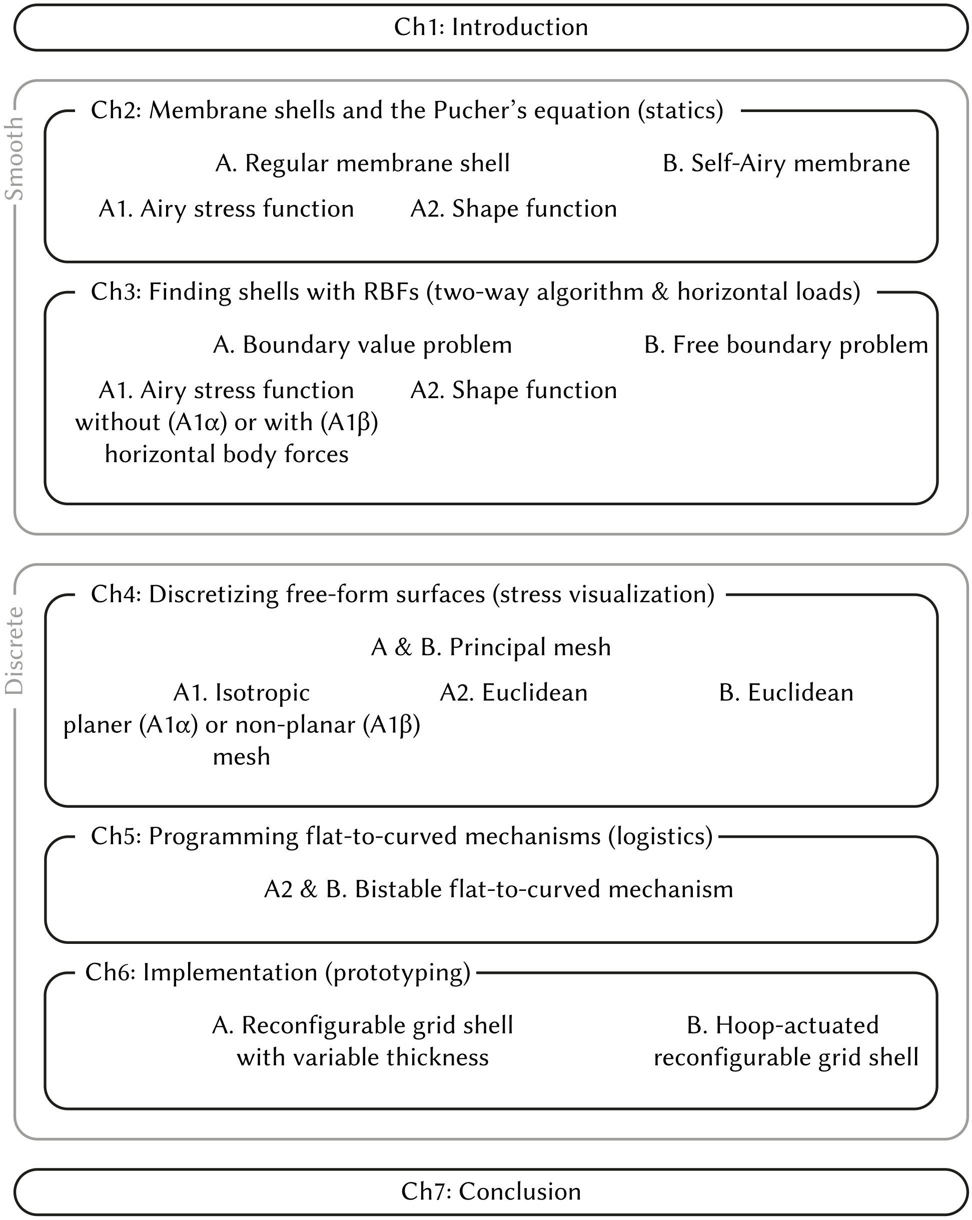

Figure 1.13: Dissertation chapters and threads. Corresponding research objectives are shown in the parenthesis next to the titles.

1.5. OUTLINE OF CHAPTERS

Figure 1.13 schematically shows the structure of this dissertation in terms of the chapters and the related research objectives. The chapters also are interwoven with multiple topic threads, which split or merge in different stages. They are organized as follows.

Chapter 2 Membrane Shells and Pucher's Equation discusses the statics of regular membranes (thread A), which is formulated in mathematical expressions with stress (thread A1) and shape (thread A2) functions. This chapter also presents *self-Airy membranes* (thread B), which are defined as shells that have Airy stress functions identical to their shape functions. This type of membrane can have a distinct actuation scheme after translation into a reconfigurable mechanism.

Chapter 3 Finding Shell Structures with Radial Basis Functions develops a method to find solutions that are in equilibrium and are close to prescribed shapes or stress distributions. When form-finding a regular membrane, the task is to solve a boundary value problem (A). In the algorithm, horizontal body forces are also considered, which bifurcates the stress functions: some excluding horizontal loads (A1α) and others including horizontal loads (A1β). Conversely, numerically finding a *self-Airy membrane* is formulated as solving a free boundary problem (B).

Chapter 4 Discretizing Free-form Surfaces and Airy Stress Functions discusses the discretization of curved surfaces into panels and concentrations of curvatures into creases. The developed technique can approximate shapes with ordinary or Euclidean principal meshes (A2 & B) to reduce the fabrication complexity of curved surfaces. This technique can also translate a smooth stress function into a polyhedral one, but relies on the *isotropic* metric instead of the ordinary or Euclidean metric. Hence, the resulting mesh is called an *isotropic* planar principal mesh (A1α), when body forces are absent. This chapter also identifies a new way to present body forces in a discretized stress function, which turns out to give an *isotropic* non-planar mesh (A1β).

Chapter 5 Programming Flat-to-Curved Mechanisms presents a mechanism that can deploy a double-curved surface from a flat configuration. The mechanism is based on the discretization results of the Euclidean principal mesh (A2 & B). For validation, prototypes are made that consist of interconnected panels made from 3D printed polylactic acid (PLA) and water-jet cut polypropylene (PP).

Chapter 6 Implementation documents three prototypes that are designed and materialized with the proposed methods. The first two are gridshells with variable thickness in order to accommodate stresses induced by load cases with different horizontal loads (A). The second one is a reconfigurable shell that can be actuated by a tension hoop, of which the shape is based on the self-Airy membrane (B).

Chapter 7 Conclusion summarizes the current findings and projects the direction for further research.

2

MEMBRANE SHELLS AND PUCHER'S EQUATION

Structural design requires an understanding "to the backbone"
of the mechanical principles of inner equilibrium.

Eduardo Torroja[1]

Parts of this chapter have been presented in *IASS Annual Symposium 2019–StructuralMembranes 2019* (Chiang, Borgart, & Li, 2019) and submitted for publication (Chiang, 2021)

[1] as cited in Picon, 2003, p.301

MEMBRANE SHELLS, which have minimized bending moments under certain load conditions, are regarded as the most efficient structural forms for enclosing a space. As suggested by Eduardo Torroja (1899-1961), structural designers should understand "to the backbone" of the equilibrium of the internal stresses (as cited in Picon, 2003, p.301). To design membrane shells, it is important to understand how the membrane stresses in the curved shape are in equilibrium with the external loads. The equilibrium of a membrane shell is governed by the Airy stress function and Pucher's equation, which together form the main themes of this chapter.

Shells are often conceptually divided into stretching and bending surfaces (Calladine, 1977). The first one carries in-plane forces but has zero bending moment capacity. The second, on the other hand, can resist the bending moment and transverse shear forces but has zero capacity of in-plane tension and compression. This dissertation follows the *membrane theory*, which assumes that the bending rigidity is negligible and external loads are fully carried by the stretching surface or a bending-pliable membrane. Unlike physical membranes such as a soap film or plastic wrap which will wrinkle when compressed, the conceptual membranes are capable of withstanding compressive forces. This dissertation refers to these compression-capable membranes as *membrane shells*, a term also used by Csonka (1987).

This chapter focuses on the equilibrium of the membrane shell using mathematical equations. The equations and the related variables will serve as the essential foundation for developing the numerical form-finding method in the further chapters.

OUTLINE

The outline of the chapter is as follows. Section 2.1 investigates the relationship between the equilibrium of a stress tensor field and the second derivatives of an Airy stress function. Section 2.2 connects the Airy stress function with Maxwell's reciprocal diagrams. Section 2.3 reveals that the external load is equilibrated by the double-inner product of the stress tensor and the shape's Hessian matrix. Section 2.4 focuses on the equilibrium at the boundaries. Section 2.5 introduces *self-Airy membranes*, special cases in which the graphs of the Airy stress functions are identical to the shapes of the membranes. Section 2.6 discusses the statical determinacy of the membrane shells. Section 2.7 summarizes this chapter.

2.1. TWO-DIMENSIONAL EQUILIBRIUM AND THE AIRY STRESS FUNCTION

The stress function is the expression that automatically satisfies the equilibrium equations (Sadd, 2009). As early as 1863, Airy proposed using a scalar function to express an arbitrary auto-equilibrated stress tensor field in a 2D domain. Let **N** denote the 2D stress resultant tensor:

$$\mathbf{N} = \begin{bmatrix} N_{xx} & N_{xy} \\ N_{xy} & N_{yy} \end{bmatrix}, \tag{2.1}$$

in which N_{xx} and N_{yy} are normal stress resultants and N_{xy} is the shear stress resultant. The stress resultant $N_{ij},\ i,j \in \{x,y\}$ is the integral of the stress σ_{ij} along the thickness of the shell as $N_{ij} = \int_{z_{bottom}}^{z_{top}} \sigma_{ij}\, dz$. While σ_{ij} has the dimension of force per unit area [force $\cdot$ length^{-2}], N_{ij} has the dimension of force per length [force $\cdot$ length^{-1}]. Equilibrium of the tensor field in directions x and y can be expressed as (Sadd, 2009, p. 67)

$$\frac{\partial}{\partial x}N_{xx} + \frac{\partial}{\partial y}N_{xy} + p_x = 0, \text{ and} \tag{2.2a}$$

$$\frac{\partial}{\partial x}N_{xy} + \frac{\partial}{\partial y}N_{yy} + p_y = 0, \tag{2.2b}$$

where p_x and p_y are the body forces per unit area [force·length^{-2}]. The directions of these forces are shown in figure 2.1.

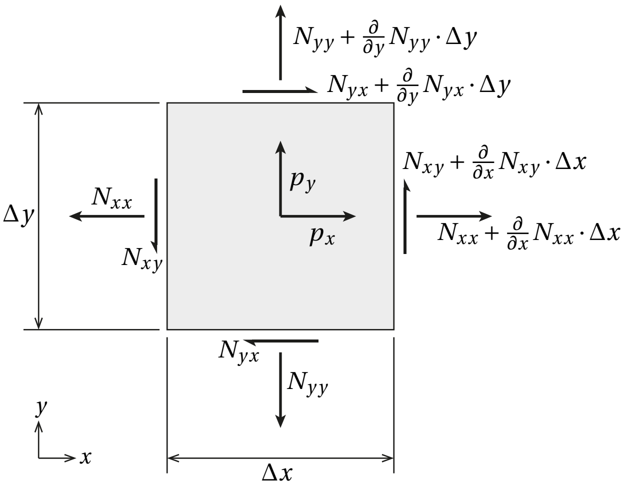

Figure 2.1: Membrane stress resultants in a plate

Airy (1863) suggested that whenever the stress resultants are derived from an arbitrary scalar function $F(x, y)$ as

$$N_{xx} = \frac{\partial^2}{\partial y^2}F - \int p_x\, dx, \tag{2.3a}$$

$$N_{xy} = -\frac{\partial^2}{\partial x \partial y}F, \text{ and} \tag{2.3b}$$

$$N_{yy} = \frac{\partial^2}{\partial x^2}F - \int p_y\, dy, \tag{2.3c}$$

the stress resultants automatically satisfy the equilibrium conditions (2.2a–b), since the equality of mixed partials guarantees $\frac{\partial}{\partial x}\frac{\partial}{\partial y}\frac{\partial}{\partial y}F = \frac{\partial}{\partial y}\frac{\partial}{\partial x}\frac{\partial}{\partial y}F$ and $\frac{\partial}{\partial x}\frac{\partial}{\partial x}\frac{\partial}{\partial y}F = \frac{\partial}{\partial y}\frac{\partial}{\partial x}\frac{\partial}{\partial x}F$. The arbitrary scalar function $F(x, y)$ in equations (2.3a–c) is called the Airy stress function in recognition of the contribution from George Biddell Airy (1801-1892) (Green & Zerna, 1968).

Matrix expression. Although equations (2.3a–c) have expressed self-equilibrating stress resultants, a one-line expression in matrix form is beneficial for follow-up discussions. Since equations (2.3a–c) have terms that are either second derivatives of the Airy stress function or the integrals of the body forces, one may store two types of terms in different matrices such as

$$\mathbf{N} = \mathbf{F} - \mathbf{P}, \tag{2.4}$$

in which **F** contains all the second derivatives and **P** contains the integrals of the body forces as diagonal elements. Matrix **P** is given by

$$\mathbf{P} = \begin{bmatrix} \int p_x \, dx & 0 \\ 0 & \int p_y \, dy \end{bmatrix}.$$

The matrix **F** shall be

$$\mathbf{F} = \begin{bmatrix} \frac{\partial^2}{\partial y^2} F & -\frac{\partial^2}{\partial x \partial y} F \\ -\frac{\partial^2}{\partial x \partial y} F & \frac{\partial^2}{\partial x^2} F \end{bmatrix}. \tag{2.5}$$

By comparing matrix **F** with the Hessian matrix $\mathbf{H}_F$ of $F(x, y)$

$$\mathbf{H}_F = \begin{bmatrix} \frac{\partial^2}{\partial x^2} F & \frac{\partial^2}{\partial x \partial y} F \\ \frac{\partial^2}{\partial x \partial y} F & \frac{\partial^2}{\partial y^2} F \end{bmatrix}, \tag{2.6}$$

one can notice that **F** and $\mathbf{H}_F$ have the same elements yet are in a different arrangement. One can introduce a rotation matrix $\mathbf{R}^{90^\circ}$ and the Hessian operator **H**:

$$\mathbf{R}^{90^\circ} = \begin{bmatrix} 0 & -1 \\ 1 & 0 \end{bmatrix}, \qquad \mathbf{H} = \begin{bmatrix} \frac{\partial^2}{\partial x^2} & \frac{\partial^2}{\partial x \partial y} \\ \frac{\partial^2}{\partial x \partial y} & \frac{\partial^2}{\partial y^2} \end{bmatrix} \tag{2.7}$$

so that equation (2.5) can be expressed as

$$\mathbf{F} = \mathbf{R}^{90^\circ} \mathbf{H} \left(\mathbf{R}^{90^\circ} \right)^{\mathrm{T}} F(x, y).$$

Let $\mathbf{H}^{r90^\circ}$ denote the rotated Hessian operator, then the stress resultant tensor **N** can be expressed as

$$\mathbf{N} = \mathbf{H}^{r90^\circ} F(x, y) - \mathbf{P}. \tag{2.8}$$

This expression concisely represents equilibrium in x- and y-direction, which is convenient for discussing the equilibrium of the third dimension in section 2.3.

The Airy stress function sufficiently describes equilibrium in a 2D domain. See section 2.3 for a description of the equilibrium in the third dimension. The purpose of the upcoming section 2.2 is to have a closer look at the Airy stress function and the related theories.

2.2. THE AIRY STRESS FUNCTION, GRAPHIC STATICS, AND RECIPROCAL DIAGRAMS

Besides the Airy stress function, equilibrium in a 2D domain can also be observed in other perspectives such as *graphic statics* and *reciprocal diagrams*. By carefully examining the

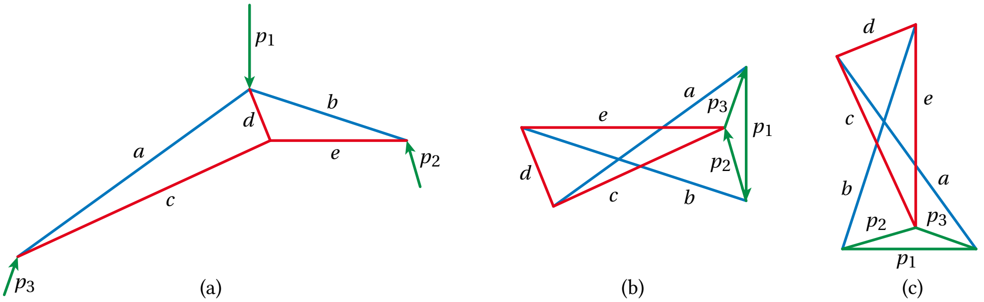

Figure 2.2: An example of graphic statics and reciprocal diagrams. (a) Form diagram. (b) Parallel force polygons. (c) Force diagram (the corresponding edges are orthogonal to their counterparts in the form diagram). Panels (a,c) are a pair of reciprocal diagrams. External loads are drawn in green, compression in blue, and tension in red.

graphic statics and reciprocal diagrams, one can develop in-depth knowledge of the Airy stress function.

Graphic statics was initially developed by Varignon (1725) and later followed by Maxwell (1864, 1868, 1870), Culmann (1866), Cremona (1875), and others. It is primarily used to analyze the forces in truss-like structures. The equilibrium of a node is represented by a closed force polygon. For instance, the top node in figure 2.2a has four forces: external load p_1 and three internal forces of bars a, b, and d. The four forces form a self-intersecting quadrilateral as the corresponding force polygon in figure 2.2b.

Among the contributors of graphic statics, the works of James Clerk Maxwell (1837-1879) are especially worth mentioning. Maxwell proposed *reciprocal diagrams*, that unify graphic statics and the Airy stress function. Maxwell published an article in 1864 discussing truss-like structures; in 1868, he published another article dealing with continuous stress fields and smooth Airy stress function. Later, in 1870, he released one more article in which he identifies that the reciprocal diagram of any polyhedral Airy stress function is the force polygon derived in graphic statics.

A marginal difference between force polygons and reciprocal diagrams is that the edges in force polygons are parallel to the corresponding bars (figure 2.2a, b) while the edges in reciprocal diagrams are perpendicular the corresponding bars (figure 2.2a, c). The seemingly counter-intuitive perpendicularity shall be discussed in the following paragraphs.

The method of reciprocal diagrams is based on a mathematical mapping between two functions, say $F(x, y)$ and $F^*(\xi, \eta)$ (Maxwell, 1868):

$$\xi = \frac{\partial F}{\partial x}, \quad \eta = \frac{\partial F}{\partial y}, \quad F^* = x\frac{\partial F}{\partial x} + y\frac{\partial F}{\partial y} - F, \tag{2.9a}$$

$$x = \frac{\partial F^*}{\partial \xi}, \quad y = \frac{\partial F^*}{\partial \eta}, \quad F = \xi\frac{\partial F^*}{\partial \xi} + \eta\frac{\partial F^*}{\partial \eta} - F^*. \tag{2.9b}$$

When $F(x, y)$ and $F^*(\xi, \eta)$ are smoothly differentiable, a point $\mathbf{x} = (x, y, F(x, y))$ maps to another point $\boldsymbol{\xi} = (\xi, \eta, F^*(\xi, \eta))$. The coordinates of $\boldsymbol{\xi}$ are the slopes and the height of z-intercept of a plane tangent to $z = F(x, y)$ at $\mathbf{x}$. The same applies the other way around. The coordinates of $\mathbf{x}$ are the slopes and the height of ζ-intercept of a plane tangent to $\zeta = F^*(\xi, \eta)$ at $\boldsymbol{\xi}$. Since the relation between the graphs of $z = F(x, y)$ and $\zeta = F^*(\xi, \eta)$ is mutually

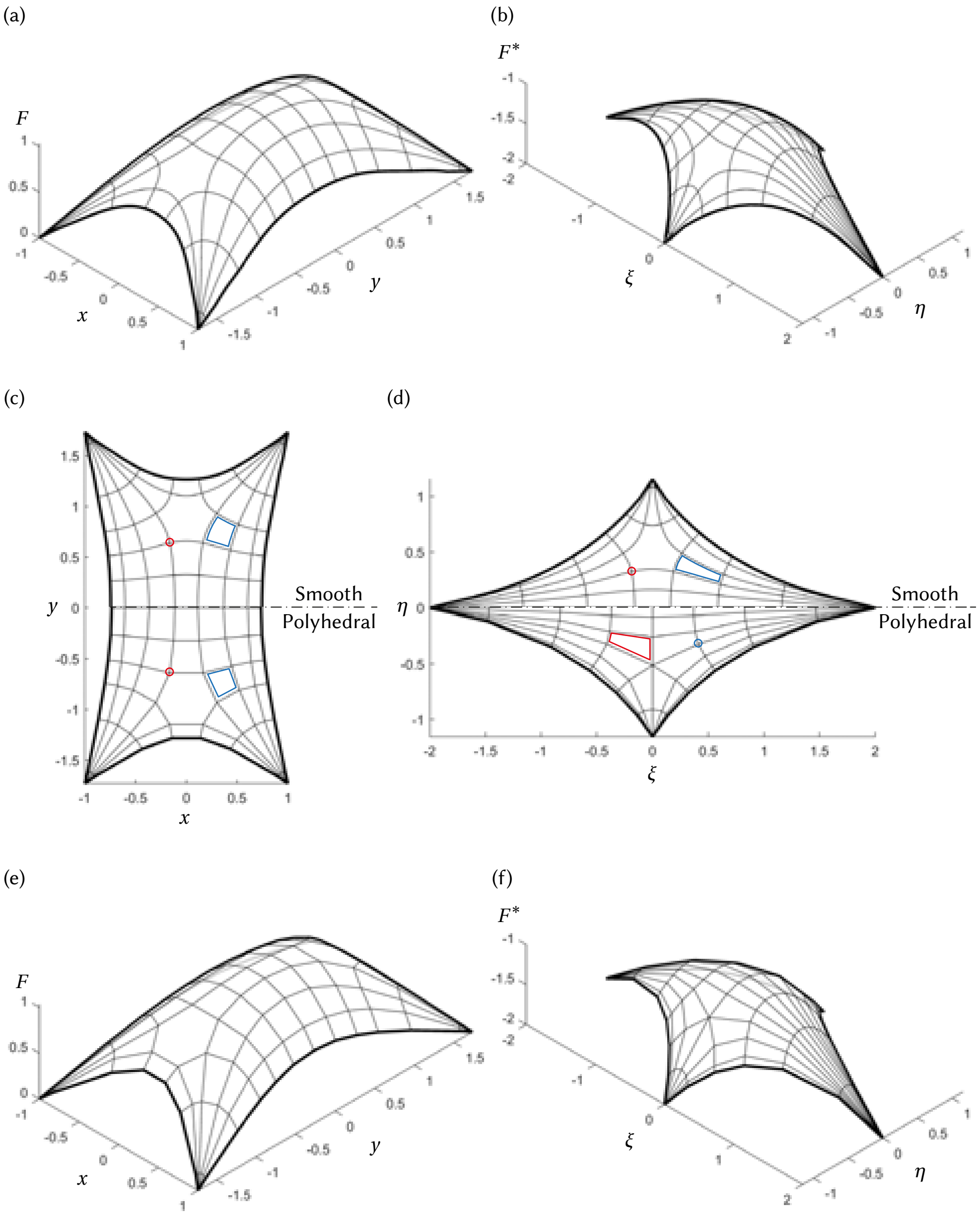

Figure 2.3: Instances of reciprocal diagrams. (a–b) Smooth diagrams and their curvature-line networks. (c–d) Top views of smooth and polyhedral diagrams. In smooth diagrams, a point maps to another point (red circles), and an area maps to another area (blue patches). In polyhedral diagrams, a vertex maps to a facet and vice versa. For example, the red circle (and the blue polygon) in (c) map to the red polygon (and the blue circle) in (d). (e–f) Polyhedral diagrams.

symmetrical, the graphs are said to be "reciprocal." Examples of reciprocal diagrams are provided in figure 2.3.

There exist three interesting features to these reciprocal diagrams.

- When the first graph is the Airy stress function and there are no body forces, the resultant force passing through an oriented line segment $\Delta\mathbf{x} = \mathbf{x}_b - \mathbf{x}_a$ is proportional to the length of its corresponding segment $\Delta\boldsymbol{\xi} = \boldsymbol{\xi}_b - \boldsymbol{\xi}_a$, and the direction of the resultant force is perpendicular to the line segment $\Delta\boldsymbol{\xi}$ (Maxwell, 1868).
- When one graph is a polyhedral surface, the corresponding graph is also a polyhedral surface. Furthermore, an edge in one graph corresponds to an edge in the other graph, and a face in one graph corresponds to a vertex in the other (Maxwell, 1870), and vice versa.
- In the absence of body forces, the (*isotropic-*)curvature lines of the Airy stress function $F(x, y)$ are the stress trajectories of $\mathbf{N}$.

In the following paragraphs, these three features will be further elaborated.

Force passing through a segment. One can break an oriented segment $\Delta\mathbf{x} = \mathbf{x}_b - \mathbf{x}_a$ into n pieces such that $\sum_{i=1}^{n} \delta\mathbf{x}_i = \Delta\mathbf{x}$. Then the resultant force $\mathbf{f}_{\Delta\mathbf{x}}$ will be the summation of n pieces of the corresponding forces $\delta\mathbf{f}_i$ so that $\sum_{i=1}^{n} \delta\mathbf{f}_i = \mathbf{f}_{\Delta\mathbf{x}}$. As n approaches infinity, the $\delta\mathbf{x}_i$ can be infinitesimal and thus $\delta\mathbf{f}_i$ can be approximated by the expression

$$\delta\mathbf{f}_i = \begin{bmatrix} N_{xy} & -N_{xx} \\ N_{yy} & -N_{xy} \end{bmatrix} \delta\mathbf{x}_i,$$

where the sign conventions of $\delta\mathbf{f}_i = \begin{bmatrix} \delta f_{x_i} & \delta f_{y_i} \end{bmatrix}^{\mathrm{T}}$ and $\delta\mathbf{x}_i = \begin{bmatrix} \delta x_i & \delta y_i \end{bmatrix}^{\mathrm{T}}$ are illustrated in figure 2.4.

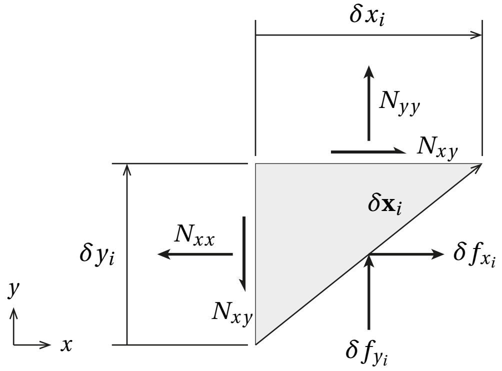

Figure 2.4: Stress resultants acting on an infinitesimal segment $\delta\mathbf{x}_i$

From equations (2.3), each N_{ij} can be expressed as a second derivative of the Airy stress function in the absence of body forces, so that

$$\delta \mathbf{f}_i = \begin{bmatrix} -\frac{\partial^2}{\partial x \partial y} F & -\frac{\partial^2}{\partial y^2} F \\ \frac{\partial^2}{\partial x^2} F & \frac{\partial^2}{\partial x \partial y} F \end{bmatrix} \delta \mathbf{x}_i .$$

Again, the matrix on the right-hand side can be expressed as a product of a rotation matrix $\mathbf{R}^{90^\circ}$ defined in equation (2.7), and the Hessian matrix $\mathbf{H}_F$ mentioned in equation (2.6), so that

$$\begin{aligned} \delta \mathbf{f}_i &= \begin{bmatrix} 0 & -1 \\ 1 & 0 \end{bmatrix} \begin{bmatrix} \frac{\partial^2}{\partial x^2} F & \frac{\partial^2}{\partial x \partial y} F \\ \frac{\partial^2}{\partial x \partial y} F & \frac{\partial^2}{\partial y^2} F \end{bmatrix} \delta \mathbf{x}_i \\ &= \mathbf{R}^{90^\circ} \mathbf{H}_F \, \delta \mathbf{x}_i . \end{aligned} \tag{2.10}$$

On the other hand, one can construct the relation between corresponding segments $\delta \mathbf{x}_i$ and $\delta \boldsymbol{\xi}_i$ via the Jacobian matrix. From the definition of the Jacobian matrix (Arfken, Weber, & Harris, 2013, p. 227) and the expressions (2.3a–b), the matrix can be derived as

$$\mathbf{J}_{\boldsymbol{\xi}/\mathbf{x}} = \begin{bmatrix} \frac{\partial}{\partial x} \xi & \frac{\partial}{\partial y} \xi \\ \frac{\partial}{\partial x} \eta & \frac{\partial}{\partial y} \eta \end{bmatrix} = \begin{bmatrix} \frac{\partial^2}{\partial x^2} F & \frac{\partial^2}{\partial x \partial y} F \\ \frac{\partial^2}{\partial x \partial y} F & \frac{\partial^2}{\partial y^2} F \end{bmatrix} . \tag{2.11}$$

Since $\delta \mathbf{x}_i$ and $\delta \boldsymbol{\xi}_i$ are infinitesimally small, the Jacobian can provide $\delta \boldsymbol{\xi}_i = \mathbf{J}_{\boldsymbol{\xi}/\mathbf{x}} \delta \mathbf{x}_i$. One can notice that the Jacobian $\mathbf{J}_{\boldsymbol{\xi}/\mathbf{x}}$ is coincidentally identical to the Hessian $\mathbf{H}_{F(x,y)}$. Therefore, equation (2.10) can be expressed as

$$\delta \mathbf{f}_i = \mathbf{R}^{90^\circ} \mathbf{J}_{\boldsymbol{\xi}/\mathbf{x}} \delta \mathbf{x}_i = \mathbf{R}^{90^\circ} \delta \boldsymbol{\xi}_i . \tag{2.12}$$

One can treat equation (2.12) as one of the addends and sum all the addends up. The result provides

$$\mathbf{f}_{\Delta \mathbf{x}} = \mathbf{R}_{90^\circ} \Delta \boldsymbol{\xi}, \tag{2.13}$$

which explains the first feature.

Reciprocal relations between vertices, edges, and faces. To explain why a vertex corresponds to a face and an edge corresponds to another edge, the following paragraphs investigate the connection between the second derivatives and the mapping.

First, the second derivatives, or the Hessian matrix, can classify whether a point is on a vertex, an edge, or a planar face. It becomes even more evident after eigendecomposition is conducted on the Hessian matrix $\mathbf{H}_{F(x,y)}$ as

$$\mathbf{H}_{F(x,y)} = \begin{bmatrix} \frac{\partial^2}{\partial x^2} F & \frac{\partial^2}{\partial x \partial y} F \\ \frac{\partial^2}{\partial x \partial y} F & \frac{\partial^2}{\partial y^2} F \end{bmatrix} = \mathbf{Q} \begin{bmatrix} \lambda_1 & 0 \\ 0 & \lambda_2 \end{bmatrix} \mathbf{Q}^{-1}, \tag{2.14}$$

in which $\mathbf{Q}$ is a 2×2 orthogonal matrix formed by the eigenvectors, and λ_1 and λ_2 are the eigenvalues. A region is planar when the local $\lambda_1 = \lambda_2 = 0$, a point is on an edge when one of the eigenvalues equals 0 and the other has infinite magnitude, and a point is on a vertex if $|\lambda_1| = |\lambda_2| = \infty$.

Regarding the mapping, the Jacobian matrix can describe how a group of surrounding points on $F(x, y)$ maps to $F^*(\xi, \eta)$. As discussed right after equation (2.11), the Jacobian $\mathbf{J}_{\boldsymbol{\xi}/\mathbf{x}}$ is coincidentally identical to the Hessian matrix $\mathbf{H}_{F(x,y)}$.

Furthermore, the inverse mapping can also be described by another Jacobian matrix, which would then be the inverse matrix of the Jacobian in the forward mapping (Arfken et al., 2013, p. 230):

$$\mathbf{J}_{\boldsymbol{\xi}/\mathbf{x}} = \left[\mathbf{J}_{\mathbf{x}/\boldsymbol{\xi}}\right]^{-1}. \tag{2.15}$$

Since the inverse Jacobian matrix should also be the Hessian matrix of $F^*(\xi, \eta)$, the Hessian matrices can substitute the Jacobian matrices in equation (2.15) as

$$\mathbf{H}_{F^*(\xi,\eta)} = \left[\mathbf{H}_{F(x,y)}\right]^{-1}, \tag{2.16}$$

where $\mathbf{H}_{F^*(\xi,\eta)}$ is the Hessian matrix corresponding to $\mathbf{H}_{F(x,y)}$. After eigendecomposition of both sides of equation (2.16), the equation can be recast as

$$\begin{aligned}\mathbf{Q}^* \begin{bmatrix} \lambda_1^* & 0 \\ 0 & \lambda_2^* \end{bmatrix} [\mathbf{Q}^*]^{-1} &= \left\{\mathbf{Q} \begin{bmatrix} \lambda_1 & 0 \\ 0 & \lambda_2 \end{bmatrix} \mathbf{Q}^{-1}\right\}^{-1} \\ &= \mathbf{Q} \begin{bmatrix} \lambda_1^{-1} & 0 \\ 0 & \lambda_2^{-1} \end{bmatrix} \mathbf{Q}^{-1},\end{aligned} \tag{2.17}$$

in which λ_1^* and λ_2^* are the eigenvalues corresponding to λ_1 and λ_2. Equation (2.17) suggests interesting relations between $F(x, y)$ and $F^*(\xi, \eta)$. First, a point on $F(x, y)$ has the same set of eigenvectors $\mathbf{Q}$ as the corresponding point on $F^*(\xi, \eta)$. Second, the eigenvalues λ_1 and λ_2 on $F(x, y)$ are the reciprocal numbers (or multiplicative inverses) of the corresponding eigenvalues λ_1^* and λ_2^* on $F^*(\xi, \eta)$. Table 2.1 classifies the types of geometric entities by the magnitudes of their eigenvalues and shows for each entity its corresponding reciprocal entity, in which a vertex corresponds to a planar facet and an edge corresponds to another edge. This description explains the second feature.

Table 2.1: Reciprocal relations between geometric entities

Entity on $F(x, y)$	$\lvert\lambda_1\rvert$	$\lvert\lambda_2\rvert$	**Entity on** $F^*(\xi, \eta)$	$\lvert\lambda_1^*\rvert$	$\lvert\lambda_2^*\rvert$
Vertex	∞	∞	Planar surface	0	0
Straight edge	∞	0	Straight edge	0	∞
Straight edge	0	∞	Straight edge	∞	0
Planar surface	0	0	Vertex	∞	∞

Principal orientation and principal stresses. Upon further extending the observation on eigendecomposition, one can find that the matrix of eigenvectors $\mathbf{Q}$ is also the principal orientation of the stress resultant field $\mathbf{N}$, and that the eigenvalues λ_2, λ_1 are the principal stress resultants.

By directly eigendecomposing the stress resultant **N**, one can find that

$$\mathbf{N} = \mathbf{Q}_N \begin{bmatrix} N_1 & 0 \\ 0 & N_2 \end{bmatrix} \mathbf{Q}_N^{-1}, \tag{2.18}$$

where N_1 and N_2 are principal stress resultants, and $\mathbf{Q}_N$ contains the vectors of the principal directions. However, one can also eigendecompose the stress resultant **N** using another approach. From equations (2.8) and (2.14), one can find that

$$\mathbf{N} = \mathbf{R}^{90^\circ}\mathbf{Q} \begin{bmatrix} \lambda_1 & 0 \\ 0 & \lambda_2 \end{bmatrix} \mathbf{Q}^{-1}\mathbf{R}^{-90^\circ} - \mathbf{P}.$$

In the absence of body forces, **P** will be a zero matrix. Since both $\mathbf{R}^{90^\circ}$ and **Q** are 2D rotation matrices, the equations $\mathbf{R}^{90^\circ}\mathbf{Q} = \mathbf{Q}\mathbf{R}^{90^\circ}$ and $\mathbf{Q}^{-1}\mathbf{R}^{-90^\circ} = \mathbf{R}^{-90^\circ}\mathbf{Q}^{-1}$ hold. Therefore, the sequence of matrix multiplication can be reorganized as

$$\mathbf{N} = \mathbf{Q}\left(\mathbf{R}^{90^\circ} \begin{bmatrix} \lambda_1 & 0 \\ 0 & \lambda_2 \end{bmatrix} \mathbf{R}^{-90^\circ}\right)\mathbf{Q}^{-1} = \mathbf{Q} \begin{bmatrix} \lambda_2 & 0 \\ 0 & \lambda_1 \end{bmatrix} \mathbf{Q}^{-1}. \tag{2.19}$$

The newly derived equation (2.19) also successfully eigendecomposes the stress resultant tensor **N**. Comparing equation (2.19) with equation (2.18), one may notice that the directions of the principal stresses are eventually given by the eigenvectors of the Hessian matrix $\mathbf{H}_F$ and the principal stress resultants are given by the eigenvalues of $\mathbf{H}_F$ with a minor difference in the order: $N_1 = \lambda_2$, $N_2 = \lambda_1$.

The directions of principal stresses are important when visualizing the stress field. One can trace how stresses flow along the *stress trajectories*. Some stress trajectories have already been shown in figure 2.3. These trajectories are sometimes called *isostatic lines*, especially in the field of photoelasticity. Section 4.3 will further show that the Hessian matrix is related to the *isotropic*-curvatures of a graph. In short, the *stress trajectories* are also *isotropic-curvature lines* of the Airy stress function. This explains the third feature.

The reciprocal relations between $F(x, y)$ and $F^*(\xi, \eta)$ have now been discussed briefly. In section 4.3, reciprocal relations will be discussed in further detail, such as the intersection of two graphs in (x, y, z) which corresponds to the surface tangent to both corresponding graphs in (ξ, η, ζ).

2.3. THREE-DIMENSIONAL EQUILIBRIUM AND PUCHER'S EQUATION

In the previous two sections, equilibrium in the 2D domain was discussed. When one projects the 2D equilibrated stress field onto a curved surface, the 2D equilibrium will be preserved, but it is still uncertain whether the equilibrium does hold in the third dimension. Let $Z(x, y)$ denote the height of the mid-plane of a membrane shell, then the third-dimensional equilibrium can be expressed using Pucher's equation (Timoshenko & Woinowsky-Krieger, 1959, p. 461):

$$N_{xx} \cdot \frac{\partial^2 Z}{\partial x^2} + 2N_{xy} \cdot \frac{\partial^2 Z}{\partial x \partial y} + N_{yy} \cdot \frac{\partial^2 Z}{\partial y^2} = p_x \cdot \frac{\partial Z}{\partial x} + p_y \cdot \frac{\partial Z}{\partial y} - p_z, \tag{2.20}$$

where $Z(x, y)$ is the elevation of the shell and p_z is the vertical load per unit area [force $\cdot$ length^{-2}]. Their directions are illustrated in figure 2.5 in which $\widetilde{N}_{ij}$ are the stress resultants of the curved surface that vertically project the 2D stress resultants N_{ij} on the horizontal plane.

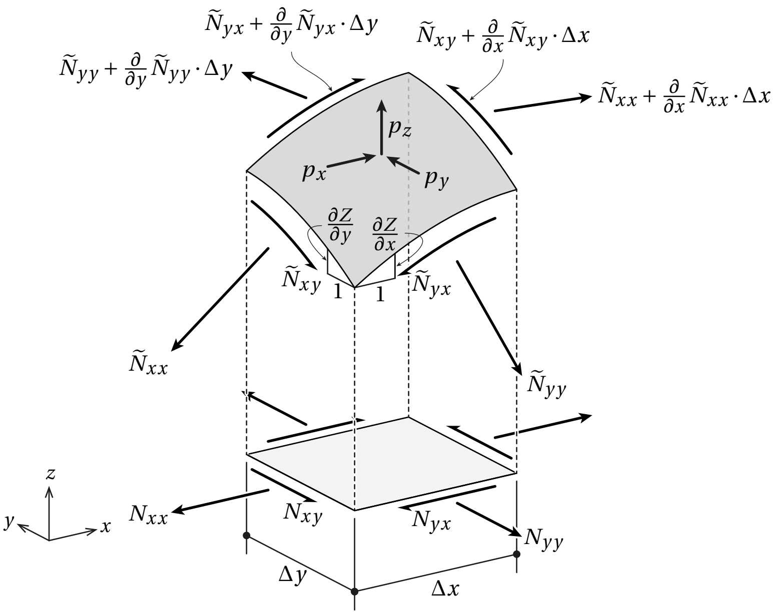

Figure 2.5: Membrane stress resultants on a curved surface. [Adapted Timoshenko & Woinowsky-Krieger, 1959, p. 461]

Matrix expressions. Pucher's equation can be turned into a matrix form as

$$\begin{bmatrix} N_{xx} & N_{xy} & -p_x \\ N_{xy} & N_{yy} & -p_y \end{bmatrix} : \begin{bmatrix} \frac{\partial^2}{\partial x^2} Z & \frac{\partial^2}{\partial x \partial y} Z & \frac{\partial}{\partial x} Z \\ \frac{\partial^2}{\partial x \partial y} Z & \frac{\partial^2}{\partial y^2} Z & \frac{\partial}{\partial y} Z \end{bmatrix} = -p_z, \tag{2.21}$$

in which the operator ":" denotes the double-inner product such that $\mathbf{A} : \mathbf{B} = \sum_i \sum_j A_{ij} B_{ij}$. The Airy stress function in equation (2.8) can be used to express the stress tensor N_{ij}. Furthermore, let vector $\mathbf{p}$ denote the horizontal body forces such that $\mathbf{p} = \begin{bmatrix} p_x & p_y \end{bmatrix}^{\mathrm{T}}$, $\mathbf{H}$ denotes the Hessian operator, and ∇ denotes the gradient operator. Pucher's equation can then be written as

$$\underbrace{\begin{bmatrix} \left(\mathbf{H}_F^{r90^\circ} - \mathbf{P}\right) & -\mathbf{p} \end{bmatrix} : \begin{bmatrix} \mathbf{H} & \nabla \end{bmatrix}}_{D_F^{Pucher}} Z(x, y) = -p_z,$$

or

$$D_F^{Pucher}\left[Z(x, y)\right] = -p_z, \tag{2.22}$$

when a new differential operator $D_F^{Pucher}[\cdot]$ is defined. The subscript $_F$ indicates that the differential operator uses the derivatives of stress function $F(x, y)$ as coefficients. Pucher's equation can also be reorganized as

$$\underbrace{\mathbf{H}_Z^{r90^\circ} : \mathbf{H}}_{D_Z^{Pucher}} F(x, y) = -p_z + \underbrace{\begin{bmatrix} \mathbf{P} & \mathbf{p} \end{bmatrix} : \begin{bmatrix} \mathbf{H}_Z & \nabla_Z \end{bmatrix}}_{p'_h},$$

or

$$D_Z^{Pucher}\left[F(x,y)\right] = -p_z + p'_h, \tag{2.23}$$

when another differential operator $D_Z^{Pucher}[\cdot]$ is introduced. The subscript $_Z$ indicates that this differential operator uses the derivatives of shape function $Z(x,y)$ as coefficients. On the right-hand side, the term p'_h has a subscript $_h$ that denotes that this term contains horizontal loads. The expressions (2.22) and (2.23) are convenient for further discussion, especially in chapter 3.

In the absence of horizontal body forces. When there are no horizontal body forces, **P** and **p** have zero values. Equation (2.21) would then simply become

$$\mathbf{H}_F^{r90^\circ} : \mathbf{H}_Z = -p_z, \tag{2.24}$$

which suggests the vertical load p_z is equilibrated by the double-inner product of two matrices: the rotated and un-rotated Hessian matrices of the Airy stress function and the shape function.

Furthermore, it becomes clear that the stress function $F(x,y)$ and the shape function $Z(x,y)$ are interchangeable in equation (2.24). In other words, $F(x,y)$ and $Z(x,y)$ are commutative.

2.4. CONDITIONS FOR BOUNDARIES AND SUPPORTS

So far, only the equilibrium within the domain has been discussed. This section shall shift the focus on equilibrium at the boundaries: the edges of shell structures. At an edge, membrane stresses exist on the curved shell from one side. There is no shell element providing membrane stresses from the other side. Nonetheless, all elements on an edge must remain in equilibrium, with or without stresses transmitting across the edge. One can decompose the stresses into normal and tangential components. The normal direction $\mathbf{n} = \begin{bmatrix} n_x & n_y \end{bmatrix}^\mathrm{T}$ is defined to be pointing outward while the tangential $\mathbf{t} = \begin{bmatrix} t_x & t_y \end{bmatrix}^\mathrm{T} = \begin{bmatrix} -n_y & n_x \end{bmatrix}^\mathrm{T}$ travels the domain counterclockwise, as illustrated in figure 2.6. The normal stress crossing the edge N_{nn}, the normal stress parallel to the edge N_{tt}, and the shear stress against the edge N_{nt} can be derived from tensor transformation (Arfken et al., 2013, p. 208):

$$\begin{bmatrix} N_{nn} & N_{nt} \\ N_{nt} & N_{tt} \end{bmatrix} = \begin{bmatrix} n_x & n_y \\ -n_y & n_x \end{bmatrix} \begin{bmatrix} N_{xx} & N_{xy} \\ N_{xy} & N_{yy} \end{bmatrix} \begin{bmatrix} n_x & -n_y \\ n_y & n_x \end{bmatrix}. \tag{2.25}$$

If all elements on an edge segment can reach equilibrium without external stresses, one can say the segment is a *free edge*, which is free from external supports. On a free edge, one should have (Csonka, 1987, p. 183)

$$N_{nn} = 0, \tag{2.26a}$$

$$N_{nt} = 0, \tag{2.26b}$$

$$N_{tt} \cdot \frac{\partial^2 Z}{\partial t^2} = p_n \cdot \frac{\partial Z}{\partial n} + p_t \cdot \frac{\partial Z}{\partial t} - p_z. \tag{2.26c}$$

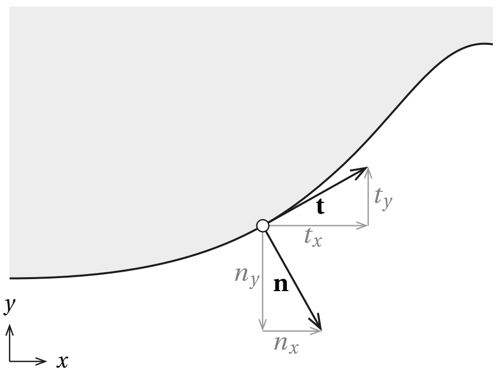

Figure 2.6: Local directions on an edge

Equation (2.26a) gives that the normal stress across the boundary equals zero, equation (2.26b) gives that the shear stress against the boundary is zero, and equation (2.26c) is a degenerated version of Pucher's equation which suggests that the boundary is in balance in the vertical direction. Horizontal body forces p_x and p_y are represented by $p_n = n_x p_x + n_y p_y$ and $p_t = -n_y p_x + n_x p_y$.

Whenever any condition of (2.26a–c) is not satisfied, external support or a special reinforcement is needed to achieve an equilibrium. Practically, it costs differently for a shell designer to violate different conditions. The condition (2.26b) can be bypassed by introducing a funicular rib (or an axial-force resistant reinforcement), the most cost-effective method to bypass one of the three conditions. The horizontal component of the tension force T in the funicular rib collects the unbalanced shear stress and tangential body force at the edge so that

$$T = \int \left(N_{nt} - p_{et}\right) ds,$$

in which p_{et} is the tangential component of body force per unit length on the edge with dimension [force · length^{-1}] and s is the distance along the projected edge. Although the force T affects the conditions of equilibrium, one can still have alternative conditions for a boundary element on a *funicular edge:*

$$N_{nn} = T\frac{d\mathbf{t}}{ds}\cdot\mathbf{n} + p_{en}, \tag{2.27a}$$

$$-N_{nn}\frac{\partial Z}{\partial n} - N_{nt}\frac{\partial Z}{\partial t} + T\frac{\partial^2 Z}{\partial t^2} = p_{en}\cdot\frac{\partial Z}{\partial n} + p_{et}\cdot\frac{\partial Z}{\partial t} - p_{ez}, \tag{2.27b}$$

where p_{en}, p_{et}, and p_{ez} are the body forces per unit length on the edge with dimension [force·length^{-1}]. Detailed locations and orientations of the forces are illustrated in figure 2.7.

A designer can also bypass condition (2.27b) by placing a vertical wall. The wall can introduce extra load in the vertical direction to absorb any unbalanced force. The only condition left for a *wall-supported edge* is

$$N_{nn} = T\frac{d\mathbf{t}}{ds}\cdot\mathbf{n} + p_{en}. \tag{2.28}$$

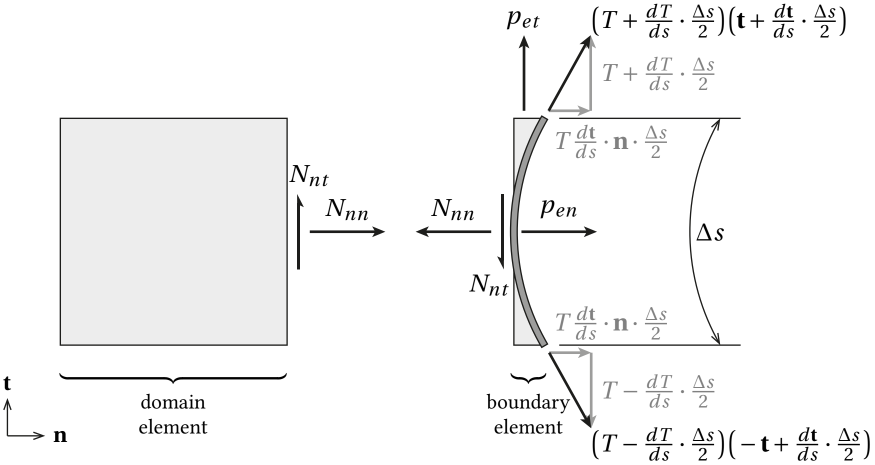

Figure 2.7: Forces and stress resultants on a rib segment

If the designer would like to bypass the last condition, then a rigid support must be provided. Since membrane shells transmit no bending moment, the support only needs to carry translational forces. Once a support capable of carrying forces in all directions is in place, there is no condition for the *fully supported edge*.

On top of the four types of supports discussed above, another type of support exists. It is not at an edge but within the domain. For a *column-supported region*, the p_z in Pucher's equation (2.20) no longer is merely the external loads (e.g., self-weight, snow load) but includes the vertical supporting force from a column. If there is no prescribed vertical supporting force, then Pucher's equation can be dismissed in this region. Equations (2.2a–b) still govern the equilibrium in the horizontal directions within the domain including the region above the column. A minor reminder is that if the column also provides horizontal forces, the values of p_x and p_y should include the horizontal supporting forces. Thus the $\int p_x\,dx$, $\int p_y\,dy$, and $F(x, y)$ must also be updated. Table 2.2 summarizes the discussed boundaries and supports and figure 2.8 shows some examples in realized projects.

Table 2.2: Conditions for boundaries and supports

Type	Condition in the direction of				
	n	t	x	y	z
Free edge	(2.26a)	(2.26b)	-	-	(2.26c)
Funicular edge	(2.27a)	Free	-	-	(2.27b)
Wall-supported edge	(2.28)	Free	-	-	Free
Fully supported edge	Free	Free	-	-	Free
Column-supported region	-	-	(2.2a)*	(2.2b)*	Free

* p_x and p_y should include the horizontal supporting forces.

(a) Free edge (b) Funicular edge (c) Wall-supported edge*

(d) Fully supported point (e) Columns supported shell

Figure 2.8: Examples of boundaries and supports. (a) *Raststätte Deitingen* [Deitingen Service Station], Deitingen, Switzerland. (b) Celebration Park, Allen, Texas, United States. (c) Kresge Auditorium*, Cambridge, Massachusetts, United States. (d) *Palazzetto dello Sport* [Small Sport Palace], Rome, Italy. (e) *Llotja de la Seda* [Silk Exchange], Valencia, Spain. [Source: (a) Peter Eigenraam; (b) PFEIFER FabriTec; (c) Daderot@commons.wikimedia.org, licensed under CC BY-SA 3.0; (d) Blackcat@commons.wikimedia.org, licensed under CC BY-SA 3.0; (e) TMaschler-@commons.wikimedia.org, licensed under CC BY-SA 3.0]

* Kresge Auditorium was initially designed with edges that have no vertical supports. After noticing unexpected deflections at the edges, the façade mullions, which were originally designed to take horizontal wind load only, were redesigned to support the shell along its edges (Plunkett & Mueller, 2015).

2.5. SELF-AIRY MEMBRANES: SPECIAL CASES OF MEMBRANE SHELLS

As mentioned in the previous sections, a membrane shell carries external loads by transmitting tensile and compressive stresses through its curved shape. In the absence of horizontal body forces, the vertical load is balanced by the double-inner product of rotated and unrotated Hessian matrices, one from the shape and the other from the Airy stress function. Although Pucher's equation (2.24) suggests the Airy stress function $F(x, y)$ and the shape function $Z(x, y)$ are commutative, the Airy stress function is often overlooked by architectural and structural designers since it is nowhere to be found in the physical world. However, when the shape of the Airy stress function coincides with the shape of the shell, it can be built as a tangible surface. This dissertation calls these special membrane shells *self-Airy membranes*, parallel to the term of *self-Airy gridshells* in Millar et al. (2021).

Motivation. The motivation to investigate the *self-Airy membranes* arises from the development of the flat-to-curved transformation mechanisms, which is discussed in detail in chapters 5 and 6. It is arguably part of the nature that research goes back-and-forth between theory and execution. At the early stage of this research, the sequence was expected to be rather linear. The research would start with mathematical membrane theory, to then transform the theory into a computational form-finding algorithm. With some form-found shapes, then, the research would perform geometrical analysis before the shapes could become flat-to-curved transforming mechanisms.

However, after prototyping some mechanisms, it was found that a simple actuation scheme is preferable for the flat-to-curved transformation. A scheme of *bottom hoop actuation* (see section 6.3) is investigated which requires the Airy stress function $F(x, y)$ and the shape function $Z(x, y)$ to have similar principal orientations and solely vertical reactions at the supports. A sufficient way to satisfy the above requirements is assuming the supports are on flat ground and $F(x, y)$ and $Z(x, y)$ have exactly the same shape, which is called a self-Airy membrane in this dissertation.

Definition. Let $S(x, y)$ denote such a self-Airy membrane. Subsequently, $Z(x, y)$ can be replaced by $S(x, y)$ and $F(x, y)$ can be replaced by $F_0 S(x, y)$, in which F_0 is a factor with dimension in force. Eventually, equation (2.24) becomes

$$\mathbf{H}_S^{r90^\circ} : \mathbf{H}_S = -\frac{p_z}{F_0}. \tag{2.29}$$

The membrane $S(x, y)$ has a dimension in length. While elements in the Hessian $\mathbf{H}_S$ are second derivatives of $S(x, y)$, these elements have dimensions that are the same as curvatures [length^{-1}]. One can check the dimension consistency by expanding the equation:

$$2\left[\frac{\partial^2 S}{\partial x^2}\cdot\frac{\partial^2 S}{\partial y^2} - \left(\frac{\partial^2 S}{\partial x \partial y}\right)^2\right] = -\frac{p_z}{F_0}. \tag{2.30}$$

The left-hand side has the same dimension as a Gaussian curvature [length^{-2}] while the right-hand side is [force·length^{-2}] over [force] leading to [length^{-2}]. The content within the square brackets of the left-hand side does not only have the same dimension as a Gaussian curvature, the content is exactly the *isotropic*-Gaussian curvature in *isotropic*-geometry

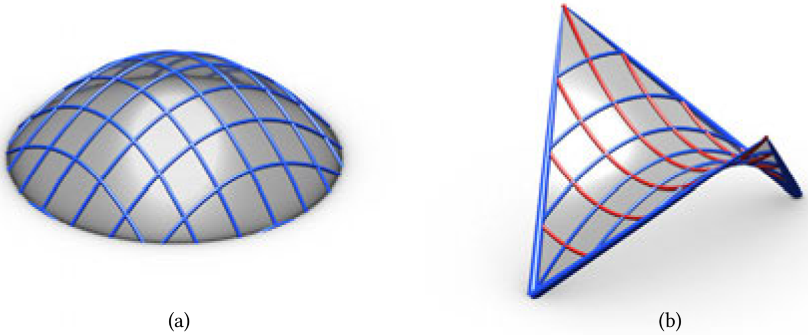

Figure 2.9: Trivial solutions to equation (2.29)

(see section 4.3). It is worth mentioning here that the content in the brackets is also the determinants of both $\mathbf{H}_S$ and $\mathbf{J}_{\boldsymbol{\xi}/\mathbf{x}}$. For an $S(x, y)$ that has constant $\det(\mathbf{H}_S)$, the reciprocal diagrams $S^*(\xi, \eta)$ also have constant $\det(\mathbf{H}_{S^*})$.

Equation (2.29) is a second-order partial differential equation, and the sign of p_z/F_0 controls whether it is elliptic or hyperbolic. Only when the external load p equals zero, the equation could be parabolic. This type of non-structural surface will not be discussed in this dissertation.

This section first mentions the motivation of the investigation of self-Airy membranes and subsequently provides some analytical solutions. Chapter 3 follows up the discussion and provides a numerical method for finding more self-Airy membranes.

2.5.1. TRIVIAL SOLUTIONS

Equation (2.29) suggests that the *isotropic*-Gaussian curvature is linearly proportional to the external load. When the load is constant as $p_z/F_0 = \pm 2$, the solutions to this equation can be as simple as paraboloids. If the constant term is negative, then the solution can be an elliptic paraboloid like $S(x, y) = \left(x^2 + y^2\right)/2$ (figure 2.9a). When the constant is positive, a hyperbolic paraboloid such as $S(x, y) = xy$ can be the solution (figure 2.9b).

2.5.2. ANALYTICAL SOLUTIONS

The inspiration for investigating potential analytical solution arises from a numerical solution in figure 3.17, which shows a triangular shell with slender legs between free edges. The profiles of these legs resemble decaying exponential curves. Therefore, this section expects the existence of an analytical solution that propagates curvature from a narrow cross-section to a wider cross-section similar to those legs.

This enlarging cross-section can be expressed mathematically by assuming an analytical solution which is the result of a standard cross-section $\beta(y_0)$ sweeping along the x-axis and gradually scaled by another function $\alpha(x)$:

$$S(x, y) = \alpha(x) \cdot \beta(y_0) + ax + by + c, \tag{2.31}$$

where $y_0 = y/\alpha(x)$, and a, b, c are constants.

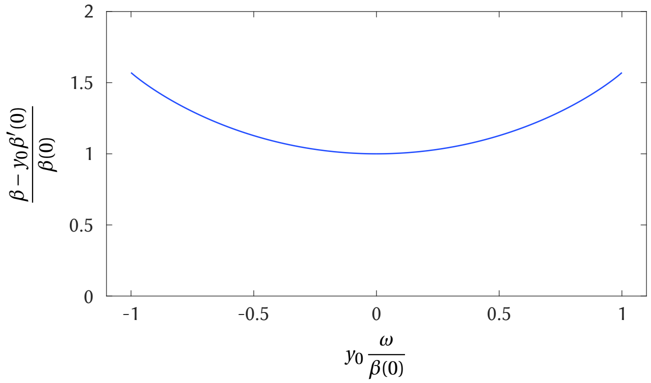

Figure 2.10: The general solution of the β-y_0 curve.

Subsequently, one can derive the second derivatives as

$$\frac{\partial^2}{\partial x^2} S = \alpha'' \beta - \alpha'' \beta' y_0 + \frac{\alpha'^2}{\alpha} \beta'' {y_0}^2, \qquad \frac{\partial^2}{\partial x \partial y} S = -\frac{\alpha'}{\alpha} \beta'' y_0, \qquad \frac{\partial^2}{\partial y^2} S = \frac{1}{\alpha} \beta''.$$

These expressions turn the governing equation (2.29) into

$$2 \frac{\alpha''}{\alpha} \beta'' (\beta - \beta' y_0) = -\frac{p_z}{F_0}. \tag{2.32}$$

Since p_z and F_0 are set to be non-zero constants, the equation can be satisfied whenever both α''/α and $\beta''(\beta - \beta' y_0)$ are non-zero constants. Function $\alpha(x)$ has three solutions:

$$\alpha(x) = d e^{\lambda x}, \qquad d \cosh(\lambda x), \quad \text{or} \quad d \cos(\lambda x), \tag{2.33}$$

in which d and λ are constants. All of the expressions have constant α''/α:

$$\frac{\alpha''}{\alpha} = \lambda^2, \qquad \lambda^2, \quad \text{or} \quad -\lambda^2.$$

While $\beta(y_0)$ can be

$$\beta(y_0) = C_0 \left[\sqrt{1 - \left(\frac{\omega}{C_0} y_0 \right)^2} + \frac{\omega}{C_0} y_0 \arcsin\left(\frac{\omega}{C_0} y_0 \right) \right] + C_1 y_0, \quad -\frac{C_0}{\omega} \le y_0 \le \frac{C_0}{\omega}, \tag{2.34}$$

in which ω is a constant, and $C_0 = \beta(0)$ and $C_1 = \beta'(0)$ are constants of integration. This expression has

$$\beta''(\beta - \beta' y_0) = \omega^2.$$

Then, these $\alpha(x)$ and $\beta(y_0)$ make equation (2.32) become $2\lambda^2\omega^2 = \pm P_z/F_0$. The general solution of $\beta(y_0)$ is plotted in figure 2.10 and the solutions of $S(x, y)$ are illustrated in figure 2.11.

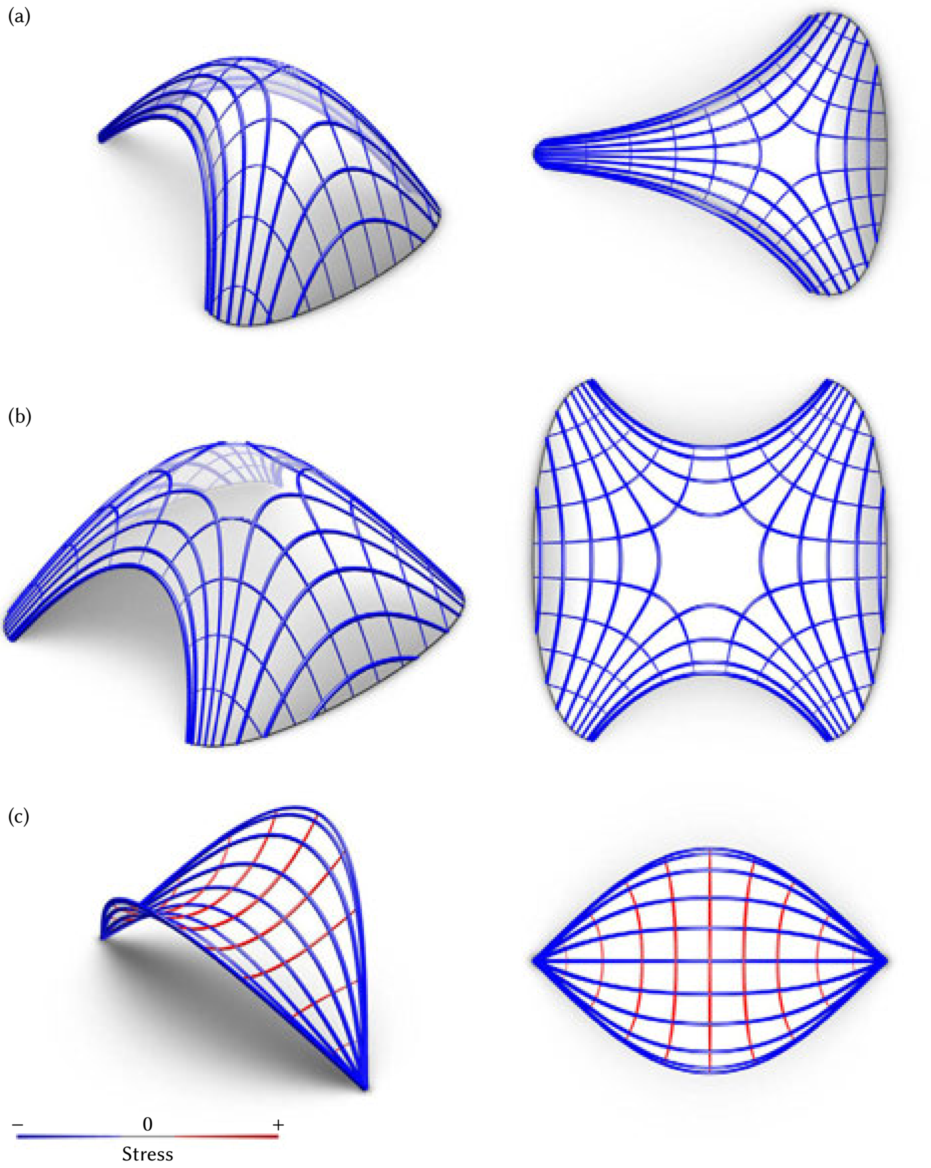

Figure 2.11: Analytical self-Airy surfaces. All surfaces are drawn with the same β-y_0 curve when $\beta(0) = 1$ and $\beta'(0) = 0$. The α curves are $-e^{\lambda x}/2$, $-\cosh(x)$ and $\cos(x)$ in (a), (b) and (c) respectively. Isometric views are drawn on the left and top views on the right. Stress networks are shown on the surfaces with compression (−) in blue and tension in red (+).

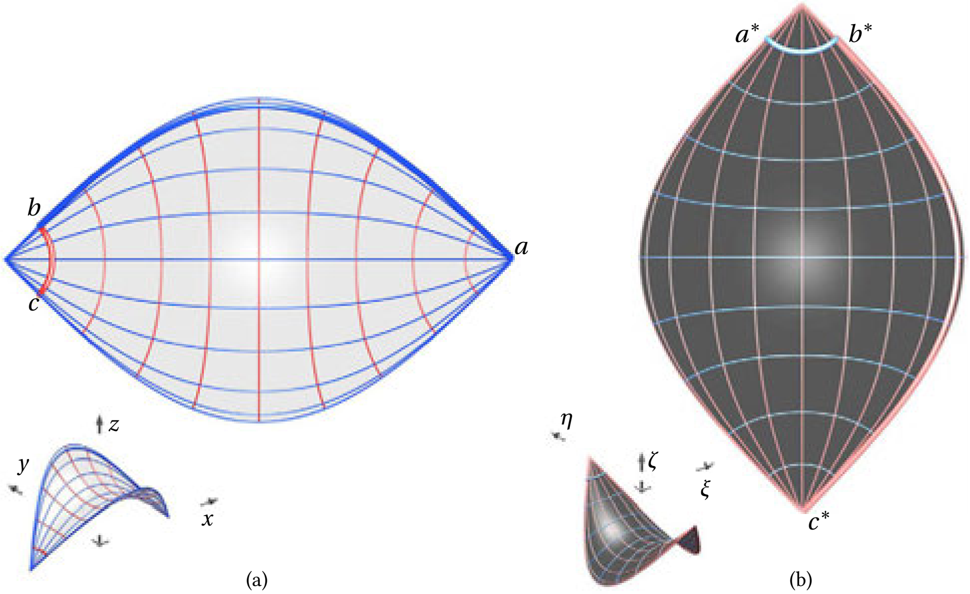

(a) (b)

Figure 2.12: The self-reciprocal membrane (a) and its reciprocal diagram (b). Curves connecting points a, b, c reciprocally map to curves connecting the corresponding points a^*, b^*, c^*.

An interesting fact is that the anticlastic solution in figure 2.11c is not only self-Airy, but also *self-reciprocal*, meaning that it has the same shape as its Maxwell reciprocal diagram. As discussed, the reciprocal diagram of a constant *isotropic*-Gaussian-curvature surface is also a constant *isotropic*-Gaussian-curvature surface. Here, the solution has an *isotropic*-Gaussian-curvature equal to 1 within its domain. Furthermore, this very solution has only two types of boundary conditions: supporting points and free edges. On a free edge, the conditions $\partial_{tt}S = 0$ and $\partial_{nt}S = 0$ require $\partial_x S$ and $\partial_y S$ to be constants (Csonka, 1987) which suggests that a free edge in $S(x, y)$ maps to a point in $S^*(\xi, \eta)$, and vice versa. Since the surface has two supporting points and two free edges, its reciprocal diagram has two free edges and two supporting points. Qualitatively speaking, the boundary of this surface allows it to be self-reciprocal. Analytically, it still requires some work to check if its reciprocal diagram indeed has the same shape as itself. The solution is believed to be original, thus worth to be mentioned and validated explicitly.

By setting $\omega = 1$, $C_0 = 1$, and $C_1 = 0$ in equation (2.34), selecting $\alpha(x) = \cos(x)$, and letting $a = b = c = 0$ in equation (2.31), one can explicitly express this surface as

$$S(x, y) = \sqrt{\cos(x) - y^2} + y \arcsin\left(\frac{y}{\cos(x)}\right), \quad -\frac{\pi}{2} < x < \frac{\pi}{2}, \quad -\cos(x) \le y \le \cos(x).$$

With the reciprocal mapping stated in equation (2.9), one can obtain the reciprocal diagram:

$$S^*(\xi, \eta) = -\sqrt{\cos(\eta) - \xi^2} - \xi \arcsin\left(\frac{\xi}{\cos(\eta)}\right), \quad -\cos(\eta) \le \xi \le \cos(\eta), \quad -\frac{\pi}{2} < \eta < \frac{\pi}{2}.$$

Apparently, the two surfaces have the same shape although the orientations are different. The reciprocity between these two surfaces is shown in figure 2.12.

2.6. Lower-bound theorem and statical determinacy

Classical shell theories deal with three major topics, namely equilibrium of forces, compatibility of displacements (and rotations), and strain-stress relations. The latter two topics relate to how a shell deforms from its original shape. In the form-finding process, there is no original shape yet, let alone deformation. Hence, the compatibility and strain-stress relations are not the main concern this dissertation.

However, focusing only on equilibrium is still relevant when designing structurally sound shells. For ductile construction systems (including masonry, reinforced concrete), one can check whether the structure is safe by using the *plastic theory*, or *lower-bound theorem*. Heyman (1977, p.71) provided a concise description of the theorem:

> *If any satisfactory equilibrium state can be found for a structure [...], then this is complete evidence that the structure is safe. The power of this theorem lies in the fact that the equilibrium state under discussion need[s] not be the actual equilibrium state; a single satisfactory solution is all that is necessary.*

The word satisfactory is referring to the stresses that are allowable for the materials and connections. One of the two crucial premises is that the structure is sufficiently ductile to redistribute (by yielding or cracking) the excessive stress to other materials or structural members. The other premise is that the structure is sufficiently stiff to maintain stability (or avoid buckling).

Applying the theorem to a shell, if there is a set of solutions of which the stress (F) and eccentricity (distance between the actual shell surface to the desired shape Z) are allowable under the considered load case (p_x, p_y, and p_z), then the shell shall be safe. Equilibrium of these five functions (F, Z, p_x, p_y, and p_z) is governed by Pucher's equation. Like a five-variable equation can determine the fifth variable when the other four variables are provided, Pucher's equation can determine the fifth function whenever the other four functions are provided. In the case of prescribed load condition (i.e., p_x, p_y, and p_z) and stress distribution $F(x, y)$, the shape of the shell $Z(x, y)$ can be provided by solving Pucher's equation. This process is a form-finding problem. Conversely, if the shape of the shell $Z(x, y)$ is given and a load case (i.e., p_x, p_y, and p_z) is assigned. The only unknown function, the stress function $F(x, y)$, can be determined with Pucher's equation as well. For a statically determinate truss, due to the absence of bending moment, the axial forces in the truss can be determined by the equilibrium equations alone. Membrane shells have a similar statical determinacy, so the membrane stresses in the shells can be determined by Pucher's equation alone.

However, an $F(x, y)$ derived from arbitrarily given $Z(x, y)$, p_x, p_y, and p_z may conflict with the desired boundary conditions. Chapter 3 provides a numerical method recommending an alternative $Z(x, y)$ that allows for the derived $F(x, y)$ to fit the boundary conditions.

2.7. SUMMARY

This chapter has revisited the statics of membrane shells. Some essential theories were extracted:

- membrane shells are curved structures that carry loads with in-plane tension and compression but without bending moments;
- the horizontal equilibrium of membrane shells can be formulated by the Airy stress functions;
- the vertical equilibrium of membrane shells is governed by Pucher's equation;
- equilibrium at boundaries is characterized by boundary conditions—free edge, funicular edge, wall-supported edge, and supported edge; and
- for ductile construction systems, the lower-bound theorem suggests that an equilibrium state that satisfies yield criteria can sufficiently prove that a structure is safe.

The main contributions of this chapter are that:

- a special type of membranes—self-Airy membrane—has been defined, of which the membrane shell has the same shape as its Airy stress function; and
- some analytical self-Airy membranes are provided.

These theories and contributions lay the foundations for later chapters (figure 1.13). Specifically, the static theories enable the numerical method, radial basis functions (see chapter 3), to explore and design the forms of membrane shells. Meanwhile, the self-Airy membrane is expected to simplify the actuation of the proposed flat-to-curved transforming mechanism (see chapters 5 and 6).

3

FINDING MEMBRANE SHELLS WITH RADIAL BASIS FUNCTIONS

> *The double-curvature vaulted structures are very economical and easy to build, but [usually] cannot be easily represented in graphic documents.*
>
> Eladio Dieste[1]

Parts of this chapter have been presented in *IASS Annual Symposium 2019 – Structural Membranes 2019* (Chiang et al., 2019) and submitted for publication (Chiang & Borgart, 2022).

[1] adapted from Anderson 2004, p.183. The original work, *Arquitectura y Construcción* [Architecture and Construction], had been published in 1980.

THE METHOD of radial basis functions is often used to approximate arbitrary scalar functions and to solve partial differential equations. When the method is used to approximate a function in a 2D domain, the graph of the function is a 3D surface, which is suitable for representing shell roofs of which the projection does not intersect itself. The represented surface is easy to be C^∞ continuously smooth. This feature simplifies curvature interrogation and subsequently fabrication-aware discretization (Pottmann, 2013). However, the method of radial basis functions has not yet been applied in form-finding tasks prior to this PhD research and related publications: Chiang et al. (2019) and Chiang and Borgart (2022).

Tasks of form-finding seek alignment between stresses, shape, loads, and supports. The relations among them are characterized by Pucher's equation and boundary conditions, which have been carefully examined in chapter 2. The current chapter focuses on how to utilize radial basis functions (RBFs) to find the right set of stresses and shape under given loading and supports. The loading may hereby include both vertical and horizontal components. The latter component is often neglected yet still important, especially for seismic hazard zones (Michiels et al., 2019). This chapter also investigates how to consider horizontal loads in the form-finding process.

OUTLINE

Section 3.1 reviews features of relevant computational form-finding methods. Section 3.2 briefly explains how to apply RBFs to represent an arbitrary function and to solve linear differential problems. Section 3.3 exhibits basic procedures of applying RBFs by finding the shape of hanging chains, which is in a 1D domain. Section 3.4 expands the application of RBFs to 2D domains and finds the stresses and shapes of membranes. Section 3.5 dives into finding self-Airy membranes and solving free boundary problems. Section 3.6 displays how horizontal loads affect stress distribution in membranes. Section 3.7 summarizes the features of the RBFs method and recommends ribs or peripheral walls to carry horizontal loads.

3.1. COMPUTATIONAL METHODS IN FORM-FINDING

Numerical algorithms can analyze the statics of shells by discretizing continuous surfaces into finite elements (Veenendaal & Block, 2012) and sometimes reconstruct them back into smooth NURBS surfaces (Pugnale, Echenagucia, & Sassone, 2014). As previously mentioned in section 1.1, these computational form-finding methods can be broken down into two categories: simulating physical hanging models or numerically solving equations of statics (figure 3.1).

Physics-based. In the category of simulating physical models, the most representative method is *dynamic relaxation* (Barnes, 1988). The computational models contain parameters such as the mass of each node, stiffness of each bar, support positions, etc. The model computes the elongation of bars and residual forces on nodes, and subsequently, updates the velocity and position of each node. Then, the model iteratively recalculates the elongation and residual forces based on the updated position until all the nodes rest at a state of equilibrium. Methods in this category are intuitive to use, but they only provide stable equilibrium solutions.

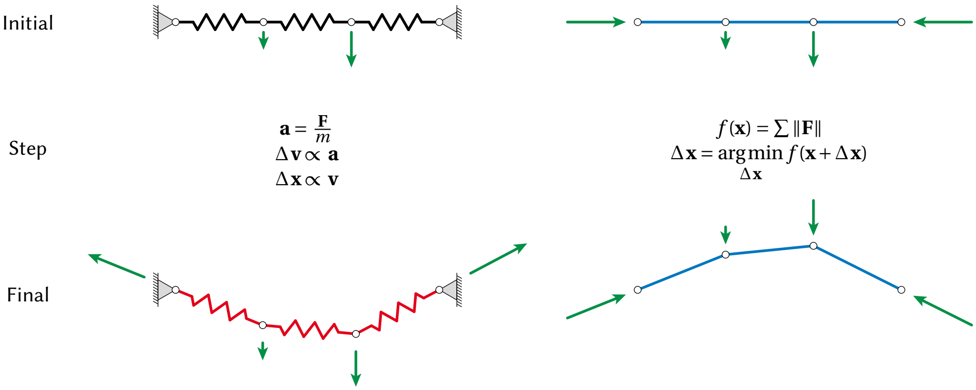

(a) Dynamic relaxation
(physics-based)

(b) Force density method
(mathematics-based)

Figure 3.1: Schemes of finding funicular structures. (a) The method of dynamic relaxation starts from a set of springs, nodes, and loads. The residual forces accelerate the nodes toward a stable equilibrium. (b) The method of geometric stiffness initializes the process with pre-stressed bars, nodes, and loads. The nodes actively search for alternative positions to minimize the residual forces.

Mathematics-based. The methods of this category, in contrast, do not include mass in their models. They solve equations of statics numerically, and sometimes are called geometric stiffness methods (Veenendaal & Block, 2012). The most representative method is the *force density method* (Schek, 1974), in which the bars have prescribed forces proportional to their lengths. The ratio of the force to the length is called the "force density". The algorithm computes the residual force of each node according to the "force densities" and the lengths and seeks the alternative position of each node to minimize its residual force. The method of *thrust network analysis* (Block & Ochsendorf, 2007) also falls under this category. Methods in this category can be perceived as somewhat abstract, but they can generate both stable and unstable equilibrium solutions.

Most of these methods are based on networks of funicular bars connected at nodes. The results from the linear meshes are affected by the connectivity of the mesh and the parameters of the bars (e.g., spring constants in dynamic relaxation and force density in the force density method). These methods can find funicular forms. However, they do no indicate how to alter the connectivity and the parameters in order to approximate a predefined shape.

This dissertation uses radial basis functions to develop a form-finding algorithm in a mathematics-based fashion. There is no mass, velocity, or acceleration in the algorithm. Radial basis functions are used to represent the Airy stress and shape functions. The first function is equivalent to the reciprocal diagrams in the thrust network analysis, while the shape function is equivalent to the elevations of nodes.

Two features of this approach are worth mentioning. First, the radial basis function method is a mesh-free method. The solution is not affected by the connectivity between nodes. The results generated by the radial basis functions are two smooth functions—an Airy stress function and a shape function. Secondly, the algorithm can also take a predefined shape as input and then find a closely compatible Airy stress function (if not fully compatible).

3.2. INTRODUCTION TO RADIAL BASIS FUNCTIONS

Radial basis functions are used to represent a smooth multivariate function. An arbitrary function $f(\mathbf{x})$ can be approximated by a set of radial basis functions $\phi\left(\left\|\mathbf{x}-\boldsymbol{\mu}_i\right\|;\rho_i\right)$ and augment polynomial terms $h(\mathbf{x})$ (Biancolini, 2017; Boyd & Gildersleeve, 2011; Buhmann, 2003):

$$f(\mathbf{x}) = \sum_{i=1}^{n} \lambda_i \phi\left(\left\|\mathbf{x}-\boldsymbol{\mu}_i\right\|;\rho_i\right) + h(\mathbf{x}) + \varepsilon, \tag{3.1}$$

in which $\mathbf{x}$ is the position of evaluation, λ_i are the magnitude coefficients of the RBFs, $\boldsymbol{\mu}_i$ are the source points, ρ_i are the shape parameters of the RBFs, and ε is the approximate error.

The radial basis functions can be as simple as the Euclidean distance as $\phi(r;\rho) = r$, thin-plate splines $\phi(r;\rho) = r^2 \log r$, Gaussian $\phi(r;\rho) = e^{-\rho^2 r^2}$, or *multiquadrics*

$$\phi\left(\left\|\mathbf{x}-\boldsymbol{\mu}\right\|;\rho\right) = \sqrt{\left\|\mathbf{x}-\boldsymbol{\mu}\right\|^2 + \rho^2}.$$

The last one is used in all cases in this dissertation because its shape parameter ρ allows the user to adjust the local intensity of the curvature. This benefit will be discussed in further detail in the upcoming section 3.3. Furthermore, there is no necessity to augment multiquadrics with polynomial terms (Boyd & Gildersleeve, 2011). Therefore, equation (3.1) can be more specific and simplistic as

$$f(\mathbf{x}) = \sum_{i=1}^{n} \lambda_i \sqrt{\left\|\mathbf{x}-\boldsymbol{\mu}_i\right\|^2 + \rho_i^2} + \varepsilon. \tag{3.2}$$

By a sufficient number of multiquadrics n and adequately arranged pairs of μ_i and ρ_i, the representable space (Buhmann, 2003)

$$S = \left\{ \sum_{i=1}^{n} \lambda_i \sqrt{\left\|\mathbf{x}-\boldsymbol{\mu}_i\right\|^2 + \rho_i^2} \,\middle|\, \{\lambda_i\} \in \mathbb{R}^n \right\} \tag{3.3}$$

shall be large enough to include all instances on function $f(\mathbf{x})$ or at least minimize the approximate errors ε. Practically, only some of the instances will be sampled and used to calibrate the λ_i. Let $\mathbf{x}_j$ denote m calibration points, and f_j denote the target values. The individual errors ε_i will then be

$$\varepsilon_j = f_j - \phi_{ji} \cdot \lambda_i,$$

where $\phi_{ji} = \phi\left(\left\|\mathbf{x}_j-\boldsymbol{\mu}_i\right\|;\rho_i\right) = \sqrt{\left\|\mathbf{x}_j-\boldsymbol{\mu}_i\right\|^2 + \rho_i^2}$. In matrix form, this can be expressed as

$$\boldsymbol{\varepsilon} = \mathbf{f} - \boldsymbol{\Phi}\boldsymbol{\lambda},$$

in which $\boldsymbol{\varepsilon}$ and $\mathbf{f}$ are two $m \times 1$ column vectors with contents of ε_j and f_j; $\boldsymbol{\lambda}$ is an $n \times 1$ column vector containing λ_i; while $\boldsymbol{\Phi}$ is an $m \times n$ rectangular matrix with elements as ϕ_{ji}. Then, the best-fit coefficient vector $\boldsymbol{\lambda}$ can be provided by minimizing the approximate errors with the ordinary *least-squares method (LSM)*:

$$\boldsymbol{\lambda} = \underset{\boldsymbol{\lambda}}{\arg\min}\, \boldsymbol{\varepsilon}^{\mathrm{T}}\boldsymbol{\varepsilon} = \left(\boldsymbol{\Phi}^{\mathrm{T}}\boldsymbol{\Phi}\right)^{-1} \boldsymbol{\Phi}^{\mathrm{T}}\mathbf{f}. \tag{3.4}$$

Equation (3.4) is often applied in such approximation problems.

Hermite interpolation and solving a differential equation. When the same scheme is applied to a *Hermite interpolation*, in which the interpolation includes not only values but also derivatives, the method can also provide solutions to differential equations. Suppose there is a linear partial differential equation problem as

$$\begin{aligned} L\left[f(\mathbf{x})\right] &= g(\mathbf{x}), \quad \mathbf{x} \in \Omega \subset \mathbb{R}^n, \\ B\left[f(\mathbf{x})\right] &= q(\mathbf{x}), \quad \mathbf{x} \in \partial\Omega, \end{aligned}$$

where Ω is the domain, $\partial\Omega$ is the boundary, $L[\cdot]$ and $B[\cdot]$ are the differential operators of the governing equation and the boundary condition respectively, and g and q are prescribed functions. When $\mathbf{x}_\Omega$ and $\mathbf{x}_{\partial\Omega}$ are selected as calibration points, radial basis functions can be used to approximate the problem as

$$\begin{aligned} g(\mathbf{x}_\Omega) &= \sum_{i=1}^{n} L\left[\phi_i(\mathbf{x}_\Omega)\right] + \varepsilon_\Omega, \qquad \mathbf{x}_\Omega \in \Omega, \\ q(\mathbf{x}_{\partial\Omega}) &= \sum_{i=1}^{n} B\left[\phi_i(\mathbf{x}_{\partial\Omega})\right] + \varepsilon_{\partial\Omega}, \quad \mathbf{x}_{\partial\Omega} \in \partial\Omega, \end{aligned}$$

or in a matrix form as

$$\begin{bmatrix} \mathbf{g} \\ \mathbf{q} \end{bmatrix} = \begin{bmatrix} \mathbf{\Phi}_L \\ \mathbf{\Phi}_B \end{bmatrix} \boldsymbol{\lambda} + \begin{bmatrix} \boldsymbol{\varepsilon}_\Omega \\ \boldsymbol{\varepsilon}_{\partial\Omega} \end{bmatrix}.$$

The least-squared method or weighted least-squared method can provide the solution:

$$\boldsymbol{\lambda} = \underset{\boldsymbol{\lambda}}{\arg\min} \begin{bmatrix} w_L \boldsymbol{\varepsilon}_\Omega \\ w_B \boldsymbol{\varepsilon}_{\partial\Omega} \end{bmatrix}^{\mathrm{T}} \begin{bmatrix} w_L \boldsymbol{\varepsilon}_\Omega \\ w_B \boldsymbol{\varepsilon}_{\partial\Omega} \end{bmatrix} = \left(\begin{bmatrix} w_L \mathbf{\Phi}_L \\ w_B \mathbf{\Phi}_B \end{bmatrix}^{\mathrm{T}} \begin{bmatrix} w_L \mathbf{\Phi}_L \\ w_B \mathbf{\Phi}_B \end{bmatrix} \right)^{-1} \begin{bmatrix} w_L \mathbf{\Phi}_L \\ w_B \mathbf{\Phi}_B \end{bmatrix}^{\mathrm{T}} \begin{bmatrix} w_L \mathbf{g} \\ w_B \mathbf{q} \end{bmatrix},$$

where w_L and w_B are the weights. The weights are crucial and have dimensions when $L[\cdot]$ and $B[\cdot]$ have different dimensions.

The generic theory of differential and the least-square operations has now been clarified. The upcoming sections employ the method to form-finding problems.

3.3. NUMERICALLY FINDING THE SHAPE OF A HANGING CHAIN

This section demonstrates how to use radial basis functions to find the form of a hanging chain in a vertical plane. The shape of a chain is governed by an ordinary differential equation. Although this problem is rather simple, it admits analytical solutions for validating the results from radial basis functions. The demonstration begins at the most simple load cases.

Governing equation and boundary conditions. When there is only vertical load, the shape of a hanging chain between two anchorages can be formulated as a boundary value problem:

$$T_h \cdot \frac{d^2}{dx^2} Z(x) = -p_z(x), \quad x \in \{x \mid a < x < b\}, \tag{3.5a}$$

$$Z(x) = q(x), \quad x \in \{a, b\}, \tag{3.5b}$$

where T_h is the horizontal component of the tension force within the chain, $Z(x)$ is the shape of the chain, $p_z(x)$ is the vertical load per unit horizontal length at position x, a and b are the positions of the anchorages, and $q(x)$ is the prescribed elevation.

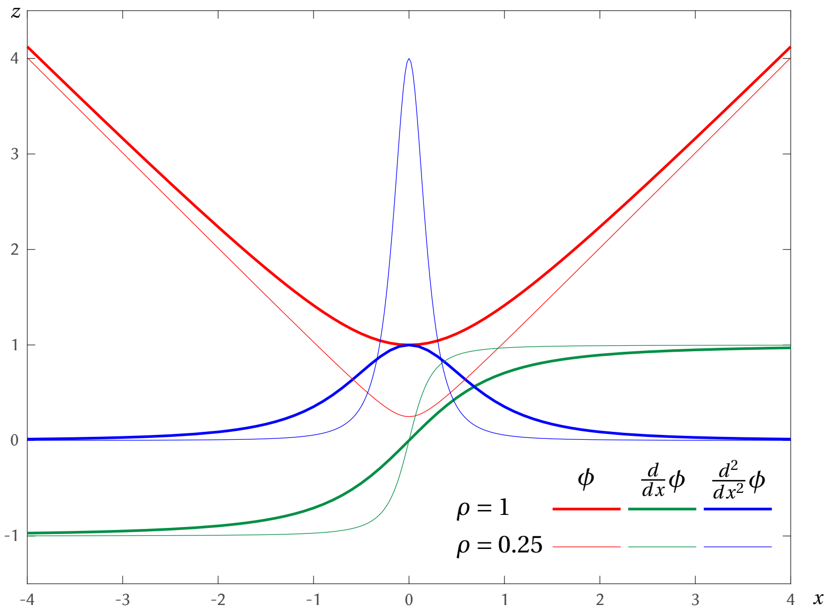

Figure 3.2: Multiquadric curves and their derivatives

Representation with RBFs. Assuming the shape function $Z(x)$ is the aggregate of radial basis functions, one can have

$$Z(x) = \sum_{i=1}^{n} \lambda_i \phi(x - \mu_i ; \rho_i) + \varepsilon.$$

Here the problem is in a 1D domain, therefore the independent variable x and the centers of the radial basis functions μ_i are scalars, and hence they are denoted by non-bold symbols. Since the governing equation (3.5a) is a second-order differential equation, it is necessary to obtain the derivatives of the basis function—multiquadrics—up to the second order:

$$\begin{aligned} \phi(x-\mu;\rho) &= \sqrt{(x-\mu)^2+\rho^2}, \\ \frac{d}{dx}\phi(x-\mu;\rho) &= \frac{x-\mu}{\sqrt{(x-\mu)^2+\rho^2}}, \\ \frac{d^2}{dx^2}\phi(x-\mu;\rho) &= \frac{\rho^2}{\left[\sqrt{(x-\mu)^2+\rho^2}\right]^3}. \end{aligned}$$

In the multiquadrics, the shape parameter ρ can affect the intensity of the second derivative. Figure 3.2 displays the functions with different values of ρ and their corresponding derivatives.

The problem of the ordinary differential equation (3.5a) and the boundary condition (3.5b) can be translated into a Hermite interpolation as

$$-p_z(x_{\Omega j}) = T_h \sum_{i=1}^{n} \lambda_i \frac{\rho_i^2}{\left[\sqrt{(x_{\Omega j}-\mu_i)^2+\rho_i^2}\right]^3} + \varepsilon_{\Omega j}, \tag{3.6a}$$

$$q(x_{\partial\Omega}) = \sum_{i=1}^{n} \lambda_i \sqrt{(x_{\partial\Omega}-\mu_i)^2+\rho_i^2} + \varepsilon_{\partial\Omega}, \tag{3.6b}$$

where, in the demonstration cases, the positions of anchorages $x_{\partial\Omega} = \{a, b\}$ are set to be $\{-2, 2\}$, and the evenly distributed calibration points $x_{\Omega j} = -2 + 4(j - .5)/m$, $j \in \{1, 2, \ldots, m\}$ have the number count m set to 64.

Arrangements of source points and shape parameters. Before deriving the magnitude coefficients λ_i, one must also determine the locations of source points μ_i and corresponding shape parameters ρ_i. As indicated in equation 3.3, the representable space is affected by the arrangement of μ_i and ρ_i. In the following paragraphs, three sets of μ_i and ρ_i are prepared. They produce different results under some testing load distributions $p_z(x)$. The results are compared with analytical solutions. Subsequently, one can develop strategies to arrange appropriate μ_i and ρ_i.

The source points are arranged at a regular spacing $\Delta\mu$ from one end of the domain to the other end, along with two extra positions outside the domain, or in a mathematical expression:

$$\mu_i \in \left(\left\{-3, 3\right\} \cup \left\{-2, -2+\Delta\mu, -2+2\Delta\mu, \ldots, 2\right\}\right).$$

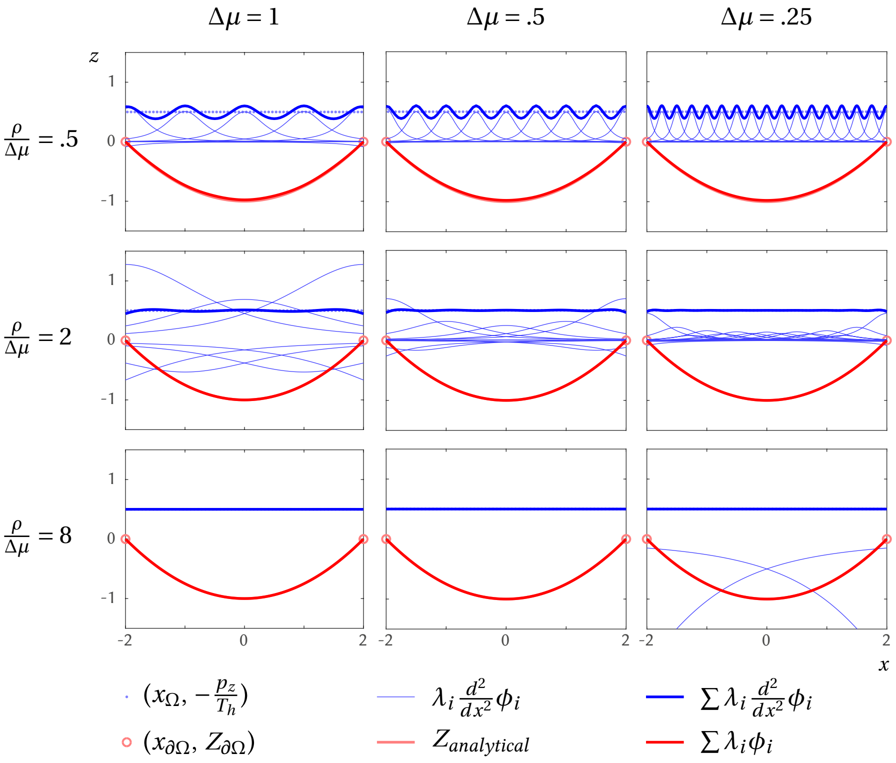

Figure 3.3: Chains under uniformly distributed load

The extra source points $\{-3, 3\}$ are placed to add extra degrees of freedom to better comply with the boundary conditions (3.6b) and to leave the main source points $\{-2, -2+\Delta\mu, -2+2\Delta\mu, \ldots, 2\}$ focusing on approximating the governing equation (3.6a). The spacing $\Delta\mu$ is tested at the values of 1, 0.5, and 0.25.

The shape parameters ρ are set to be proportional to the spacing $\Delta\mu$. A third of the cases has the shape parameter $\rho = 0.5 \cdot \Delta\mu$, another third has $\rho = 2 \cdot \Delta\mu$, and the final third has $\rho = 8 \cdot \Delta\mu$.

Load distributions. Three load cases are tested out. Although the distributions are different, the totals remain constant: $\int_{-2}^{2} p_z(x)\,dx = -2 \cdot T_h$. The distributions include a uniformly distributed load $p_z(x) = -T_h/2$, a triangular distributed load $p_z(x) = T_h \cdot (x-2)/4$, and a uniformly distributed load over half of the span $p_z(x) = -T_h \cdot H(-x)$, where $H(\cdot)$ is the Heaviside step function. Figures 3.3–5 are dedicated to the three distributions.

Result. In total, there are 27 cases, which are located in a $3 \times 3 \times 3$ array. A location in the array means a unique combination of arrangements. Each *sheet* has a load distribution, each *row* has a constant $\rho/\Delta\mu$ ratio, and each *column* has a constant source point spacing $\Delta\mu$. All of them have the same calibration points $x_{\Omega j}$ and $x_{\partial\Omega}$ at the same positions (see

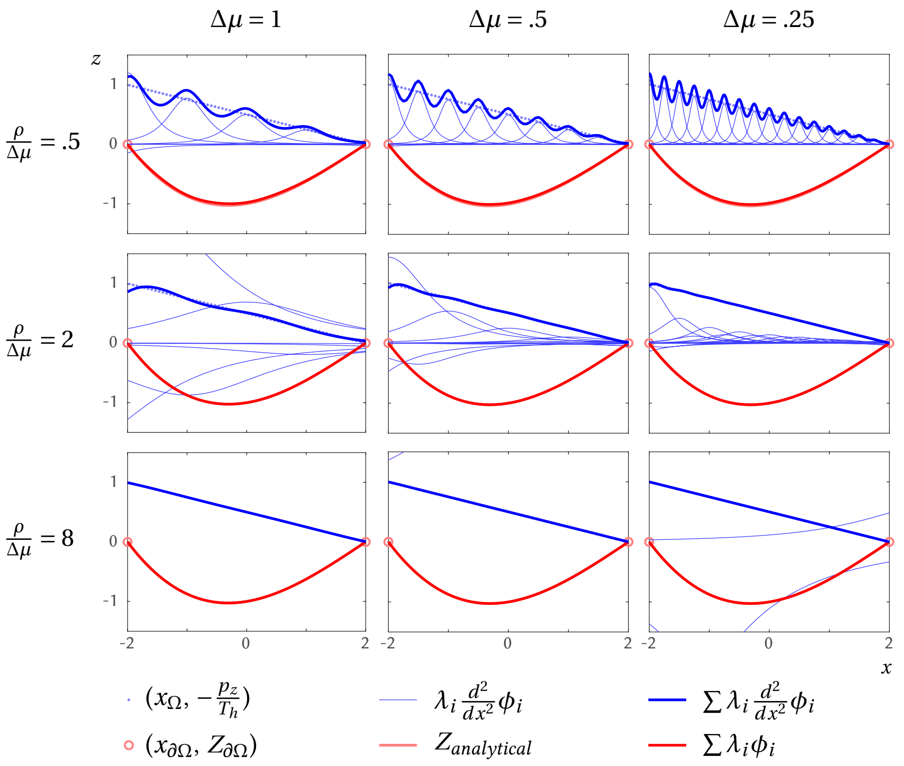

Figure 3.4: Chains under triangular distributed load

equations (3.6a–b)). With the least squared method, one can derive the best fit λ_i for each case. The results of the 27 cases are plotted in figures 3.3–5.

Discussion and error estimation. Across the three sheets or three figures 3.3–5, all cases show that the results of the RBFs $\sum \lambda_i \phi_i$ (the red curves in the figures) match the theoretical shapes $Z_{analytical}$ (the pink curves). Only in the first rows, where $(\rho/\Delta\mu) = .5$, the results $\sum \lambda_i \phi_i$ slightly deviate from the theoretical $Z_{analytical}$, especially in the last sheet.

The errors in the second derivative are more noticeable. One can see that the aggregate of the second derivatives $\sum \lambda_i \cdot d_{xx}\phi_i$ (the bold blue curves) undulates around the ideal values $-p_z/T_h$ (blue dots). Different settings in the spacing $\Delta\mu$ and the ratio $\rho/\Delta\mu$ yield different results. Because the multiquadric curves have a bell shape, the small $\rho/\Delta\mu$ ratio gives narrow and isolated bells, the $d_{xx}\phi_i$ (thin blue curves). When the $\rho/\Delta\mu$ ratio becomes even smaller, the bells will look like nails on a bed. That will lead to even worse results than in the first rows. However, it does not mean a larger $\rho/\Delta\mu$ ratio is always the better choice. When the ratio is too large, the matrix inverse in the least square method would be singular. Based on these test, the ratio of $\rho/\Delta\mu$ is recommended to be set between 2 and 8.

The ratio $\rho/\Delta\mu$ controls the magnitude of the undulation of the second derivative curve around the ideal value, while the spacing $\Delta\mu$ affects the *wavelength*. Especially at the bottom

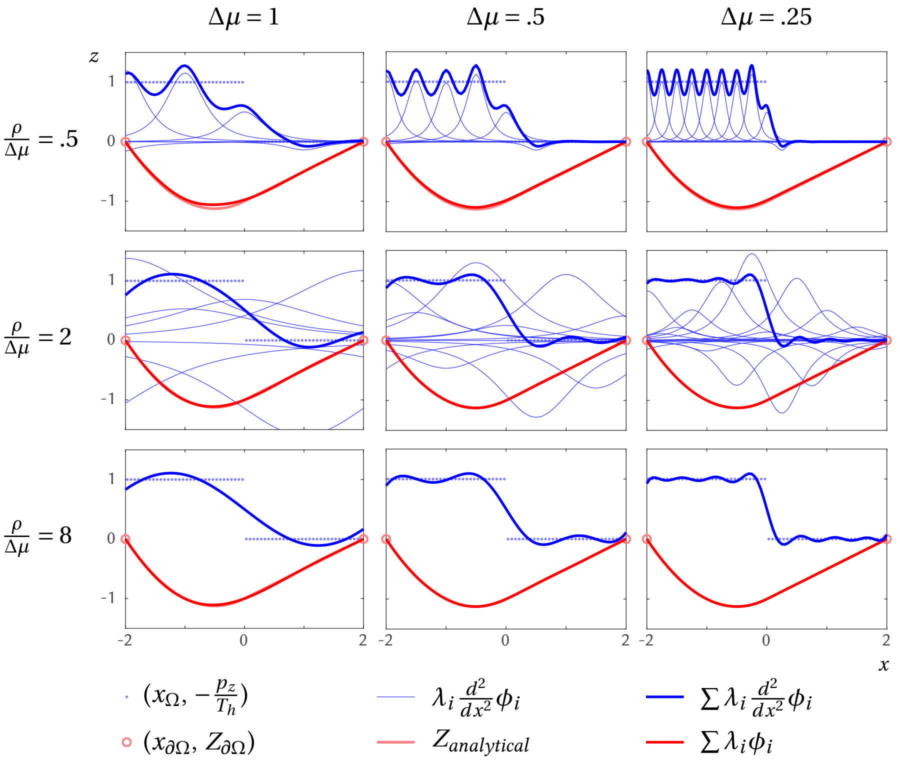

Figure 3.5: Chains with distributed load over half span

row of figure 3.3, one can see all the bold blue curves can not closely match the steep rise of the step function. But when $\Delta\mu$ is smaller, the curve with a shorter wavelength can converge to the plateau within a shorter range. Upon closer observation, one can find that the wavelength is around two times the spacing $\Delta\mu$ when the ratio $\rho/\Delta\mu$ allows certain overlap between the bell curves. Assuming the pattern of the error of the second derivative is approximately a sine curve with an amplitude α'' and wavelength $2\Delta\mu$:

$$\varepsilon''(x) \approx \alpha'' \sin\left(\frac{\pi}{\Delta\mu}x\right).$$

The error in the shape function is roughly

$$\varepsilon(x) \approx -\alpha'' \frac{\Delta\mu^2}{\pi^2} \sin\left(\frac{\pi}{\Delta\mu}x\right).$$

Let α denotes the amplitude of the error ε (x). The amplitude α can be estimated by

$$\alpha \approx \frac{\Delta\mu^2}{\pi^2}\alpha''. \tag{3.7}$$

Equation (3.7) explains that although the deviation of the second derivatives (bold blue curves) from the ideal values (blue dots) is similar in rows of figures 3.3–5, the error $\varepsilon_{\max}$ is smaller when the spacing between radial basis functions $\Delta\mu$ is smaller. Figure 3.6 compares the error patterns of the results of the ordinary discrete approach with the radial basis functions.

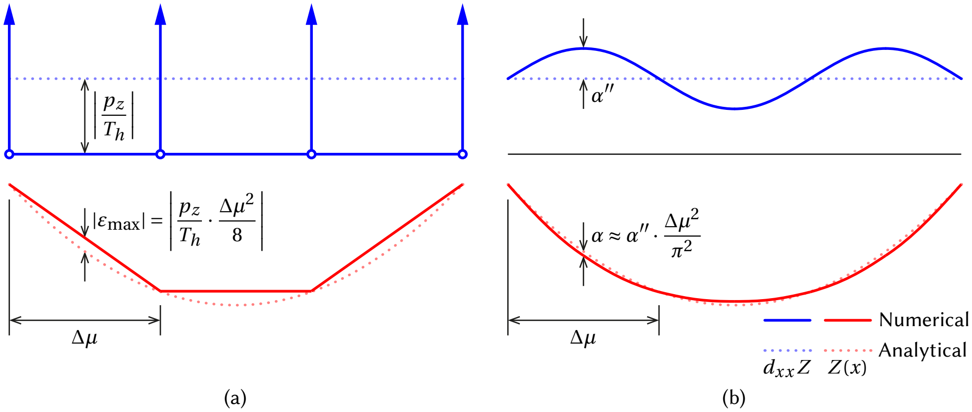

Figure 3.6: Patterns of the errors. (a) Discrete approach. The infinite second derivatives are represented with Dirac delta functions (arrows). (b) Radial basis functions.

3.4. FINDING MEMBRANE SHELLS

When finding the form of a membrane shell, the radial basis functions are used to represent two unknown functions of stress $F(\mathbf{x})$ and shape $Z(\mathbf{x})$:

$$F(\mathbf{x}) = \sum_{i=1}^{n} \lambda_{F,i}\phi\left(\left\|\mathbf{x} - \boldsymbol{\mu}_i\right\|; \rho_i\right) + \varepsilon_F,$$

$$Z(\mathbf{x}) = \sum_{i=1}^{n} \lambda_{Z,i}\phi\left(\left\|\mathbf{x} - \boldsymbol{\mu}_i\right\|; \rho_i\right) + \varepsilon_Z.$$

The second derivatives of the Airy stress function $F(\mathbf{x})$ are horizontal components of the membrane stresses, which are equivalent to the T_h (the horizontal component of the tension force) in finding a hanging chain as in section 3.3. The functions $F(\mathbf{x})$ and $Z(\mathbf{x})$ will satisfy Pucher's equation (see section 2.3) at points within the domain $\mathbf{x}_\Omega$ and will also satisfy boundary conditions (see section 2.4) at points on the boundary $\mathbf{x}_{\partial\Omega}$.

In this section, the above theory will be demonstrated on a point-supported membrane shell with free edges—the most demanding boundary. The load conditions are given externally, or more specifically, the vertical load is set to be unit constant ($p_z = 1$), and horizontal loads are set to be zero ($p_x = p_y = 0$), in this section. Non-zero horizontal loads will be introduced in section 3.6.

For the shape of such points-supported shell, the relevant conditions can be translated into a Hermite interpolation problem:

$$-p_z(\mathbf{x}_\Omega) = \sum_{i=1}^{n} \lambda_{Z,i} D_F^{Pucher}\left[\phi\left(\left\|\mathbf{x}_\Omega - \boldsymbol{\mu}_i\right\|; \rho_i\right)\right] + \varepsilon_Z^{Pucher}, \tag{3.8a}$$

$$Z_{\partial\Omega,s} = \sum_{i=1}^{n} \lambda_{Z,i}\phi\left(\left\|\mathbf{x}_{\partial\Omega,s} - \boldsymbol{\mu}_i\right\|; \rho_i\right) + \varepsilon_Z^{Support}. \tag{3.8b}$$

where $D_F^{Pucher}[\cdot]$ is a linear differential operator introduced in equation (2.22), and $Z_{\partial\Omega,s}$ are prescribed elevations at the positions of the supports $\mathbf{x}_{\partial\Omega,s}$.

On the other hand, for the stress function of such free-edge shell, the constraints include

$$-p_z(\mathbf{x}_\Omega) + p_h'(\mathbf{x}_\Omega) = \sum_{i=1}^{n} \lambda_{F,i} D_Z^{Pucher}\left[\phi\left(\left\|\mathbf{x}_\Omega - \boldsymbol{\mu}_i\right\|; \rho_i\right)\right] + \varepsilon_F^{Pucher}, \tag{3.9a}$$

$$q^{Normal}(\mathbf{x}_{\partial\Omega,e}) = \sum_{i=1}^{n} \lambda_{F,i} D^{Normal}\left[\phi\left(\left\|\mathbf{x}_{\partial\Omega,e} - \boldsymbol{\mu}_i\right\|; \rho_i\right)\right] + \varepsilon_F^{Normal}, \tag{3.9b}$$

$$q^{Shear}(\mathbf{x}_{\partial\Omega,e}) = \sum_{i=1}^{n} \lambda_{F,i} D^{Shear}\left[\phi\left(\left\|\mathbf{x}_{\partial\Omega,e} - \boldsymbol{\mu}_i\right\|; \rho_i\right)\right] + \varepsilon_F^{Shear}, \tag{3.9c}$$

$$F_{\partial\Omega,s} = \sum_{i=1}^{n} \lambda_{F,i}\phi\left(\left\|\mathbf{x}_{\partial\Omega,s} - \boldsymbol{\mu}_i\right\|; \rho_i\right) + \varepsilon_F^{Support}. \tag{3.9d}$$

Equation (3.9a) originates from equation (2.23), in which $p_h'(\cdot)$ is a function related to horizontal loads and $D_Z^{Pucher}[\cdot]$ is a linear differential operator. Equations (3.9b) and (3.9c) originate from conditions (2.26a–b) concerning zero normal stress and zero shear stress at the edges. Since the conditions (3.9a–c) only refer to the second derivatives of the stress function, extra conditions to fix the three degrees of freedom on the overall value and the first-order derivatives are necessary. Therefore, condition 3.9d is added.

The prescribed functions $q^{Normal}(\cdot)$, $q^{Shear}(\cdot)$ and the differential operators $D_Z^{Normal}[\cdot]$, $D_Z^{shear}[\cdot]$ can be provided by

$$q^{Normal}(\mathbf{x}) = n_x^2 \int p_x\, dx + n_y^2 \int p_y\, dy, \tag{3.10a}$$

$$D^{Normal}[\cdot] = n_x^2 \frac{d^2}{dy^2}[\cdot] - n_x n_y \frac{d^2}{dxdy}[\cdot] + n_y^2 \frac{d^2}{dx^2}[\cdot], \tag{3.10b}$$

$$q^{Shear}(\mathbf{x}) = -n_x n_y \int p_x\, dx + n_x n_y \int p_y\, dy,, \tag{3.10c}$$

$$D^{Shear}[\cdot] = -n_x n_y \frac{d^2}{dy^2}[\cdot] - (n_x^2 - n_y^2) \frac{d^2}{dxdy}[\cdot] + n_x n_y \frac{d^2}{dx^2}[\cdot]. \tag{3.10d}$$

With two unknown functions and only one governing equation, the form-finding problem is under-determined. However, for a membrane that has free edges, its stress function $F(x, y)$ holds two boundary conditions (2.26a–b), which make the free edges over-determined. Generally speaking, finding a membrane shell with free edges is a problem with countless solutions yet in a certain subset. The upcoming algorithm provides a method to identify if an arbitrarily given shape or stress function is one of the countless solutions. When it is not, the algorithm can tweak the given function to reach the solution subset.

3.4.1. PROPOSED ALGORITHM

The sequence of the proposed algorithm is illustrated in figure 3.7. The critical steps are as follows:

1. Determine the ground plane. List the boundary conditions of the shell.
2. Describe load distributions (p_x, p_y, and p_z).
3. Identify potential *singular points* and arrange the basis functions accordingly.
4. Provide either (a) a initial stress function or (b) a initial shape function.
5. (a) When a stress function is provided, find the corresponding stress function with Pucher's equation.
   (b) When a shape function is provided, find the corresponding shape function with Pucher's equation.
6. Revise the stress function according to the updated shape, and revise the shape function according to the updated stress until they converge.
7. Export the stress and shape functions.

The singular points mentioned in step 3 refer to points that have stress concentration (for the stress function) or large curvature (for the shape function). This idea will be more clear in the following demonstration.

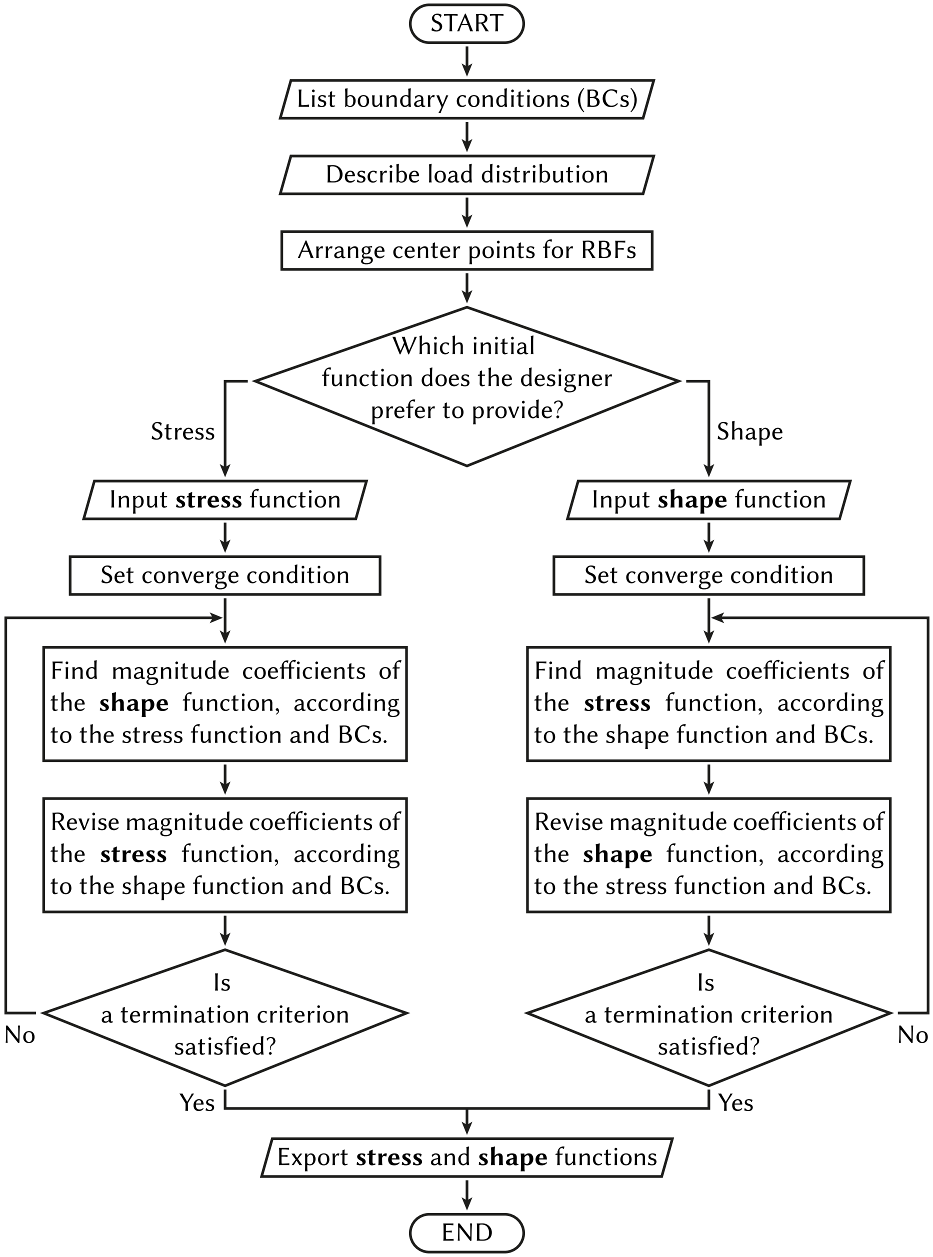

Figure 3.7: Flowchart of the algorithm

3.4.2. STEPS 1–3: CALIBRATION POINTS AND SOURCE POINTS

The first 3 steps are eventually arranging two types of calibration points ($\mathbf{x}_{\Omega}$ and $\mathbf{x}_{\partial\Omega}$) and the prescribed values on these points (e.g., $p_z(\mathbf{x}_{\Omega})$, $Z(\mathbf{x}_{\partial\Omega})$) as well as the source points ($\boldsymbol{\mu}$ along with ρ). The arrangement of calibration points is rather simple once the ground plane and boundary conditions are determined. For the calibration points of domain type $\mathbf{x}_{\Omega}$, one can scatter the points evenly within the domain Ω. Regarding calibration points of boundary type $\mathbf{x}_{\partial\Omega}$, there is often more than one type of boundary (see section 2.4 and table 2.2). The boundary can be divided into segments that have distinct boundary conditions from their neighbors.

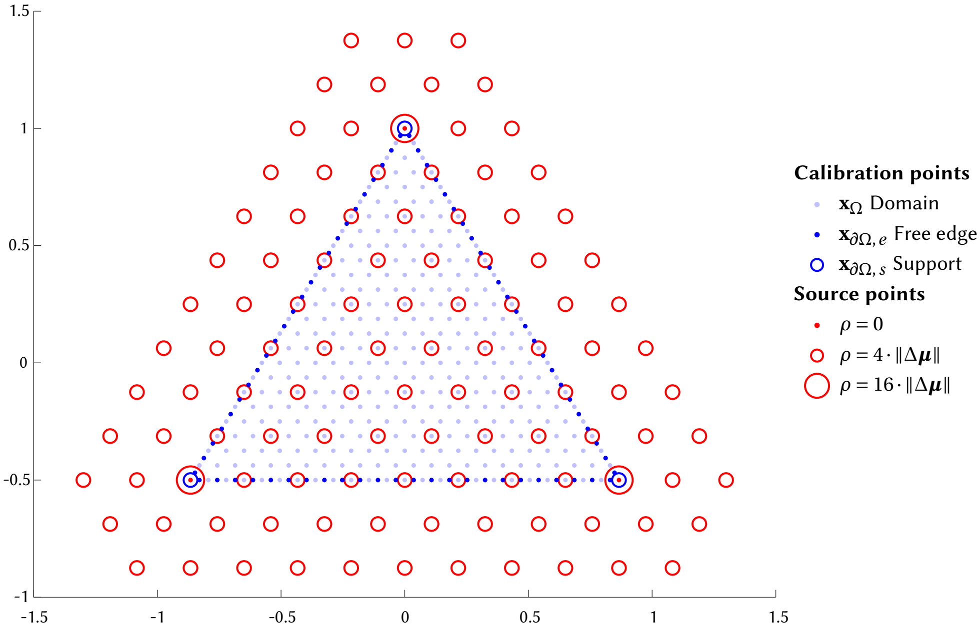

Figure 3.8: Distribution of calibration points and source points for the triangular shell

Figure 3.8 shows the arrangement of the calibration points and source points for the demonstration shell, which has a triangular domain, which is anchored to the ground at the corners, and is subjected to a uniformly distributed vertical load. Triangular grid points are arranged to be the domain type calibration points $\mathbf{x}_{\Omega}$. Regarding calibration points of the boundary type, the first group $\mathbf{x}_{\partial\Omega,e}$ contains points on the three edges, and the second group $\mathbf{x}_{\partial\Omega,s}$ includes three vertices of the triangle. The edges are set to be free edges. Since the edges are straight, the normal and tangential directions, which are needed for the free-edge conditions (3.9b–c), are straightforward to be defined.

Regarding the source points $\boldsymbol{\mu}$ of the basis functions, grid points within and around the domain Ω are used. The shape parameters are set to be 4 times the spacing of the grid ($\rho = 4 \cdot \|\Delta\boldsymbol{\mu}\|$) for most of the source points. Considering there will be stress concentration around the corners, each corner gets two source points. One of them has $\rho = 0$ and the other $\rho = 16 \cdot \|\Delta\boldsymbol{\mu}\|$. Since the least-squares method will be used, the source points $\boldsymbol{\mu}$ can have less density than domain calibration points $\mathbf{x}_\Omega$ (see figure 3.8).

3.4.3. STEPS 4–5: TWO PATHS TO FIND THE BALANCE

After the common setup built in the first two steps, the remaining demonstration is split into two paths. The first path starts with an initial stress function, and the second path starts with an initial shape function.

Path A: stress initiation. In the path, the demonstration initiates the process from an analytical stress function provided by Csonka (1987, p. 587). The initial input of the stress function goes as

$$F(x, y) = \frac{2(L_0 \cdot L_1 \cdot L_2)}{15(L_0 \cdot L_1 \cdot L_2) + 6(x^2 + y^2 - 1)},$$

where L_i, $i \in \{1, 2, 3\}$ are linear functions that $L_i(x, y) = \cos(2\pi i/3)\, x + \sin(2\pi i/3)\, y - 1/2$. This stress function automatically satisfies the free edge conditions (3.9b–c). Figure 3.9 displays this stress function and its principal curvature network.

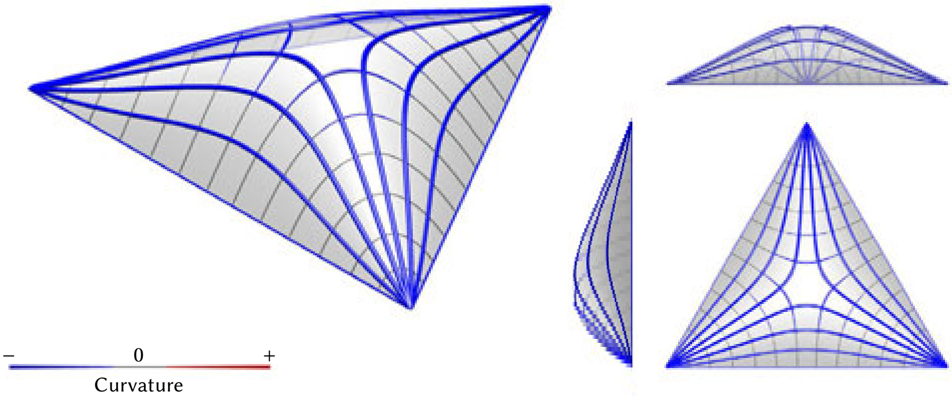

Figure 3.9: Stress function and its principal curvature network

The only part left unknown is the shape function $Z(x, y)$, or $\lambda_{Z,i}$ which can be given by minimizing the errors in equations (3.8). One can derive the coefficients for the differential operator $D_F^{Pucher}[\cdot]$ in the governing equation (3.8a) by evaluating the second derivatives of the stress function $F(x, y)$ at the calibration points $\mathbf{x}_\Omega$. Along with the boundary condition (3.8b), $\lambda_{Z,i}$ can be provided by the method of least squares (see equation (3.4)). The shape solution provided by radial basis functions, together with the principal stress network, is illustrated in figure 3.10.

The residual errors ε_F^{Pucher} and ε_Z^{Pucher} are eventually the same. Both of them represent the difference between prescribed p_z and the supporting stress that $F(\mathbf{x})$ and $Z(\mathbf{x})$ are actually provided. The error is within $\pm 0.02 p_z$ at most of the surface as depicted in figure 3.11.

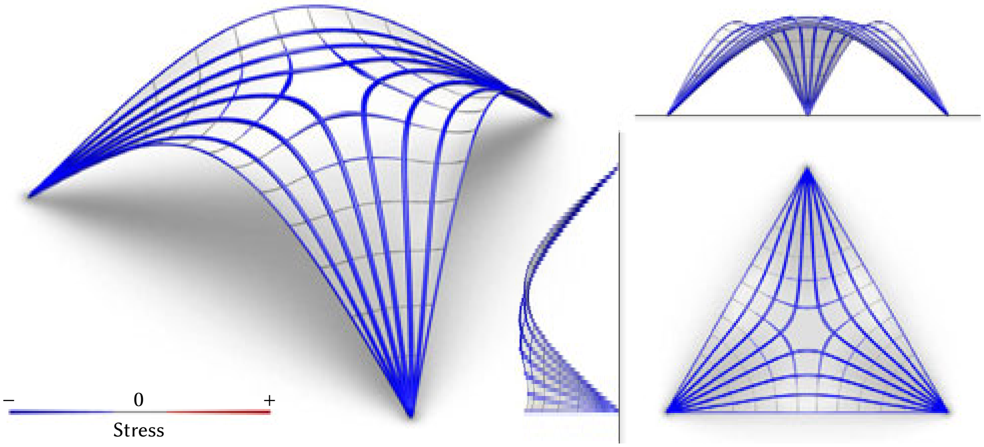

Figure 3.10: Shape function and the principal stress network

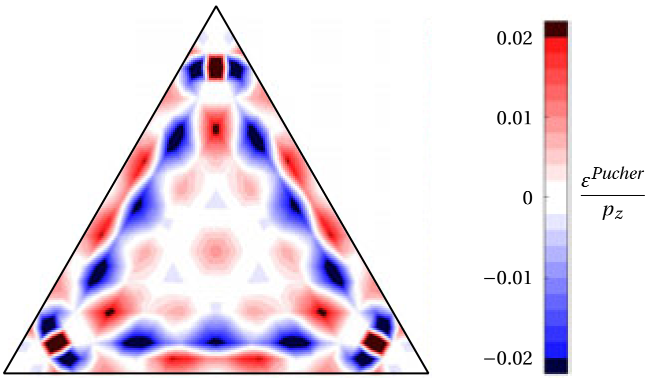

Figure 3.11: Distribution of the residual error

Path B: shape initiation. For most ground plans, there may not be an analytical stress function available. The designer can choose path B to input an initial shape, then the algorithm can tweak the shape to meet the prescribed boundary conditions. For instance, the designer can provide a paraboloid as the initial shape:

$$Z(x,y)=\frac{7}{10}(-x^2-y^2+1).$$

The initial shape function provides crucial coefficients to the differential operator D_Z^{Pucher} in the governing equation (3.9a). As suggested by Csonka (1987), the paraboloid cannot simultaneously be compatible with the two free-edge conditions (3.9b–c). The designer may be obliged to place walls below the edges to reinforce and support the paraboloid shell to bypass the condition (3.9c). The corresponding stress function and the initial shape function are displayed in figures 3.13a and 3.14a.

The designer can also impose condition (3.9c), which will result in a different solution for the stress function. Then, based on the updated stress function, the algorithm will find the *tweaked* shape. The algorithm will alternately tweak or modify the stress and shape functions before the convergence condition is satisfied. When the iteration does not converge satisfactorily, the designer can first impose the condition (3.9c) with lower weight and then gradually increase it. In this demonstration, the algorithm consists of four stages of iteration. Each stage has a different value of the weight, which is set to be 0.25 in the first 10 iterations (1–10), 0.5 in the following 20 iterations (11–30), 0.75 in another group of 30 iterations (31–60), and eventually to be 1 in the last 40 iterations (61–100). Figure 3.12 shows that the residual errors evolve along with the iterations. The overall root-mean-square error $\varepsilon^{Overall}=\sqrt{\sum(w\varepsilon)^2/\sum w^2}$ monotonically decreases, and jumps only when the weights are changed.

Figures 3.13b and 3.14b show intermediate stress and shape functions after the first 30 iterations. Then, the stress and shape functions are turned into a free-edged shell after 100 iterations as illustrated in figures 3.13c and 3.14c.

3.4.4. Steps 6–7: convergence and export

Pucher's equation consists of the double-inner product of derivatives of stress function and shape function. When both stress function and shape function are unknown (or both $\boldsymbol{\lambda}_F$ and $\boldsymbol{\lambda}_Z$ are unknown), finding the solution set of the stress function and shape function is a non-linear problem.

The proposed algorithm adjusts the stress function and shape function alternately. In an individual adjustment, either $\boldsymbol{\lambda}_F$ or $\boldsymbol{\lambda}_Z$ is treated as unknown and the other is treated as an externally given constant vector. In this perspective, the error vector has a linear relation to the unknown coefficient vector ($\boldsymbol{\lambda}_F$ or $\boldsymbol{\lambda}_Z$). The method of linear least square can provide best fit magnitude coefficients without further trials, unlike the method of gradient descent (Curry, 1944).

However, the overall path of the proposed algorithm still shows striking similarities to the gradient descent (figure 3.15). In the gradient descent, there are three features. First, the overall path is monotonically descent. Secondly, each step ends at the tangent point to a contour of the minimizing function. Thirdly, any subsequent step is perpendicular to the previous steps. In the proposed algorithm, each adjustment ends at a conditional

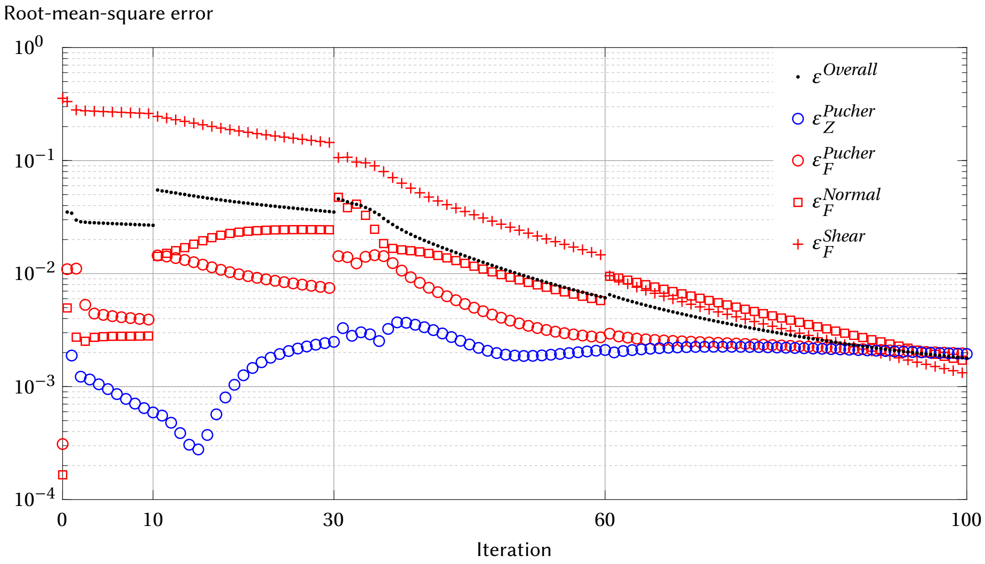

Figure 3.12: Root-mean-square errors decaying with the iteration

global minimum, thus the overall path is monotonic and each endpoint tangents to the minimizing function. Let $\boldsymbol{\lambda} = \left[\begin{array}{cc} \boldsymbol{\lambda}_F^{\mathrm{T}} & \boldsymbol{\lambda}_Z^{\mathrm{T}} \end{array}\right]^{\mathrm{T}}$. Due to the nature of alternatively adjusting $\boldsymbol{\lambda}_F$ or $\boldsymbol{\lambda}_Z$, each step increment $\delta\boldsymbol{\lambda}_i$ equals $\left[\begin{array}{cc} \mathbf{0} & \delta\boldsymbol{\lambda}_{Z,i}^{\mathrm{T}} \end{array}\right]^{\mathrm{T}}$ or $\left[\begin{array}{cc} \delta\boldsymbol{\lambda}_{F,i}^{\mathrm{T}} & \mathbf{0} \end{array}\right]^{\mathrm{T}}$. Then, $\delta\boldsymbol{\lambda}_{i+1}$ is always perpendicular to $\delta\boldsymbol{\lambda}_i$. Additionally, given that all the calibration points are at the non-singular region, thus the smoothness of minimizing function $\sum[w\varepsilon(\boldsymbol{\lambda})]^2$ is guaranteed. These features ensure that the proposed algorithm will converge at stationary points so that the gradient of the minimizing function is zero: $\frac{\partial}{\partial\boldsymbol{\lambda}}\sum(w\varepsilon)^2 = \mathbf{0}$.

Practically, the sequence can be terminated when

- the minimizing function is smaller than a prescribed standard: $\sum(w\varepsilon)^2 \leq (\varepsilon^{std1})^2$, or
- the process is near a stationary point: $\|\frac{\partial}{\partial\boldsymbol{\lambda}}\sum(w\varepsilon)^2\| \leq \varepsilon^{std2}$.

If the sequence reaches $\|\frac{\partial}{\partial\boldsymbol{\lambda}}\sum(w\varepsilon)^2\| \leq \varepsilon^{std2}$ before $\sum(w\varepsilon)^2 < (\varepsilon^{standard})^2$, then it is necessary to redesign the arrangement of μ_i and ρ_i or increase their number.

Regarding the export, the algorithm will export the centers μ_i and the shape coefficients ρ_i as well as the magnitude coefficients $\lambda_{F,i}$ and $\lambda_{Z,i}$. For some users, a graphical output may be more relevant than numbers. This chapter uses sets of stress trajectories, or *principal stress networks*, to visualize the result. The widths of the trajectories are proportional to the stress and are inversely proportional to the distances to the adjacent trajectories.

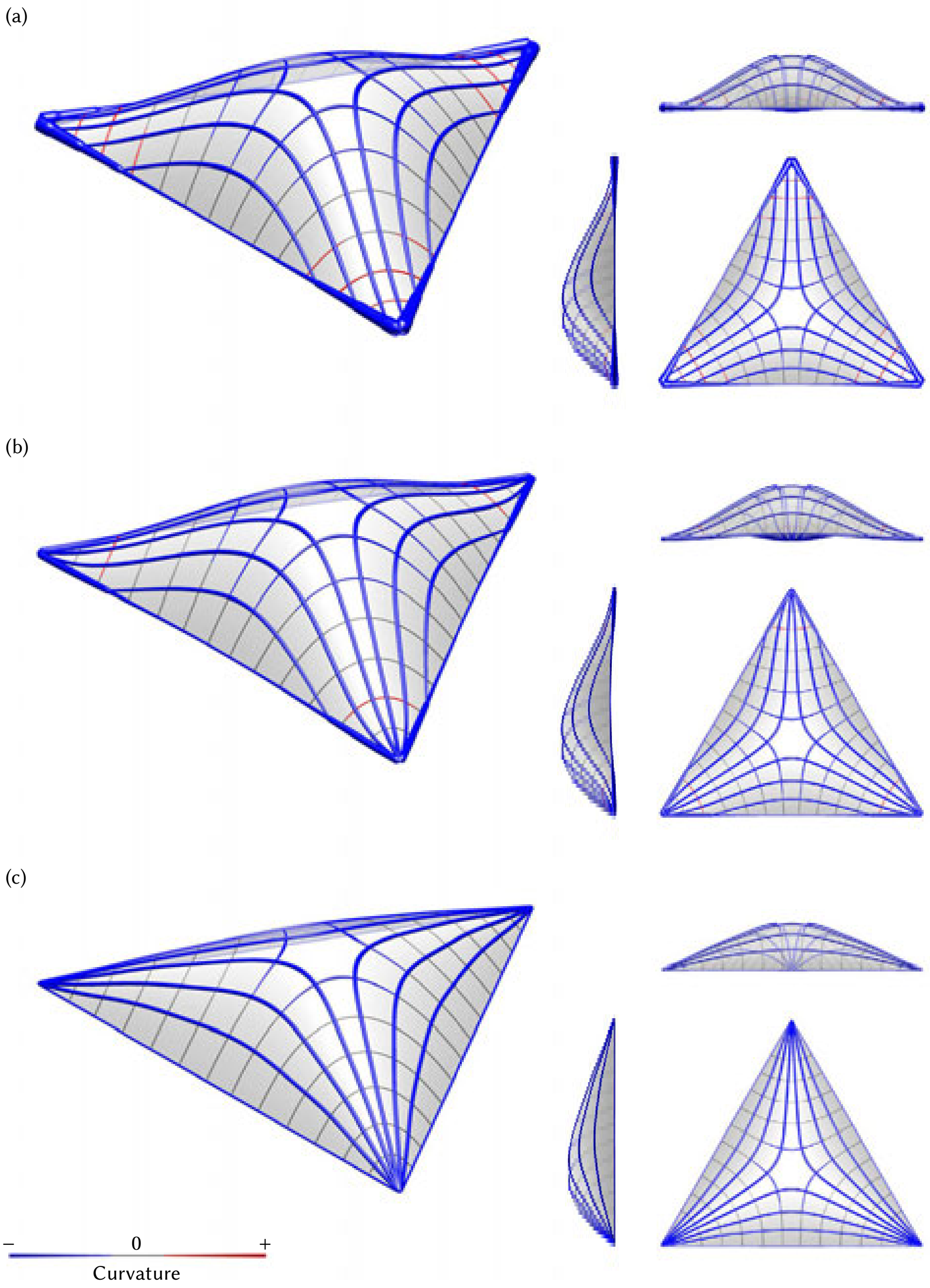

Figure 3.13: Stress function and its principal curvature network. (a) Stress function when the paraboloid shell is supported on walls. The stress function is elliptic around the center and hyperbolic near the corners. (b) Evolution toward satisfying free-edges conditions. (c) Result of the last iteration, which is parabolic near the corners.

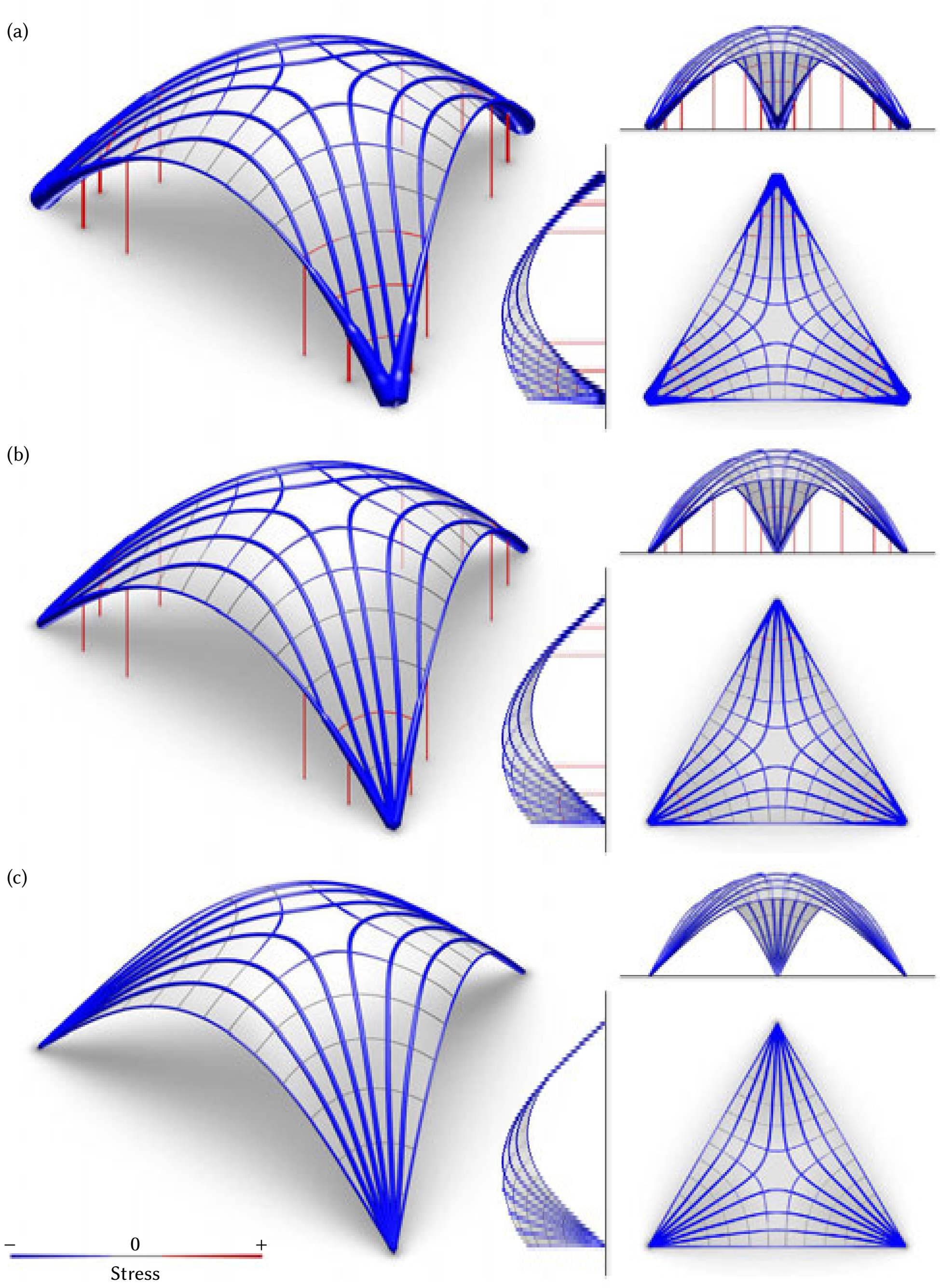

Figure 3.14: Shape function and the principal stress network. (a) Paraboloid shell and stress network when it is supported on walls. The shell is purely compressed around the center and has tension stress near the corners. (b) Evolution toward a free-edge shell. (c) Result of the last iteration, which has stress concentration at the corners.

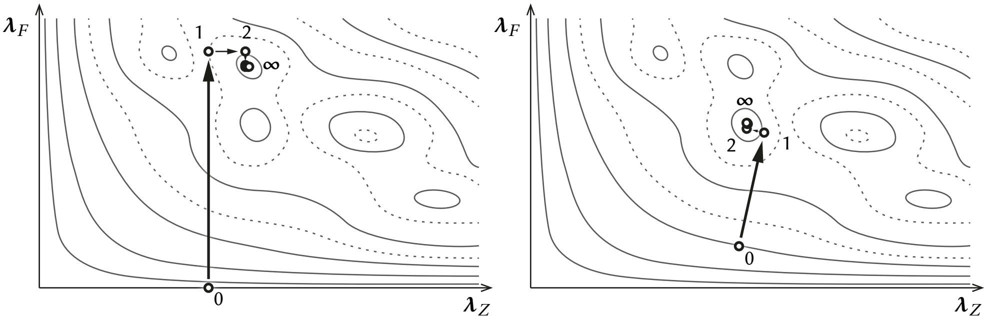

(a) Path of proposed algorithm (b) Path of typical gradient descent

Figure 3.15: Converging path to a local minimum of $\sum(w\varepsilon)^2$

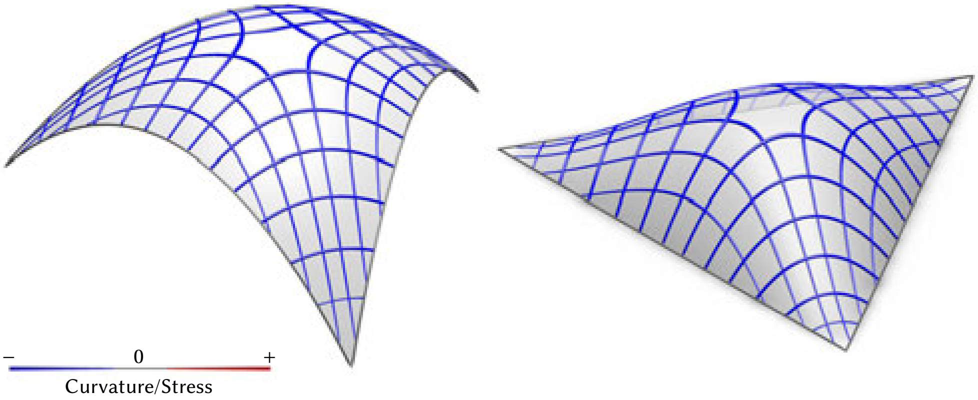

Figure 3.16: Stress and shape functions of a triangular bubble shell

3.5. FINDING SELF-AIRY MEMBRANES

The self-Airy membranes are the special cases of membrane shells of which the shape function coincides with the Airy stress function when there is no horizontal load. The detailed definition and features have been introduced in section 2.5. With the numerical tool proposed in this chapter, this section briefly revisits and visualizes the duality of the stress and shape functions in ordinary shells. More importantly, this section finds numerical solutions of self-Airy membranes and imposes the free-edge conditions on *free boundaries* (Friedman, 2000; Apushkinskaya, 2018).

Duality of the general membranes. For a general membrane shell, when there is no horizontal load, the Airy stress function $F(\mathbf{x})$ and shape function $Z(\mathbf{x})$ have a commutative relation, such that their Hessian matrices satisfy

$$\mathbf{H}_F^{r90^\circ} : \mathbf{H}_Z = \mathbf{H}_Z^{r90^\circ} : \mathbf{H}_F = -p_z, \tag{3.11}$$

where $\mathbf{H}_F$ and $\mathbf{H}_Z$ denote the Hessian matrices of stress and shape functions respectively, the superscript ${}^{r90^\circ}$ denotes 90-degree rotation, and ":" refers to the double-inner product. This commutative property allows the stress and shape functions to interchange roles. For instance, the previous paraboloid shell in figures 3.13a and 3.14a has a parabolic shape function. The parabolic shape (uniformly distributed curvature) can be reinterpreted as the stress function of a soap film (uniformly distributed stress). At the same time, the stress function can be reinterpreted as the shape of a *compressed* bubble soap film under a vertical load as depicted in figure 3.16.

Self-Airy membranes and free-boundary problems. In contrast, a self-Airy surface $S(\mathbf{x})$ follows governing equation (2.29) or a copy as follows:

$$\mathbf{H}_S^{r90^\circ} : \mathbf{H}_S = -\frac{p_z}{F_0}, \tag{3.12}$$

in which $\mathbf{H}_S$ is the Hessian matrix and F_0 is a factor with dimension in force. This equation is a second-order non-linear partial differential equation. For this type of membrane, the function $S(\mathbf{x})$ has to satisfy the boundary conditions for both stress and shape functions.

For the free edge, the stress function at a free edge has to be tangent to a plane in the absence of horizontal body forces (Csonka, 1987; Miki, Igarashi, & Block, 2015), and thus the conditions (2.26a) and (2.26b) are automatically satisfied. Here, function $S(\mathbf{x})$ inherits the same conditions. Therefore, for a point $\mathbf{x} = (x, y)$ on a free edge, one gets (Csonka, 1987, 185)

$$S(x, y) = Ax + By + C, \tag{3.13a}$$

$$n_x \frac{\partial}{\partial x} S(x, y) + n_y \frac{\partial}{\partial y} S(x, y) = n_x A + n_y B, \tag{3.13b}$$

where A, B, C are the constants of the tangent plane, and (n_x, n_y) is the normal vector of the boundary. These conditions are rather demanding for a second-order partial differential equation. If they are imposed around the membrane shells at arbitrary edges, the overall

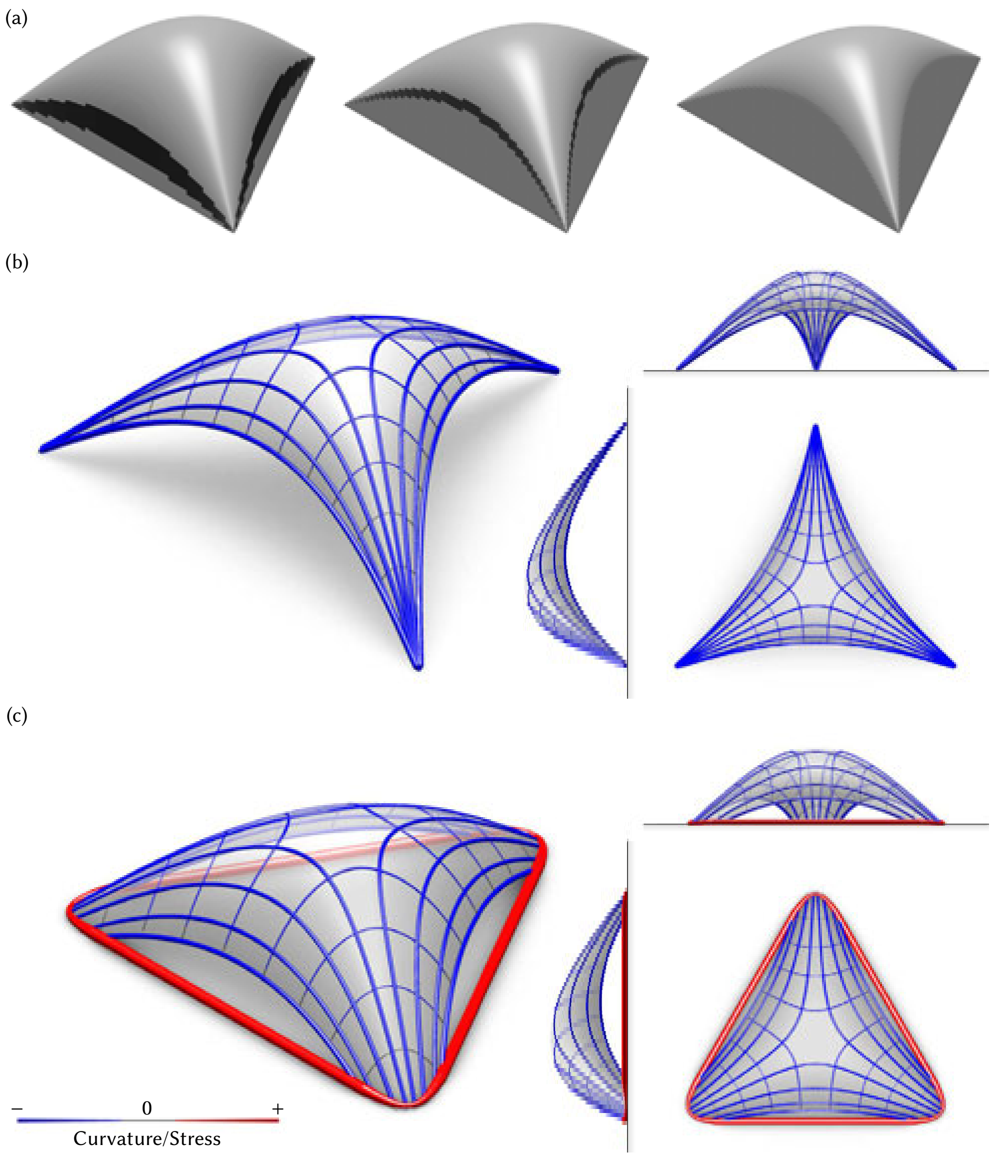

Figure 3.17: Triangular self-Airy membranes. (a) The moving free edges and the intermediate products in the converging process. (b) The result of the point-supported self-Airy membrane. (c) An instance of the truncation and the resulting bottom hoop.

problem might be overdetermined. To realistically find the solution, the free-edge conditions must apply on a *free boundary*, which is free to adjust its location, hence the name. In ordinary boundary value problems, both the value and location of the boundary are predefined at the outset of the problem. Conversely, the location of the *free boundary* is not predefined in the problem. Only when the problem is solved, the location shall be answered as part of the solution. Such a problem is called a *free boundary problem* (Friedman, 2000; Apushkinskaya, 2018).

Consider a symmetrical self-Airy membrane supported by three points and bounded by three free edges, like the shells in the previous section. This section expresses the potential locations of a free edge with polynomials

$$y = \sum_{i=1}^{n} \alpha_i \left(x^2 - 1\right)^i ,$$

where α_i are unknown coefficients waiting to be adjusted to control the shape of the boundary. The curve, which is symmetrical and passes points $(\pm 1, 0)$, can be rotated and scaled to connect the fixed ends of a free boundary. Meanwhile, the radial basis functions are used to represent the potential height of the self-Airy membrane

$$S(\mathbf{x}) = \sum_{i=1}^{n} \lambda_{S,i} \phi\left(\left\|\mathbf{x} - \boldsymbol{\mu}_i\right\| ; \rho_i\right) + \varepsilon_S .$$

To find the coefficients of α_i and $\lambda_{S,i}$, the method of non-linear least squares is used. After providing the preliminary guess of α_i and $\lambda_{S,i}$, the Gauss-Newton method can suggest the directions of changes for the coefficients. The magnitudes of changes can be turned down to ensure convergence. A converging process and result are shown in figure 3.17a.

The free-edge conditions (3.13) together with the governing equation 3.12 require the second-order derivatives to approach zero and infinity as

$$\frac{\partial^2}{\partial t^2} S \to 0, \qquad \frac{\partial^2}{\partial n \partial t} S \to 0, \qquad \frac{\partial^2}{\partial n^2} S = \frac{-2 p_z / F_0}{\left(\partial^2 / \partial t^2\right) S} \to \infty .$$

In other words, large curvature is demanded at the free edges. To understand the location of the free edges, one can run the free-boundary algorithm first with regularly distributed source points $\boldsymbol{\mu}$ of radial basis functions (figure 3.8). After understanding the approximate location of the free edges, one can rearrange the source points $\boldsymbol{\mu}$ accordingly. Thus, the residual error can be reduced. At edges and the corners where the edges meet, the error is still high relative to the inner domain. Nonetheless, other than the critical area, the error can be less than $\pm 0.05 p_z$ as shown in figure 3.18.

Self-Airy membranes have an interesting feature that any plane intersecting the $S(\mathbf{x})$ also cuts it into a closed surface. The intersection can be interpreted as a hoop that provides all horizontal thrust and leaves the supports to only provide vertical reactions (figure 3.17c). This feature also benefits the actuation scheme for a flat-to-curved mechanism in section 6.3.

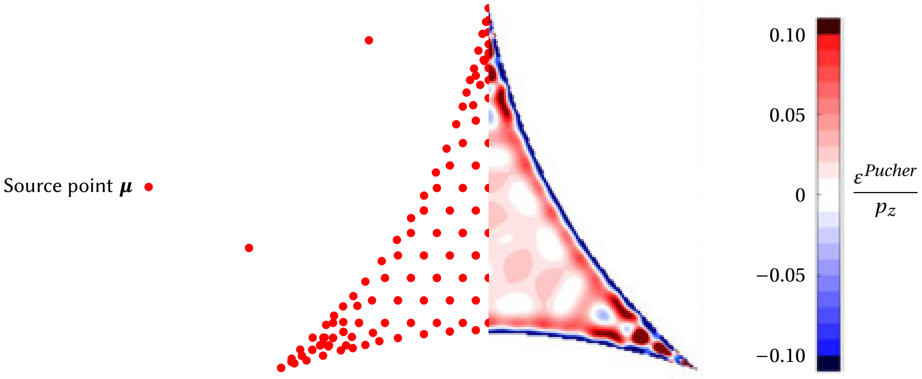

Figure 3.18: Distribution of the rearranged source points and the resulting residual error

3.6. Membrane shells under horizontal loads

This section shows how boundary conditions affect the distribution of membrane stresses when horizontal loads are acting. For cases in which the original shape function (or the thrust surface) cannot contain horizontal loads, this section also shows how the thrust surface deviates from the original position.

The shape in figure 3.10 is put under this horizontal loading analysis. The shape is regarded as the initial shape in the proposed form-finding algorithm introduced in section 3.4. The load cases contain horizontal loads, which are set to be 30% of the p_z in various directions:

$$\left(p_x, p_y\right) = 0.3\left\|p_z\right\|(\cos\theta, \sin\theta), \qquad \theta \in \mathbb{R}.$$

For these uniform horizontal loads, a potential function $V(x, y)$ can be introduced (Sadd, 2009, p. 144):

$$V(x, y) = p_x x + p_y y,$$

which satisfies $\partial_x V = p_x$ and $\partial_y V = p_y$. The potential function can replace $\int p_x\, dx$ and $\int p_y\, dy$ in equations 3.10a and 3.10c. In this arrangement, the principal curvatures of the stress function $F(x, y)$ still align with the principal stresses. This arrangement is not necessary, but it simplifies the visualization of the upcoming figures.

The membrane shell is supported in two ways. In section 3.6.1, the corners of the shell are anchored to the foundation and the reinforced edges rest on vertical walls, which only provide vertical reactions. In section 3.6.2, the walls and the edge reinforcements are removed. The shell is supported as its form-finding configuration. More explicitly, it is anchored in the three corners, and edges between the corners are free from any support and reinforcement. These two support conditions generate quite distinct results. In the first case, the initial shape function can sufficiently carry different load cases. On the other hand, the second case requires the shape function to deviate significantly from the initial geometry.

3.6.1. Walls-supported shell

As previously discussed and shown in section 3.4, not all arbitrary shapes are compatible with free-edge conditions under the uniform vertical load. This incompatibility also occurs when horizontal loads are introduced. The designer may opt for edge reinforcements and supporting walls to bypass condition (3.9c). Thus, it is possible to find the appropriate stress function under a given shape function.

Although the shape function can remain in the original geometry, the stress function changes dramatically in response to the horizontal loads. Condition (3.9b) asks the stress function to curve at the edges, and equation (3.9a) governs the stress function in the domain. Figure 3.20 displays the stress functions under horizontal loads and figure 3.21 shows the stress flows on the shell and the supporting walls. The shear force next to an edge accumulates as the axial force in the reinforcement. This axial force, which is also curved in the vertical plane, requires vertical stress in order to reach the balance. Such vertical stress can be provided by the supporting wall. The stresses can be drawn as concentrated forces as in figure 3.19, which shows the forces induced by a uniform horizontal load. In practice, the vertical supporting forces can be provided by structural mullions, for instance.

3.6.2. Point-supported shell

Another way to set the boundary condition is to remove the edge reinforcements and the supporting walls. As a result, when horizontal loads appear, the shape function must deviate from the initial input. Even if the input is the form-found shape under the vertical load, the deviation is still necessary in order to recover the balance from the altered load condition. The algorithm proposed in section 3.4 can provide the solution sets of stress and shape functions.

Figure 3.22 displays the solutions of the stress functions in response to the horizontal loads. In the presence of horizontal body forces, the Airy stress functions must curve according to condition (3.9b), which is shared with the stress functions in figure 3.20. Therefore, the edges of the stress functions in these two figures have the same curves. Readers are encouraged to flip the pages back and forth to observe this alignment.

However, the stress functions for free-edges must exclusively follow condition (3.9c), which demands the stress functions to twist specifically at the edges. As a result, the principal orientation of stresses will be parallel to one of the edges. One can see the curvature lines on stress functions are parallel or normal to the edges. The orientation of stress functions' principal curvatures is the same as the orientation of the principal stresses, since the potential function $V(x, y)$ is adopted to represent the integrals $\int p_x \, dx$ and $\int p_y \, dy$. There-

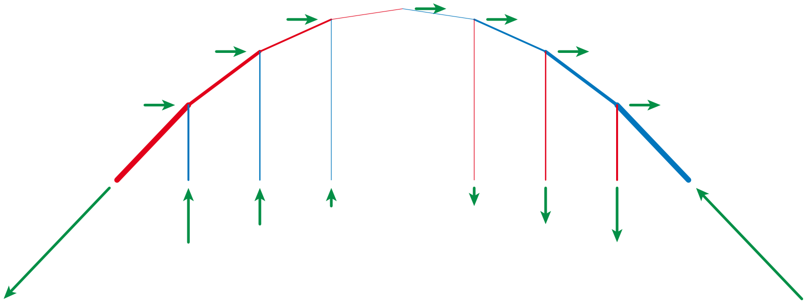

Figure 3.19: A wall-supported edge under horizontal loads. The external forces are represented by the green arrows. Meanwhile, the red and blue lines represent tensile and compressive forces, respectively.

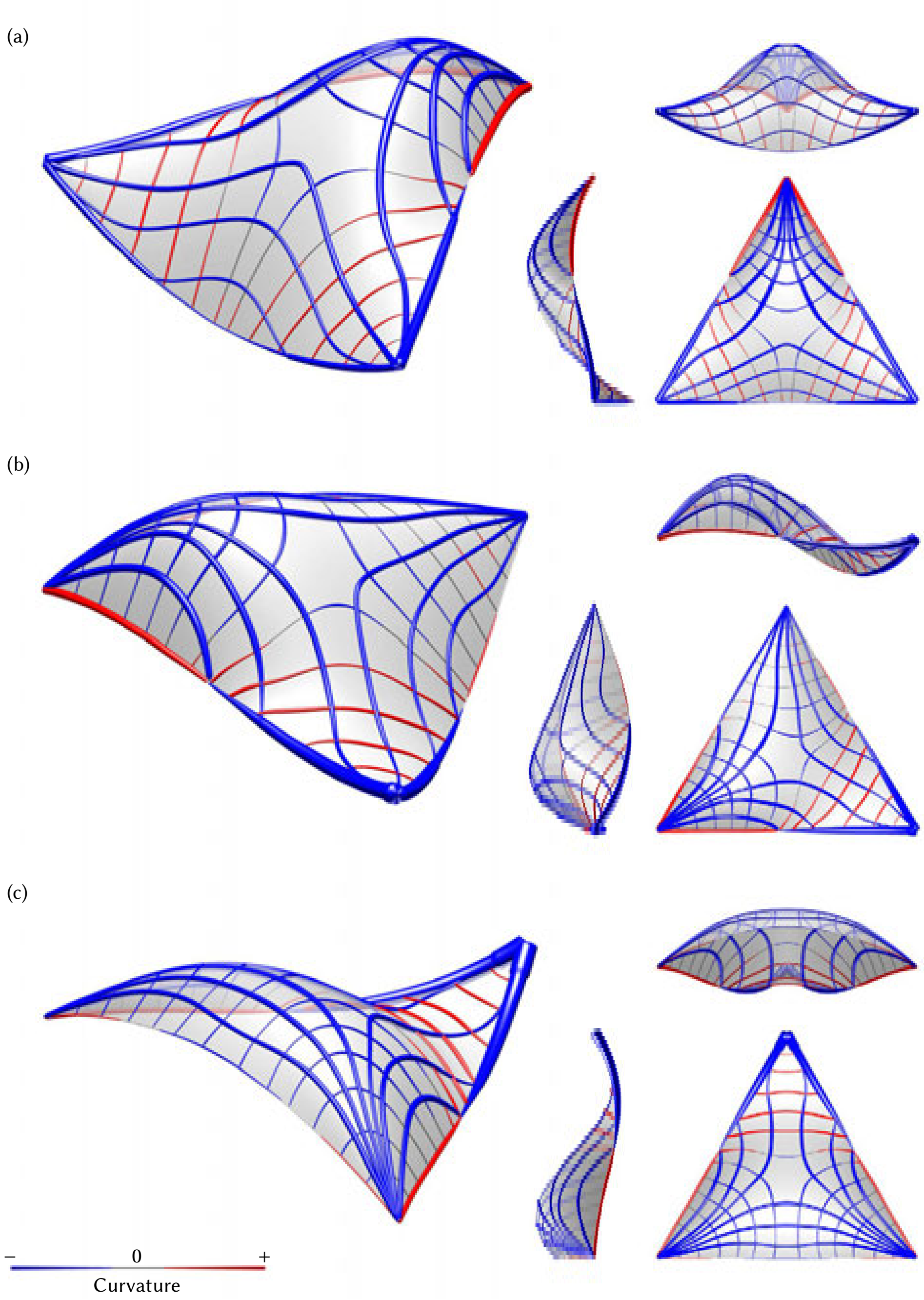

Figure 3.20: Stress functions and their principal curvature networks of the walls-supported shell under horizontal loads of different directions. (a) $\theta = -90°$. (b) $\theta = 0°$. (c) $\theta = 90°$.

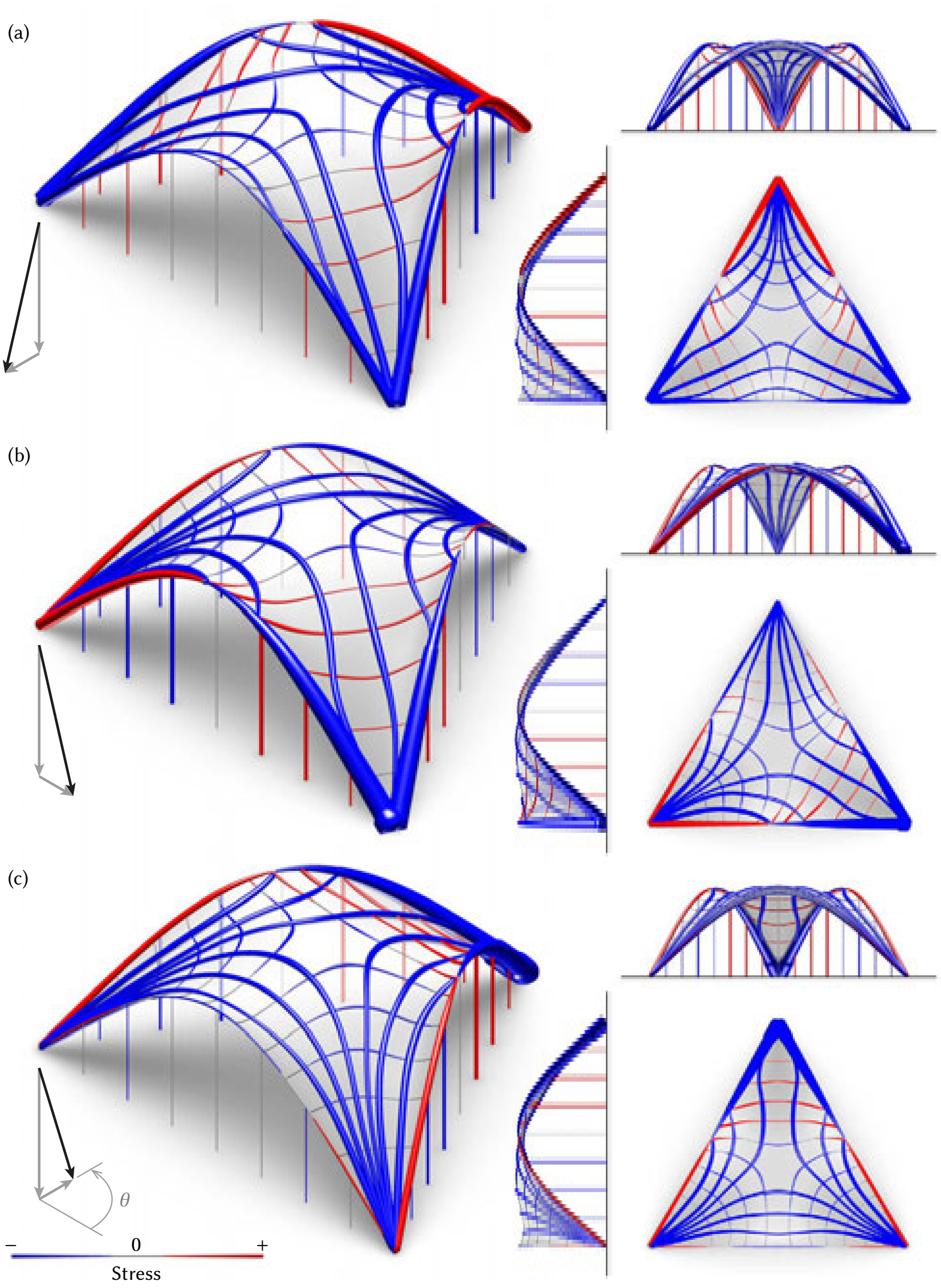

Figure 3.21: Shape functions and the principal stress networks of the walls-supported shell under horizontal loads of different directions. (a) $\theta = -90°$. (b) $\theta = 0°$. (c) $\theta = 90°$.

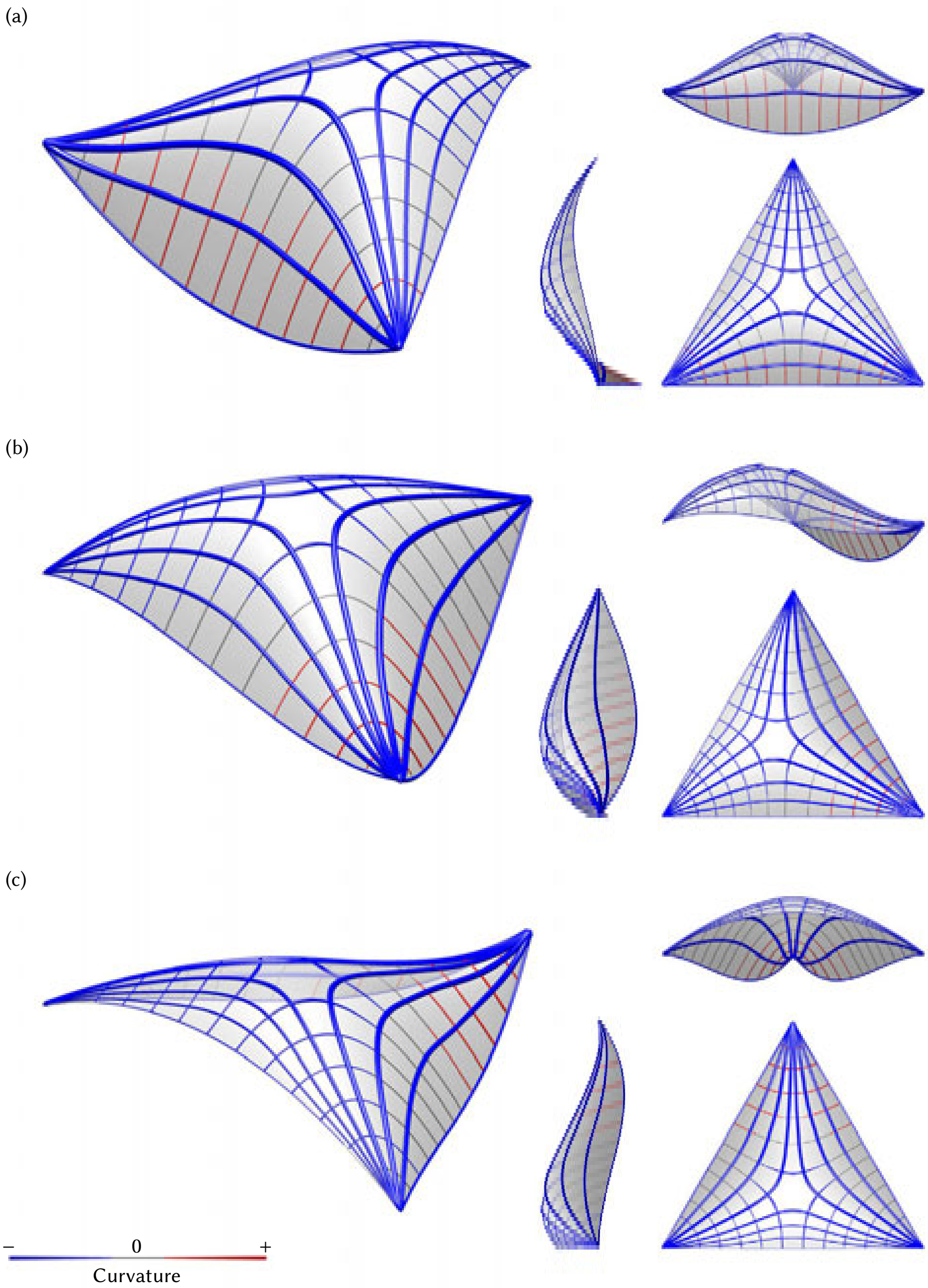

Figure 3.22: Stress functions and their principal curvature networks under horizontal loads of different directions. (a) $\theta = -90°$. (b) $\theta = 0°$. (c) $\theta = 90°$.

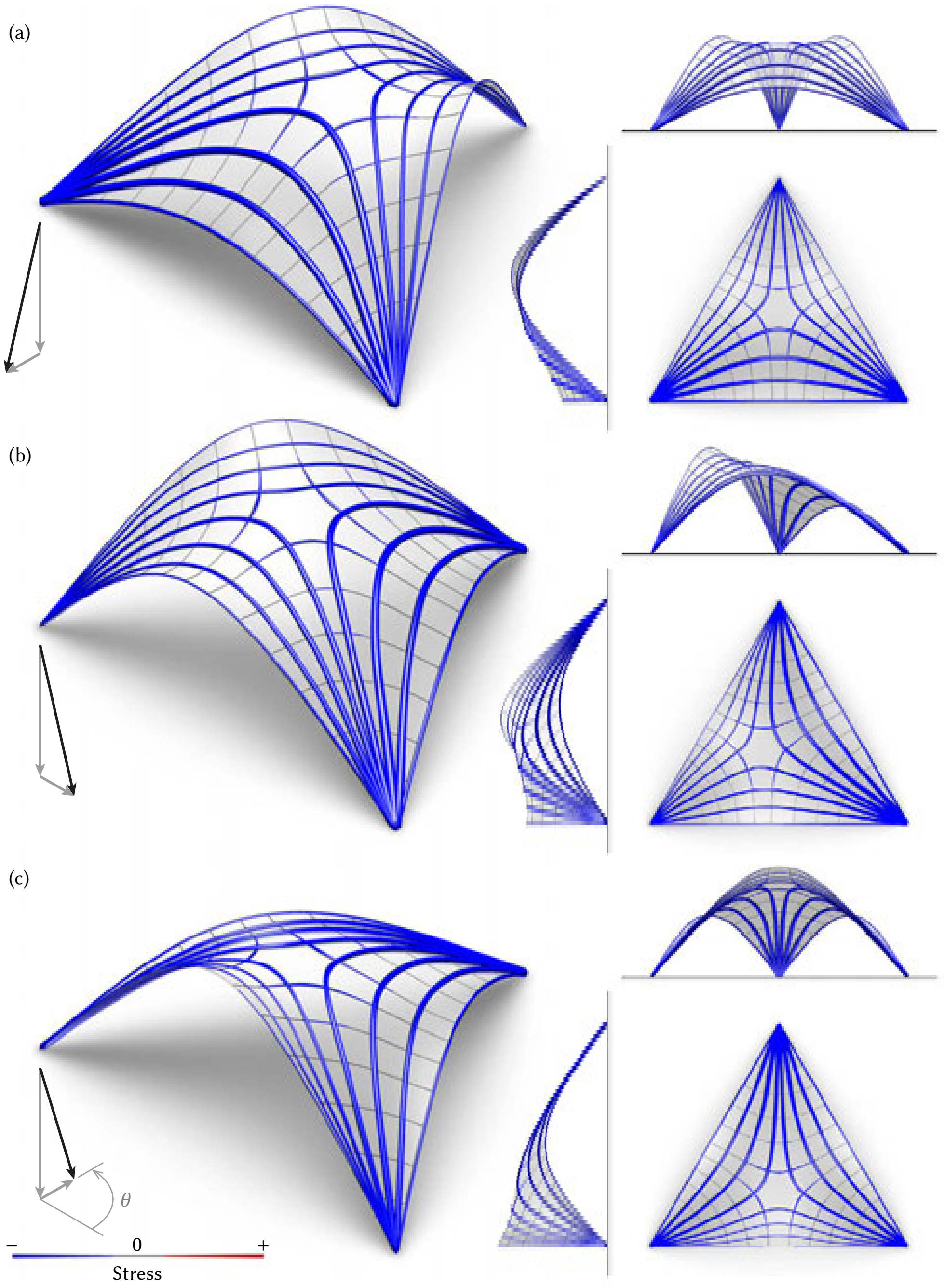

Figure 3.23: Shape functions and the principal stress networks under horizontal loads of different directions. (a) $\theta = -90°$. (b) $\theta = 0°$. (c) $\theta = 90°$.

fore, the parallelism between edges and curvature lines also shows parallelism between the edges and principal stresses, which is required by condition (3.9c).

A side effect of condition (3.9c) is that the initial shape function may no longer satisfy Pucher's equation. The proposed algorithm can be used to find an alternative shape function. After the iterations in the algorithm, one can get the shape functions in figure 3.23. These shape functions only have three pin supports and no supporting forces from the walls. The shapes must deviate from the original symmetrical geometry and lean into horizontal loads as a cyclist leans into a strong crosswind.

The shape functions of various horizontal loads collectively define a pair of upper and lower envelopes (see figure 3.24). The distance between the envelopes suggests the potential eccentricity of the membrane stress in the shell. For this point-supported shell, the edges tend to have larger eccentricities than the middle part, and the middle of an edge has larger eccentricity than the ends. These envelopes can inform the design of the thickness of a masonry vault. When the structural system can accept moderate stress eccentricity, the structure can be much thinner than the distance between the envelopes. Nevertheless, this distance variation can still indicate the rational design on the thickness variation or for depths of reinforcing ribs.

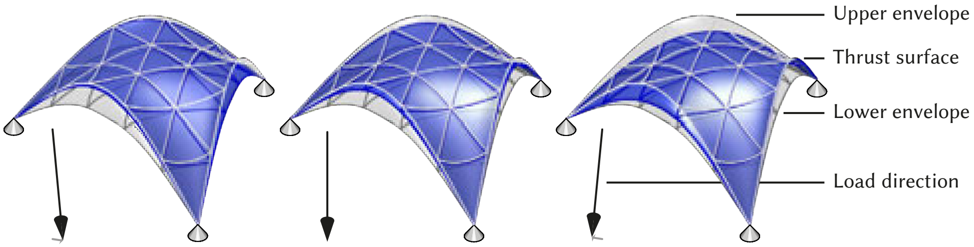

Figure 3.24: The envelopes defined by the thrust surfaces under various horizontal loads

3.7. Summary and discussion

This chapter has presented the first research on utilizing the numerical method of radial basis function to form-find membrane shells by solving Pucher's equation. Some observations:

- the physics-based algorithms can only provide stable equilibrium configurations while the mathematics-based algorithms can generate a wider range of solutions of both stable and unstable equilibrium states;
- radial basis functions can smoothly interpolate generic multivariate functions; and
- when the method of radial basis functions is applied to Hermite interpolation, in which the interpolation includes values and derivatives, the method can also solve differential equations.

The main contributions of this chapter include:

- translating the form-finding problem into a weighted interpolation of Hermite type;

- developing an algorithm that can work in two ways: providing a shape function based on an initial stress function, and providing a stress function based on an initial stress function;
- showing a boundary condition can be switched on or off by changing its weight in the weighted Hermite interpolation;
- formulating the form-finding of the self-Airy membranes with a free-edge condition as a free-boundary problem and solving it;
- incorporating horizontal loads in the form-finding process; and
- identifying peripheral walls or variable cross-section ribs that are desirable to brace a shell against horizontal loads.

The current algorithm uses Pucher's equation which only concerns the stretching stresses and regards the difference between the external loads and the carried loads as residual errors. A future refinement can be to incorporate the bending surface, which can carry part of the loads by bending stresses. Then the refined algorithm would able to analyze both stretching and bending surfaces in a shell.

4

DISCRETIZING FREE-FORM SURFACES AND AIRY STRESS FUNCTIONS

The discrete geometric theory turns out to be
as rich as its smooth counterpart,
if not even richer.

Bobenko & Suris [1]

Parts of this chapter have been published in *Advances in Architectural Geometry 2020* (Chiang, Buskermolen, & Borgart, 2021)

[1] Bobenko and Suris 2008, p. xiv

EACH MEMBRANE shell can be represented by two surfaces: its shape and the graph of its Airy stress function. This chapter applies geometric methods to discretize both surfaces. For fabrication of the physical shapes, the free-form shapes of the shells are discretized into planar *principal meshes*, which permit planar ribs and torsionless nodes. To visualize the stress tensor field, the graphs of the Airy stress functions are discretized into panels, which have curvatures that embody body forces. These rather intangible curvatures can then be concentrated into the readable creases between panels, akin to distributed stresses condensed into forces.

OUTLINE

Section 4.1 reviews how architects and builders used to—and still do—benefit from geometric tools, and combines the fabrication methods with the resulting surfaces. Section 4.2 discusses the properties of principal meshes. Section 4.3 introduces how a graph of a function can be visualized in *isotropic geometry*. Section 4.4 presents a method to discretize the Airy stress function to include body forces. Section 4.5 summarizes the finding of this chapter and discusses further implementation of the discretization method.

4.1. GEOMETRY, ARCHITECTURAL NOTATION, AND DIGITAL FABRICATION

Geometry can be regarded as an indispensable vocabulary in architectural design. For instance, the primary shapes (e.g., squares, cubes, circles, spheres, prisms, cones, polyhedra, etc.) are ubiquitously found in buildings of various ancient civilizations, even though they were built by master builders who spoke different languages. It seems as if they unanimously used the primary forms in their architectural expression. Arguably, these primary forms were the common architectural language, and they have ever since dominated the design of our daily lives.

There must be a reason for these geometrical forms to be so universal. It might be due to practicality. These primary forms are easily defined and reproduced. A designer can define the form to scale in the design studio, then the crafter and builder can reproduce the drawing at actual size on workpieces or construction sites.

Since the advent of computers, the designers' expression is no longer limited to traditional drafting tools (e.g., ruler, compass, protractor, French curve) (Mitchell, 2001). Computer-aided-design (CAD) software allows designers to denote free-form curves with a few mouse clicks (e.g., Bézier curve). Manufacturing is also no longer bound to drafting tools nor physical templates. Computer numerically controlled (CNC) machinery permits manufacturers to produce free-form products from merely digital data.

However, the current technology does not guarantee that a free-form geometry can be manufactured by any given CNC machine. Different geometrical complexities require different fabrication techniques (see table 4.1). Although it is technically possible to reach enormous design freedom using sophisticated 5-axis milling and 3D printing, these tools are still not economically viable for most building construction. The size and quantity of components needed for a building would require a significant amount of hours of milling or 3D printing machinery.

Fortunately, in free-form architectural construction, methods exist to discretize 3D free-form surfaces into series of 2D flat panels (Pottmann, Eigensatz, Vaxman, & Wallner, 2015),

Table 4.1: Geometric features resulting from the fabrication methods

Fabrication technique		Resulting geometry
Machining	2-axis cutting	Prism
	3-axis milling	Surface without overhang
	4-axis cutting	Beveled prism and ruled surface
	5-axis milling	Free-form surface
	3D printing	Free-form object
Deforming	Curved sheet	Developable surface
	Shrink wrap	Minimal surface
	Bent grid	Chebyshev net
	And more*	-

* See chapter 5 and figure 5.3

and thus being relatively economical to fabricate. As discussed by Zipkin (2001), two-dimensional manufacturing processes are always easier than three-dimension ones. The flat components can be economically fabricated with a 2-axis (sometimes 4-axis, two axes for moving and the other two axes for tilting), CNC cutting machine from planar materials. The CNC machine may be equipped with a water-jet, laser, plasma torch, milling spindle, circular saw, etc. depending on what material is being processed. The flat panels can then be assembled into the designed 3D free-form surface.

Besides assembling 3D surfaces from flat panels, 3D curved surfaces can also be obtained through deforming sheet material, such as curving flat lathes or planks (Correa, Krieg, & Meyboom, 2019; Liddell, 2015; Schling, 2018), and other techniques, which will be further investigated in chapter 5. The current chapter focuses on assembling flat rigid components.

Relevance to shell construction. As discussed in chapters 1 and 2, shells can have rather complex curvatures. Before the existence of computers, only a few analytical forms of shells (e.g., hyperbolic, spherical shells) could be economically produced. Form work was generally reused in the construction of free-form concrete shells in order to distribute the formwork expense across multiple copies. Although not many concrete shells have been built in the last decades, shells are still being built in other forms such as tessellated glass roof (e.g., the Great Court of the British Museum, see Brown, 2005) and timber plate assembly (e.g., the BUGA Wood Pavilion, see figure 4.1). The panels of these double-curved surfaces have different dimensions and angles. Computer software is used to translate the unique geometry of each panel into a cutting path for CNC machinery. This CNC machinery can then economically "mass-customize" (Zipkin, 2001) each panel to its unique dimension (figure 4.1c–d).

Planar quadrilateral meshes. The two built cases previously mentioned are represented by a planar triangular mesh and a planar hexagonal mesh, respectively. A triangular mesh

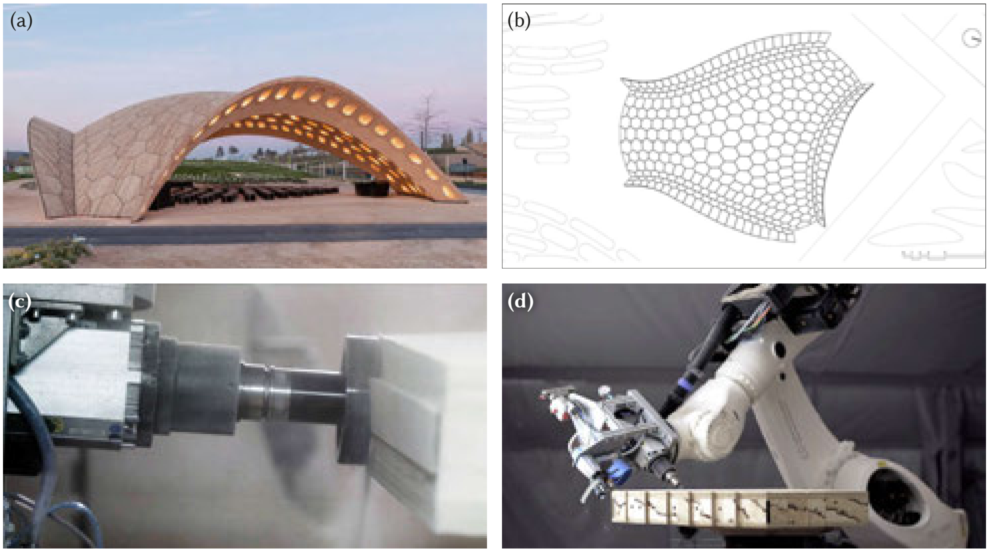

Figure 4.1: BUGA Wood Pavilion. (a) The completed structure. (b) The top view drawing. (c–d) One of the panels being machined by an industrial robot. [Source: *BUGA Wood Pavilion*, 2019]

naturally has planar panels as three vertices determine a plane. In the case of a hexagon-dominated mesh with a uniform nodal valency of three, it is also easy to have planar panels, as three planes naturally define three edges intersecting at a single vertex.

In contrast, it is not so trivial to generate planar quadrilateral meshes (Y. Liu, Pottmann, Wallner, Yang, & Wang, 2006). Before sophisticated computation tools existed, planar quadrilateral meshes could only be achieved by simple geometric rules, such as rotational symmetry as in the Glass Pavilion designed by Bruno Tout (1880–1938) and the transitional mesh as in the house for hippopotami (figure 4.2) at the Berlin Zoo, engineered by the Schlaich Bergermann Partner (Glymph et al., 2004; Schlaich & Schober, 1997).

Geometric theories and tools to generate free-form planar mesh keep evolving. The numerical algorithm designed by Y. Liu et al. (2006), for instance, takes a non-planar quadrilateral mesh as input, and gradually tweaks the positions of vertices to make all faces planar; and the method of *Marionette Meshes* introduced by Mesnil, Douthe, Baverel, and Leger (2017) pulls nodes of a 2D quadrilateral pattern up into the air to meet the planar criteria and the given spatial guide curves.

Moreover, some meshes not only permit planar facets but also co-planar node axes, which allows for simplified fabrication and assembly. These benefits come from stricter geometric constraints, which will be discussed in the next section.

4.2. Principal meshes and grid shells

Principal meshes are quad-dominant meshes that can effectively reveal principal curvatures of the surfaces (Y. Liu et al., 2006). Three types of such meshes exist: circular, conical, and Koebe meshes, along with their parallel meshes (Pottmann, Liu, et al., 2007; Pottmann, Asperl, Hofer, & Kilian, 2007; Zadravec, Schiftner, & Wallner, 2010; Sechelmann, Rörig, &

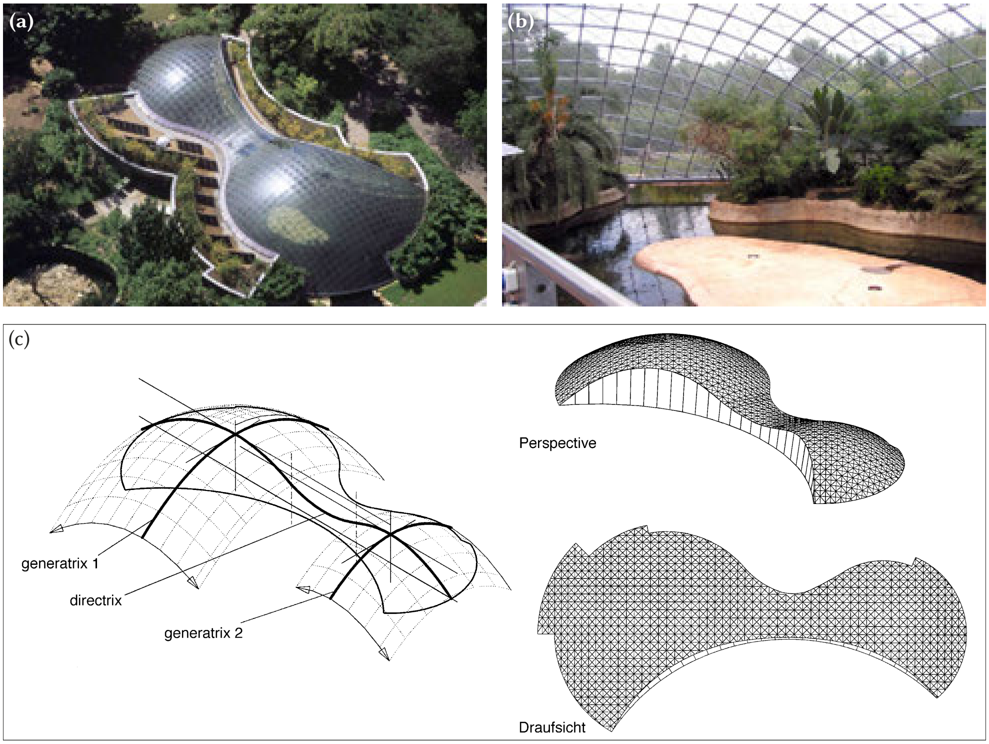

Figure 4.2: House for hippopotami at the Berlin zoo. (a) Aerial. (b) Interior. (c) Mesh generated form translation. [Source: (a–b) *House for Hippopotamus, Zoo Berlin*, 1994; (c) Glymph et al., 2004]

Bobenko, 2012). These planar meshes have the offset property which offers great fabrication and assembly simplicity. The mesh can be physically built out of planar panels and ribs, and the planar ribs intersect at the nodes without twisting or torsion (figure 4.3b).

However, the third type of principal meshes—Koebe meshes, and the parallel meshes of this kind— has creation limitation. They cannot faithfully approximate general surfaces but *isothermic surfaces* and some special cases (Sechelmann et al., 2012; Young, 1909). Thus, only the first two types, namely circular and conical, are under detailed discussion in this dissertation. A brief description of the first two types of meshes has been provided by Pottmann and Wallner (2008):

> *Circular meshes are quadrilateral meshes all of whose faces possess a circumcircle, whereas conical meshes are planar quadrilateral meshes where the faces which meet in a vertex are tangent to a right circular cone [or a sphere].*

These principal meshes have interesting offset properties. Offset for conventional smooth surfaces means corresponding points have constant distance and parallel tangency planes. To discuss the concept of offset for discretized surfaces, the parallelism has to be provided. Two discrete surfaces $\mathcal{M}$ and $\mathcal{M}'$ are parallel if they have the same combinatorics (i.e., same quantities of the vertices and the same connecting structure of edges and faces) and

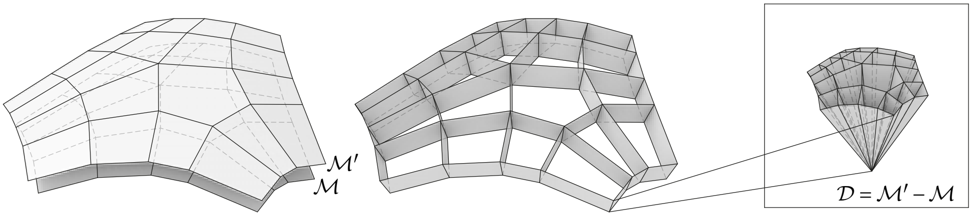

(a) Offset meshes

(b) Rib layout

(c) Displacement Mesh (scaled)

Figure 4.3: Notions of offset meshes. (a) A pair of meshes $\mathcal{M}$ and $\mathcal{M}'$ with the same combinatorics. (b) When $\mathcal{M}$ and $\mathcal{M}'$ are parallel, the corresponding edges form planar trapezoids, which can serve as a rib layout for free-form construction. (c) When the distances between $\mathcal{M}$ and $\mathcal{M}'$ approximate to a constant, the displacement mesh $\mathcal{D}$ approximates to a sphere.

all corresponding edges and faces are parallel. Then, one can check whether the Euclidean distances between corresponding vertices, edges, and faces are constants. If the distances are roughly equal to a constant d, the displacement of every vertices pair of $\mathcal{M}$ and $\mathcal{M}'$ shall approximate a sphere of radius d.

Let $\mathcal{D} = \mathcal{M}' - \mathcal{M}$ denote such a displacement mesh, which is also a parallel mesh of $\mathcal{M}$ (as $\mathcal{M}'$ is parallel to $\mathcal{M}$). The mesh $\mathcal{D}$ can hardly be a perfect smooth sphere, but it can fairly approximate one (figure 4.3). To be more precise, it can be as organized as all vertices are on the sphere of radius d (figure 4.4a), or all edges are tangent to the sphere (figure 4.4b), or all faces are tangent to the sphere (figure 4.4c). In these three cases, $\mathcal{M}$ and $\mathcal{M}'$ are constant vertex, edge, and face offset meshes, respectively (table 4.2).

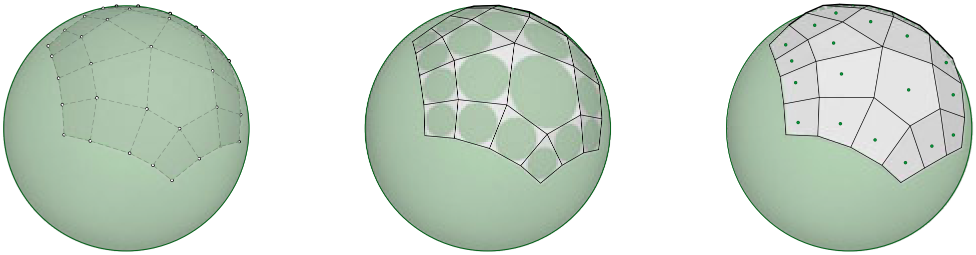

(a) Circular mesh

(b) Koebe mesh

(c) Conical mesh

Figure 4.4: Three types of displacement meshes for constant offset. (a) A displacement mesh is inscribed in the sphere—all vertices are on a sphere. Thereby, all faces possess a circumcircle. (b) A mesh possesses a *midsphere*—all edges are tangent to a sphere. (c) A mesh is circumscribed about a sphere—all faces are tangent to a sphere. Thereby, all vertices possess a circular cone of revolution which is tangent to the surrounding faces.

The unit displacement mesh $\mathcal{S}$ can also be defined as $\mathcal{S} = \mathcal{D}/d$, which can be seen as a discretized unit sphere. One can derive another offset mesh $\mathcal{M}''$ of the base $\mathcal{M}$ by $\mathcal{M}'' = \mathcal{M} + \delta\mathcal{S}$, where δ is the offset distance. For any parallel mesh $\mathcal{M}_p$ of $\mathcal{M}$ or $\mathcal{S}$ (parallel meshes of $\mathcal{M}$ and $\mathcal{S}$ are eventually the same set of meshes), the offset mesh $\mathcal{M}'_p$ can also

Table 4.2: Fabrication benefits resulting from committing to specific geometric constrains

Type of mesh	**Fabrication benefit**
Planar mesh	Planar panels
Principal mesh	Planar ribs and torsionless nodes
Circular mesh	Constant vertex offset
Koebe mesh or its parallel mesh	Constant edge offset
Conical mesh	Constant face offset

be derived with the same unit displacement mesh $\mathcal{S}$ as $\mathcal{M}'_p = \mathcal{M}_p + \delta\mathcal{S}$.

The discretized sphere $\mathcal{S}$, roughly has uniform curvature on every part and in every direction. When a quadrilateral on $\mathcal{S}$ is elongating and forming a facet on the parallel mesh $\mathcal{M}_p$, the curvature is more *diluted* when the elongation is larger. When the elongations differ in directions, the resulting diluted curvatures also differ. For a quadrilateral, there are two degrees of freedom of parallel deforming, which are roughly parallel to the two pairs of opposite edges. Thus, the orientations of the quadrilaterals resemble the orientations of principal curvature on $\mathcal{M}_p$.

Principal meshes may sound unfamiliar to most architects and engineers. However, architects do design with a simple case of principal mesh, arguably on a daily basis. The *cube* is one of the most common Platonic polyhedra, which is a special instance that sits at the intersection of the three types of principal meshes (figure 4.5). All sorts of *cuboids*, or rectangular boxes, which frequently appear in almost every building, are parallel meshes of the cube. Thus, these rectangular boxes enjoy the constant vertex, edge, and face offset. Principal meshes, in a way, generalize the offset property of a cube to other free-form meshes.

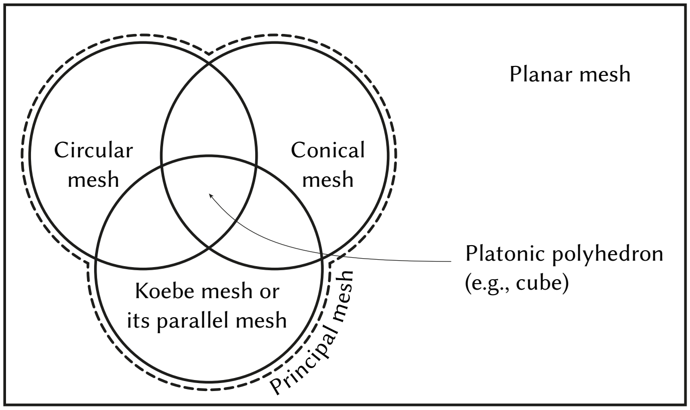

Figure 4.5: The Venn diagram of types of principal meshes

4.3. ISOTROPIC GEOMETRY

Isotropic geometry is used in this dissertation to analyze the graphs of the Airy stress functions. In geometry, the term *isotropic* suggests the direction in which the length measurement degenerates (Professor H. Pottmann, personal communication, June 23, 2020). Unlike in materials science, isotropic means equal in all directions. In isotropic geometry, the term "isotropic direction" refers to the distinct direction.

In general, isotropic geometry studies an n-variable scalar function as a graph in the $(n+1)$-dimensional space (Chen, Decu, & Verstraelen, 2014; Pottmann & Liu, 2007; Pottmann & Opitz, 1994). This way, a scalar function $f : D \subset \mathbb{R}^2 \rightarrow \mathbb{R}$ defined on a 2D domain D becomes a 3D surface

$$\left\{(x, y, f(x, y)) \in \mathbb{R}^3 \,\middle|\, (x, y) \in D\right\}.$$

Subsequently, the original intangible function can be discussed as a visualized surface from a geometric point of view, so that the gradients of a function become slopes of a surface, and the second derivatives turn into curvatures.

One can plot the Airy stress function as a surface in the 3D space and apply principal meshes to discretize the Airy stress *surface* and thus visualize the principal stresses. Since the curvatures on the Airy stress surfaces are the second derivatives indicating stresses, principal meshes ultimately display the principal stresses. As the third dimension of the Airy stress surfaces is not a physical dimension, it is essential to apply their counterparts in isotropic geometry, *isotropic*-circular and *isotropic*-conical meshes (from here on referred to as *i*-circular and *i*-conical meshes, respectively).

In isotropic geometry, the notions of distance, circle, and sphere differ from their Euclidean counterparts. For detailed definitions, see Pottmann and Opitz (1994) and Pottmann and Liu (2007). Here, this section briefly mentions the notions that are crucial to *i*-circular and *i*-conical meshes.

***Isotropic*-distance.** The major distinction of 3D isotropic geometry from the ordinary 3D Euclidean geometry is that the first two dimensions are more important than the last one. The *i*-distance between two points $\mathbf{x}_1 = (x_1, y_1, z_1)$ and $\mathbf{x}_2 = (x_2, y_2, z_2)$ is barely affected by the third dimension, such that (Pottmann & Liu, 2007)

$$\|\mathbf{x}_1 - \mathbf{x}_2\|_i := \lim_{\epsilon \to 0} \sqrt{(x_1 - x_2)^2 + (y_1 - y_2)^2 + \epsilon^2 (z_1 - z_2)^2},$$

in which the third dimension is almost negligible as $\epsilon \to 0$ and the subscript i following the norm symbol $\|\cdot\|$ stands for *isotropic*.

***Isotropic*-sphere.** Following the definition of *i*-distance, the *i*-sphere is the set of all points $\mathbf{x} = (x, y, z)$ with a constant distance r from a center $\mathbf{x}_c$ such that $\|\mathbf{x} - \mathbf{x}_c\|_i = r$ or

$$(x - x_c)^2 + (y - y_c)^2 + \epsilon^2 (z - z_c)^2 = r^2.$$

When $0 < \epsilon^2 < 1$, the *sphere* looks like an ellipsoid obtained by rotating an ellipse about the z-axis, which has two foci. Let (x_c, y_c, z_1^{focus}) denote the higher focus and (x_c, y_c, z_2^{focus}) the lower. When $\epsilon \to 0$, the ellipsoid degenerates into a circular cylinder (as $z_1^{focus} \to \infty$ and

$z_2^{focus} \to -\infty$), or a paraboloid of revolution (as one of $|z_1^{focus}|$ and $|z_2^{focus}|$ approaches infinity while the other stays finite). The former degenerated ellipsoid is the *i*-sphere of cylindrical type

$$(x - x_c)^2 + (y - y_c)^2 = r^2,$$

and the latter is the *i*-sphere of parabolic type

$$(x - x_c)^2 + (y - y_c)^2 + c_1 z = c_2,$$

where c_1 and c_2 are constants that relate to z_c and r^2. Thus the unit *i*-sphere of parabolic type Σ_0 is defined as

$$\Sigma_0 := \left\{ \left(x, y, \frac{1}{2}(x^2 + y^2) \right) \middle| (x, y) \in \mathbb{R}^2 \right\}.$$

***Isotropic*-principal meshes and reciprocal diagrams.** In isotropic geometry, the definition of spheres is changed. As a result, the definitions of *i*-circular meshes and *i*-conical meshes must be updated as well. A paraphrase from Pottmann and Liu (2007):

- *I*-circular meshes refer to meshes where the vertices forming a face are on the intersection between a plane and an *i*-sphere;
- *I*-conical meshes refer to planar meshes where the faces meeting in a vertex are tangent to an *i*-sphere of parabolic type.

An *i*-circular mesh inscribed in the unit *i*-sphere Σ_0 is reciprocal to an *i*-conical mesh circumscribed about the unit *i*-sphere Σ_0 (Pottmann & Liu, 2007). This dissertation extends this notion and shows that an *i*-circular mesh inscribed in a surface $\big(x, y, F(x, y)\big)$ is *reciprocal* to an *i*-conical mesh circumscribed about the *reciprocal* surface $\big(\xi, \eta, F^*(\xi, \eta)\big)$. The *reciprocal* relation is defined in equations (2.9). A copy is repeated here:

$$\xi = \frac{\partial F}{\partial x}, \quad \eta = \frac{\partial F}{\partial y}, \quad F^* = x\frac{\partial F}{\partial x} + y\frac{\partial F}{\partial y} - F, \tag{4.1a}$$

$$x = \frac{\partial F^*}{\partial \xi}, \quad y = \frac{\partial F^*}{\partial \eta}, \quad F = \xi\frac{\partial F^*}{\partial \xi} + \eta\frac{\partial F^*}{\partial \eta} - F^*. \tag{4.1b}$$

The proof consists of two steps:

1. Planes tangent to $\big(\xi, \eta, F^*(\xi, \eta)\big)$ at points $\boldsymbol{\xi}_i = \big(\xi_i, \eta_i, F_i^*\big)$ meet at one vertex if and only if the corresponding points $\mathbf{x}_i = (x_i, y_i, F_i)$ are on a common plane.
2. Planes tangent to $\big(\xi, \eta, F^*(\xi, \eta)\big)$ at points $\boldsymbol{\xi}_i = \big(\xi_i, \eta_i, F_i^*\big)$ are tangent to an *i*-sphere if and only if the corresponding points $\mathbf{x}_i = \big(x_i, y_i, F_i\big)$ are on a common *i*-sphere.

In the first step, let $\boldsymbol{\xi}_i$ denote a point on 3 distinctive points, in which $i \in \{1, 2, 3\}$, and $\mathbf{x}_i$ denote the corresponding points. Planes tangent to the graph of $F^*(\xi, \eta)$ at $\boldsymbol{\xi}_i$ can be expressed as

$$\zeta = F^*(\xi_i, \eta_i) + \frac{\partial}{\partial \xi}F^*(\xi_i, \eta_i) \cdot (\xi - \xi_i) + \frac{\partial}{\partial \eta}F^*(\xi_i, \eta_i) \cdot (\eta - \eta_i).$$

From equation (4.1b), the tangent planes are

$$\zeta = x_i \cdot \xi + y_i \cdot \eta - F_i. \tag{4.2}$$

Let $\boldsymbol{\xi}_v = (\xi_v, \eta_v, \zeta_v)$ denote the intersection of the three tangent planes defined by the three points. The intersection $\boldsymbol{\xi}_v$ is provided by

$$\begin{bmatrix} \xi_v \\ \eta_v \\ \zeta_v \end{bmatrix} = \begin{bmatrix} x_1 & y_1 & -1 \\ x_2 & y_2 & -1 \\ x_3 & y_3 & -1 \end{bmatrix}^{-1} \begin{bmatrix} F_1 \\ F_2 \\ F_3 \end{bmatrix} \tag{4.3}$$

Any non-vertical plane that passes through $\boldsymbol{\xi}_v$ and is tangent to the graph of $F^*(\xi, \eta)$ at points $\boldsymbol{\xi}_t = (\xi_t, \eta_t, F_t^*)$ should meet the condition:

$$\zeta_v = x_t \cdot \xi_v + y_t \cdot \eta_v - F_t, \tag{4.4}$$

where $\mathbf{x}_t = (x_t, y_t, F_t)$ is the point corresponding to $\boldsymbol{\xi}_t = (\xi_t, \eta_t, F_t^*)$. Equation (4.4) describes that each valid point of tangency $\boldsymbol{\xi}_t$ corresponds to the $\mathbf{x}_t$ which is on the plane $F_t = \xi_v \cdot x_t + \eta_v \cdot y_t - \zeta_v$ in the space of (x, y, z) as figure 4.6 shows.

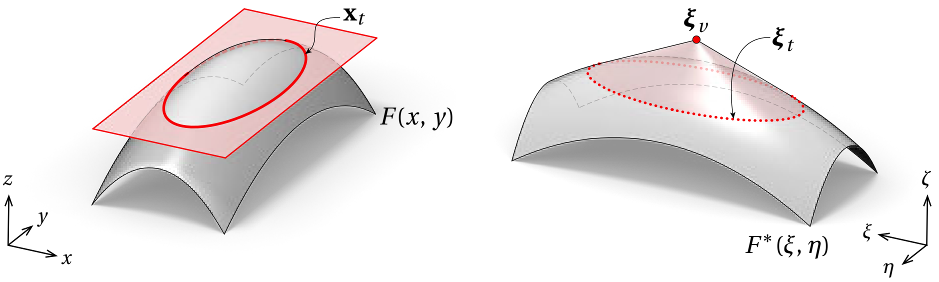

Figure 4.6: The intersection of the graph of $F(x, y)$ and a plane is $\mathbf{x}_t$, which corresponds to a set of tangency points $\boldsymbol{\xi}_t$ that define planes passing through $\boldsymbol{\xi}_v$.

In the second step, the reciprocal diagrams of $\big(x, y, F(x, y)\big)$ and $\big(\xi, \eta, F^*(\xi, \eta)\big)$ are under discussion along with the reciprocal diagrams of i-spheres. Let S denote an i-sphere of hyperbolic type in (x, y, z)

$$S = \left\{ \left(x, y, \frac{a}{2}\left((x - x_s)^2 + (y - y_s)^2\right) + z_s \right) \middle| (x, y) \in \mathbb{R}^2 \right\}.$$

Each i-sphere S has four parameters a, x_s, x_s, and z_s denoting the curvature and the position. Let S^* denote the corresponding i-sphere of S. By equations (4.1), one can derive

$$S^* = \left\{ \left(\xi, \eta, \frac{1}{2a}\left((\xi + a x_s)^2 + (\eta + a y_s)^2\right) - z_s - \frac{a}{2}(x_s^2 + y_s^2) \right) \middle| (\xi, \eta) \in \mathbb{R}^2 \right\}.$$

If an i-sphere S^* is inscribed by the planes, from equation (4.2), the slopes of planes should match the slopes of the i-sphere S^* at the points of tangency $\boldsymbol{\xi}_{S^*i} = (\xi_{S^*i}, \eta_{S^*i}, \zeta_{S^*i})$. For the slope in the x-direction, one has

$$\frac{\partial}{\partial \xi}(x_i \cdot \xi + y_i \cdot \eta - F_i)\Big|_{\xi=\xi_{S^*i},\,\eta=\eta_{S^*i}} = \frac{\partial}{\partial \xi}\left(\frac{1}{2a}\left((\xi + a x_s)^2 + (\eta + a y_s)^2\right) - z_s - \frac{a}{2}(x_s^2 + y_s^2)\right)\Big|_{\xi=\xi_{S^*i},\,\eta=\eta_{S^*i}}.$$

It can be simplified as

$$\xi_{S^*i} = a(x_i - x_s).$$

In the same manner, the condition in the y-direction gives $\eta_{S^*i} = a(y_i - y_s)$. The tangent planes and the i-sphere S^* shall have the same ζ coordination, so that

$$x_i \cdot a(x_i - x_s) + y_i \cdot a(y_i - y_s) - F_i = \frac{a}{2}(x_i^2 + y_i^2) - z_s - \frac{a}{2}(x_s^2 + y_s^2),$$

which is equivalent to

$$F_i = \frac{a}{2}\left((x_i - x_s)^2 + (y_i - y_s)^2\right) + z_s. \tag{4.5}$$

The graph of equation (4.5) is exactly identical to the i-sphere S, which suggests that if the unit i-sphere S^* is inscribed in the tangent planes defined by $\boldsymbol{\xi}_i$, the corresponding i-sphere S is circumscribed about the corresponding points $\mathbf{x}_i$.

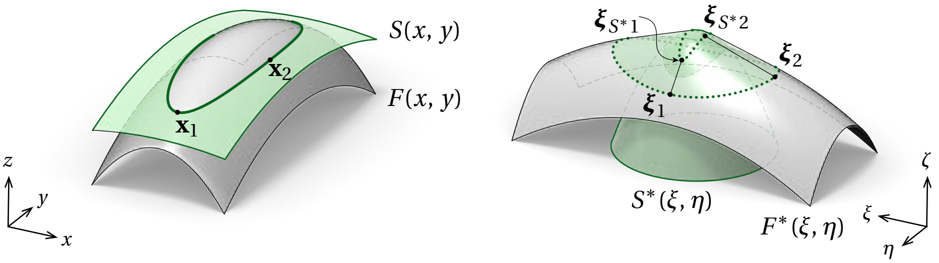

Figure 4.7: Points on the intersection of $F(x, y)$ and $S(x, y)$ correspond to lines tangent to both $F^*(\xi, \eta)$ and $S^*(\xi, \eta)$ at $\boldsymbol{\xi}_i$ and $\boldsymbol{\xi}_{S^*i}$ respectively. Two instances of the tangent lines are explicitly drawn.

A vertex (x_i, y_i, F_i) on the graph of $F(x, y)$ is reciprocal to a plane tangent to the graph of $F^*(\xi, \eta)$ at the corresponding points (ξ_i, η_i, F_i^*). Considering equations (4.4) and (4.5), one can say that when (x_i, y_i, F_i) is a set of i-concyclic vertices, the reciprocal planes meet at one point and are circumscribed about an i-sphere. Thus, an i-circular mesh inscribed in $F(x, y)$ corresponds to an i-conical mesh that is circumscribed about $F^*(\xi, \eta)$.

4.4. VISUALIZING AND DISCRETIZING AIRY STRESS FUNCTIONS

Visualization of stress fields is a more complicated task than visualization of a scalar field. In the absence of body forces, an equilibrium stress field can be characterized by an Airy stress function, which can be further discretized into a polyhedral surface, with which the forces can be visualized via Maxwell's reciprocal theory (1864; 1868; 1870). However, there is no theory that includes body forces in the discretization of Airy stress functions. This section extends the notion of polyhedral Airy stress functions by incorporating body forces.

Stress fields are tensor fields, which have three scalar quantities at each position instead of one. Contours or graded color maps are only appropriate for scalar fields, whereas a scalar function, or an Airy stress function, can denote a stress tensor field. However, the viewer has to observe and understand the curvatures to decipher the stress (figure 4.8a–b).

Other methods are often used in visualizing stress fields. Stress trajectory networks, or isostatic lines, are often used to show the principal stress orientation of stress fields (figure 4.8c). Unfortunately, the magnitudes of principal stresses are omitted in such networks. Quivers are also often used, which can show the orientation and the magnitudes at once (figure 4.8d). However, the overall stress flow is in this case not as clear as a stress trajectory network.

Conversely, a polyhedral stress function can effectively condense distributed stresses into forces. The resultant network can be drawn with linewidth proportional to the forces. Although one may use a triangular or hexagonal mesh to discretize an arbitrary stress function (Fraternali, Angelillo, & Fortunato, 2002), the derived information is not structured and not intuitively perceptible (Bobenko & Suris, 2007) (figure 4.8e). *I*-principal meshes provide a better solution. These meshes have edges as discretized curvature lines, which may also be discretized isostatic lines (or stress trajectories), which are commonly used to indicate the orientation of principal stresses. Unlike a generic triangular or hexagonal mesh, an *i*-principal mesh has the customized edge arrangement to the Airy stress function being approximated. Combined with the forces on the edges, the principal meshes of stress functions can display principal orientation, the magnitude of principal stresses, and the overall pattern in one diagram. (figure 4.8f)

Discretizing Airy stress functions into planar *i*-principal meshes is an effective way to visualize the stress tensor field. The techniques introduced in section 4.3 can be applied to discretizing Airy stress functions without body forces into *i*-principal meshes. However, to the best of the author's and supervisors' knowledge, there exists no theory yet to integrate body forces in discretized Airy stress functions into *i*-principal meshes or general meshes. This dissertation extends the notion of polyhedral Airy stress function from flat panels to curved ones. The method is presented as follows.

4.4.1. BODY FORCES IN A SMOOTH AIRY STRESS FUNCTION

The Airy stress function $F(x, y)$ can easily integrate body forces p_x and p_y once it is combined with the integrals $\int p_x\,dx$ and $\int p_y\,dy$, as clearly shown in an equation:

$$\mathbf{N} = \begin{bmatrix} N_{xx} & N_{xy} \\ N_{xy} & N_{yy} \end{bmatrix} = \begin{bmatrix} \frac{\partial^2}{\partial y^2} F & -\frac{\partial^2}{\partial x \partial y} F \\ -\frac{\partial^2}{\partial x \partial y} F & \frac{\partial^2}{\partial x^2} F \end{bmatrix} - \begin{bmatrix} \int p_x\,dx & 0 \\ 0 & \int p_y\,dy \end{bmatrix}, \tag{4.6}$$

in which $\mathbf{N}$ is the stress resultant tensor. This equation is a copy of (2.8). More detailed discussion can be found in chapter 2.

Hydrostatic pressure. For demonstration, a simple two-dimensional stress field is represented by the Airy stress function. The pressure or the stress in a pool of static liquid is

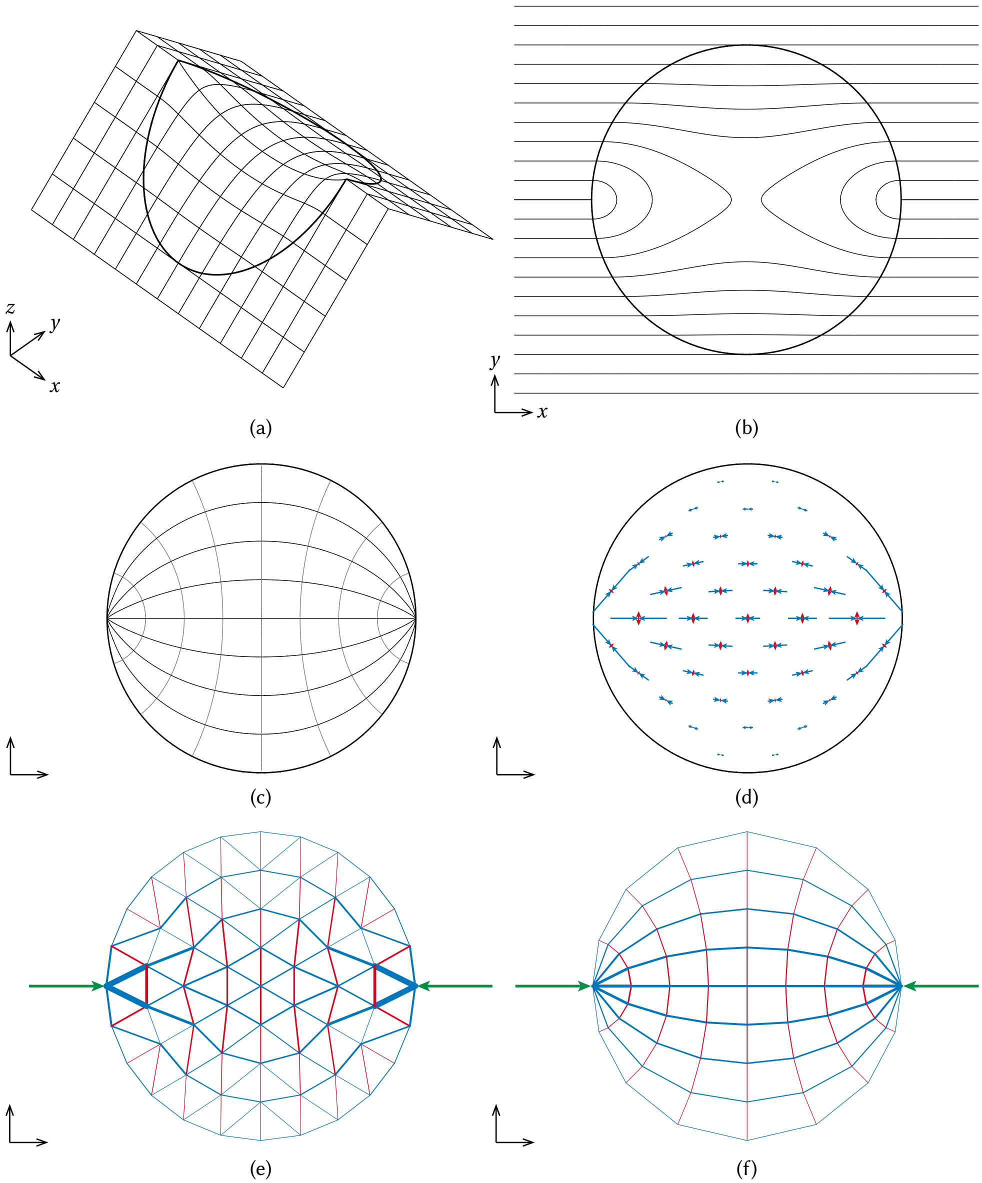

Figure 4.8: Visualizations of stresses in a compressed disc without body forces. The method of planar *i*-principal meshes provides ideal results, but it can only work on cases without body forces. (a) Axonometric view of the Airy stress function. (b) The contours of the stress function. (c) Stress trajectories of the stress tensor field. (d) Quiver plot of the stress tensor field. (e) Triangular mesh of discretized Airy stress function. (f) *I*-circular mesh of discretized Airy stress function. Edges of the meshes are drawn in widths proportional to their forces. Compression is drawn in blue, tension in red, and external forces in green.

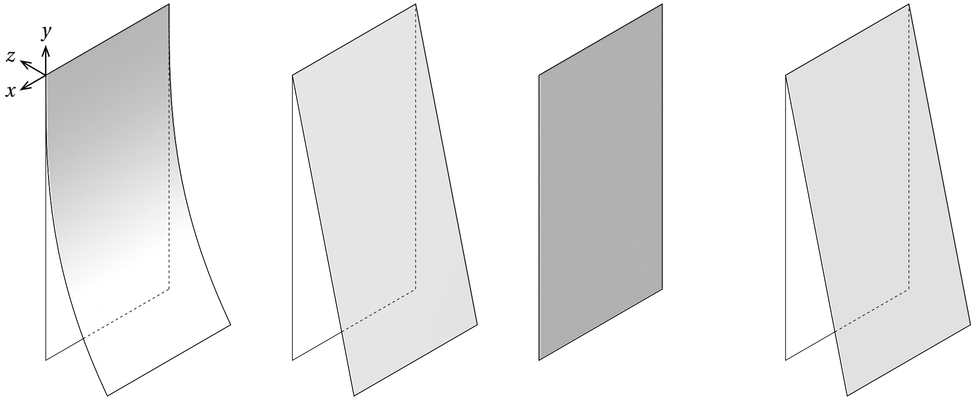

(a) $F(x, y)$ (b) $\partial_{yy}F$ (c) $\int p_x\,dx$ (d) N_{xx}

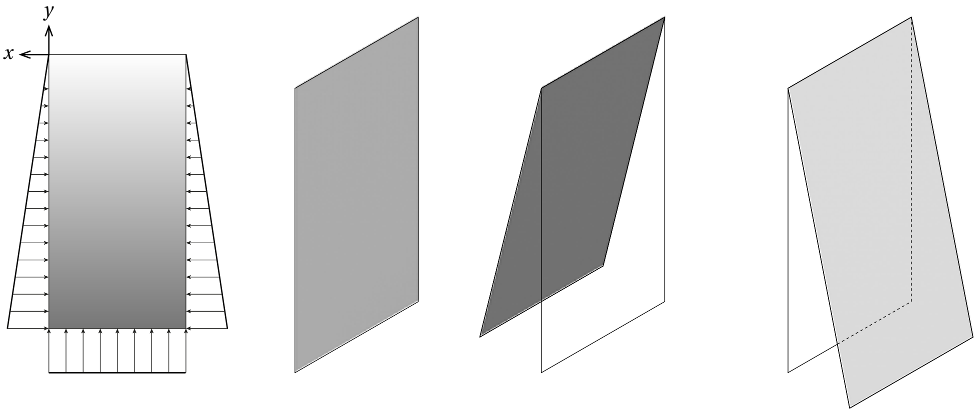

(e) Stress distribution (f) $\partial_{xx}F$ (g) $\int p_y\,dy$ (h) N_{yy}

Figure 4.9: Hydrostatic pressure. (a) The Airy stress function. (b–d) The process of deriving the normal stress N_{xx}. The second-derivative $\partial_{yy}F$ (b) minus the integrals of the body forces $\int p_x\,dx$ (c) equals the stress N_{xx} (d). (f–h) The process of deriving the normal stress N_{yy}, equivalent to (b–d) but in the perpendicular direction. (e) The stress distribution along the boundaries.

caused by gravity: $p_y = -\rho g$, in which g is the gravitational load and ρ is the fluid density. Since the fluid has no shear force capacity in any direction, the shear stress N_{xy} equals zero and the normal stresses are equal: $N_{xx} = N_{yy}$. If the surface of the liquid is set as $y = 0$, the stress equals

$$\mathbf{N}^{hydro} = \begin{bmatrix} \rho g y & 0 \\ 0 & \rho g y \end{bmatrix}. \tag{4.7}$$

Regarding the integrals of body forces, one can set

$$\int p_x \, dx = 0, \tag{4.8a}$$

$$\int p_y \, dy = -\rho g y. \tag{4.8b}$$

Then, from equation (4.6), the stress function shall satisfy $\partial_{xx} F^{hydro} = \rho g y$ and $\partial_{yy} F^{hydro} = 0$. By setting the constant of integration to zero, a sufficient solution to satisfy these conditions is

$$F^{hydro}(x, y) = \frac{1}{6} \rho g y^3. \tag{4.8c}$$

Figure 4.9 shows the graphs of the stress function, its second-derivatives, integrals of body forces, and the resulting stresses. (Both $\partial_{xy} F$ and N_{xy} are left out since they are both zero functions.) Although this case is rather simple, its intricate inner structure will be unveiled once it is discretized.

4.4.2. BODY FORCES IN DISCRETIZED AIRY STRESS FUNCTION

Different from stresses distributed across a continuous domain, discretized structures only have stresses concentrated in nodes and bars, and thus zero stresses in the voids (i.e., all of the space other than the nodes and bars). As the width of a bar approaches zero so that the stresses become highly concentrated, one may refer to the overall stress as the *axial force*. The result is a substitute truss that approximates the original continuous structure. Body forces cannot be applied in the voids, as there are no structural members to transfer the load. Hence, the substitute loads (equivalent to the body forces) must apply at either the nodes or the bars. In this dissertation, bars are chosen to bear the body forces, which means the integrals of body forces must be discretized into step-wise functions. In every void, since $p_x = p_y = 0$, the $\int p_x \, dx$ and $\int p_y \, dy$ are constant. Loads in the x-direction are represented by the difference in $\int p_x \, dx$ across two adjacent voids. Equally, loads in the y-direction are characterized by the difference in $\int p_y \, dy$ across the voids.

At the same time, the Airy stress function is discretized into vertices, edges, and faces which correspond to the nodes, bars, and voids of the substitute structure. Each face in the Airy stress function represents a void bearing zero stress in the substitute structure. Hence, in the voids, the Airy stress function $F^{void}(x, y)$ should satisfy $\mathbf{N}^{void} = \mathbf{0}$. Following from (4.6), it can be derived that

$$\frac{\partial^2}{\partial y^2} F^{void} = \int p_x \, dx, \tag{4.9a}$$

$$\frac{\partial^2}{\partial x^2} F^{void} = \int p_y \, dy. \tag{4.9b}$$

Since both $\int p_x \, dx$ and $\int p_y \, dy$ are constant in a void, F^{void} should simply be a paraboloid. Subsequently, the creases between these paraboloids should be conic sections in top view. It must be noted that the second derivatives at the creases are extremely intense, or more precisely, approach infinity. However, the integrals of such second derivatives are still a finite number, which can be interpreted as the slope differences across the creases. The differences between slopes represent the axial forces of the corresponding bars. As the second

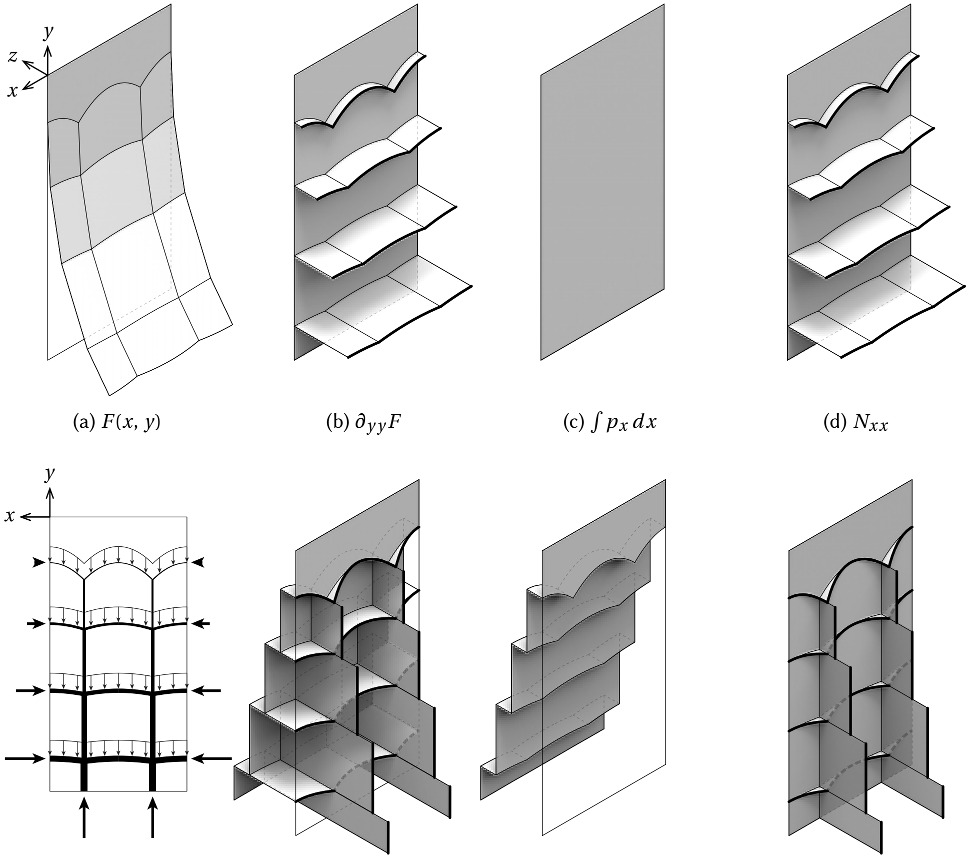

(a) $F(x, y)$ (b) $\partial_{yy}F$ (c) $\int p_x \, dx$ (d) N_{xx}

(e) Stress pattern (f) $\partial_{xx}F$ (g) $\int p_y \, dy$ (h) N_{yy}

Figure 4.10: Discretization of hydrostatic pressure. (a) The discretized Airy stress function, with curved faces and creases. (b–d) The derivation of the normal stress N_{xx}. The second-derivative F_{yy} (b) minus the integrals of the body forces in the x-direction $\int p_x \, dx$ (c) equals the stress N_{xx} (d). (f–h) The derivation of the normal stress N_{yy}, with the same process in (b–d). In panels (b, d, f, and h), the protruding surfaces ended by the black lines are a schematic representation of the Dirac delta function. The distance from the curve to the xy-plane is proportional to the crease angle of the stress function. (e) The structure approximating the hydrostatic pressure.

derivatives and the stresses approach infinity, the Dirac delta function (Arfken et al., 2013, p. 75) will be used to represent them.

Discretizing hydrostatic pressure. Grid points $\mathbf{x}_{ij}$ are used to construct the Airy stress functions in the voids F_{ij}^{void}. Grid points are given by

$$\mathbf{x}_{ij} = (\delta \cdot i, \delta \cdot j),$$

where δ is the spacing and i, j are the indices such that $i \in \mathbb{Z}$, $j \in \{0, -1, -2, \ldots\}$. Function F_{ij}^{void} is defined as polynomials that satisfy equations (4.9) and are tangent to the smooth

Airy stress function given in equation (4.8c). The result is

$$F_{ij}^{void} = \rho g \left(\frac{1}{6}\delta^3 j^3 + \frac{1}{2}\delta^2 j^2 (y - \delta j) - \frac{1}{2}\delta j (x - \delta i)^2 \right). \tag{4.10}$$

Each F_{ij}^{void} intersects with its adjacent faces. The intersection of two faces defines a curved bar, and the intersection between bars defines a node. Figure 4.10 shows the result of the discretized stress function, and figure 4.10e shows the inner structure of hydrostatic pressure. At a deeper location, the rise of the arch is shallower as the thrust is larger, while the column is thicker.

The proposed discretization method does not invent the structure, but rather discovers its natural existence. Similar structures have been discovered by architects centuries ago. Figure 4.11 displays how Christopher Wren (1632-1723) managed to use the inverted arch and horizontal thrust to generate vertical support from an area of soil to the columns.

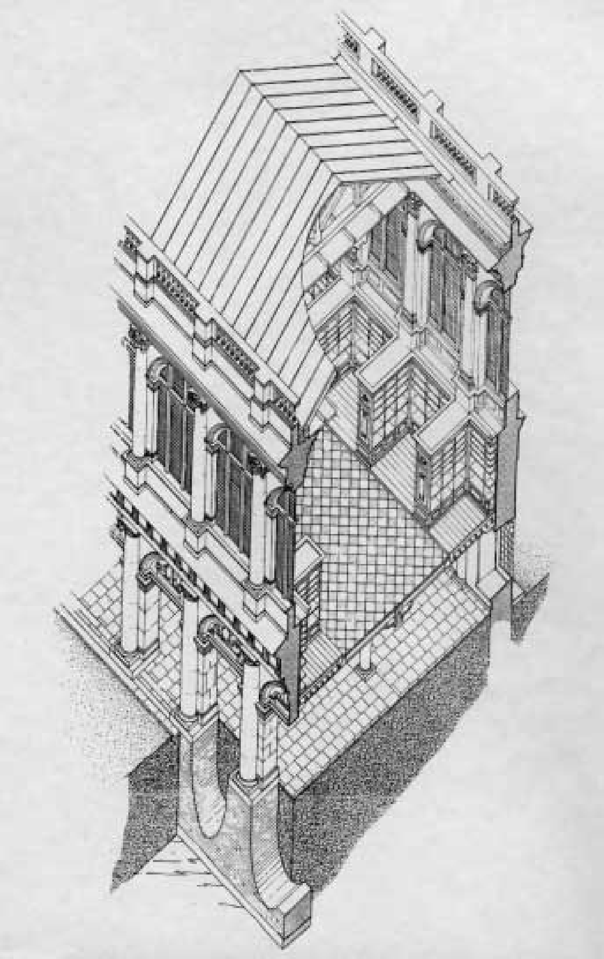

Figure 4.11: The inverted arches as the foundations of Wren's Library for Trinity College, Cambridge. [Source: McKitterick, 1995, image courtesy of Cambridge University Press]

4.4.3. BODY FORCES IN GRAPHIC STATICS AND RECIPROCAL DIAGRAMS

Besides analytical discussion via mathematical expressions, the idea of body forces represented by the curvatures of Airy stress function in voids can also be shown via graphic statics and reciprocal diagrams.

Graphic statics is primarily used to analyze the forces in a truss-like structure (see section 2.2). A classical demonstration of graphic statics is given by the analysis of a cable's shape by hanging several weights as figure 4.12a shows. The form diagram shows the cable deformed due to three weights, and the closed *force polygons* indicate that each node is in equilibrium.

When another cable (figure 4.12b) hangs right below the previous one, aggregate force polygons are formed as in figure 4.12c. The force polygons corresponding to the lower chain in figure 4.12c show that it is not the absolute magnitude of the applied load b'_i determining the shape of the lower chain, but that the shape is determined by the difference between the axial forces in a_i and b'_i. In other words, part of b'_i is passing the lower chain and only $(b'_i - a_i)$ is interacting with the lower chain. Figure 4.12d shows the force polygons when the loads are not just applied at three points, but all along the chain, as if they were distributed.

The last two rows of figure 4.12 display the stress functions and the reciprocal diagrams. The stress functions in columns (a) and (b) add up into the stress function in (c), which has vertical edges to represent the loads of a_i and b'_i. The stress function in (d) has smooth cylindrical surfaces with countless straight lines to represent distributed loads.

Regarding the reciprocal diagram, the principal curvatures at the corresponding points have the same orientation and multiplicative inverse curvatures (see section 2.2 and equation (2.17)). The feature suggests a cylindrical panel of $F^{void}(x, y)$, which has principal curvatures consisting of a finite value and a zero $\{a, 0\}$, corresponds to a curve line, which has multiplicative inverse principal curvatures that consist of a finite and an infinite value $\{a^{-1}, \pm\infty\}$. For instance, in figure 4.12d, the middle patch in the stress function corresponds to the middle curved crease in the reciprocal diagram. The reciprocal relations between other types of surfaces are organized and displayed in table 4.3 and figure 4.13.

Table 4.3: Reciprocal relations between geometric entities

Entity in $F(x, y)$	$\lvert\lambda_1^F\rvert$	$\lvert\lambda_2^F\rvert$	**Entity in** $\phi(\xi, \eta)$	$\lvert\lambda_1^\phi\rvert$	$\lvert\lambda_2^\phi\rvert$
Vertex	∞	∞	Planar surface	0	0
Curved edge	$0\cdots\infty$	∞	Developable surface	$0\cdots\infty$	0
Straight edge	0	∞	Straight edge	∞	0
double-curved surface	$0\cdots\infty$	$0\cdots\infty$	double-curved surface	$0\cdots\infty$	$0\cdots\infty$
Developable surface	0	$0\cdots\infty$	Curved edge	∞	$0\cdots\infty$
Planar surface	0	0	Vertex	∞	∞

Reciprocal diagrams for hydrostatic pressure. To find the reciprocal diagram of the discretized stress function discussed in section 4.4.2, one may directly apply equations (4.1). The result is the self-intersecting surface in figure 4.14b. To *untangle* the self-intersecting

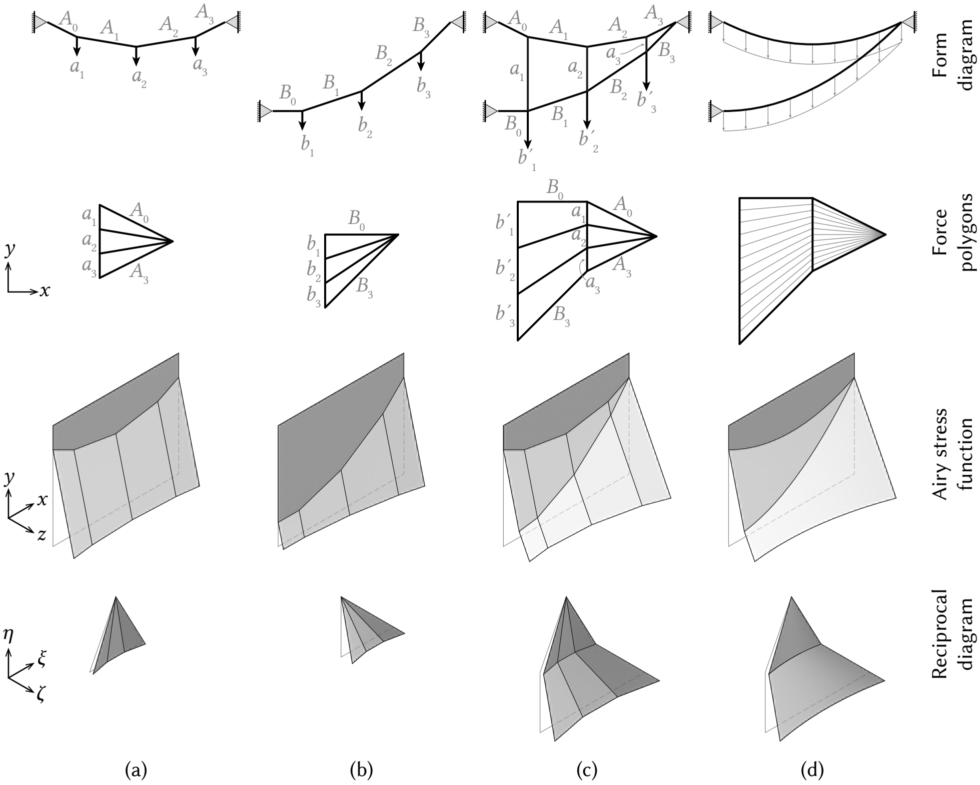

Figure 4.12: Hanging-chain models with corresponding force polygons and Airy stress functions. (a) A chain supporting three weights and anchored at leveled supports. (b) Another chain anchored at differing heights. (c) Two hanging chains in the same vertical plane. (d) Two chains with evenly distributed loads.

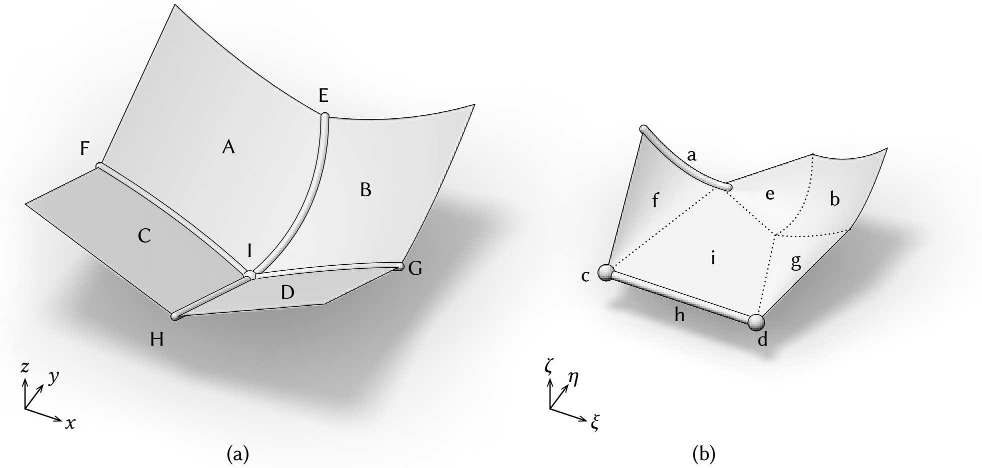

(a) (b)

Figure 4.13: A pair of reciprocal diagrams. (a) the left diagram consists of four surfaces (A: developable, B: double-curved, C–D: planar), four edges (E–G: curved, H: straight), and one vertex (I). (b) The corresponding entities are labeled in lowercase letters. Surfaces b, e, f, g, and i are continuous in slopes, and the borders between surfaces A, B, C, and D have crease angles.

surface, instead of discretizing the stress function in expressions (4.8), one can choose different constants of integration as

$$\int p_x \, dx = \rho g C, \tag{4.11a}$$

$$\int p_y \, dy = -\rho g y + \rho g C, \tag{4.11b}$$

$$F^{hydro}(x, y) = \frac{1}{6}\rho g y^3 + \frac{1}{2}\rho g C\left(x^2 + y^2\right), \tag{4.11c}$$

where C is such a constant of integration. Then, the subsequent discretization will lead to

$$\begin{aligned} F_{ij}^{void} = \rho g \Bigg(& \frac{1}{6}\delta^3 j^3 + \frac{1}{2}C\left(\delta^2 i^2 + \delta^2 j^2\right) + C\delta i\left(x - \delta i\right) + \left(\frac{1}{2}\delta^2 j^2 + C\delta j\right)\left(y - \delta j\right) \\ & + \frac{1}{2}\left(-\delta j + C\right)\left(x - \delta i\right)^2 + \frac{1}{2}C\left(y - \delta j\right)^2 \Bigg). \end{aligned} \tag{4.12}$$

Figure 4.14c–d graphs this alternative discretized Airy stress function and its reciprocal diagram ($C = -5\delta$). The reciprocal diagram has a series of *patches*. At a deeper location, the sizes of the patches are smaller and thus the gaps between them are wider. The wider gaps correspond to the larger axial forces of the *arches* and *columns* (see figure 4.10e). The widths of the gaps in (ξ, η, ζ) are determined by the sizes of patches $(F_{ij}^{void})^*$, which are determined by the curvatures of the corresponding patches F_{ij}^{void} in (x, y, z). Thereby, a local change in the curvatures of F_{ij}^{void} will locally change the magnitudes of axial forces. This observation once again connects the body forces with the curvatures of the Airy stress function in the voids.

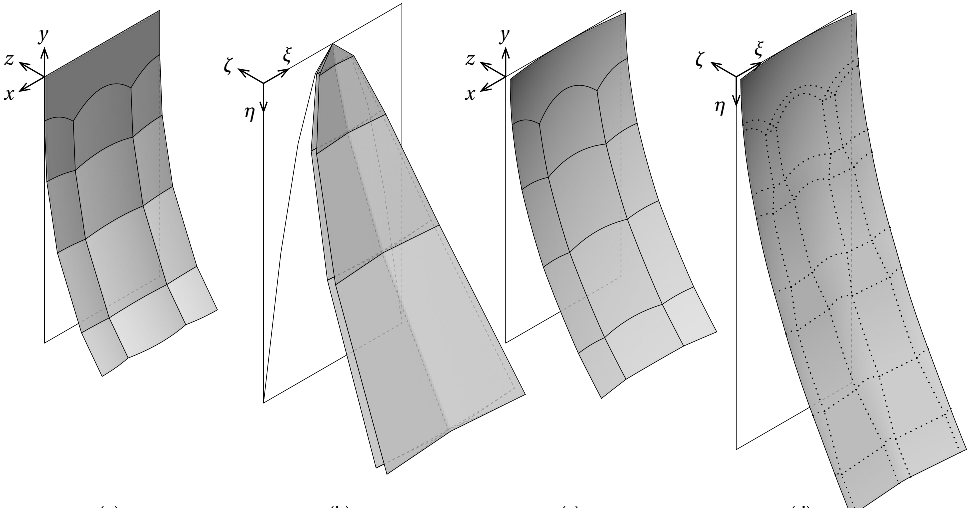

(a) (b) (c) (d)

Figure 4.14: Reciprocal diagrams of the discretized Airy stress functions for the example of hydrostatic pressure. (a–b) Stress function (4.10) and its reciprocal diagram. (c–d) Stress function (4.12) and its reciprocal diagram.

Relief-like discretized stress function. Despite the different constants of integration, both expressions (4.8) and expressions (4.11) represent the same stress distribution $\mathbf{N}^{hydro}$ stated in equation (4.7). Thereby, the two versions of discretization in equations (4.10) and (4.12) are also the same. One may subtract the smooth Airy stress function (4.8c) from the discretized version (4.10) and obtain

$$F_{ij}^{void} = \rho g \left(\frac{1}{6} \left(\delta^3 j^3 - y^3 \right) + \frac{1}{2} \delta^2 j^2 \left(y - \delta j \right) - \frac{1}{2} \delta j \left(x - \delta i \right)^2 \right). \tag{4.13}$$

The resulting graph will look like a relief shown in figure 4.15. Subtracting equation (4.11c) from equation (4.12) will deliver the exact same result. In a way, the relief-like version corresponds to the reciprocal diagram that has patches $(F_{ij}^{void})^*$ overlap one another. At the same time, it is invariant to the constants of integration.

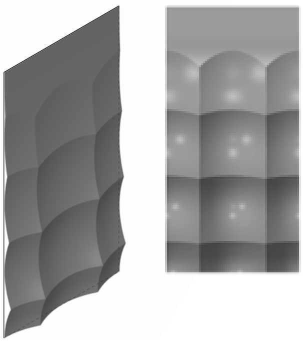

Figure 4.15: The relief-like discretized Airy stress functions. Left: Isometric view. Right: Front view.

4.4.4. NON-PLANAR QUADRILATERAL *I*-CIRCULAR AND *I*-CONICAL MESHES

When body forces are introduced, the discretized Airy stress function should have curved faces to meet the zero stress conditions (4.9). Given that the existing definitions on *i*-circular and *i*-conical meshes are restricted to planar faces, here generalized definitions of *i*-circular and *i*-conical meshes are proposed.

- Non-planar *i*-circular meshes are quadrilateral dominant meshes that the vertices of each face are on an *i*-sphere of cylindrical type;
- Non-planar *i*-conical meshes are quadrilateral meshes that the surrounding faces of each vertex are tangent to lateral faces of a pyramid at the apex, and the pyramid is circumscribed about an *i*-sphere of parabolic type.

Non-planar *i*-circular mesh. Figure 4.16 shows two sets of points $\mathbf{x}_i$ that are on the intersections of cylindrical *i*-spheres S, the graph of the local zero-stress stress functions F^{void}, and two smooth stress functions F. One is elliptic and the other is hyperbolic. These $\mathbf{x}_i$ would be legitimate vertices for non-planar *i*-circular meshes.

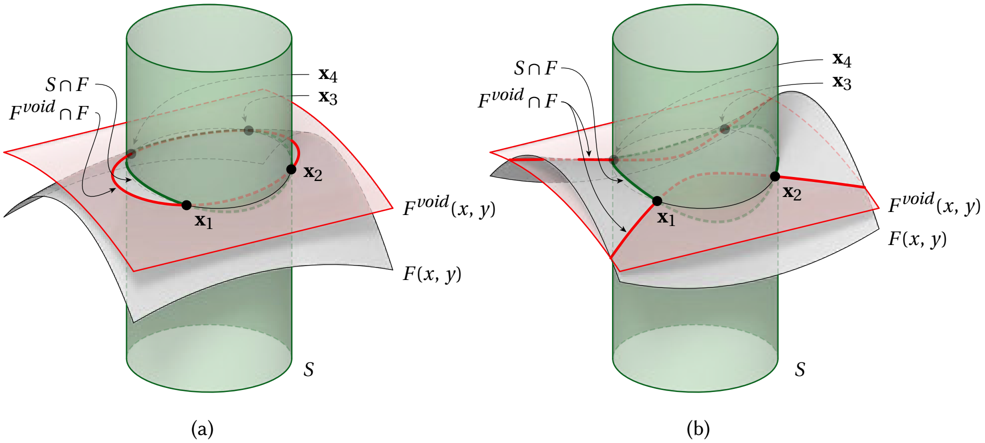

Figure 4.16: Points $\mathbf{x}_i$ on the intersection of an *i*-sphere of cylindrical type S, the graph of the local zero-stress stress function $z = F^{void}(x, y)$, and the graph of the stress function $z = F(x, y)$. (a) A case in which F has positive Gaussian curvature. (b) A case in which F has negative Gaussian curvature.

In a discretization problem, a smooth Airy stress function $F(x, y)$ and smooth integrals of body forces $P_x(x, y) = \int p_x \, dx$ and $P_y(x, y) = \int p_y \, dy$ are assumed to be provided externally. A systematic way is needed to translate $F(x, y)$, $P_x(x, y)$, and $P_y(x, y)$ into their discrete counterparts. This dissertation proposes a method to translate them.

Let functions $F^{void}(x, y)$, $P_x^{void}(x, y)$, and $P_y^{void}(x, y)$ denote the counterparts in a void region, which is bounded by four points $\mathbf{x}_i$ on $F(x, y)$, in which only the first three points are known. The first three points can determine the center (x_c, y_c) and the radius of an *i*-sphere of cylindrical type S. Then, the $P_x^{void}(x, y)$ and $P_y^{void}(x, y)$ are set to be constant functions as discussed in section 4.4.2 and conditions (4.9). They can be arranged as

$$P_x^{void}(x, y) = P_x(x_c, y_c), \qquad P_y^{void}(x, y) = P_y(x_c, y_c).$$

Subsequently, F^{void} can be defined in a polynomial form:

$$F^{void}(x, y) = \frac{P_y(x_c, y_c)}{2}x^2 + \frac{P_x(x_c, y_c)}{2}y^2 + ax + by + c, \tag{4.14}$$

in which a, b, c are constants which can be determined by $F^{void}(\mathbf{x}_{i\in\{1,2,3\}}) = F(\mathbf{x}_{i\in\{1,2,3\}})$. In this way, conditions (4.9) are automatically satisfied. Thus, F^{void} and S are determined. The fourth point can be located at the intersection of F, F^{void}, and S. This method can derive one point of a 2-by-2 mesh when three points are given. In regions with no umbilical point (Porteous, 2001), the method can derive a quadrilateral mesh with m-by-n points when $(m+n-1)$ points are given.

In the cases where $\int p_x\,dx$ and $\int p_y\,dy$ equal zero, all faces of $F^{void}(x, y)$ are planar, and the derived mesh degenerates into a conventional planar i-circular mesh. Moreover, a planar i-conical mesh circumscribed about $F(x, y)$ can also be derived by applying this method, by discretizing the reciprocal diagram $F^*(\xi, \eta)$ into an i-circular mesh first. Then the reciprocal mesh is an i-conical mesh in the x, y, z environment as discussed in section 4.3.

Non-planar *i*-conical mesh. Regarding a non-planar i-conical mesh that circumscribes about a smooth graph of $F(x, y)$, an example of hydrostatic pressure was shown in section 4.4.2. In that example, each void region of the discretized Airy stress function was constructed based on a grid point, so that the $F^{void}(x, y)$ were constructed as

$$\begin{aligned} F^{void}(x, y; x_b, y_b) = {} & \frac{P_y(x_b, y_b)}{2}(x - x_b)^2 + \frac{P_x(x_b, y_b)}{2}(y - y_b)^2 \\ & + \frac{\partial}{\partial x}F(x_b, y_b)(x - x_b) + \frac{\partial}{\partial y}F(x_b, y_b)(y - y_b) + F(x_b, y_b), \end{aligned} \tag{4.15}$$

where (x_b, y_b) is the base point. The curvatures of $F^{void}(x, y)$ are informed by $P_y(x_b, y_b)$ and $P_x(x_b, y_b)$, and the overall slope and elevation are determined such that $F^{void}(x, y)$ is tangent to $F(x, y)$ at the base point (x_b, y_b).

Suppose there are four base points $\mathbf{x}_i = (x_i, y_i, z_i)$ that construct a set of $F_i^{void}(x, y)$. The first three graphs of $F_i^{void}(x, y)$ can easily meet at one point, say $\mathbf{x}_v = (x_v, y_v, z_v)$. If the fourth face also passes the same point with correct slopes, then the criteria for non-planar conical meshes can be fulfilled. The passing through the point $\mathbf{x}_v$ is expressed relatively easily in an equation:

$$F_4^{void}(x_v, y_v; x_4, y_4) = z_v. \tag{4.16}$$

Regarding the slopes, one can approach $\mathbf{x}_v$ from different base points $\mathbf{x}_i$. The observed slope can be expressed as

$$\begin{aligned} x\text{-component: } \xi_{vi} &= \frac{\partial}{\partial x}F_i^{void}(x_v, y_v; x_i, y_i), \\ y\text{-component: } \eta_{vi} &= \frac{\partial}{\partial y}F_i^{void}(x_v, y_v; x_i, y_i). \end{aligned}$$

In other words, the slopes $(\partial_x F_i^{void}, \partial_y F_i^{void})$ can be regarded as points (ξ_{vi}, η_{vi}) in Maxwell's reciprocal diagram, and the vertex $\mathbf{x}_v$ corresponds to the polygon formed by points (ξ_{vi}, η_{vi}).

Whenever the polygon is cyclic, the orientation of planes tangent to F_i^{void} at $\mathbf{x}_v$ will circumscribe an i-sphere, thus meet the criteria for i-conical meshes. The polygon is cyclic when the following equation is met:

$$(\xi_{vi}-\xi_c)^2+(\eta_{vi}-\eta_c)^2=\rho_c^2, \tag{4.17}$$

in which (ξ_c, η_c) is the center and ρ_c is the radius of the circumscribed circle (see figure 4.17). Equations (4.16) and (4.17) together can determine the legitimate fourth base point and make the vertex $\mathbf{x}_v$ meet the i-conical condition.

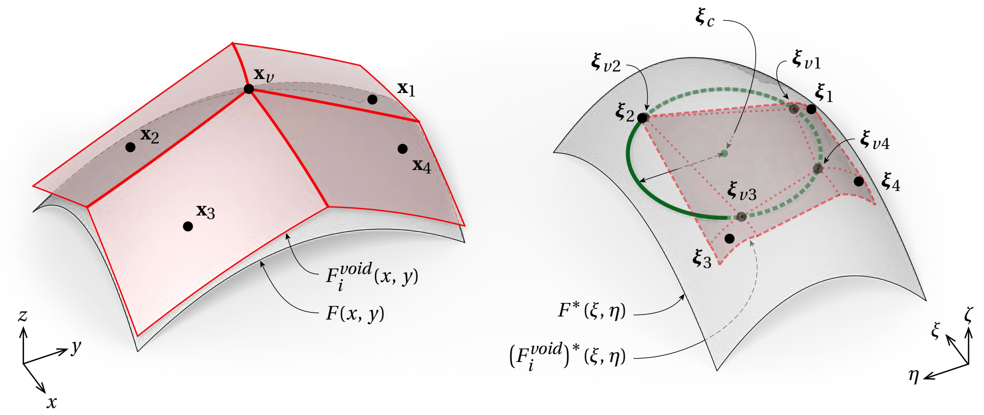

(a) (b)

Figure 4.17: Reciprocal diagrams of the smooth stress function $F(x, y)$ and faces of the discretized stress function $F_i^{void}(x, y)$. The faces tangent to $F(x, y)$ at the base points $\mathbf{x}_i$. Correspondingly, their reciprocal counterparts $(F_i^{void})^*(\xi, \eta)$ tangent to $F^*(\xi, \eta)$ at $\boldsymbol{\xi}_i$. The vertex $\mathbf{x}_v$ meets the i-conical condition when it corresponds to a polygon (with the four vertices $\boldsymbol{\xi}_{vi}$) having a circumscribed circle (the green circle).

The method can locate one base point when the other three base points are given. In regions with no umbilical point, the method can derive a quadrilateral mesh with m-by-n base points when $(m+n-1)$ base points are given.

4.4.5. Application: Discretizing the stress function of beams

In linear elasticity, when compatibility is considered and the body forces are zero or uniform, the Airy stress function should follow the bi-harmonic equation (Sadd, 2009, p. 145):

$$\frac{\partial^4 F}{\partial x^4}+2\frac{\partial^4 F}{\partial x^2 \partial y^2}+\frac{\partial^4 F}{\partial y^4}=0. \tag{4.18}$$

A solution to the governing equation (4.18) for a simply supported beam with reinforced ends can be expressed as (Sadd, 2009, pp. 157-158)

$$F(x, y)=-\frac{2R}{L}\left[\left(x^2-\frac{L^2}{4}\right)\frac{y^2}{H^2}\left(\frac{y}{H}-\frac{3}{2}\right)-\frac{y^2}{5}\left(\frac{y}{H}-\frac{1}{2}\right)\left(\frac{y}{H}-1\right)^2\right], \tag{4.19}$$

in which R denotes the reaction force at one of the supports, L the length of the beam, and H the depth.

This analytical stress function can be interpreted as body forces being zero and all loads acting at the top. Subsequently, the stress function can be discretized into a planar i-circular mesh. The mesh highlights the principal curvatures of the graph (Bobenko & Suris, 2007; Pottmann & Liu, 2007), or the principal stresses of the beam, as figure 4.18a shows. The stress N_{yy} equals $2R/L$ at the top and gradually becomes 0 at the bottom of the beam.

One can also interpret the same stress function (4.19) when body forces are

$$p_x = 0, \qquad p_y = \frac{2R}{LH}.$$

In this case, the beam is loaded by its self-weight and there is no external load at the top. Accordingly, one must discretize the stress function into a non-planar i-circular mesh, as figure 4.18b shows. In this case, the stress N_{yy} equals 0 at the top, middle, and bottom of the beam. Furthermore, by subtracting the smooth stress functions from the discretized ones, one can get the relief-like stress function as in figure 4.18c–d.

These two load cases have the same governing equation and are represented by the same smooth stress function. But after different ways of discretization, the planar and curved faces develop different crease angles at the edges and therefore reveal different stresses in the bars.

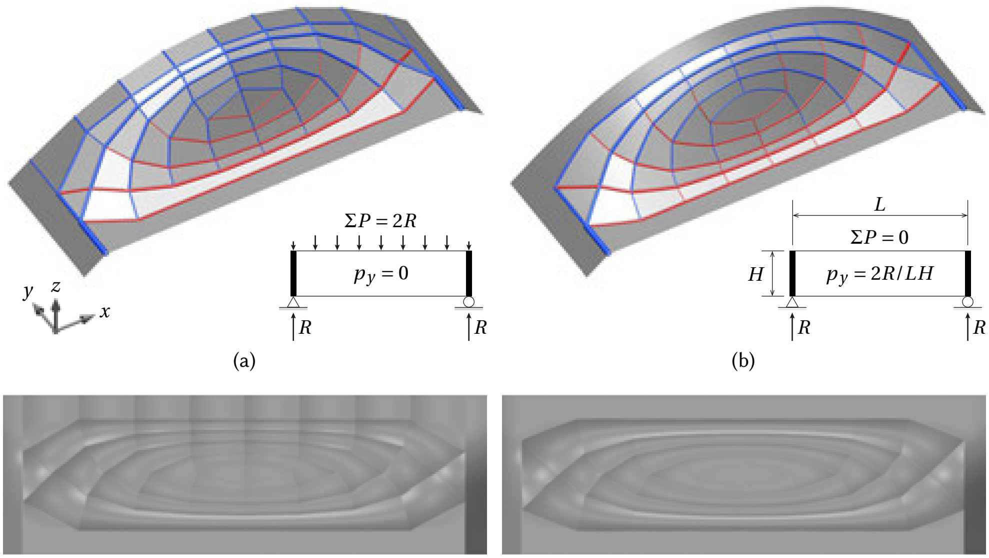

(a) (b)

(c) (d)

Figure 4.18: Discretized Airy stress functions of simply-supported beams. (a) The beam loaded on top without body forces. (b) The beam loaded by its own weight. The diameters of the bars are proportional to their axial forces. Blue bars resemble compression and red bars resemble tension. (c–d) Top views of the relief-like stress functions.

4.5. SUMMARY AND DISCUSSION

This chapter has discussed the application of geometry in fabrication-aware design and discretizing Airy stress functions. Some observations are made:

- principal meshes can approximate free-form surface with flat panels and planar ribs intersecting at torsionless nodes;
- there are three types of principal meshes and two of them are appropriate for approximating arbitrary surfaces—circular meshes and conical meshes;
- principal meshes are parallel meshes of polyhedral spheres;
- rectangular boxes are a family of principal meshes based on the same polyhedral sphere—cube;
- *isotropic*-geometry is suitable for discussing a 2D Airy stress function as a graph in a virtual 3D space;
- a smooth Airy stress function without body forces can be discretized into an *isotropic*-principal mesh, in which the edges can visualize the principal stresses; and
- when a discretized Airy stress function undergoes Maxwell's reciprocal mapping, a face maps to a vertex, an edge maps to an edge, and a vertex maps to a face.

Based on the observations, the main contributions of this chapter are that:

- a method is proposed to discretize Airy stress functions, as well as body forces;
- the integrals of body forces are discretized into step-wise functions;
- Airy stress functions are discretized into curved meshes, in which the faces have curvatures that echo the step-wise integrals of body forces;
- definitions of non-planar *isotropic*-circular and conical meshes are proposed, which can visualize the principal stresses of a stress field with body forces; and
- when a discretized non-planar Airy stress function undergoes Maxwell's reciprocal mapping, other than the ordinary reciprocal relationship (a face maps to a vertex, an edge maps to an edge, a vertex maps to a face), a curved edge maps to a developable surface, a developable surface maps to a curved edge, and a double-curved face maps to a double-curved face.

In later chapters, the conical mesh is used for discretizing synclastic shells and flattening them into reconfigurable mechanisms (chapters 5 and 6). For further developments in visualizing stress fields, the proposed method currently only focuses on planar structures with in-plane, or membrane, stresses. For curved shells, it can further be developed how to consider the slopes of the shells when the Airy stress function is under discretization. For bent plates, the method can be used to visualize the stresses of the top and the bottom layers, while the shear forces between the two layers can be treated as body forces. Regarding validating whether this visualization technique actually generates more perceptible results, experiments could also be designed and executed, which is beyond the scope of this dissertation.

5

PROGRAMMING FLAT-TO-CURVED MECHANISMS

New structural ideas are useless
unless they are based on practical and
efficient construction procedures.

Pier Luigi Nervi[1]

Parts of this chapter have been published in *Advances in Architectural Geometry 2018* (Chiang, Mostafavi, & Bier, 2018) and in *archiDOCT, 6*(2) (Chiang, 2019)

[1] Nervi, 1956, p. 57

The emerging demand for double-curved surfaces challenges designers and manufacturers. Utilizing sheet material to produce curved surfaces is an economical solution, given that such materials can be produced and processed with ease. To exploit the economical benefits of sheet materials, numerous researchers investigate how to decompose a free-form surface into planar components on an architectural scale (see section 4.2). Meanwhile, various advanced approaches have been proposed to transform flat mechanisms into double-curved surfaces, and pilot prototypes have been produced on laboratory scales, such as paper origami (Tachi, 2013), reconfigurable prestressed composite (Aldinger, Margariti, & Suzuki, 2018) or deployable auxetic membranes (Konaković-luković, Konaković, & Pauly, 2018). These approaches make materials reconfigurable, yet leave them vulnerable to bending stresses and prone to buckling.

This chapter presents a novel flat-to-curved mechanism that enables the resulting double-curved structure to resist moderate bending stresses and thus giving it stability under compression. The mechanism consists of nearly vertical hinges and connected blocks. Blocks can rotate about the hinges and thus the overall mechanism contracts or expands. Non-uniform contraction or expansion causes change of the Gaussian curvature.

Geometrically, the major challenge lies in how to identify the set of hinges that can allow the blocks to be reconfigured from a flat to a curved state without residual strain or permanent deformation. Such hinges enable the material to stably maintain the desired shape instead of returning to its initial configuration. Figure 5.1 illustrates an overview of the design steps, which are explained in the following sections.

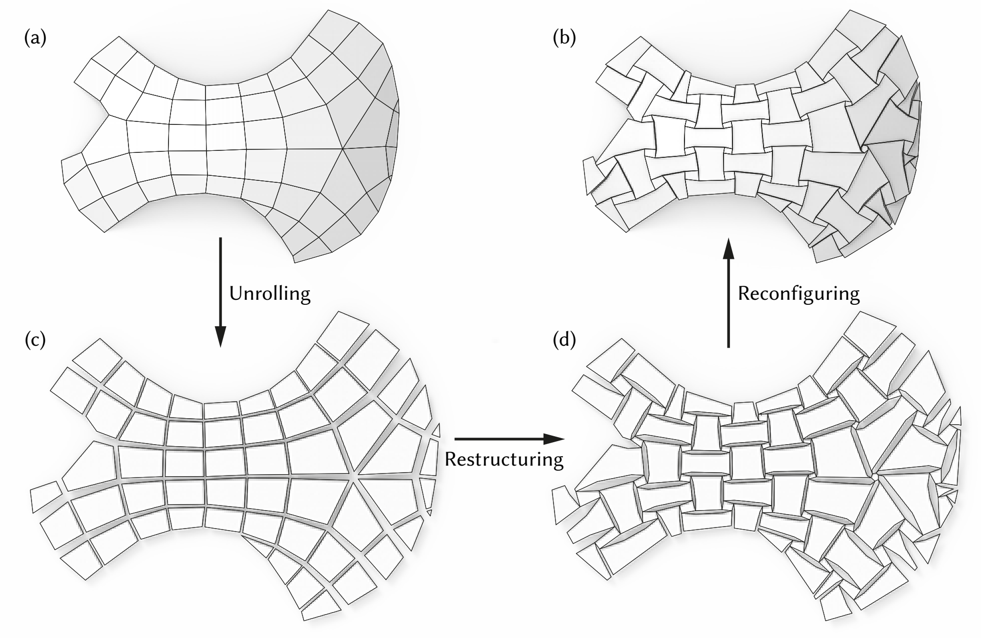

Figure 5.1: The proposed workflow of the design process. (a) The quadrilateral conical mesh. (b) Unrolled panels. (c) Restructured panels with connectors. (d) The free-form synclastic surface formed by the reconfigurable mechanism.

OUTLINE

In this chapter, relevant studies and mechanisms are reviewed in section 5.1. Section 5.2 introduces the mechanical principles and the geometrical features of the bi-stable mechanism. With these fundamental insights in mind, section 5.3 explains how to employ the explored approaches to transform a synclastic surface into its flat configuration. For validation, pilot prototypes have been produced, and the production is reported in section 5.4. Consequently, features of the current method and future works are summarized in section 5.5.

5.1. RECONFIGURABLE MECHANISM AND ARCHITECTED MATERIALS

Since the 2000s, the demand for free-form architecture has gradually increased (Pottmann et al., 2015). The most effective way to build a large free-form surface is to decompose the curved surface into a series of flat panels (Pottmann, Liu, et al., 2007). Although a considerable amount of unique components will be generated in the process, numerically controlled machinery can economically produce all components from either 2D sheet materials (e.g., steel plates, float glass) or 1D profiles (e.g., steel tubes, extruded aluminum). However, the assembly of components is still a labor-intensive and challenging task for builders. Introducing a bi-stable mechanism, this research aims to develop a fabrication method of flat material that can be reconfigured into the target curved states. With this objective, the research is built around the premise that such mechanisms can make the assembly process more efficient and less labor-intensive.

Reconfigurable mechanism. In recent years, numerous ways have been proposed to deliver flat-to-curved reconfiguration for fast deployment. The reconfigurable systems may include embedded actuators or focus on the mechanisms to be actuated. In the first category, two approaches can be distinguished. Some researchers build responsive reconfiguration systems by layering materials with different expansion rates to moisture or temperature changes (Reichert, Menges, & Correa, 2015; Tibbits, 2014; van Manen, Janbaz, & Zadpoor, 2017). With the ambient changes the layered materials expand unevenly, which cause the composites to curve. Other researchers deposit stiff components on pre-tensioned membranes (Aldinger et al., 2018; Guseinov, Miguel, & Bickel, 2017; Jourdan, Skouras, Vouga, & Bousseau, 2021). Once the pre-tensioning is removed, the contracting membranes actuate the composites to the curved configurations.

The research in the second category, on the other hand, concentrates more on the mechanism than actuation. The researchers investigate how to arrange the flexible joints to permit mechanisms to be reconfigured into the desired shapes. In the research pursued by Konaković et al. (2016), sheet materials are homogeneously cut into triangular panels, and the connections between the triangles are considered as ball joints. The material can then be stretched and bent into various free-form shapes. In the cases of origami and kirigami explored by Tachi (2013) and J. Liu, Liu, Eggers, and Sabin (2018) respectively, all components are connected by linear hinges, or the crease lines, laying in the plane of the sheet material. The sizes and shapes of the components are informed by the desired curved surface. The difference between the approaches of Tachi and J. Liu et al. is that origami forbids the designer to cut the sheet materials while kirigami allows one to do so. The ball joints and the linear hinges of these approaches make the flat materials pliable. This attribute makes the products—in their target configurations—incompatible with bending stresses.

In contrast to arranging linear hinges in the plane, Haghpanah, Salari-Sharif, Pourrajab, Hopkins, and Valdevit (2016) place the hinges vertically and produce another type of mechanism. The mechanism consists of multiple units that can be sequentially expanded to other configurations and can stably maintain the shapes. This feature is termed bi-stability. Although both the initial shape and the reconfigured shape are confined in the plane, it suggests that the reconfigurable mechanism can also work on thick materials, which promises certain bending resistance.

Rafsanjani and Pasini (2016) arrange the bi-stable unit in a way that the overall mechanism is *auxetic*. *Auxetic* is a property that an object shrinks (or expands) in all directions when it is only compressed (or stretched) in one direction. Figure 5.2 shows the design of Rafsanjani and Pasini. A feature has been pointed out that the sides of the rotating squares (cyan squares in the figure) can adjust the expansion rate between the two stable states. The feature encourages the author to find ways to distribute different expansion (or contraction) rates at different positions to induce double-curved transformation.

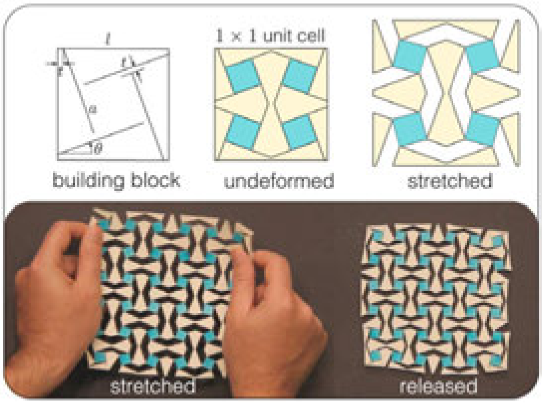

Figure 5.2: One of the bi-stable auxetic mechanisms presented by Rafsanjani and Pasini. [Source: Rafsanjani & Pasini, 2016]

A revised bi-stable mechanism is proposed in this PhD research, in which the linear hinges are not arranged vertically but in various tilted orientations in the thickened sheet that allows one of the stable states to be on a plane and the other on a double-curved surface. Figure 5.3 recapitulates the classification of some of the latest developments in reconfigurable mechanisms and positions this research among others.

Architected materials Part of this research is inspired by materials scientists who investigate the *architected materials*. The *architected materials* refer to the notion that the overall material properties are determined not solely by the constituent materials but also by the spatial configuration of voids and solids (Schaedler & Carter, 2016). The materials scientists' approach is to miniaturize the mechanical units into microscopic scales and refer to them as materials instead of mechanisms. However, in this research, the mechanical units stay at a macroscopic scale, and are therefore denoted as mechanisms.

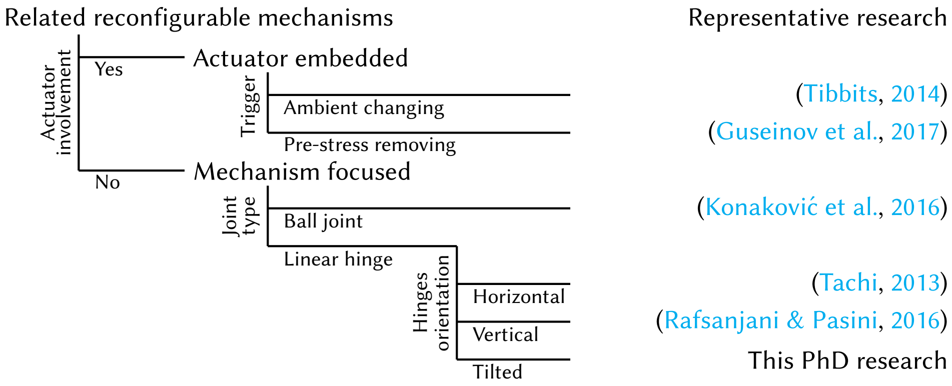

Figure 5.3: Classification of related reconfigurable mechanisms.

5.2. Bi-stability and geometry

The bi-stable mechanism is also termed snap-through buckling (Huang & Vahidi, 1971). The term refers to the features that when the mechanism is switched from one stable state to another, the mechanism suddenly snaps through the unstable gap. This section reviews the mechanical features of snap-through buckling and introduces the principles of designing a snap-through mechanism capable of spatial reconfiguration.

One of the simplest in-plane bi-stable units is illustrated in figure 5.4, which consists of two tilted bars (with cross-sectional area A, material elastic modulus E, length L, and initial tilting angle α) hinged to each other at one ends and pinned to the supports at the other ends. When an external force P is applied at the middle hinge, the two members are compressed and rotated and the middle hinge is displaced with distance δ. Once the external force exceeds the critical load, the reconfigurable unit will suddenly deviate from the critical state to the alternative state. After the external force is removed, the elasticity of the material brings the mechanisms back to the relaxed length, which leads the unit to the final state. A simple load-displacement relation can be established when the bars are compressed linearly (or without Euler buckling). The relation can be formulated as

$$P = 2EA\left(1-\frac{\delta}{L\sin\alpha}\right)\left[\frac{1}{\sqrt{\cot^2\alpha+(1-\delta/L\sin\alpha)^2}}-\sin\alpha\right].$$

At the same time, the total displacement of the middle hinge in the two stable states is

$$\delta_T = 2L\cdot\sin\alpha, \tag{5.1}$$

which suggests that the total displacement δ_T is proportional to the rotating arm L and the sine of the tilting angle α.

From an energy point of view, the stable states correspond to the local minimum points of the energy-displacement graph (figure 5.4). The energy disused here is excursively the internal strain energy in the bars as the hinges are assumed to dissipate and store no energy. As a result, the stable states are mirror images of each other. In this dissertation, all hinges are assumed to behave ideally, in order to design bi-stable mechanisms with geometrical principles.

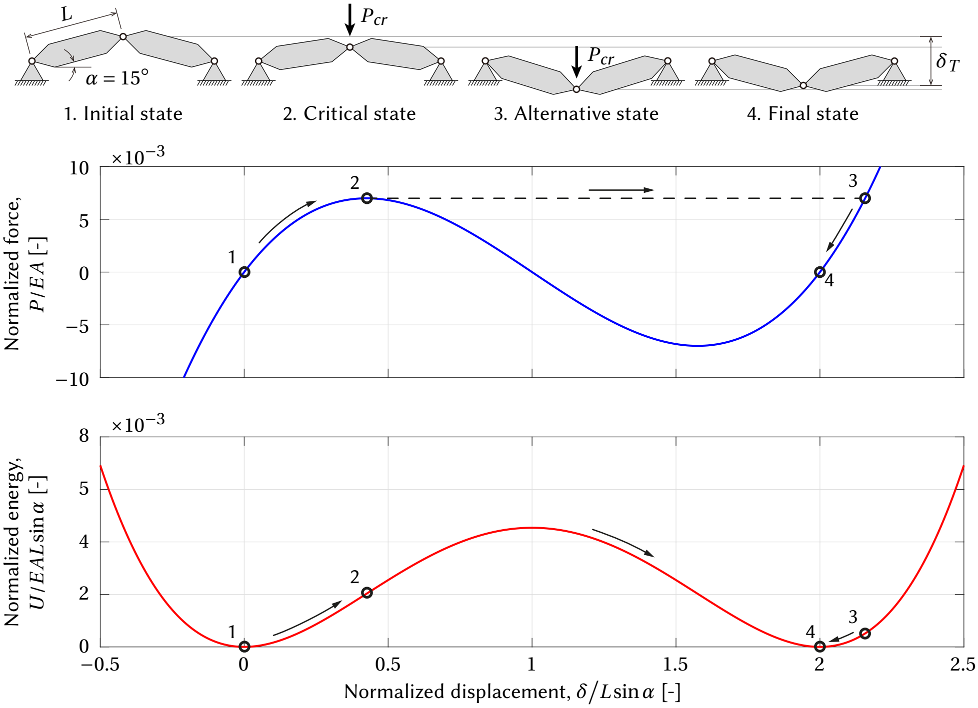

Figure 5.4: The reconfiguration process of the idealized bi-stable mechanism with two elements.

To make the mechanisms capable of conducting spatial reconfiguration, one can adjust the length of the rotating arms L while keeping the rotating angle α constant. Four preliminary examples are shown in figure 5.5, where snap-through units are installed between two panels. The bars have lengths L_a, L_b at the top layer and L_c, L_d at the bottom. When all lengths are the same, the panels have the translational motion between two stable states (figure 5.5a). If one of the bars is longer than the other, in-plane rotation is introduced in the reconfiguration (figure 5.5b). When the lengths at the top layer are different from the bottom, the two layers contract unevenly. Therefore, out-of-plane rotation, or bending, occurs (figure 5.5c). In-plane rotation and bending can co-exist as figure 5.5d shows.

To control the spatial transformation more precisely, one can first locate the *virtual axes of rotation*, and then point the hinges through it as illustrated in figure 5.6a–b. Three rigid blocks are interconnected with ideal hinges and the side hinges are coplanar. The other stable configuration would be the mirror image against the plane defined by the side hinges. The center block to which another panel would attach, located between the two configurations, rotates around the virtual axes of rotation (dash-dotted line). The virtual rotation axes must rest in the plane which bisects the dihedral angle of the two panels. To physically make a mechanism resemble the ideal case, the material must be thickened to approximate the stiff blocks while the compliant hinges must be notched to minimize the strain energy it might store (figure 5.6c–d).

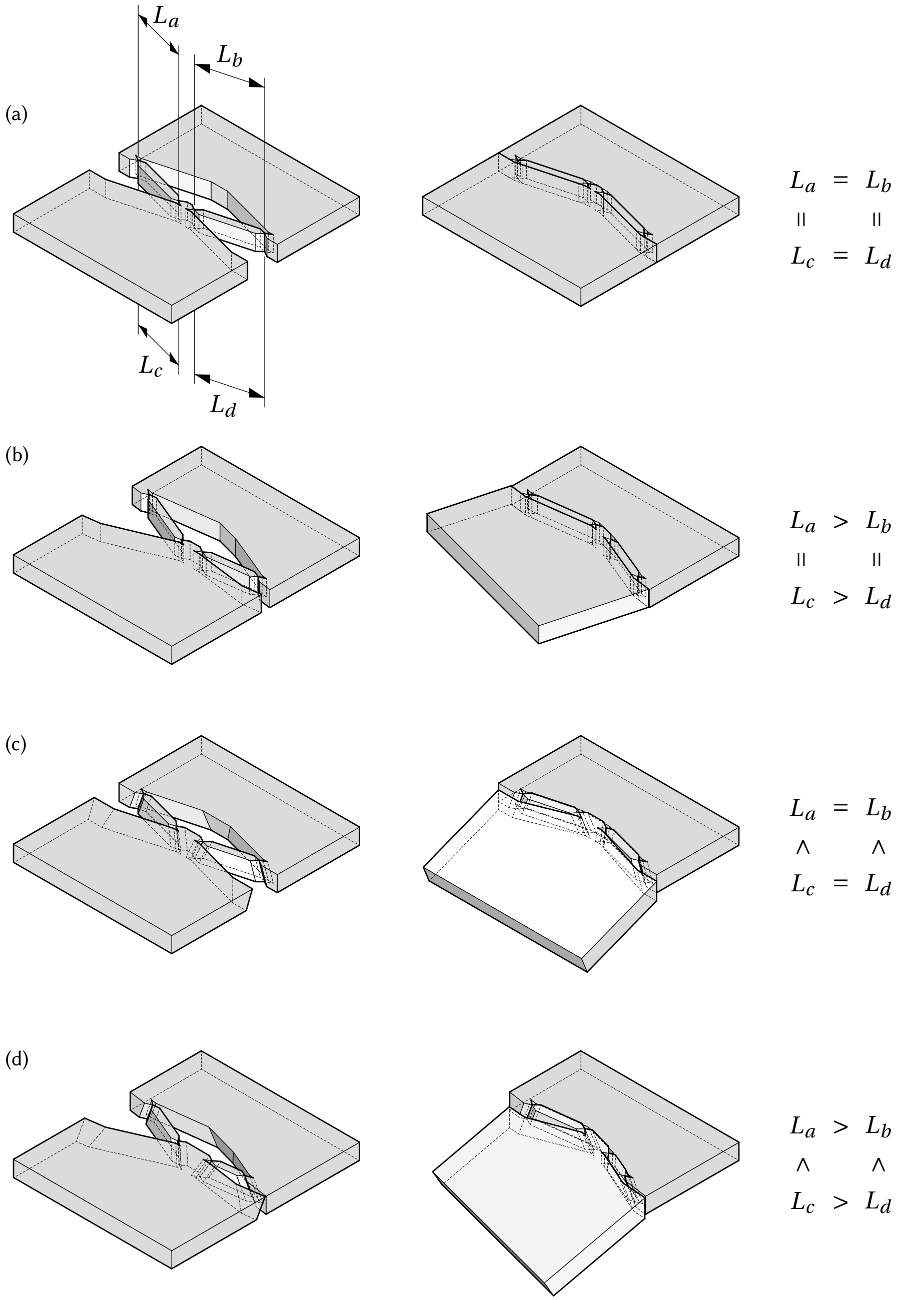

Figure 5.5: Joints with different degrees of freedom. Flattened states and curved states are shown in the left and middle column, respectively. The different arrangements of the rotating arm (right column) can result in different degrees of freedom in the reconfiguration.

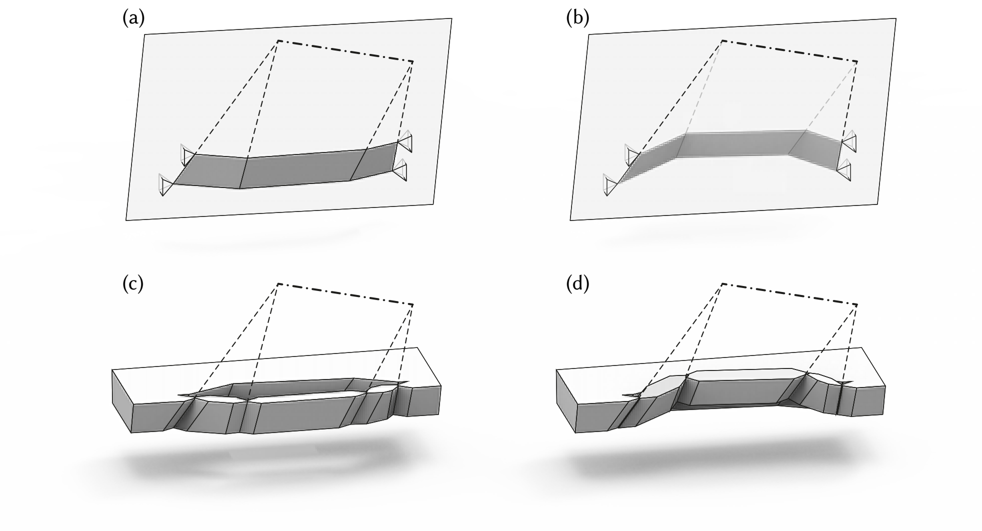

Figure 5.6: The proposed spatial bi-stable unit. (a-b) Two stable states of a conceptual bi-stable unit. They are mirror images of each other against the mirror defined by the four anchors. (c-d) Two stable states of the corresponding physically manufacturable bi-stable unit. The dashed lines are the extension of the hinges. They intersect at points defining the dash-dotted line which serves as the virtual rotation axis of the center piece.

This section has described the temporary elastic deformation during reconfiguration. After the bi-stable unit sets in the stable states, the deformation vanishes. Nevertheless, given that the hinges store negligible strain energy, the two stable states are simply mirror images of each other against the plane defined by the corner anchors. The next section introduces the method for applying this spatial reconfigurable unit to synclastic surfaces.

5.3. FLAT-TO-CURVED BI-STABLE AUXETIC MECHANISM

As demonstrated by Rafsanjani and Pasini (2016), the bi-stable auxetic mechanism can be achieved by arranging rotating quadrilaterals around concave octagons for in-plane reconfiguration. To create a flat-to-curve mechanism, this paper revises two approaches of the previous research. The homogeneously repeated pattern and the perpendicular cutting are replaced by a heterogeneously graded pattern and tilted cutting. This way, the thick sheet material can be reconfigured from flat to double-curved.

5.3.1. BASIC ELEMENTS IN THE PROPOSED MECHANISM

Figure 5.7 illustrates how to build up the proposed mechanism with the spatial bi-stable units. Basically, every spatial bi-stable unit defines a hexagonal void in the sheet material, and the void can be closed in the other configuration. Between the hexagonal voids, there are rotating connectors and restructured panels, which are discussed in more detail in section 5.3.3. Additionally, the rotating connectors were prisms in the case presented by Rafsanjani and Pasini (2016). Here, the connectors are rendered as pyramidal frustums. The different lengths at the top and the base cause different displacements as suggested by equation (5.1). In the case depicted in figure 5.7, the bottom surfaces with larger rotating arms introduce larger displacement during the reconfiguration and deliver the desired curvature without troubling bending stresses, which are commonly observed in other formative manufacturing processes, such as cold forging.

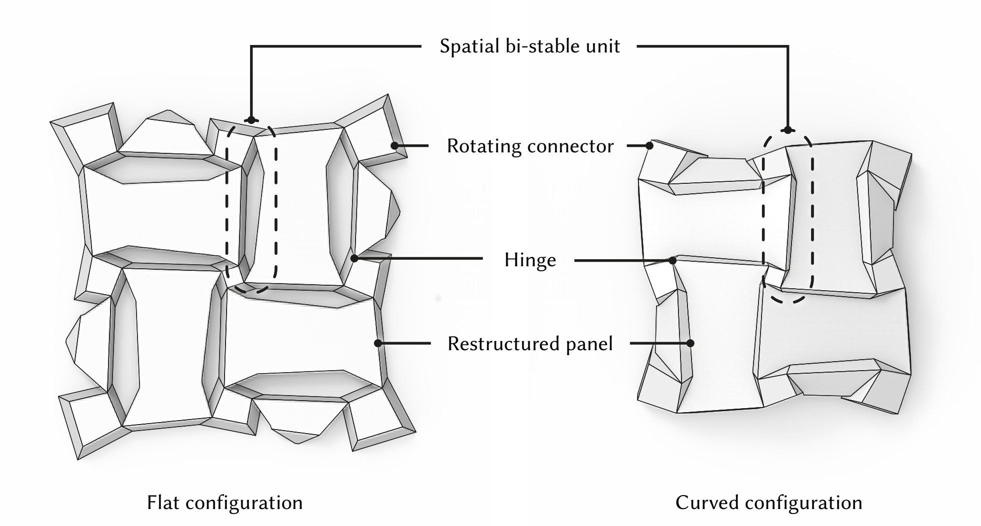

Figure 5.7: The reconfigurable material consists of two types of blocks: rotating connectors and restructured panels. The blocks are interconnected with hinges.

To arrange the hexagonal voids, the designers have to consider the voids as an interrelated system rather than multiple independent units. Given the fact that each hinge is affiliated to two hexagonal voids of two spatial bi-stable unit, the two units have to agree on the position and the orientation of the shared hinges. Furthermore, the angle of rotation of the hinge is also shared by the two voids. However, there is an outward method to design the interrelated voids, for an arbitrary conical synclastic mesh; in other words, no recursive iteration is required.

In the following sub-sections, a workflow is proposed to locate such solutions of the synclastic surfaces. The process starts with a conical mesh, which guarantees that the solution exists.

5.3.2. UNROLLING AN ARBITRARY SYNCLASTIC CONICAL MESH

Conical meshes belong to a type of principal meshes that have been discussed in section 4.2. In a conical mesh, each node has an axis intersected by all bisector planes of the dihedral angles between surrounding facets. As pointed out in section 5.2, firstly, axes of rotation shall lay in the planes bisecting the dihedral angles between panels. Secondly, the linear hinges shall point to the rotation axes. For a conical mesh, the linear hinges can conveniently point to points on the node axes, then the two geometry constraints will easily be satisfied.

Here, a method for unrolling a synclastic conical mesh $\mathcal{M}$ is proposed to systematically rotate all panels to a horizontal position. As shown in figures 5.1 and 5.7, a node in the mesh corresponds to a rotating connector in the mechanism, an edge corresponds to a spatial bi-stable unit, and a face corresponds to a restructured panel. This method assumes, in the curved configuration, that all linear hinges of a rotating connector pass through a point on the node axis of the conical mesh $\mathcal{M}$. The focal points of the rotating connectors define a mesh, denoted as *neutral surface* $\mathcal{N}$, on which the edges are the virtual rotation axes of the spatial bi-stable unit. The rotation axes do not expand or shrink in the reconfiguration, hence the name of the mesh—*neutral surface*.

The set of axes of rotation, or collectively the *neutral surface* $\mathcal{N}$, is rather rigid. One of its admissible deformations is vertically flipping inside out. Then, the corresponding faces on mesh $\mathcal{M}$ can spread out into isolated panels as depicted in figure 5.8.

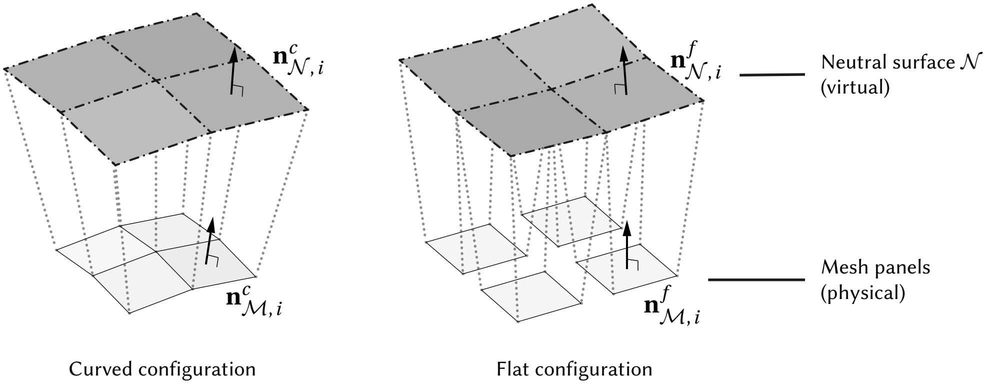

Figure 5.8: The axes (dash-dotted lines), around which the mesh panels rotate, form the mesh of the *neutral surface*. The inclination of the neutral surface is half that of the corresponding mesh panel. During the reconfiguration, the neutral surface is turned inside out, which suggests that the inclination angles are opposite to the original. The corresponding mesh panels will then follow the rotation of the neutral surface and turn to zero inclination in the end.

The targeted normal vector of the unrolled panels can be set as the unit vertical vector $\mathbf{e}_z$, which is expressed as $(0, 0, 1)$ in Cartesian coordinates or as $(1, 0, \varphi)$ in spherical coordinates, where the vector has a unit length, a zero polar angle, and an azimuth angle φ that can be any real number. Let $\mathbf{n}^c_{\mathcal{M},i}$ be a normal vector of a panel in the curved mesh (where the subscript $\mathcal{M}$ denotes the conical mesh and the superscript c denotes the curved mesh), which in spherical coordinates can be expressed as

$$\mathbf{n}^c_{\mathcal{M},i} = (1, \theta_i, \varphi_i).$$

The functional *neutral surface* shall have the corresponding normal vector

$$\mathbf{n}^c_{\mathcal{N},i} = (1, \frac{\theta_i}{2}, \varphi_i).$$

To unroll the conical mesh, the synclastic neutral surface shall be turned concave-side convex, or be turned inside out (or be mirrored against the horizontal plane). Thus the normal vector of the flipped neutral surface will be

$$\mathbf{n}^{f}_{\mathcal{N},i} = (1, -\frac{\theta_i}{2}, \varphi_i),$$

where the superscript f stands for both flipped and flattened. Before and after the unrolling, the facets of the neutral surface are turned $-\theta_i$ in total. Let every mesh panel of the curved conical mesh be turned as the corresponding facet on the neutral surface does, which means that the inclination of the mesh panel will also be turned $-\theta_i$. Then the normal vectors of the unrolled panels will be

$$\mathbf{n}^{f}_{\mathcal{M},i} = (1, 0, \varphi_i).$$

During the flipping of the neutral surface, the rotation angles make the normal vectors point upright as desired. The unrolling process is illustrated in figure 5.8. Unrolling a synclastic conical mesh via such a neutral surface allows for the legitimate hinges to be found in a straightforward manner. The application of the unrolling method is also demonstrated in figures 5.13 and 5.15.

The term neutral surface echoes the neutral plane in the conventional bending theory. In bending, all lengths on the neutral plane are preserved, which means that there is no compression or tension. While the material on either side of the neutral plane gets either compressed or tensioned. A similar feature can be observed in the reconfiguration process, as shown in figure 5.11. The material above or below the neutral surface reconfigures to the curved state by either stretching or contracting.

5.3.3. Connecting panels with rotating pyramidal frustum

The primary task of this section is to locate the legitimate hinges, which dictate how the blocks rotate around each other. Ideally, the hinges should bring all scattered nodes in the flat configuration back to the same position in the curved configuration. Figure 5.9 shows a set of functional hinges (dashed lines) that merges the panels and closes the gaps.

There are only three independent degrees of freedom (DoFs) available for a node when designing the hinges, considering the hinges and the rotation axes have to correspond with each other. In general, there are five degrees of freedom (DoFs) in a rotation in 3D space. Two of them are the position of the axis of rotation, two of them are the orientation of the axis, and the other one is the rotation angle. For an unrolled node (as shown in figure 5.9), the axes of rotation should pass through the node on the neutral plane which fixes two of the DoFs for every panel. If one of the panels is assigned with 3 values to fix the three undetermined DoFs, all other panels have to rotate dependently of the first panels. Therefore, there are only three independent DoFs; two of them can be regarded as the orientation of the merged axis (black dotted line in figure 5.9), and the other one is the magnitude of the rotation angle.

Once the hinges are determined, the intersection points of the hinges and the mesh panels define a polygon. For a node with four edges, the polygon is quadrilateral. When the sheet material has a certain thickness, the quadrilateral becomes a frustum of a quadrilateral pyramid. The gaps between the mesh panels have to be restructured accordingly as shown in figure 5.9.

As discussed, for each node, there are three independent DoFs to define the rotating connectors. But the nodes on the same edge of the mesh still have to agree on the inclination

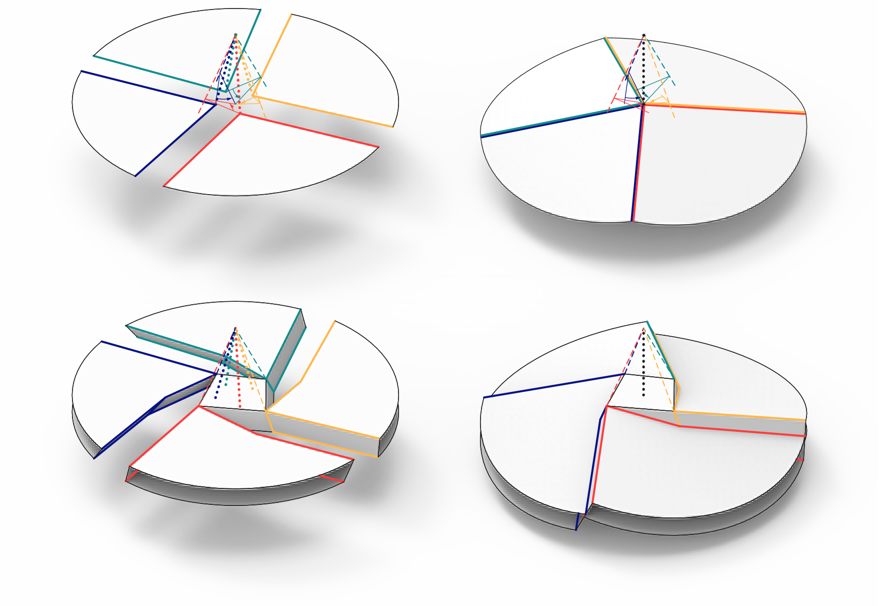

Figure 5.9: Close up of panels rotated around the hinges (dashed lines). Each panel has its hinge (in the same color), while all panels merge at the same axis (the center black dotted line).

of the gap in the flat configuration. In other words, for a mesh with n internal nodes and m internal edges, there are $3n - m$ DoFs to be determined for all of the rotating connectors. One way to omit the iteration is to determine the rotating connectors node by node. A node that is determined later has to align itself to the previously determined nodes. Therefore, only the first node has three DoFs. Other nodes may have two or only one DoF, depending on how the determination propagates. Figure 5.10 shows an example of how the process propagates across all nodes of a free-form mesh.

So far, this section has presented the methods to unroll a synclastic conical mesh, locate the legitimate hinges, and restructure the mesh panels. Figure 5.11 visually recapitulates the relationship between the neutral surface and the legitimate hinges. It is noteworthy that if hinges are extended to the other side of the neutral surface, a curved-by-stretching solution can also be identified.

5.4. Pilots prototypes

Following the discussion on mechanical and geometrical features of the bi-stable joint, unrolling of conical meshes, and the rotating connectors, this section describes the validation of the proposed methods through physical prototyping undertaken by the author during the course of this PhD research. The prototypes are produced using fused filament 3D printing with polylactic acid (PLA) and 4-axis water-jet cutting on sheets of polypropylene (PP). The hinge between connectors and panels are fabricated as compliant hinges. Although the bi-stable mechanism does not have to be manufactured with compliant hinges, it is a convenient methods to embed the hinges into the mechanisms.

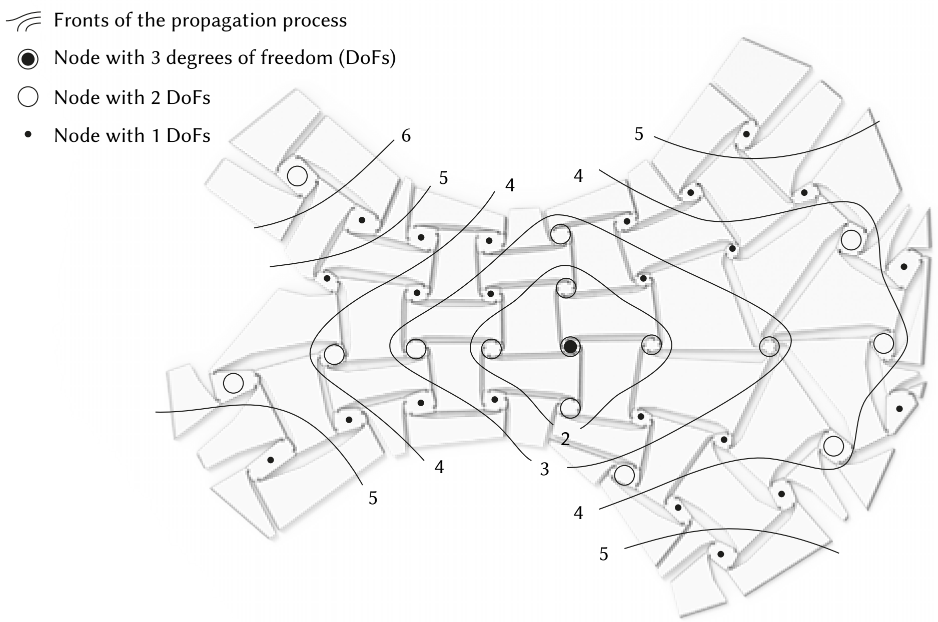

Figure 5.10: The propagation map of the free-form conical mesh

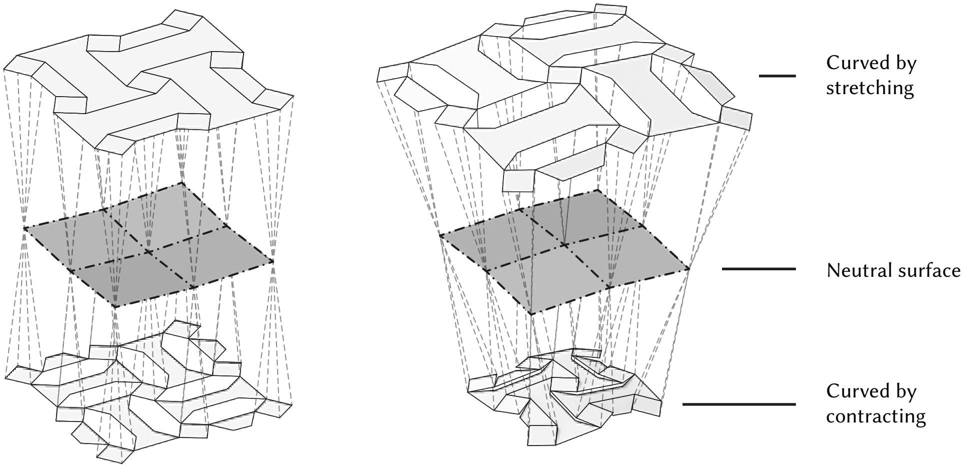

Flat configuration

Curved configuration

Figure 5.11: The focal points of the hinges are located on the neutral surface. The neutral surface is mirrored during the reconfiguration, which means that all lengths on the neutral surface remain constant before and after the reconfiguration. On the other hand, above and below the neutral surface lie the expanding zone and contracting zone, respectively.

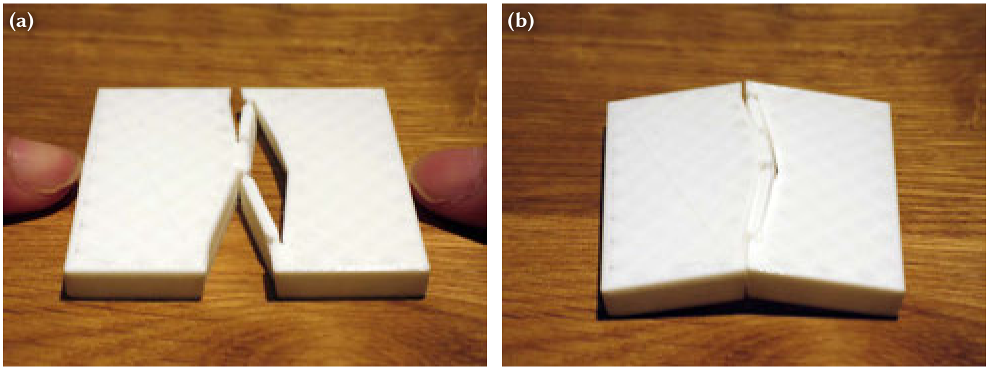

Figure 5.12: Test of a bi-stable joint. (a) Pushing the panels from the sides. (b) The resulting curved configuration. A video of the actuation is available on https://vimeo.com/503767095.

3D printed polylactic acid (PLA). One of the first successful prototypes of the spatial bi-stable unit is shown in figure 5.12, which consists of 5 mm thick panels and 0.5 mm wide compliant hinges. Indeed, PLA is rather stiff and brittle, which is not ideal for compliant hinges, therefore this prototype cannot survive more than 10 cycles of reconfiguration. However, it is the most accessible material for hobbyist 3D printers. Meanwhile, in this initial exploration of new mechanisms, the main purposes of prototyping are validating and demonstrating the geometric design. This prototype shows a fruitful result.

Instead of a simple test on two panels with a curved edge, figures 5.13 and 5.14 show a free-form design. A form-found smooth surface is first obtained via the algorithm presented in chapter 3, then the smooth surface is approximated by a conical mesh via the process stated in chapter 4. After the conical mesh is unrolled by the method of the neutral surface in section 5.3.2, the rotating connector is generated by feeding the geometry into a computer script, which is available at https://github.com/ChiangYuChou/SpatialAuxetic. Then, the basic geometry is subjected to some detailed modification for physical production. The 3D printed result shows even a mechanism made out of brittle PLA can be reconfigured into the double-curved surface (figure 5.14).

Water-jet cut polypropylene (PP). Material of PP performs better than PLA, or more precisely, PP is more flexible and has better fatigue resistance. Assisted and sponsored by a water-jet cutting fabricator, OH Precision Corporation, two prototypes are produced via a 4-axis CNC water-jet.

The first one is a synclastic discretized spherical surface, which has a discretized parabolic surface as neutral surface (figure 5.15). Then, using the proposed workflow, the unrolled mesh is restructured as an inter-connected mechanism and finally translated into the tool path for the CNC water-jet (figure 5.16). The result is shown in figure 5.17.

Anticlastic saddle surface, which also consists of hexagonal voids as bi-stable units, is also possible to be fabricated with the reconfigurable technique as shown in figure 5.18. However, in this case, the hinges of a rotating connector do not focus on a single point but form a tetrahedron. To date, there is no systematic method to discretize and unroll an anticlastic surface; this could be an interesting topic for future exploration.

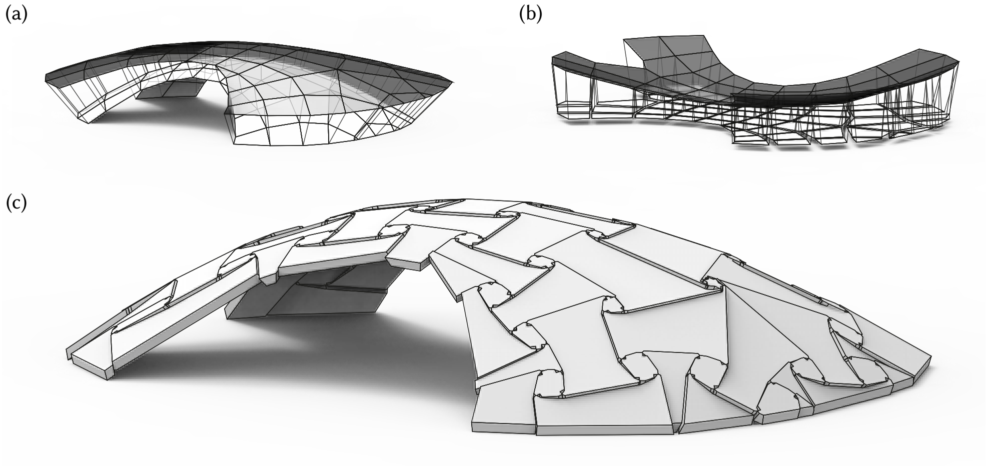

Figure 5.13: Geometric design of a free-form surface. (a–b) Unrolling the mesh panels with the neutral surface (gray transparent mesh). (c) Perspective view of the resulting mechanism. In the conical mesh, there is a six-edge node which is the umbilical point of the curved surface. The six-edge node becomes the hexagonal rotating connector in the mechanism.

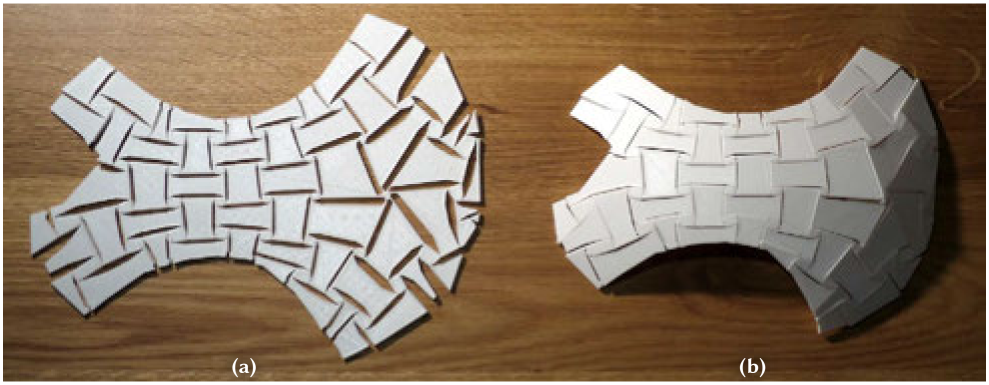

Figure 5.14: The 3D printed prototype of a free-from shell. (a) Flat configuration. (b) Curved configuration.

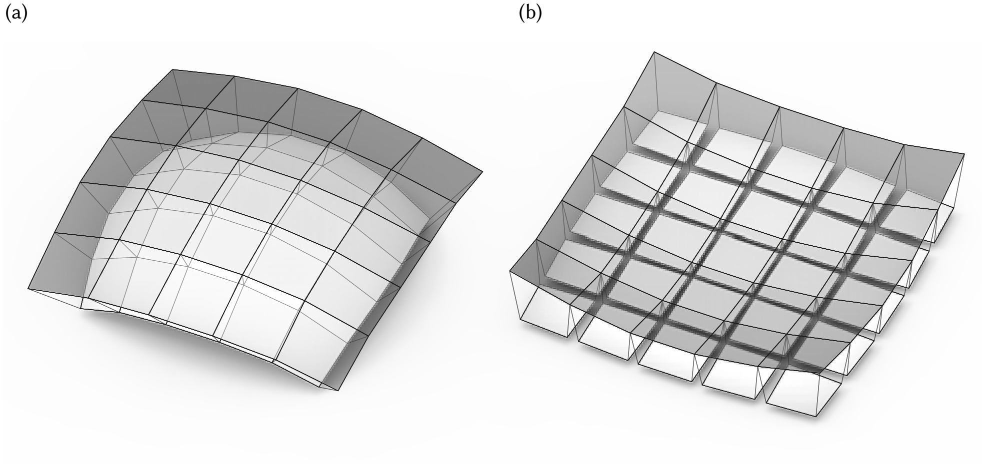

Figure 5.15: Geometry design of a spherical surface and the neutral surface (gray transparent mesh). (a) Curved configuration. (b) Flat configuration.

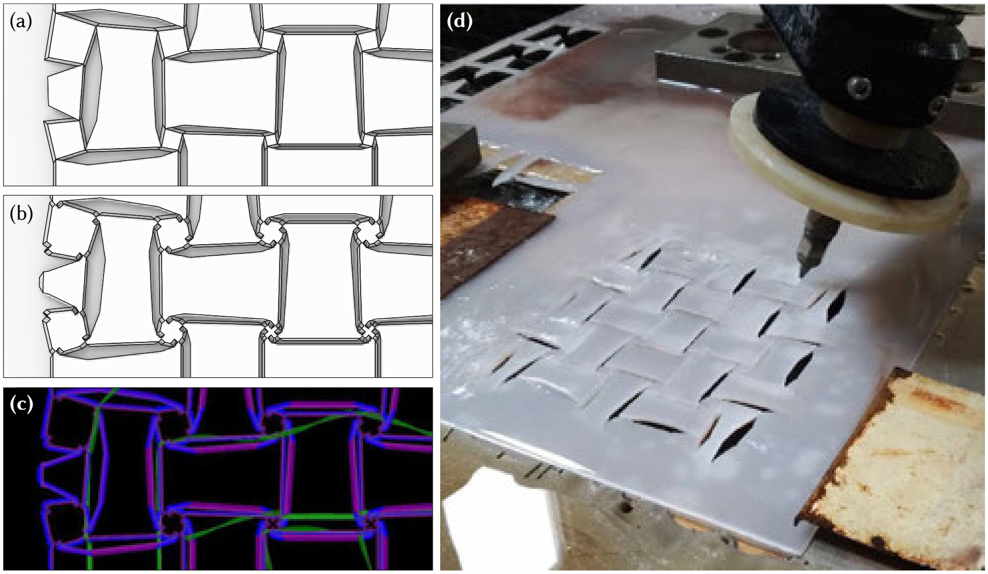

Figure 5.16: The production process and the result of a 25-panel spherical surface. (a) Close-up of the geometrical solution. (b) The producible solution. (c) The tool path for waterjet cutting. (d) Production with a 5-axis CNC waterjet machine. A timelapse video is available on https://vimeo.com/317286896.

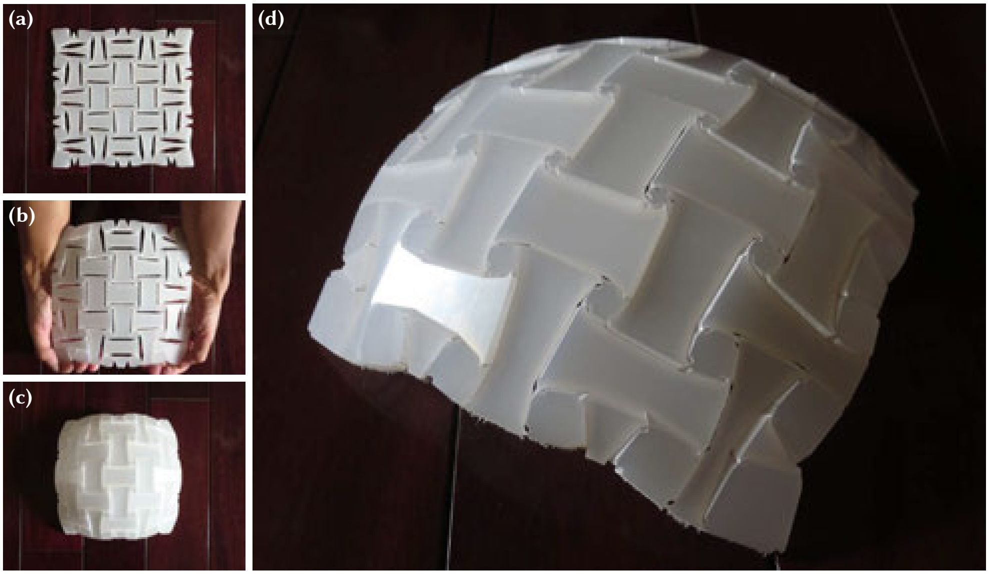

Figure 5.17: The result of water-jet cut flat-to-synclastic mechanism. (a) Flat configuration. (b) Actuation. (C) Top view of the curved configuration. (d) Perspective view. A video of the actuation is available on https://vimeo.com/317286292

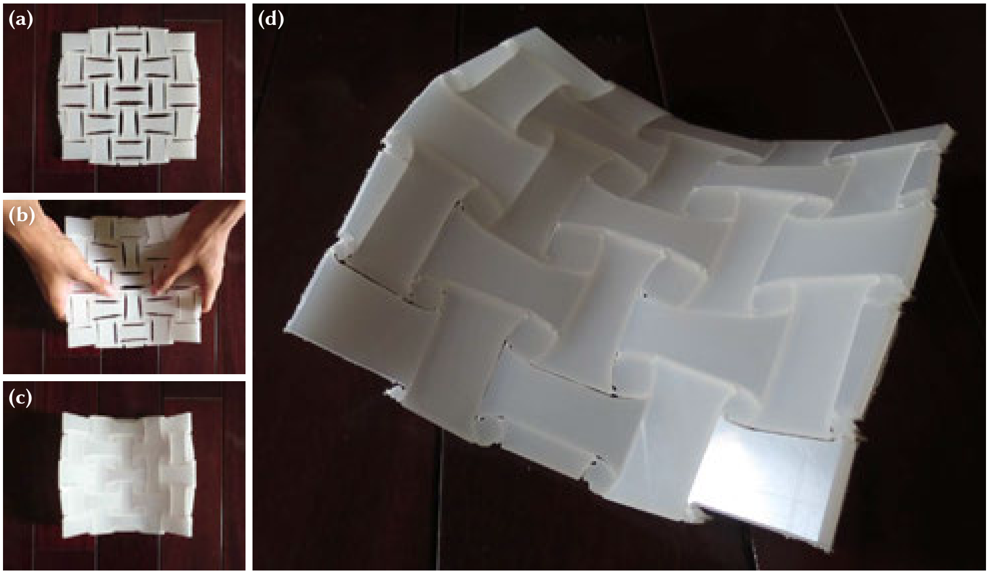

Figure 5.18: The result of water-jet cut flat-to-anticlastic mechanism. (a) Flat configuration. (b) Actuation. (C) Top view of the curved configuration. (d) Perspective view. A video of the actuation is available on https://vimeo.com/454308849

Iterative processes between design and fabrication. There were trials and errors in the background that facilitated the resulting prototypes mentioned above. The designs underwent two processes before they became physical products. First, computer-aided-manufacturing (CAM) software converts the geometries of the designs into "tool paths" for the CNC machines. Then the CNC machines physically fabricate the prototypes by executing and tracing the tool paths. Either one of them needs some trials to identify and overcome potential obstacles.

The main challenging is to produce compliant hinges that store negligible strain energy and can undergo reconfiguration. In other words, the hinges need to be as thin as possible, on one hand, yet strong enough to withstand the critical load, on the other.

For 3D printing, the design geometry can be easily converted into a mesh then sent to a slicer (CAM software for 3D printing) for generating a printing path. It took a few trials to figure out the thinnest design of a compliant hinge is around 0.5 mm wide for a 3D printer with a nozzle of 0.4 mm diameter. By default, the slicer ignores any part that is narrower than the nozzle's diameter. However, due to errors introduced by remeshing, the width larger than 0.5 mm is reliable that the slicer will not miss. The fabrication side had only some minor issues of tuning parameters (e.g., printing temperature) of the 3D printers.

For the water-jet cutting, both the generation of tool paths and the fabrication of prototypes encountered notable issues. There was no program sophisticated enough to convert the complex designs into tool paths with tilting information. The only available programs can generate either simple tiling tool paths or complex 2D tool paths without tilting. Luckily, the tool paths for the CNC water-jet are G-code-like ASCII files. The first part of the solution is to learn the syntax of tilting tool paths from the ASCII files generated by the first program. The second part is to write a piece of computer code, *MATLAB* (2018) in this case, that can fill tilting angles into the 2D tool paths generated by the second software. Then, the second program can work alongside the MATLAB code to generate complex and tilting tool paths.

Regarding physical production, the first trial had compliant hinges that were too narrow so that the resulting prototype fell apart. After calibrating the kerf width of the water-jet and a few more revisions of the design, the resulting products became robust enough to withstand multiple cycles of reconfiguration.

Manual actuation. It is a particular experience to actuate one of these prototypes by hands. The person can feel the mechanism resists the load initially but suddenly *gives up* and contracts on its own. The haptic experience may not be easy to convey in words. However, the actuation processes are easy to record in videos. Accessible through the hyperlinks in the captions of figures 5.12, 5.17, and 5.18, the videos capture the snap-through phenomena of the mechanisms. The audio tracks contain the snap sounds, which were caused by the sudden releases of the strain energy into vibrations of the mechanism and the nearby air (and microphone).

These pilot prototypes prove the configurable mechanisms are feasible at the scale of 10^2 mm, in plastics, and manual actuation. The next chapter will investigate other scales, materials, and actuation schemes.

5.5. SUMMARY AND DISCUSSION

This chapter has reviewed some emerging reconfiguration mechanisms. Some observations are made:

- some active mechanisms are built with layered materials that expand or contract differently which induces flat-to-curved transformation; and
- some passive mechanisms are built by arranging ball joints or linear hinges, but the existing arrangements provide either no compression stability or no flat-to-doubly-curved capability.

This chapter has also presented a method to translate free-form synclastic conical meshes into mechanisms, in which a node is translated into a rotating connector, an edge into a hexagonal void, and a face into a concave panel. The ordinal method has components including:

- a spatial bi-stable unit, which can connect two thick panels rotating about a remote axis;
- unrolling of a synclastic conical mesh with the method of the neutral surface, which automatically introduces gaps with appropriate widths between the spread-out panels;
- locating the linear hinges and rotating connectors, which automatically distribute different displacements at the top and bottom surfaces;
- converting the geometric solutions into producible designs; and
- validating the designs by producing 3D-printed and water-jet-cut prototypes.

To investigate the capacity of the proposed mechanisms, some further explorations need to be continued. So far, neither the applicability on larger scales nor the dynamic behavior during the reconfiguration has been explored. Additionally, the proposed unrolling method of the neutral surface is not compatible with anticlastic surfaces, even though the spatial bi-stable unit can still work for anticlastic surfaces. After these topics are addressed, broader applications may be achieved.

6

IMPLEMENTATION

Ideas are useless unless used.
The proof of their value is their implementation.
Until then they are in limbo.

Theodore Levitt [1]

Innovation is always risky
but without risk we don't advance.

David Blockley [2]

---

[1] Levitt, 2002
[2] Blockley, 2012

CHAPTERS 2–5 in this dissertation have yielded results independently, including analytical solutions of membrane shells in section 2.5; numerical shells found with radial basis functions in sections 3.4 and 3.6; relief-like discretized stress function from section 4.4.3; and water-jet-cut polypropylene reconfigurable mechanisms in section 5.4. Conversely, this chapter presents the prototypes that employ methods across multiple chapters from form-finding to the reconfigurable mechanism.

This chapter implements the theories to build two sets of prototypes. The first set includes triangular shells spanning 0.8 m and 4 m, which need to be actuated sequentially. The second set of prototypes use *self-Airy membranes* as the target surfaces which allows actuation by contracting their bottom hoops.

OUTLINE

Section 6.1 reports the 0.8m-span triangular shell which is built with 3D-printed components. Section 6.2 repeats a similar design at a 4m-span scale with laser-cut pieces. Section 6.3 utilizes *self-Airy membranes* as the target surfaces to design the flat-to-curve mechanisms, which can be actuated with their bottom hoops. Section 6.4 discusses the results from these prototypes.

6.1. 3D-PRINTED TRIANGULAR RECONFIGURABLE SHELL

This section not only integrates form-finding but also explores different production methods from the pilot prototypes in chapter 5. First, all reconfigurable mechanisms produced in the previous chapter are either printed or cut in one piece and the components are connected by compliant hinges. This section extends the investigation to a structure that is larger than its production machines. To achieve that, the structures are produced in individual components, which are later connected with pins instead of compliant hinges. Secondly, the scale of the finished prototype span a 0.8 m distance, which is also larger than the previous mechanisms (ca. 20 cm). Thirdly, instead of a quadrilateral mesh and quadrilateral rotating connectors, this section employs a hexagonal mesh, which has valence-3 nodes that automatically meet the criteria for being a conical mesh. Critical steps of design and fabrication include designing the overall form, discretization into a hexagonal mesh, converting the mesh into a flat mechanism, designing connection details, and finally printing and assembling the components. The following paragraphs explain the process as well as the salient design decisions.

Overall form. The design process starts at finding the overall form, which has a triangular footprint, three free edges, and three supports at the vertices. Both the shape and its variable thickness are determined by the algorithm of radial basis functions in chapter 3. Using the algorithm, a series of shape functions is derived. Each shape function migrates from a common provisional shape (section 3.4) to another shape that accommodates the stresses of a load case. The load cases have a common vertical component and variable horizontal body forces in various directions. Then the shape functions collectively determine the upper and lower envelopes which give the variable thickness (figure 6.1).

Discretizing and converting into the flat mechanism. To design the flat mechanism introduced in chapter 5, the lower envelope is discretized into a hexagonal mesh, in which

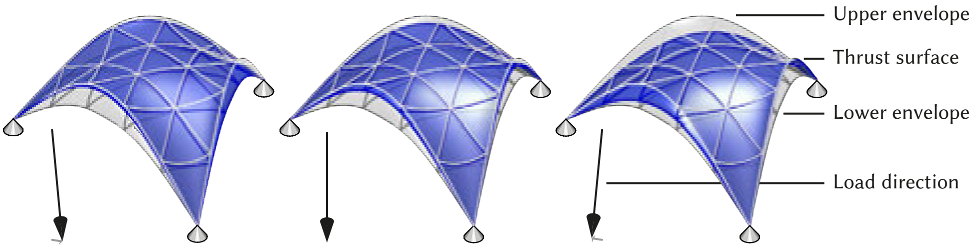

Figure 6.1: The general form is form-found with the radial basis function algorithm, and the thickness is determined by envelopes of shape functions, or thrust surfaces, under tilted loads.

all vertices of the mesh have valence 3 (i.e., all vertices connecting to 3 edges). Since faces that meet in a 3-valence vertex are tangent to a right circular cone, the hexagonal mesh also meet the criteria of a conical mesh. Then, the lower envelope can be unrolled via the neutral surface (section 5.3.2). Subsequently, rotating connectors are generated with a computer script, which has also been uploaded to an open-access repository (Chiang, 2020). Figure 6.2 shows the intermediate results of this stage. For simplicity, the upturned edges are kept in the flat configuration. Meanwhile, the thickness of the shell follows the envelopes that were form-found in the previous step. The shell is thinner at the center and supports, and thicker at the mid-points of the edges.

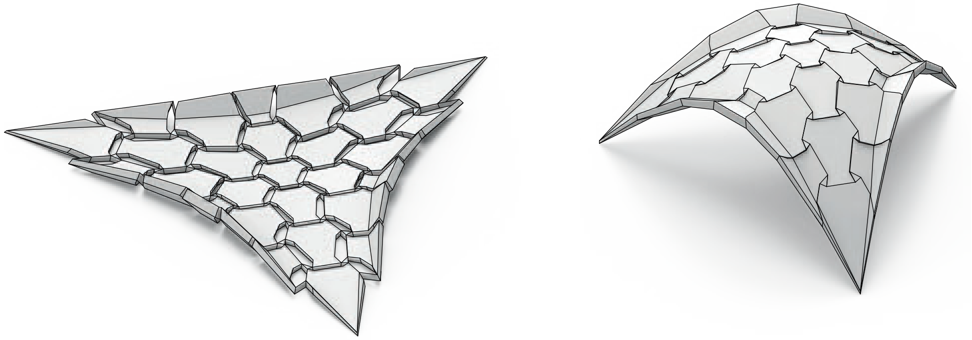
Flat configuration

Curved configuration

Figure 6.2: The shell is subsequently divided into a hexagonal mesh and converted to the flat-to-curved mechanism.

Connections and details. From this step onwards, the design process includes more production consideration. Occasionally, the design decision inclines to visual simplicity when there are multiple producible alternatives.

The most crucial details are the pin joints between panels and rotating connectors. Dressmaking pins (ca. 0.8mm diameter) are used, and the knuckles (1mm thick) are 3D printed along with the linked components. Additionally, the panels are hollowed out for weight purposes. The voids also make the variable thickness more visible. The remain-

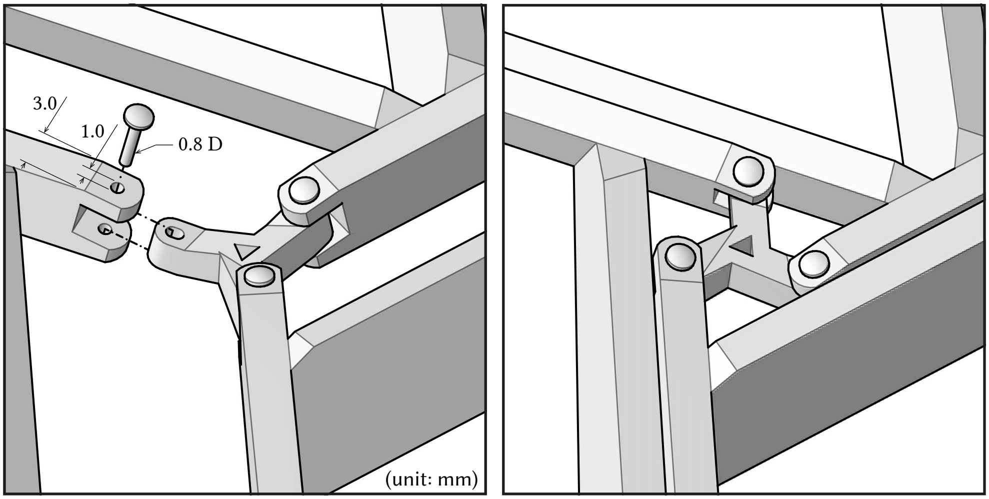

(a) (b)

Figure 6.3: Design details. (a) Dimensions of the hinge. (b) Reciprocal pattern in a triangular connector.

ing walls have a thickness 3 mm for sufficient clearance between pins and the surrounding knuckles (figure 6.3a).

The reconfigurable mechanism requires each edge to have a translational eccentricity, such that each polygon has sides offset alternatively outward or inward. The sides are connected by some short segments bordering the rotating connectors. When the short segments are omitted, the pattern is coincidentally identical to a *reciprocal frame* or *nexorades* from the translation method (Mesnil, Douthe, Baverel, & Gobin, 2018), in which every node has a uniform valence of 2. The design adopts the pattern of the *reciprocal frame* and extends it to the triangular nodes (figure 6.3b).

Printing, assembling, and reconfigurating. The dimensions of the hollowed hexagonal panels range from 178 × 89 × 19 mm to 73 × 63 × 8 mm, which fit well in the employed 3D printer (Ultimaker 2+, build volume: 223 × 220 × 205 mm). The panels and connectors are pinned in a flat configuration, which later can be transformed into the prescribed curved configuration. The completed structure is supported on the three vertices of the triangle. Between the supports, the free edges span a 0.8-meter distance. The scale of the overall prototype is rather modest, yet it is still larger than the build plate of the employed 3D printer. The reconfiguration runs with the click-sound when the mechanism snaps through the critical state (see video on https://vimeo.com/523523759). Figure 6.4 displays the resulting prototype.

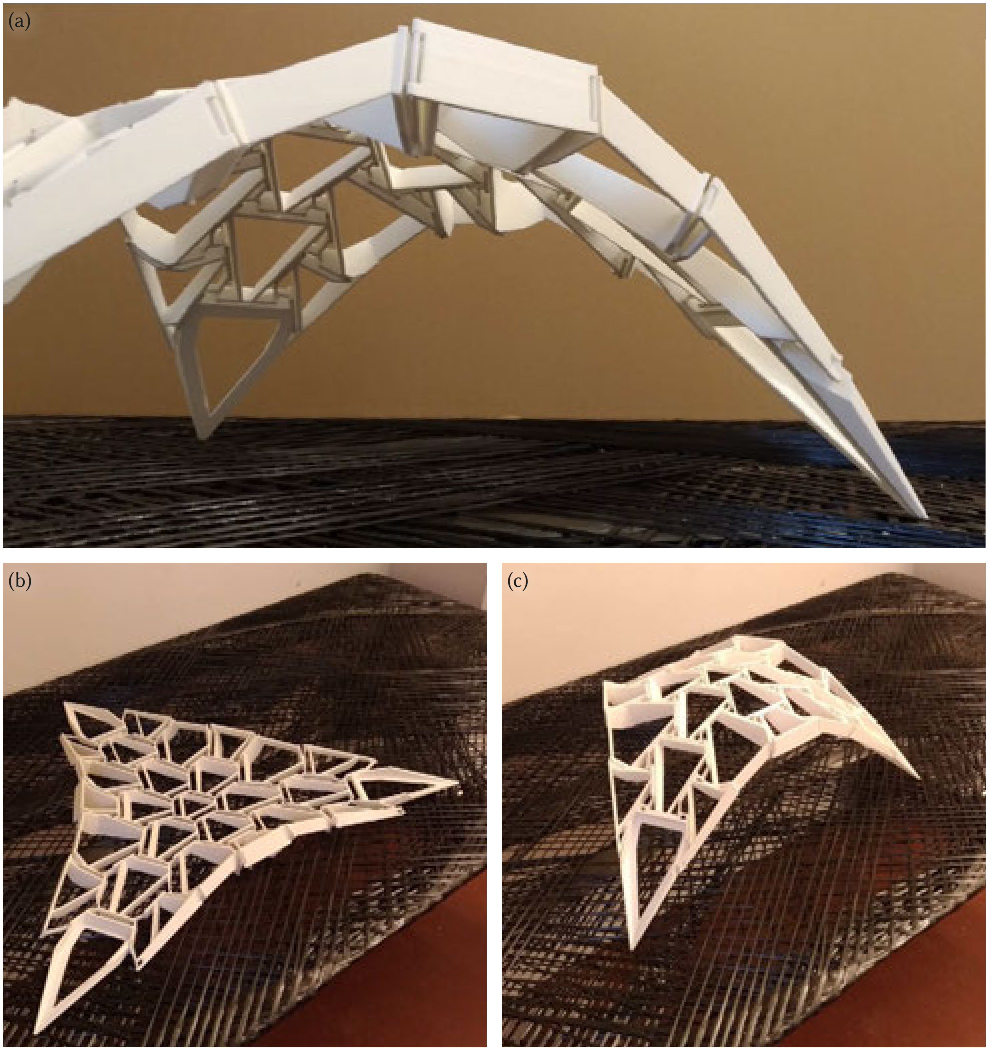

Figure 6.4: Assembled prototype. (a) Close-up view. (b-c) Before and after reconfiguration. A video is available on https://vimeo.com/523523759.

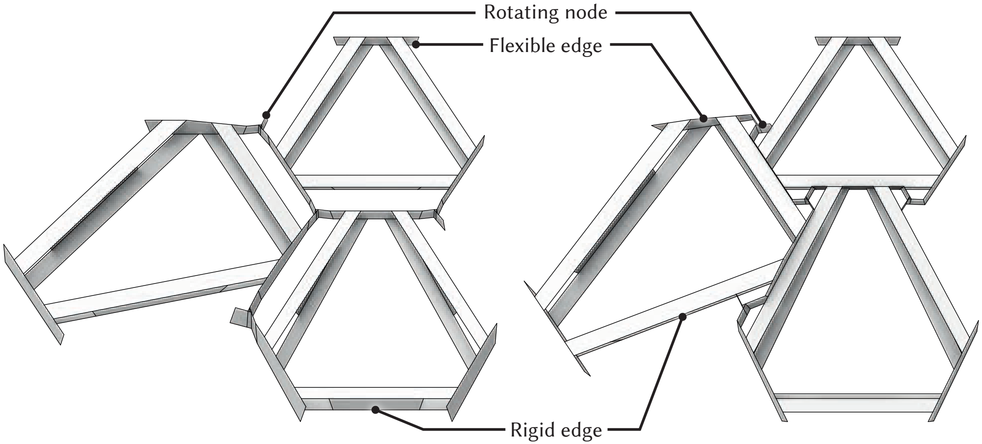

(a) Flat configuration (b) Curved configuration

Figure 6.5: Designs of the edges.

6.2. LASER-CUT TRIANGULAR RECONFIGURABLE SHELL

This section repeats the same basic design from the previous section, but in a different material and on a larger scale. Explicitly, plywood is used to build a 4m-span structure, which has a clear height of 1.6 m at the center and has a thickness from 120 mm (mid-points of free edges) to 40 mm (center and corners). After fabrication of the components, a crowd of volunteers assembled the components on the ground and lifted the mechanism into the double-curved configuration. The reconfiguration process was repeated with an overhead crane again, which shows the sequential process more clearly.

Design. The overall form and the hexagonal discretization are the same as the previous prototype. Some modifications on connections and details are necessary due to the changes in material, scale, and fabrication machinery. Since the mechanism requires temporary deformation for snapping-through and long-term rigidity for structural integrity, the hexagonal units have two different designs for the edges. Each outwardly offset edge, which is hinged with connectors, is simply materialized as one piece of plywood. Each inwardly offset edge, which will work in bending, is built with three plywood pieces forming a c-shaped profile (figure 6.5). Meanwhile, sheets of plastic, working as compliant ligaments, are placed between plywood units and nodes (figure 6.6).

Fabrication, assembly, and reconfiguration. The plywood planks and the plastic sheets are fabricated by 2D CNC machines: a laser cutter, and an oscillating knife. Embedded mortise and tenon guide the assembly and gluing process. On-site, the components were assembled on the ground by untrained volunteers in less than 2 hours. It was initially attempted to reconfigure the structure via ratchet tie-down straps (orange straps in figure 6.8) but this caused some mortise-tenon joints to be dislocated. Instead, the structure was raised by lifting the mechanism and sequentially squeezing it. Using this approach, it took merely 10 minutes to reconfigure the structure and peg it down to the ground (figure 6.10a-f). The

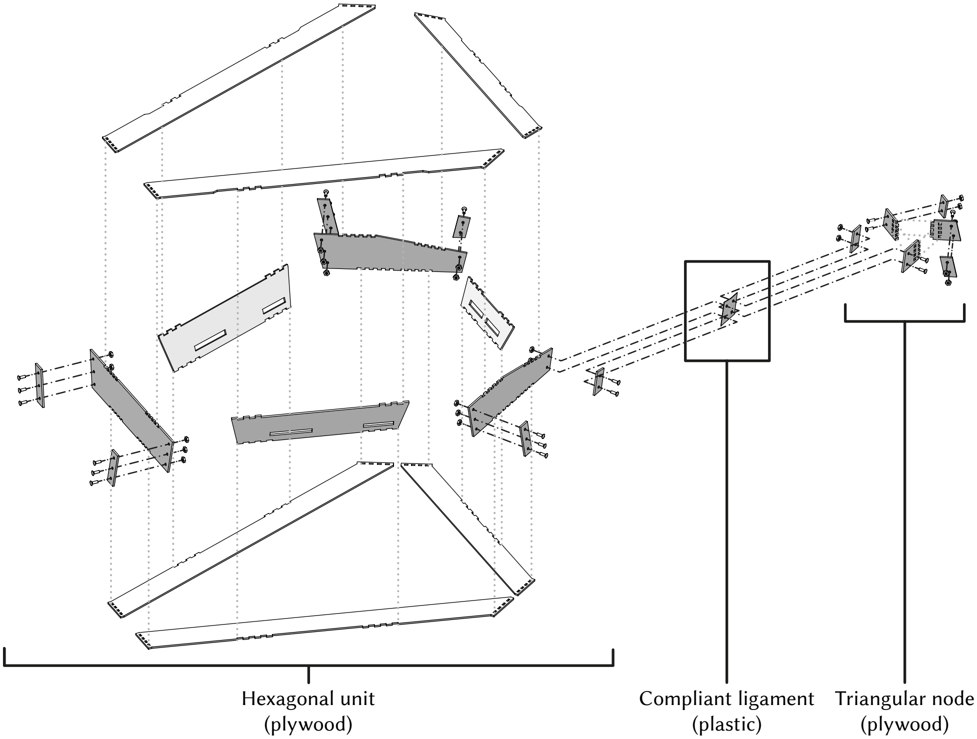

Figure 6.6: The units are built with laser-cut plywood. Plastic sheets work as compliant hinges connecting hexagonal units and the triangular nodes.

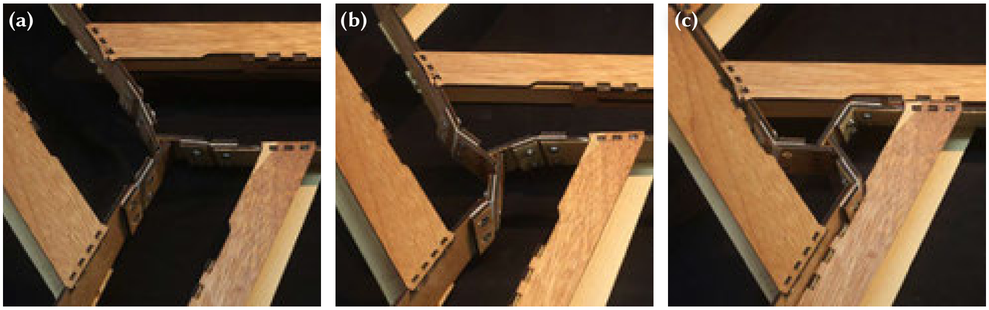

Figure 6.7: The reconfiguration process. (a) Flat configuration. (b) The triangular node rotates and the plywood deforms significantly before the mechanism rests in the targeted configuration. (c) Curved configuration.

reconfiguration is also reversible as shown in figure 6.10g-h. A time-lapse video of the first reconfiguration test is available on https://vimeo.com/523592087. The second reconfiguration test was aided by an overhead crane which reconfigured the mechanism in the same sequential manner as the 3D printed 0.4m-span prototype. The video of the second test is available on https://vimeo.com/523593297.

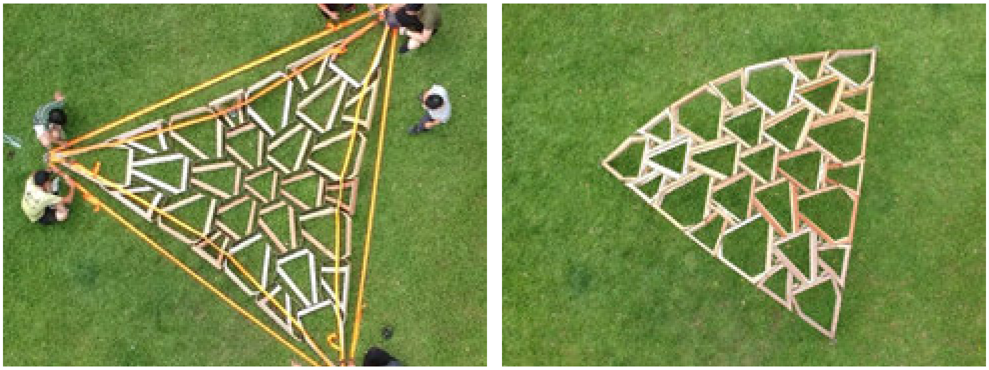

Figure 6.8: Top views of the mechanism in its flattened (left) and curved (right) configuration

Figure 6.9: Photo of the finished shell

Figure 6.10: The reconfiguration processes. Time-lapse videos can be accessed via https://vimeo.com/523592087.

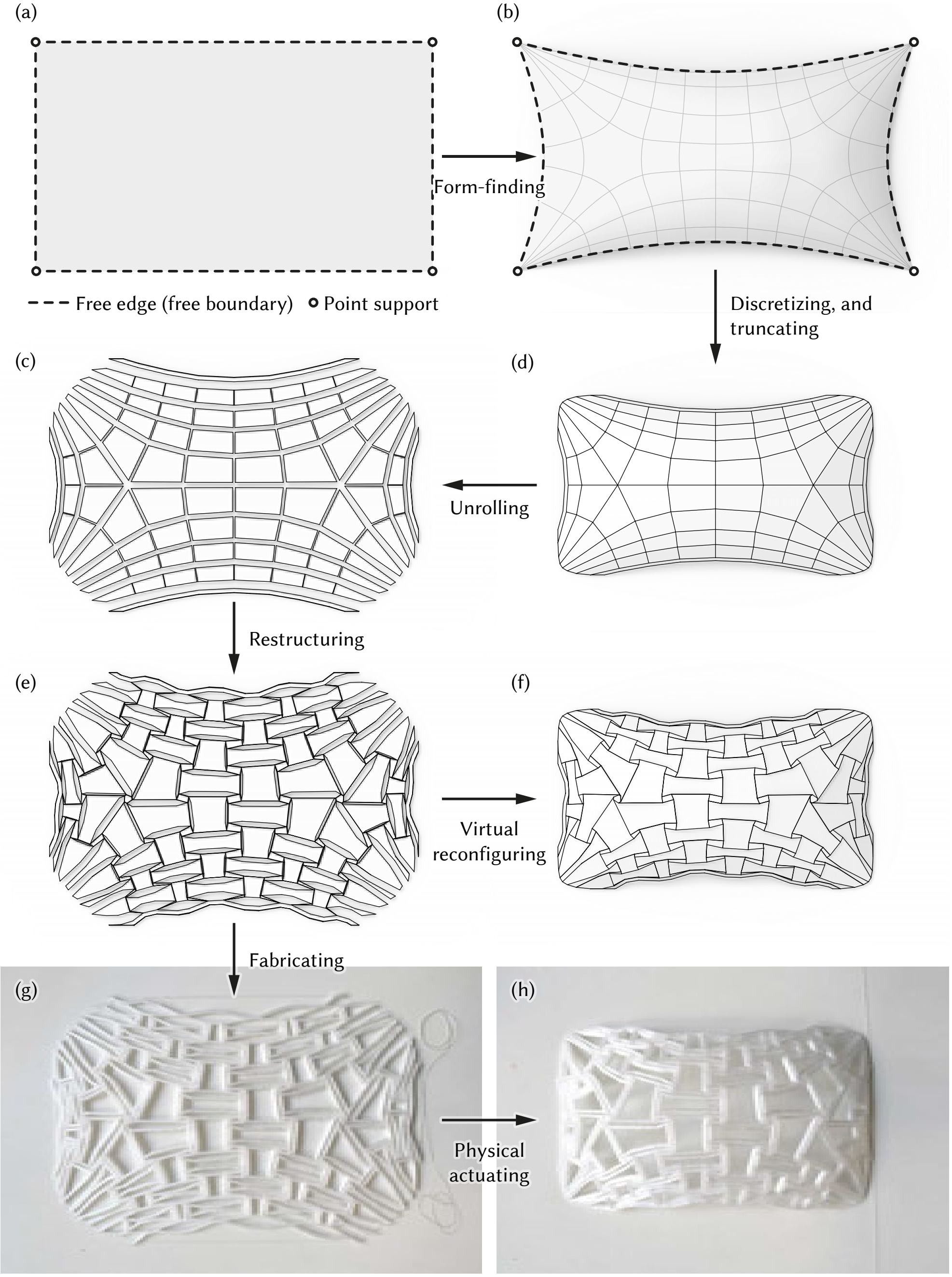

Figure 6.11: The workflow of designing the hoop-actuated mechanism: from providing boundary conditions (a) to 3D printing and actuation (h).

6.3. HOOP-ACTUATED MECHANISM

The inspiration for seeking hoop actuation came from the unsuccessful attempt of using ratchet tie-down straps to actuate the triangular shell in the previous section. Although the attempt was an immature speculative idea, it hinted at the simple actuation scheme in which a continuous bottom hoop provides the actuation forces. To design such shells, this research iterates the steps from numerical form-finding to mechanical detailing (figure 6.11).

To find shells for which the horizontal thrusts are provided by the bottom hoops, a sufficient condition is that the shapes of the Airy stress functions coincide with the shapes of the shells. Such shells are called *self-Airy membranes* (section 2.5). A *self-Airy membrane* provides a convenient feature that any intersection with a horizontal plane locates a hoop.

As a self-Airy membrane is discretized, the force and bending moment can be also visualized, given that its shape is also its Airy stress function. When a smooth self-Airy membrane is discretized into a planar conical mesh, the differences in slopes show the axial forces. Much more interestingly, when the planar mesh is further converted into the flat-to-curved mechanism, vertical *jumps* across the edges emerge. Since the vertical discontinuities in the stress function represent bending moments (Williams & McRobie, 2016), these jumps actually display bending moments. Figure 6.12 shows a simple paraboloid example, which has hollowed-out panels connected by hinges. The hollowed-out voids require the stress function to be planar locally, and the hinges require vertical continuity. The bent bars in figure 6.12c-d are widened according to their bending moments.

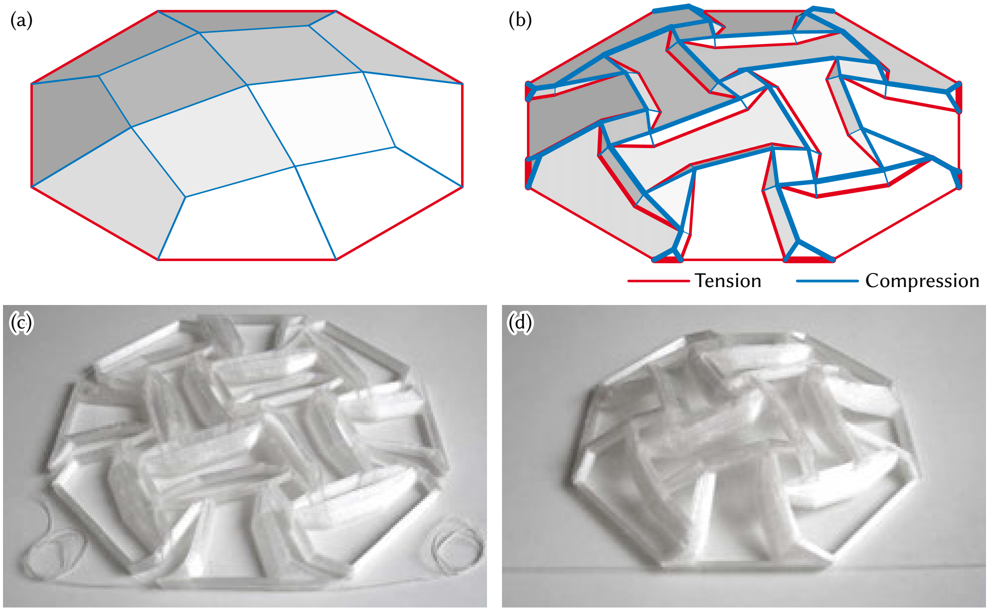

Figure 6.12: Bending moments in a reconfigurable self-Airy shell. (a) The Airy stress function of the initial planar conical mesh. (b) The Airy stress function of the reconfigurable reciprocal frame. (c) Flat configuration. (d) Curved configuration.

Numerical form-finding and mechanism converting. As discussed in section 3.5, a free edge in finding a self-Airy membrane has to be formulated as a *free boundary problem*, in which the exact location of the boundary is not prescribed but part of the solution. Although the free boundary problem adds some complexity, the algorithm of RBFs can handle it as non-linear optimization and deliver a smooth solution (figure 6.11a-b). Then, the smooth surface is discretized into a conical mesh and truncated to leave the singular corners out. The mesh is further unrolled and restructured into a preliminary design of the mechanism (figure 6.11c-f).

Compliant hinges and monostability. For fast validation of the hoop-actuation scheme, the prototype is 3D printed in one piece. Previously, the 3D-printed compliant hinges in chapter 5 were defined by notches, causing intense strains and potentially inducing fatigue failure for some materials (polylactic acid, or PLA). For a more durable design, this section uses thin-walled circular arcs to distribute the strain across a wider area. Figure 6.13 shows how the schematic design based on ideal hinges (the greenish-blue circles) is translated into the producible design (black lines) in which the hinges are replaced by thin flexures.

Furthermore, the mechanism can be monostable instead of bistable. In chapter 5 the panels are solid (figure 6.14a), but here the panels are hollowed out (figure 6.14b). As a result, the base of each reconfigurable unit is not as rigid as in previous examples. In combination with the flexural spring of the compliant hinges, the mechanism can be monostable—the mechanism can bounce back to the original configuration when the hoop tension is removed. The feature of monostability might be helpful since the bottom hoop provides full control of both flat-to-curved and curved-to-flat transformations. The recovery transformation can be done by simply releasing the hoop, so that the mechanism can return to its initial shape.

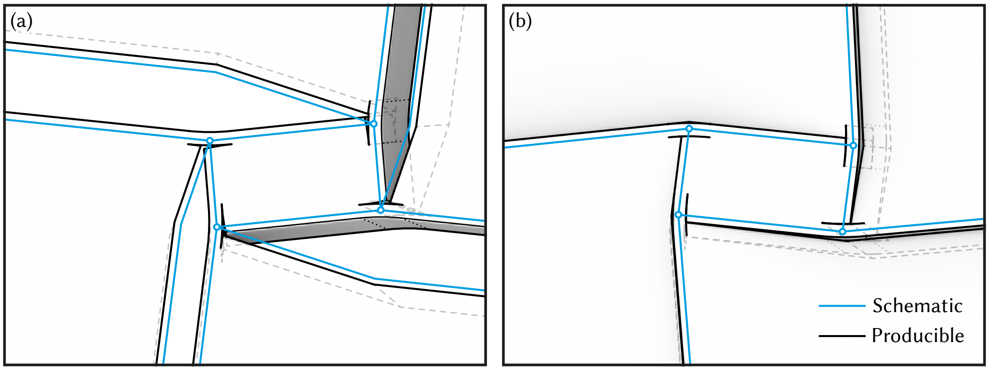

Figure 6.13: Close up of the compliant hinge. (a) Flat configuration. (b) Curved configuration.

Printing and reconfiguring. The section uses a 3D printer (Anycubic Chiron, build volume: 400 × 400 × 450 mm, nozzle diameter: 0.4 mm) for printing the prototypes with the material of glycol-modified polyethylene terephthalate (PET-G). The hinge width is drawn as 1 mm which is the minimal printable width under the used slicer and relevant parameters (Cura ver:3.6.0, *line width* = 0.4 mm, and *horizontal expansion* = −0.2 mm).

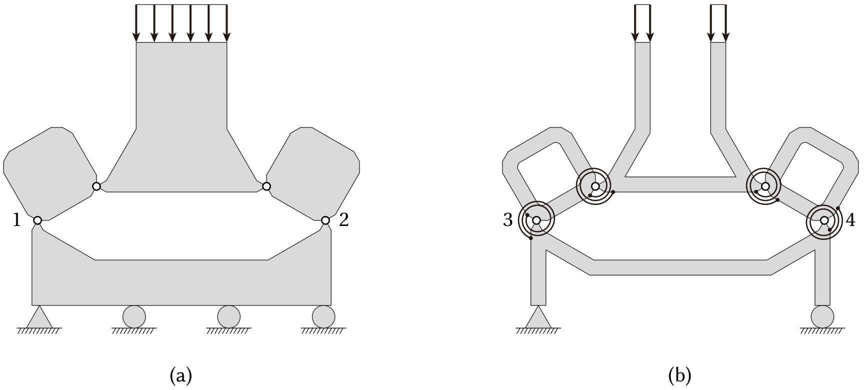

(a) (b)

Figure 6.14: Schematic representations of the reconfigurable units. (a) Bistable reconfigurable unit, in which the solid panels are connected by ideal hinges (hollow circles), the distance between hinges 1 and 2 is rather rigid. (b) Monostable reconfigurable unit, in which the hollowed panels are connected by flexural hinges (black spirals schematically represent the elasticity) and the distance between hinges 3 and 4 is relatively flexible.

Two designs are printed: a free-edge shell and a dome. The former is shown in figure 6.11g-h. Figures 6.15 and 6.16 display the mechanism in larger frames. The other design has also been disclosed in figure 6.12c-d. Figure 6.17 shows the top views of the dome. Deployment of both cases was filmed, the links for the online videos are provided in the figures' captions.

6.4. Discussion

This chapter has presented the design and fabrication of prototypes that integrate the proposed form-finding method and the reconfigurable mechanism. The resulting reconfigurable shells include a 0.8m-span 3D printed one, a 4m-span plywood-built one, and a 0.3m-span hoop-actuated one. Some different design and production processes were also examined in this chapter. Specific learning from the prototyping includes that

- the hexagonal mesh is demonstrated compatible with the reconfigurable mechanism;
- the reconfigurable mechanism can work up to 4 m span;
- both pin and flexural hinges allow for some sleek designs;
- self-Airy membranes can help the design of hoop-actuated mechanism; and
- flexural hinges with hollowed-out panels can make the mechanism monostable.

Figure 6.15: Flat configuration of the free-edge shell

Figure 6.16: Curved configuration of the free-edge shell. The green arrows indicate the external forces applied to the string. A video of the transformation is available at https://vimeo.com/575721997.

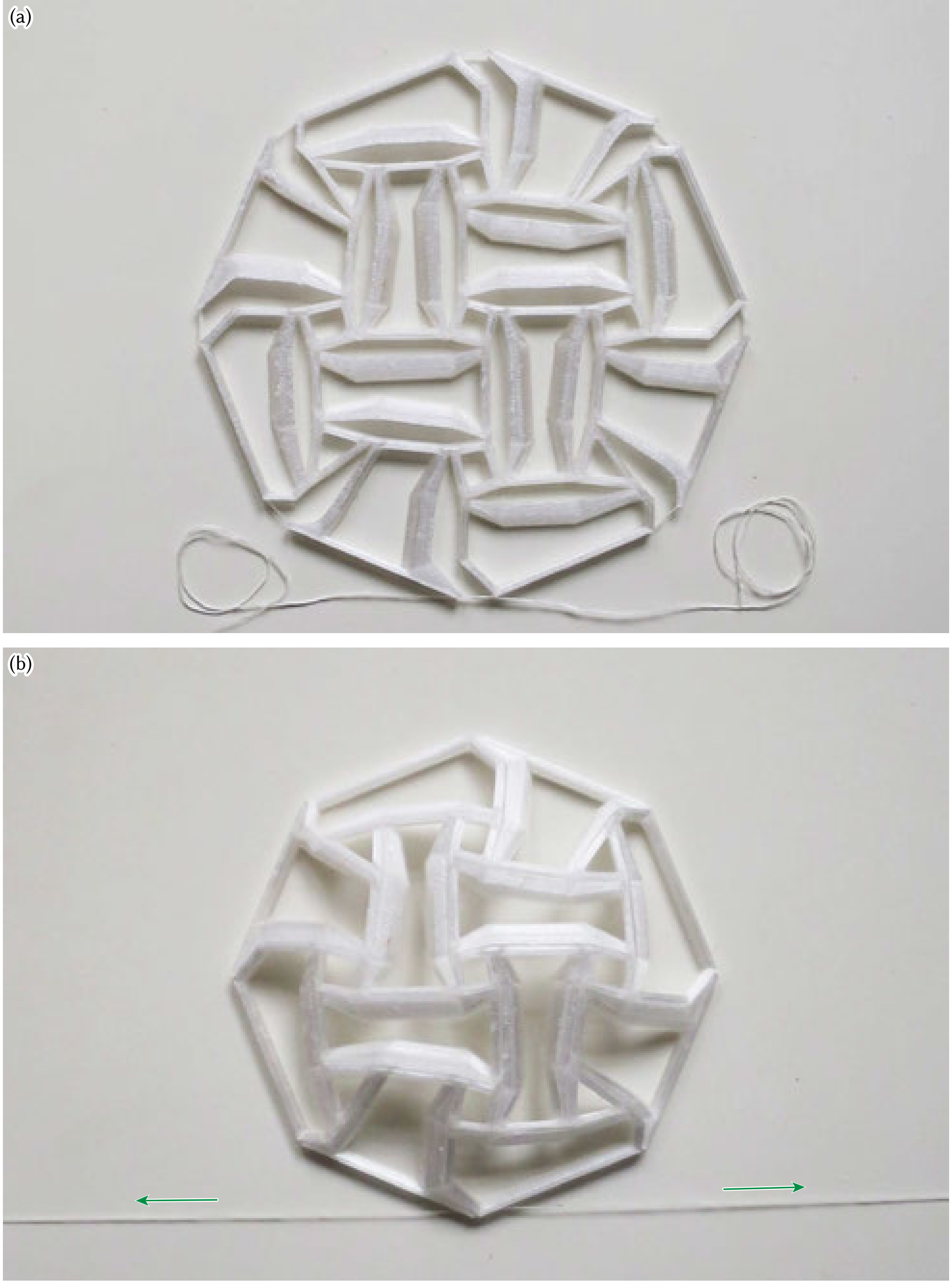

Figure 6.17: Deployment of the hoop-actuated dome. (a) Flat configuration with a loose bottom string. (b) Curved configuration when the string is tightened. The green arrows indicate the external forces applied to the string. A video is available at https://vimeo.com/573955920

7

CONCLUSION

THIS DISSERTATION has presented novel ways of design and fabrication of shell structures. Specifically, designing the membrane shells with smooth radial basis functions (RBFs), discretizing smooth surfaces into principal meshes, displaying the 2D stress tensor fields by discretizing Airy stress functions with and without body forces, and fabricating double-curved surfaces with the flat-to-curved mechanisms. The overarching prototype—the hoop-actuated reconfigurable mechanism—displays an interesting reciprocal frame, in which the deployed structure has a shape identical to the graph of its Airy stress function. The observer can infer the flow of forces from the dihedral angles at the edges.

7.1. CONTRIBUTIONS

The dissertation contributes to the study of shell structures by investigating novel approaches to numerical form-finding and digital fabrication. The form-finding aspect was achieved by closely revisiting the statics of membrane shells, especially the mathematical formulations: the Airy stress function and Pucher's equation. Then, the numerical method of RBFs is adopted to find and represent free-form shells and their stress functions. Theories from discrete differential geometry were applied to discretize free-form shells into economically producible flat panels and extended to discretize stress functions into visually legible force networks. Fabrication was executed by introducing an auxetic mechanism that enables the fabrication of shells in a flat and interconnected configuration. The flat mechanism can be deployed into the double-curved configuration. To validate the mechanism, various prototypes at scales ranging from 0.2 to 4 m were produced. Specifically, the contributions to new knowledge are as follows:

- Identifying the mathematics-based form-finding methods that have a wider range of solution space, including shells that contain both compression and tension stresses (sections 1.1, 3.1).
- Proposing the definition of *self-Airy membranes* and providing some analytical solutions (section 2.5).

- Developing a form-finding algorithm based on radial basis functions (RBFs) that works in two ways: finding the form based on a given stress distribution, and finding the stress distribution based on a given form (section 3.4). The algorithm is also compatible with horizontal body forces (section 3.6).
- Identifying that how a shell is supported might be more important than how its shape curves to resist the ever-changing load (section 3.6).
- Proposing a method to translate continuous stress tensor fields into visually legible force networks by discretizing Airy stress functions into quadrilateral meshes, and customizing the connectivity to fit the given stress distribution (section 4.4).
- Identifying that body forces require Airy stress functions to be discretized into non-planar quadrilateral meshes (section 4.4).
- Inventing a type of bi-stable auxetic mechanism which can perform flat-to-curved transformations (section 5.3.1).
- Proposing the method of the neutral surface for converting a given synclastic surface into a bi-stable mechanism (section 5.3.2).
- Producing reconfigurable prototypes up to a 4 m span (section 6.2).
- Producing a reconfigurable reciprocal frame with legible bending stresses (section 6.3).

7.2. FUTURE WORK

There are, however, some limitations associate with the methods used and developed in this study. In particular, the following unresolved matters may be worth investigating further to make additional contributions to the design and fabrication of shell structures:

- Although the RBFs can bypass limitations induced by the connectivity of conventional meshes, the locations of RBFs' centers and their shape parameters still affect the set of representable functions. A clear strategy to arrange and fine-tune these meta-parameters is desirable.
- The algorithm of RBFs currently excludes bending stresses. It would be more realistic to consider bending in some load cases.
- There does not yet exist a systematic method to translate an anticlastic surface into the bi-stable auxetic mechanism. Therefore, it might be worthwhile to develop one. Otherwise, integrating current flat-to-synclastic mechanisms with other complementary systems (such as deployable cable nets which can easily form anticlastic surfaces) will also broaden the solution set.
- Both algorithms for form-finding and the mechanism design are in the form of *MATLAB* (2018) scripts without user-friendly interfaces. Further development into a robust and user-friendly subroutine is desired.

7.3. FINAL REMARKS

This research focuses on membrane actions and funicular networks of shells. In contrast to beams that have underutilized materials between zones of high *tension* and *compression*, funicular structures are lean. This does not mean that bending moments should be avoided at all costs. For instance, the self-tied structures (e.g., self-anchored suspension bridges, tied-arch bridges, hoop-tied shells in figure 3.17c) have tension members (e.g., cables, ties, hoops) and compression members (e.g., compressed deck, arch, shell) forming simply supported bending-resistant structures. The merit of these self-tied structures is that the spaces between the *tension* and *compression* are available for peoples' activities while minimizing the loads on the foundations.

7.4. PERSONAL REFLECTIONS

Shell structures exhibit astonishing slenderness, especially for a Taiwanese civil engineer. When the shells were popular in Europe and the Americas between the 1920s and the 1970s, Taiwan was ruled by autocratic regimes and experienced only modest economic development. Therefore, Taiwan had little exposure and there was not a single notable instance of such structures. In a way, thin shells are mythical structures for most Taiwanese students in architecture and civil engineering. As a result of this historical and cultural context, the author initially approached this subject with distant awe. However, throughout this research, he progressively understood the relevant theories and contributed his efforts to this subject. The author looks forward to sharing the pleasure of learning about this fascinating structural system and, even more so, to anticipating the construction or conservation of such structures.

REFERENCES

Addis, W. (2007). *Building: 3000 years of design engineering and construction.* London: Phaidon.

Airy, G. B. (1863). On the strains in the interior of beams. *Philosophical Transactions of the Royal Society of London*, *153*, 49–79.

Aldinger, L., Margariti, G., & Suzuki, S. (2018). Tailoring self-formation: Fabrication and simulation of membrane-actuated stiffness gradient composites. In *Proceedings of the IASS annual symposium 2018.* Boston.

Anderson, S. (Ed.). (2004). *Eladio Dieste: Innovation in structural art.* Princeton Architectural Press.

Apushkinskaya, D. (2018). *Free boundary problems: Regularity properties near the fixed boundary* (Vol. 2218). Springer.

Arfken, G. B., Weber, H. J., & Harris, F. E. (2013). *Mathematical methods for physicists* (Seventh Edition ed.). Boston: Academic Press.

Barnes, M. R. (1988). Form-finding and analysis of prestressed nets and membranes. *Computers & Structures*, *30*(3), 685–695.

Biancolini, M. E. (2017). *Fast radial basis functions for engineering applications.* Cham: Springer. doi: https://doi.org/10.1007/978-3-319-75011-8

Billington, D. P. (1983). *The tower and the bridge: The new art of structural engineering.* Princeton University Press.

Block, P., & Ochsendorf, J. (2007). Thrust network analysis: A new methodology for three-dimensional equilibrium. *Journal of the International Association for Shell and Spatial Structures*, *48*(155), 167–173.

Blockley, D. (2012). *Bridges: the science and art of the world's most inspiring structures.* Oxford University Press.

Bobenko, A. I., & Suris, Y. B. (2007). On organizing principles of discrete differential geometry. Geometry of spheres. *Russian Mathematical Surveys*, *62*(1), 1–43. doi: 10.4213/rm5589

Bobenko, A. I., & Suris, Y. B. (2008). *Discrete differential geometry: Integrable structure.* Providence, Rhode Island: American Mathematical Society. doi: http://dx.doi.org/10.1090/gsm/098

Boyd, J. P., & Gildersleeve, K. W. (2011). Numerical experiments on the condition number of the interpolation matrices for radial basis functions. *Applied Numerical Mathematics*, *61*(4), 443–459.

Brown, S. M. (2005). Millennium and beyond. *The Structural Engineer*, *83*(20), 34–42.

BUGA Wood Pavilion. (2019). Retrieved from https://www.icd.uni-stuttgart.de/projects/buga-wood-pavilion-2019/

Buhmann, M. D. (2003). *Radial basis functions.* Cambridge.

Calladine, C. R. (1977). The static–geometric analogy in the equations of thin shell structures. *Mathematical Proceedings of the Cambridge Philosophical Society*, *82*(2), 335–351.

Calladine, C. R. (1989). *Theory of shell structures.* Cambridge University Press.

Calvo-Lópe, J. (Ed.). (2020). *Stereotomy: Stone construction and geometry in Western Europe 1200–1900.* Cham: Birkhäuser.

Carlson, S. C. (2021). Catenary. In *Encyclopædia Britannica.* Retrieved from https://www.britannica.com/science/catenary

Chen, B.-Y., Decu, S., & Verstraelen, L. (2014). Notes on isotropic geometry of production models. *Kragujevac Journal of Mathematics*, *38*(1), 23–33.

Chiang, Y.-C. (2019). Programming flat-to-synclastic reconfiguration. *archiDOCT*, *6*(2), 64–79. Retrieved from http://www.archidoct.net/Issues/vol6_iss2/ArchiDoct_vol6_iss2%2004%20Programming%20Flat%20to%20Synclastic%20Chiang.pdf

Chiang, Y.-C. (2020). *SpatialAuxetic* [MATLAB code]. GitHub repository. Retrieved from https://github.com/ChiangYuChou/SpatialAuxetic

Chiang, Y.-C. (2021). *Maxwell-Rankine stress functions of membrane shells and their relation to that of planar funicular gridshells.* (Manuscript submitted for publication)

Chiang, Y.-C., & Borgart, A. (2022). A form-finding method for membrane shells with radial basis functions. *Engineering Structures*, *251*, 113514. doi: 10.1016/j.engstruct.2021.113514

Chiang, Y.-C., Borgart, A., & Li, Q. (2019). Finding membrane shells subjected to horizontal body forces with radial basis functions. In *Proceedings of the IASS annual symposium 2019 and Structural Membranes 2019* (pp. 1556–1563). Barcelona. Retrieved from https://www.ingentaconnect.com/content/iass/piass/2019/00002019/00000018/art00022

Chiang, Y.-C., Buskermolen, P., & Borgart, A. (2021). Discretised Airy stress functions and body forces. In *Advances in architectural geometry 2020* (pp. 62–83). Champs-sur-Marne. Retrieved from https://thinkshell.fr/wp-content/uploads/2019/10/AAG2020_04_Chiang.pdf

Chiang, Y.-C., Mostafavi, S., & Bier, H. (2018). Assembly of shells with bi-stable mechanism. In *Advances in architectural geometry 2018* (pp. 54–71). Gothenburg. Retrieved from https://research.chalmers.se/en/publication/504188

Chilton, J. (2000). *The engineer's contribution to contemporary architecture: Heinz Isler.*

Thomas Telford.

Collins, G. R. (1963). Antonio Gaudí: Structure and form. *Perspecta*, 63–90. Retrieved from https://www.jstor.org/stable/1566905

Correa, D., Krieg, O. D., & Meyboom, A. (2019). Beyond form definition: Material informed digital fabrication in timber construction. In *Digital wood design* (pp. 61–92). Springer.

Cremona, L. (1875). *Elements of projective geometry.* Clarendon Press.

Csonka, P. (1987). *Theory and practice of membrane shells.* Düsseldorf: VDI Verlag.

Culmann, C. (1866). *Die graphische statik.* Zürich: Meyer & Zeller.

Curry, H. B. (1944). The method of steepest descent for non-linear minimization problems. *Quarterly of Applied Mathematics*, *2*(3), 258–261.

Faber, C. (1963). *Candela: The shell builder.* Reinhold Publishing Corporation.

Frampton, K. (1983). Toward a critical regionalism: Six points for an architecture of resistance. In H. Foster (Ed.), *The anti-aesthetic: Essays on postmodern culture.* Port Townsend, Washington: Bay Press.

Frampton, K. (1995). *Studies in tectonic culture: The poetics of construction in nineteenth and twentieth century architecture.* Cambridge, Massachusetts: MIT Press.

Fraternali, F., Angelillo, M., & Fortunato, A. (2002). A lumped stress method for plane elastic problems and the discrete-continuum approximation. *International Journal of Solids and Structures*, *39*(25), 6211–6240. doi: 10.1016/S0020-7683(02)00472-9

Friedman, A. (2000). Free boundary problems in science and technology. *Notices of the American Mathematical Society*, *47*(8), 854–861.

Funicular structure. (2021). In *Encyclopædia Britannica.* Retrieved from https://www.britannica.com/technology/funicular-structure

Glymph, J., Shelden, D., Ceccato, C., Mussel, J., & Schober, H. (2004). A parametric strategy for free-form glass structures using quadrilateral planar facets. *Automation in Construction*, *13*(2), 187–202.

Grasshopper 3D [Computer software]. (2020). Retrieved from https://www.grasshopper3d.com/

Green, A. E., & Zerna, W. (1968). *Theoretical elasticity.* New York: Dover.

Guseinov, R., Miguel, E., & Bickel, B. (2017). CurveUps: Shaping objects from flat plates with tension-actuated curvature. *ACM Transactions on Graphics*, *36*(4).

Haghpanah, B., Salari-Sharif, L., Pourrajab, P., Hopkins, J., & Valdevit, L. (2016). Architected materials: Multistable shape-reconfigurable architected materials. *Advanced Materials*, *28*(36), 8065–8065.

Heyman, J. (1977). *Equilibrium of shell structures.* Oxford: Oxford University Press.

Heyman, J. (1995). *The stone skeleton: Structural engineering of masonry architecture.* Cambridge University Press.

Holgate, A. (1997). *The art of structural engineering: The work of Jörg Schlaich and his team.* Fellbach, Germany: Edition Axel Menges.

House for Hippopotamus, Zoo Berlin. (1994). Retrieved from https://www.sbp.de/en/project/house-for-hippopotamus-zoo-berlin/

Huang, N., & Vahidi, B. (1971). Snap-through buckling of two simple structures. *International Journal of Non-Linear Mechanics*, *6*(3), 295–310.

Jourdan, D., Skouras, M., Vouga, E., & Bousseau, A. (2021). Printing on fabric meta-material for self-shaping architectural models. In *Advances in architectural geometry 2020* (pp. 285–264). Champs-sur-Marne.

Kilian, M., Pellis, D., Wallner, J., & Pottmann, H. (2017). Material-minimizing forms and structures. *ACM Transactions on Graphics*, *36*(6). doi: 10.1145/3130800.3130827

Konaković, M., Crane, K., Deng, B., Bouaziz, S., Piker, D., & Pauly, M. (2016). Beyond developable: Computational design and fabrication with auxetic materials. *ACM Transactions on Graphics*, *35*(4).

Konaković-luković, M., Konaković, P., & Pauly, M. (2018). Computational design of deployable auxetic shells. In *Advances in architectural geometry 2018* (pp. 94–111). Gothenburg. Retrieved from https://research.chalmers.se/en/publication/504188

KUKA|prc [Computer software]. (2019). Retrieved from https://www.robotsinarchitecture.org/kuka-prc

Leach, N., Turnbull, D., & Williams, C. J. (2004). *Digital tectonics.* Wiley.

Levitt, T. (2002). Creativity is not enough. *Harvard Business Review*, *80*, 137–144.

Liddell, I. (2015). Frei Otto and the development of gridshells. *Case Studies in Structural Engineering*, *4*, 39–49. doi: 10.1016/j.csse.2015.08.001

Liu, J., Liu, J., Eggers, M., & Sabin, J. E. (2018). Responsive kirigami: Context-actuated hinges in folded sheet systems. In *Proceedings of the symposium on simulation for architecture and urban design.* Delft.

Liu, Y., Pottmann, H., Wallner, J., Yang, Y.-L., & Wang, W. (2006). Geometric modeling with conical meshes and developable surfaces. *ACM Transactions on Graphics*, *25*(3), 681–689. doi: 10.1145/1141911.1141941

MATLAB [Computer software]. (2018). Retrieved from https://www.mathworks.com/products/matlab.html

Maxwell, C. (1864). On reciprocal figures and diagrams of forces. *The London, Edinburgh, and Dublin Philosophical Magazine and Journal of Science*, *27*(182), 250–261. doi: 10.1080/14786446408643663

Maxwell, C. (1868). On reciprocal diagrams in space and their relation to Airy's function of stress. *Proceedings of the London Mathematical Society*, *1*(1), 58–63.

Maxwell, C. (1870). On reciprocal figures, frames, and diagrams of forces. *Earth and Environmental Science Transactions of the Royal Society of Edinburgh*, *26*(1), 1–40.

McKitterick, D. (1995). *The making of the Wren Library: Trinity College, Cambridge.* Cambridge University Press.

Mesnil, R., Douthe, C., Baverel, O., & Gobin, T. (2018). Form finding of nexorades using the translations method. *Automation in Construction*, *95*, 142–154. doi: https://doi.org/10.1016/j.autcon.2018.08.010

Mesnil, R., Douthe, C., Baverel, O., & Leger, B. (2017). Marionette meshes: Modelling free-form architecture with planar facets. *International Journal of Space Structures*, *32*(3-4), 184–198. doi: 10.1177/0266351117738379

Meyer, C., & Sheer, M. (2005). Do concrete shells deserve another look? *Concrete International*, *27*(10), 43–50.

Michiels, T., Adriaenssens, S., & Dejong, M. (2019). Form finding of corrugated shell structures for seismic design and validation using non-linear pushover analysis. *Engineering Structures*, *181*, 362–373.

Miki, M., Igarashi, T., & Block, P. (2015). Parametric self-supporting surfaces via direct computation of Airy stress functions. *ACM Transactions on Graphics*, *34*(4). doi: 10.1145/2766888

Millar, C., Mitchell, T., Mazurek, A., Chhabra, A., Beghini, A., McRobie, A., & Baker, W. (2021). On funicular gridshells and Airy stress functions. In *Proceedings of the IASS annual symposium 2021.*

Mitchell, W. J. (2001). Roll over Euclid: How Frank Gehry designs and builds. In J. F. Ragheb (Ed.), *Frank Gehry: Architect* (pp. 353–363). New York: Guggenheim Museum Publications.

Nervi, P. L. (1956). *Structures.* New York: F.W. Dodge.

Ochsendorf, J., & Block, P. (2014). Exploring shell forms. In S. Adriaenssens, P. Block, D. Veenendaal, & C. Williams (Eds.), *Shell structures for architecture* (pp. 7–12). Abingdon: Routledge.

Picon, A. (2003). Architecture, science, technology, and the virtual realm. In A. Picon & A. Ponte (Eds.), *Architecture and the sciences: Exchanging metaphors* (pp. 292–313). Princeton Architectural Press.

Pinto, C., & Fonseca, J. (2020). Effects of initial form-finding models on shape, force paths, and buckling of anti-funicular shells with free edges. *Structures*, *23*, 472–480.

Plunkett, J. W., & Mueller, C. T. (2015). Thin concrete shells at MIT Kresge Auditorium and the 1954 conference. In *Proceedings of the 5th international congress on construction history.* Chicago.

Porteous, I. R. (2001). *Geometric differentiation: For the intelligence of curves and surfaces.*

Cambridge University Press.

Pottmann, H. (2013). Architectural geometry and fabrication-aware design. *Nexus Network Journal*, *15*(2), 195–208.

Pottmann, H., Asperl, A., Hofer, M., & Kilian, A. (2007). *Architectural geometry*. Bentley Institute Press.

Pottmann, H., Eigensatz, M., Vaxman, A., & Wallner, J. (2015). Architectural geometry. *Computers & Graphics*, *47*, 145–164. doi: 10.1016/j.cag.2014.11.002

Pottmann, H., & Liu, Y. (2007). Discrete surfaces in isotropic geometry. In *IMA international conference on mathematics of surfaces* (pp. 341–363). Berlin: Springer. doi: 10.1007/978-3-540-73843-5_21

Pottmann, H., Liu, Y., Wallner, J., Bobenko, A., & Wang, W. (2007). Geometry of multilayer freeform structures for architecture. *ACM Transactions on Graphics*, *26*(3).

Pottmann, H., & Opitz, K. (1994). Curvature analysis and visualization for functions defined on Euclidean spaces or surfaces. *Computer Aided Geometric Design*, *11*(6), 655–674.

Pottmann, H., & Wallner, J. (2008). The focal geometry of circular and conical meshes. *Advances in Computational Mathematics*, *29*(3), 249–268. doi: 10.1007/s10444-007-9045-4

Pugnale, A., Echenagucia, T. M., & Sassone, M. (2014). Computational morphogenesis: Design of freeform surfaces. In S. Adriaenssens, P. Block, D. Veenendaal, & C. Williams (Eds.), *Shell structures for architecture* (pp. 225–236). Abingdon: Routledge.

Rafsanjani, A., & Pasini, D. (2016). Bistable auxetic mechanical metamaterials inspired by ancient geometric motifs. *Extreme Mechanics Letters*, *9*, 291–296.

Reichert, S., Menges, A., & Correa, D. (2015). Meteorosensitive architecture: Biomimetic building skins based on materially embedded and hygroscopically enabled responsiveness. *Computer-Aided Design*, *60*, 50–69. doi: 10.1016/j.cad.2014.02.010

Rippmann, M., & Block, P. (2011). Digital stereotomy: Voussoir geometry for freeform masonry-like vaults informed by structural and fabrication constraints. In *Proceedings of the IABSE-IASS symposium.*

Rippmann, M., & Block, P. (2013). Funicular funnel shells. In C. Gengnagel, A. Kilian, J. Nembrini, & F. Scheurer (Eds.), *Proceedings of the design modeling symposium Berlin 2013* (pp. 75–89). Berlin, Germany.

Sadd, M. H. (2009). *Elasticity: Theory, applications, and numerics* (2nd ed.). Burlington: Academic Press.

Schaedler, T. A., & Carter, W. B. (2016). Architected cellular materials. *Annual Review of Materials Research*, *46*(1), 187-210. doi: 10.1146/annurev-matsci-070115-031624

Schek, H.-J. (1974). The force density method for form finding and computation of general networks. *Computer Methods in Applied Mechanics and Engineering*, *3*(1), 115–134. doi:

10.1016/0045-7825(74)90045-0

Schlaich, J. (2004). Conceptual design of light structures. *Journal of the International Association for Shell and Spatial Structures*, *45*(3), 157–168.

Schlaich, J., & Schober, H. (1997). Glass roof for the hippo house at the Berlin Zoo. *Structural Engineering International*, *7*(4), 252–254.

Schling, E. (2018). Design and construction of curved support structures with repetitive parameters. In *Advances in architectural geometry 2018.*

Schumacher, P. (2014). Tectonic articulation: Making engineering logics speak. *Architectural Design*, *84*(4), 44–51.

Sechelmann, S., Rörig, T., & Bobenko, A. I. (2012). Quasiisothermic mesh layout. In *Advances in architectural geometry 2012* (pp. 243–258). Paris.

Tachi, T. (2013). Designing freeform origami tessellations by generalizing Resch's patterns. *Journal of Mechanical Design*, *135*(11), 111006. doi: 10.1115/1.4025389

Tellier, X., Douthe, C., Hauswirth, L., & Baverel, O. (2020). Linear-Weingarten membranes with funicular boundaries. *Structural Concrete.*

Tibbits, S. (2014). 4D printing: Multi-material shape change. *Architectural Design*, *84*(1), 116–121.

Timoshenko, S. P., & Woinowsky-Krieger, S. (1959). *Theory of plates and shells.* McGraw-Hill.

van Manen, T., Janbaz, S., & Zadpoor, A. A. (2017). Programming 2D/3D shape-shifting with hobbyist 3D printers. *Materials Horizons*, *4*(6), 1064–1069.

Varignon, P. (1725). *Nouvelle mecanique ou statique: Dont le projet fut donné en m. dc. lxxxvii.* Jombert.

Veenendaal, D., & Block, P. (2012). An overview and comparison of structural form finding methods for general networks. *International Journal of Solids and Structures*, *49*(26), 3741–3753. doi: 10.1016/j.ijsolstr.2012.08.008

von Buelow, P. (2007). *Genetically engineered architecture: Design exploration with evolutionary computation.* Saarbrücken, Germany: VDM Verlag.

von Meiss, P. (2000). The aesthetics of gravity. *arq: Architectural Research Quarterly*, *4*(3), 237–246. doi: 10.1017/S1359135500000269

Vouga, E., Höbinger, M., Wallner, J., & Pottmann, H. (2012). Design of self-supporting surfaces. *ACM Transactions on Graphics*, *31*(4). doi: 10.1145/2185520.2185583

Williams, C. (2014). What is a shell? In S. Adriaenssens, P. Block, D. Veenendaal, & C. Williams (Eds.), *Shell structures for architecture* (pp. 21–32). Abingdon: Routledge.

Williams, C., & McRobie, A. (2016). Graphic statics using discontinuous Airy stress functions. *International Journal of Space Structures*, *31*(2-4), 121–134. doi: 10.1177/0266351116660794

Young, A. E. (1909). On a certain class of isothermic surfaces. *Transactions of the American Mathematical Society*, *10*(1), 79–94.

Zadravec, M., Schiftner, A., & Wallner, J. (2010). Designing quad-dominant meshes with planar faces. *Computer Graphics Forum*, *29*(5), 1671–1679.

Zipkin, P. (2001). The limits of mass customization. *MIT Sloan Management Review*, *42*(3), 81–87.

INDEX

Curriculum Vitæ

Yu-Chou Chiang

姜毓洲

1987-10-21	Born in Taoyuan, Taiwan.

Education

2006–2010	Bachelor of Science in Civil Engineering with a Minor in Economics National Taiwan University
2010–2012	Master of Science in Hydraulic Engineering National Taiwan University
2017–2022	Candidate for Doctor of Philosophy Delft University of Technology *Thesis:* Design and Fabrication of Shell Structures: Aided by radial basis functions and reconfigurable mechanisms *Promotor:* Prof.dr. M. Overend and Dr.ir. F. Veer

Awards

2008 & 2009	The Presidential Award, National Taiwan University
2010	The Dean's List Award, National Taiwan University
2012	Best Design Project Tutor, Dept. of Civil Engineering, National Taiwan University
2016	Scholarship to Study Abroad, Taiwan Ministry of Education

Journal articles

2022 **Chiang, Y.-C.** & Borgart, A. (2022). A form-finding method for membrane shells with radial basis functions. *Engineering Structures, 251,* 113514. https://doi.org/10.1016/j.engstruct.2021.113514

2019 **Chiang, Y.-C.** (2019). Programming flat-to-synclastic reconfiguration. *archiDOCT, 6*(2), 64–79. http://www.archidoct.net/Issues/vol6_iss2/ArchiDoct_vol6_iss2%2004%20Programming%20Flat%20to%20Synclastic%20Chiang.pdf

2018 **Chiang, Y.-C.,** Bier, H., & Mostafavi, S. (2018). Design to robotic assembly: An exploration in stacking. *Frontiers in Digital Humanities, 5.* https://doi.org/10.3389/fdigh.2018.00023

Conference papers

2021 Huang, Z., **Chiang, Y.-C.**, & Sabin, J. E. (2021) Automating Bi-Stable Auxetic Patterns for Polyhedral Surface. In *ACADIA2021 Realignments: Toward Critical Computation.*

Chiang, Y.-C., Buskermolen, P., & Borgart, A. (2021). Discretised Airy stress functions and body forces. In *Advances in Architectural Geometry 2020* (pp. 62–83). Champs-sur-Marne, France. https://thinkshell.fr/wp-content/uploads/2019/10/AAG2020_04_Chiang.pdf

2019 **Chiang, Y.-C.,** Borgart, A., & Li, Q. (2019). Finding membrane shells subjected to horizontal body forces with radial basis functions. In *IASS Annual Symposium 2019–Structural Membranes 2019* (pp. 1556–1563). Barcelona, Spain. https://www.ingentaconnect.com/content/iass/piass/2019/00002019/00000018/art00022

2018 **Chiang, Y.-C.,** Mostafavi, S., & Bier, H. (2018). Assembly of shells with bistable mechanism. In *Advances in Architectural Geometry 2018* (pp. 54–71). Gothenburg, Sweden. https://research.chalmers.se/en/publication/504188

Manuscript

2021 **Chiang, Y.-C.** (2021). *Maxwell-Rankine stress functions of membrane shells and their relation to that of planar funicular gridshells* [Manuscript submitted for publication].

Github repository

2020 **Chiang, Y.-C.** (2020). *SpatialAuxetic* [MATLAB code]. GitHub repository. https://github.com/ChiangYuChou/SpatialAuxetic

22#03

Design and Fabrication of Shell Structures

Aided by Radial Basis Functions and Reconfigurable Mechanisms

Yu-Chou Chiang

Shell structures carry loads with their thin yet curved shapes. Being thin means shells require little material, which is desirable for minimizing embodied carbon footprints. However, the feature of being curved implies shells require immense effort to design and fabricate. To address the challenges, this dissertation consists of three parts: developing a design algorithm based on radial basis functions (RBFs), inventing a fabrication technique based on reconfigurable mechanisms, and producing prototypes based on the new algorithm and mechanism.

The first part of this dissertation introduces a new algorithm based on RBFs for designing smooth membrane shells, which is more versatile than existing methods. The algorithm can generate membranes with both tensile and compressive stresses. It can also tweak an initial shape to meet free-edge conditions. It can also incorporate horizontal loads in the form-finding process.

The second part of the dissertation presents a new system of flat-to-curved mechanisms, which allows a shell to be fabricated in a flat configuration and deployed into a double-curved state. Such a mechanism consists of panels connected by tilted hinges. The mechanism can contract non-homogeneously and change its Gaussian curvature.

The last part of this dissertation demonstrates the integral application of the RBFs form-finding algorithm and the flat-to-curved mechanisms. The prototypes designed and produced deliver form-found shapes that have spans ranging from 0.2 to 4 meters.

This dissertation contributes to the development and distribution of shell structures by developing computer algorithms and digital fabrication techniques to minimize the hurdles of designing and fabricating shell structures.

A+BE | Architecture and the Built Environment | TU Delft BK